Towards the industrial use of synchrotron x-ray nano-tomography for 3D integration failure analysis

Alexandra Fraczkiewicz

Communauté UNIVERSITÉ Grenoble Alpes

THÈSE

Pour obtenir le grade de

DOCTEUR DE LA COMMUNAUTÉ UNIVERSITÉ GRENOBLE ALPES

Spécialité : PHYSIQUE DES MATERIAUX

Arrêté ministériel : 25 mai 2016

Présentée par

Alexandra FRACZKIEWICZ

Thèse dirigée par **Pierre BLEUET**, UGA

préparée au sein du **Laboratoire Laboratoire d'Electronique et de Technologie de l'Information (LETI - CEA)**
dans **l'École Doctorale Physique**

Développement de la tomographie par rayons X en synchrotron pour l'industrie : application à l'analyse de défaillance en intégration 3D

Towards the industrial use of synchrotron x-ray nano-tomography for 3D integration failure analysis

Thèse soutenue publiquement le **12 décembre 2017**,
devant le jury composé de :

Monsieur MARCO CANTONI
DIRECTEUR DE RECHERCHE, ECOLE POLYTECH. FEDERALE LAUSANNE SUISSE, Rapporteur
Madame FRANÇOISE PEYRIN
DIRECTRICE DE RECHERCHE, INSERM DELEGATION RHONE-ALPES, AUVERGNE, Rapporteur
Monsieur LUC SALVO
PROFESSEUR, GRENOBLE INP, Président
Monsieur DE VOS JOERI
INGENIEUR DE RECHERCHE, IMEC - BELGIQUE, Examinateur

Remerciements

J'aimerais ici en tout premier lieu remercier Jean Claude Royer et Nicolas Lhermet, les deux directeurs successifs du Service de Caractérisation des Matériaux et Composants (SCMC) au sein duquel s'est déroulée ma thèse. Merci de m'avoir accueillie dans ce service, où j'ai énormément grandi et découvert un domaine qui me passionne.

Je tiens à exprimer toute ma gratitude aux membres de mon jury. Merci à Marco Cantoni et à Françoise Peyrin d'avoir accepté de relire mon manuscrit et d'y avoir apporté leurs commentaires. Merci également à Joeri De Vos et à Luc Salvo d'avoir participé à ce jury, et tout particulièrement à Luc d'avoir accepté d'en être le président. Enfin, merci à Ennio Capria d'avoir accepté notre invitation à rejoindre ce jury. La discussion menée durant la soutenance a été très stimulante, et enrichie de vos contributions venues de milieux bien différents.

Cette thèse n'aurait pas été la même sans mon directeur de thèse et encadrant, Pierre Bleuet, ainsi que Frédéric Lorut, qui a co-encadré ce travail. Je tiens ici à les remercier chaleureusement pour leur soutien au cours de ces trois années. Vous avez su me laisser libre de poursuivre ma thèse dans la direction qui me passionnait sans pour autant que je me sente perdue. Vous m'avez permis d'en faire réellement ma thèse. Pierre, merci pour tes explications, ta patiente, et bien sûr ton sens de l'humour et de la répartie ! Je tiens ici encore une fois à remercier Ennio, pour sa qualité de soutien « ESRF ». Tu nous as énormément aidés, et as toujours été là pour me rendre la vie plus facile.

Ce travail s'est déroulé au sein du CEA, avec une collaboration forte avec l'ESRF et ST Microelectronics. Beaucoup de personnes ont accepté de jouer le jeu, de croire au projet, que ce soit du côté matériau ou caractérisation. Je les en remercie vivement. Merci aux équipes de ID01, ID16A, et ID19 pour leur aide et conseils, et merci tout particulièrement à Julio Da Silva, Peter Cloetens, Maxime Hubert, et Marie Ingrid Richard pour avoir répondu à mille questions ! Un grand merci pour votre disponibilité et votre patience. Merci également aux équipes intégration 3D du CEA et de ST, et tout particulièrement à Sandrine Lhostis et Stéphane Moreau pour leurs explications et leur intérêt pour mon travail. Merci à Amandine Jouve, Frank Fournel, Thierry Mourier et Nicolas Bresson d'avoir répondu présents aux « appels aux dons d'échantillons » ! Merci également à David Bouchu pour toutes les discussions passionnantes que l'on a eues au coin du PFIB. Et puisque l'on parle du PFIB, un grand merci à Guillaume Audoit pour m'avoir formée sur cette machine et avoir répondu à toutes mes questions. Merci au PFIB lui-même, avec qui on a partagé des moments forts et/ou particulièrement frustrants ! J'ai aussi eu l'opportunité durant ce travail d'encadrer un excellent stagiaire, Pierre Olivier Autran, que je remercie chaleureusement ici pour son travail et cette expérience enrichissante.

J'ai eu la chance de faire ma thèse dans un grand laboratoire, et ai ainsi pu côtoyer un grand nombre de personnes d'horizons différents. Je tiens donc ici à remercier toute l'équipe de la PFNC, tous acronymes barbares confondus. Merci pour les discussions en salle café ou dans les couloirs. Merci tout particulièrement au groupe de thésards et post-docs, ainsi qu'à The Office of Sin, ces trois années n'auraient pas été les mêmes sans vous : Aurèle, Amandine, Lynda, Tristan, Edouard, Audrey, Maxime, Laszlo, Luis, Victor, Andrea, Julien, Loïc, Martin, Tony, et Rémy (mais nous y reviendrons). Zineb, merci pour les lundi, c'était un moment fort de ma semaine ! Constantin, pour les petites discussions qui font du bien. Isabelle, un immense merci pour ta présence, ton soutien, et les pauses cafés virtuelles ou non, bien méritées ou seulement nécessaires. Enfin, à tous, à très bientôt !

Un grand merci à tout mon entourage d'avoir été là, dans les moments funs et moins funs. Merci à la rue Chenoise, Manon, Marie, Philippe, et Arnaud, pour le Tonneau, le Dr D, et le gap inexpliqué entre minuit et 5h du mat. Milie, merci d'être toi, merci d'être venue et merci d'être toujours là. Un gigantesque merci à mes parents, Anna et Georges, qui me guident et me soutiennent de manière exceptionnelle, et qui osent maintenir que c'est normal. Merci à Hugoland. A Mathieu, mon frère, pour les discussions toujours sans fin, mais parfois avec un sens. A Suzy, pour ta gentillesse et ton indulgence envers les jeux de mots. Et à Hugo, qui nous apporte à tous tant de joie.

Enfin, merci à Rémy, qui a su croire en moi au point de me convaincre.

And now, for something completely different ...
Monty Python

Contents

General introduction **1**

Introduction générale **5**

1 Characterization for 3D integration **11**
1.1 Towards 3D integration . . . 12
1.2 Objects of interest . . . 15
1.2.1 Through Silicon Via (TSV) . . . 16
1.2.2 Wafer-to-wafer (W2W) bonding . . . 16
1.2.3 Copper pillar (CuP) . . . 18
1.3 Characterization methods . . . 20
1.3.1 Characterization needs . . . 20
1.3.2 Strain measurement method . . . 20
1.3.3 Imaging methods . . . 20

2 Electron and Ion based microscopes **23**
2.1 General overview and relevant values . . . 24
2.2 Sources of electrons and ions . . . 26
2.2.1 Electron guns . . . 26
2.2.2 Ion guns . . . 28
2.3 Objects/matter interactions and applications . . . 30
2.3.1 Milling . . . 32
2.3.2 Matter deposition . . . 35
2.3.3 Imaging . . . 35
2.4 Applications of Focused Ion Beam microscopes . . . 37
2.4.1 Slice and View procedure . . . 37
2.4.2 Sample preparation: lift-out procedures . . . 40

3 X-ray imaging methods **45**
3.1 Elements of x-ray physics . . . 46
3.1.1 Obtaining an x-ray beam . . . 46
3.1.2 X-ray/matter interactions . . . 53
3.2 Experimental setups . . . 57
3.2.1 ID16A: a nano-tomography beamline . . . 58
3.2.2 ID19: a versatile tool for coherent imaging and diffraction . . . 60
3.2.3 ID01: Local strain measurement . . . 61
3.3 X-ray transmission 3D imaging . . . 62
3.3.1 2D image formation . . . 62
3.3.2 Obtaining a 3D reconstruction . . . 70
3.3.3 Sample Preparation . . . 74

3.4 Strain measures by Bragg diffraction . . . 76
3.4.1 Monochromatic Bragg Diffraction . . . 76
3.4.2 The ID01 workflow . . . 78
3.4.3 Sample Preparation . . . 82

4 Development of 3D imaging in a single column PFIB 85
4.1 Automation of the data acquisition . . . 86
4.1.1 The iFast software . . . 86
4.1.2 Data acquisition workflow . . . 88
4.2 Data post-processing . . . 94
4.2.1 Calculation of the actual slicing step . . . 96
4.2.2 Slices registration . . . 96
4.2.3 Volume re-sampling . . . 98
4.3 Results . . . 99
4.4 Limits of the technique and possible improvements . . . 104
4.5 Conclusion . . . 107

5 Contribution to the ID16A workflow for 3D integration 111
5.1 Original ID16A workflow . . . 112
5.2 New sample preparation scheme . . . 114
5.2.1 New sample supports . . . 115
5.2.2 Making the most of the sample preparation and installation . 115
5.3 Reduction of the number of projections . . . 123
5.4 Automation of the post-processing . . . 126
5.5 Time gain and discussion . . . 128
5.6 Application to 3D integration imaging . . . 130
5.6.1 Imaging of a large number of post-electromigration samples . 130
5.6.2 Morphology study on copper pillars . . . 133
5.6.3 Towards a larger field of view . . . 137
5.7 Conclusion . . . 139

6 Local strain measurements in stacks 143
6.1 Hybrid bonding stack strain measure in silicon . . . 144
6.1.1 Simultaneous observation of two silicon layers . . . 144
6.1.2 Strain maps and morphology correlation . . . 146
6.2 Direct bonding in-situ strain measure in copper . . . 148
6.3 Conclusion . . . 151

General conclusion and perspectives 153

Conclusion générale et perspectives 157

Bibliography 161

List of abbreviations

3Di	3D integration
CuP	Copper pillar
EBID	Electron Beam Induced Deposition
ESRF	European Synchrotron Radiation Facility
FIB	Focused Ion Beam
GIS	Gas Insertion System
IBID	Electron Beam Induced Deposition
IC	Integrated Circuit
ID	Insertion Device
ICP	Inductively Coupled Plasma
IRT	Institut de Recherche Technologique
KB	Kirkpatrick-Baez (mirror)
LMIS	Liquid Metal Ion Source
PFIB	Plasma Focused Ion Beam
ROI	Region Of Interest
SAC	SnAgCu alloy
SaV	Slice and View
SE	Secondary Electron
SEM	Scanning Electronic Microscope
SI	Secondary Ion
TEM	Transmission Electron Microscope
TSV	Through Silicon Via
W2W	Wafer to Wafer

General introduction

In the microelectronics industry, one of the main areas of interest for development has been, in the last 50 years, to reduce the size of the devices, at every scale. So far, the main strategy to do so has been to reduce the size of the transistors, which triggered the reduction of the connections size. This allows to increase the transistors density, reduce the device footprint, and therefore to increase the global performances of the device. Today however, we face the limits of this miniaturization, both because the transistors size reaches physics limits and because the corresponding connections length increases the Joule heating too much, increasing the signal propagation time.

To overcome this issue, another geometry for microelectronic devices has been developed, since the 1980s. It relies on stacking the dies in the vertical direction, instead of setting them next to one another. This technology, called 3D integration (3Di), allows both for the reduction of connection length and the global device footprint, without reducing the transistors size. As such, it has been of growing interest in the last ten years, both in the academical and industrial communities [1]. Figure 1 confirms this trend: the number of articles answering to the keywords "3D integration" and the typical objects it features has been constantly increasing since the 1980s.

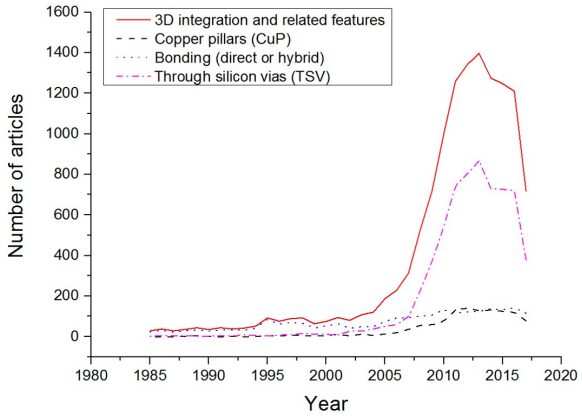

Figure 1: Number of articles per year answering to the keyword "3D integration" or keywords connected to 3D integration, such as "Hybrid bonding", "Direct bonding", "copper pillars", "copper bumps", "copper pillars", and "through silicon vias", as found in the Scopus database (*https: //www.scopus.com*)

This new direction of development rises new difficulties. The geometry being different from previous technologies, new connections had to be designed. Among them, Through Silicon Vias (TSVs) allow for connections between two sides of a given wafer or die, and have been widely investigated. Their fabrication process

is today mostly mastered, and the mechanisms that govern it are well-known. To connect dies and wafers together, other objects, such as copper pillars or hybrid bonding, are used. They are still under development, and their characterization, be it electrical, mechanical, of morphological, is of high value for the process and failure analysis communities. We here focus on those specific objects, and more precisely on several micron wide copper pads and several tens of micron wide copper pillars.

Electrical or mechanical failure tests allow to obtain information about the global functioning of the device, but do not provide information about the origin of a failure. Imaging, on the contrary, provides information about the morphology of the device, that can be linked to its further behavior. In practice, the observation of defects (voids for example) at the interface of wafer to wafer bonding is crucial for the monitoring of the bonding process and reduce the risk of failure. Such studies necessitate a routine imaging process, which allow to obtain easy to process statistical information.

Classically, in the field of microelectronics, such morphological characterizations can be performed on SEMs (Scanning Electron Microscopes) or TEMs (Transmission Electron Microscopes). However, as the geometry of the observed objects is not the same, classical imaging methods must be adapted. In fact, the imaging of 3Di devices is quite demanding, due to several reasons. (i) The objects to characterize are in three dimensions. Although they offer high reoslution information (up to the nanometer for SEM and the angstrom for TEM), electron microscopes only provide information on a very thin layer (less than 100 nm) of the sample. 3D imaging method therefore have to be set in place. (ii) 3D imaging methods exist and are applicable to the industry. It is the case for example of lab x-ray tomographs. However, their resolution is often limited to the micrometer, mainly because of their source size. In the case of 3D integration objects, the searched defects can be as small as several nanometers, and most of them are several tens of nanometers large [2]. The imaging technique must therefore provide a resolution that is compatible with those dimensions. (iii) As mentioned before, the investigated objects are quite big, up to several tens of micrometers. High resolution local techniques, such as electron tomography, require 50 nm wide samples, and therefore cannot be applied. FIB/SEM (Focused Ion Beam / Scanning Electron Microscope) Slice and View techniques, are often limited to samples of 10 μm in width, and therefore reach their limits in the case of 3D integration objects. (iv) Due to the industrial context of the study, the chosen technique should be able to provide statistical information. This implies either an even larger field of view, or an automated imaging process. More generally, the chosen technique should be as automatic and fast as possible, and provide easy-to-process data.

The goal of the work presented here is to develop new characterization techniques, well-suited for 3D integration imaging. The focus is set on the morphology and diffraction imaging of both to copper pillars and pads. We here aim at developing those 3D techniques, for them to become routine tools for 3D integration characterization. To do so, a large field of view (100 μm) has to be combined with a high resolution ($<$ 100 nm), and the complete workflow, from the sample prepa-

ration to the post-processing, must be made as automatic as possible. This work is closely linked to industry, and the conducted experiments were adapted to the samples under constant development. It is however quite exploratory, as it benefits from very recent techniques, which were often not originally meant for automation and industrial application.

The main techniques investigated here have been developed in the last few years. They include the ID16A and the ID01 beamlines from the ESRF (the European Synchrotron Radiation Facility). Both were built during the first phase of the ESRF upgrade, that last from 2009 to 2015, and benefit from state-of-the-art technologies from various fields, including x-ray optics, detectors, large data processing clusters, and engineering. The ID01 beamline offers the possibility for nano-diffraction imaging of large samples (100 μm in width), providing a local strain information, since the beam offered on this beamline can be focused down to 200 nm. Experiments have been conducted on this beamline, showing it possibilities for large area local strain measurements. The ID16A beamline is the first hard x-ray beamline dedicated to nano-tomography. It aims at 3D resolutions down to 50 nm, for samples below 100 μm in width. The main work presented here has been conducted on this beamline, with the goal to adapt it to industry statistical imaging needs. A third ESRF beamline, already well-established for industrial needs, has also been investigated: on the ID19 beamline, tomography and laminography were carried out. The preparation of the samples was made possible by a PFIB (Plasma Focused Ion Beam). Such machines have been commercially available only for the last few years. During this work, a 3D imaging techniques has also been developed on the same machine, originally only designed for sample preparation.

This PhD thesis widely benefits from brand new samples and characterization techniques. The access to such equipments was made possible by the specific context of this work. It was in fact realized in the frame of the IRT[1] Nanoelec, and more specifically inside the *Grands instruments* program. This program aims at bringing large instruments such as synchrotrons (and more precisely here the ESRF) closer to industrial needs. In particular, three actors took a part in this work: the CEA LETI, the ESRF, and ST Microelectronics, all located near Grenoble, as presented in Figure 2. The results presented here were obtained in the frame of an iLTP (innovation-led Long Term Project) funded by a collaboration between those three actors. This iLTP ensured synchrotron beam time on three beamlines (ID16A for 71%, ID19 for 17%, and ID01 for 12%) during the time of the PhD thesis. This very valuable access, together with brand new samples and the equipments of the PFNC[2], made this work and the results it led to possible.

The first three chapters are dedicated to the context of this work. In a first chapter, general principles of 3D integration are presented, together with the objects of interest mainly studied. The focus is set on the characterization needs of such

[1] Institut de Recherche Technologique

[2] PlateForme de NanoCaractérisation, the nano-characterization platform at CEA

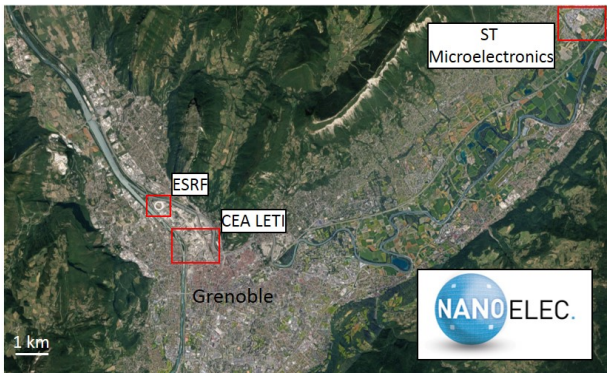

Figure 2: Industrial and academical actors involved in this work: the ESRF, CEA LETI, and ST Microelectronics.

objects and the possible answers. A second chapter is dedicated to electron and ion based microscopes. Their common and specific working principles are presented, together with two of their applications, used during this PhD. In chapter 3, the x-ray characterization methods used in the frame of this work are described. Lab and synchrotron sources and experimental setups are depicted, both for imaging and strain measurements.

The next three chapters aim at presenting the main results obtained during this PhD. In chapter 4, the development of the PFIB/PFIB Slice and View imaging is detailed, presenting both the automation of the data acquisition and the post-processing. A discussion about the possibilities, limits, and possible improvements of such a setup is provided. Chapter 5 is dedicated to the ID16A beamline, on which most of the experiments and developments were conducted. The original workflow of the beamline is presented, together with strategies aiming at making this beamline a routine tomography tool for the industry. A global discussion is led on the time saved using the proposed workflow, followed by selected applications realized on the ID16A beamline. Chapter 6 presents two studies realized on the ID01 beamline, respectively obtained on two silicon layers of a stack, and on a full-sheet copper layer, performed both at room temperature and at 400°C.

Finally, a summary of the work done in the frame of this PhD is provided, together with a global assessment of the techniques developed or used. Perspectives for routine characterization of 3D integration devices are proposed for further work.

Introduction générale

Dans l'industrie de la micro-électronique, l'augmentation des performances des composants s'est faite, durant les 50 dernières années, par la diminution de leur taille. En particulier, cela passe par la diminution de la taille des transistors, ce qui entraine la réduction de la taille de toutes les connections. De cette manière, la densité de transistors augmente, réduisant la taille globale du composant et la longueur de chaque connection, augmentant alors les capacités de l'appareil. Aujourd'hui cependant, cette course à la miniaturisation atteint ses limites. En effet, la taille des transistors atteint les limites de la physique, et la longueur globale des connections est telle que l'effet Joule dans le composant devient trop important et limite le temps de propagation de l'information.

Afin de répondre à ces difficultés, une nouvelle géométrie pour les composants micro-électronique se développe depuis les années 1980. Il s'agit, non plus de placer les éléments d'une même puce les uns à côté des autres, mais de les empiler. Cette technique est appelée intégration 3D (3Di). Elle réduit à la fois la longueur des connections et l'empreinte au sol du composant final, sans réduire la taille du transistor. Au cours des 10 dernières années, cette technique a gagné en intérêt et popularité, à la fois dans les mondes industriel et académique [1]. La Figure 3 souligne cette tendance, puisqu'elle montre que le nombre d'articles publiés comportant le mot clé "3D integration" ou un mot-clé associé est en constante augmentation depuis 1985.

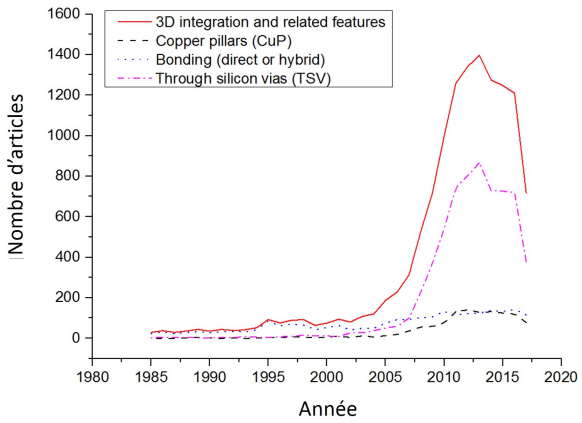

Figure 3: Nombre d'articles par an comportant le mot clé "3D integration" ou des mots clés assimilés ("Copper pillars", "hybrid bonding", "direct bonding", "Through Silicon Vias"), selon la base de données Scopus (*https://www.scopus.com*)

Bien qu'apportant des réponses technologiques intéressantes, cette nouvelle direction de développement apporte aussi de nouvelles difficultés. En effet, la géométrie utilisée en intégration 3D étant nouvelle, de nouveaux types de connections ont du

être développés. Les TSV (Through Silicon Vias), qui connectent deux faces d'un même wafer ou d'une même puce, ont notamment fait l'objet de nombre d'études. Aujourd'hui, leur procédés de fabrication ainsi que les mécanismes les commandant sont pour la plupart connus et maîtrisés. D'autres objets, tels les piliers de cuivre (ou CuP) et les pads de cuivre, sont utilisés pour connecter électriquement et mécaniquement les wafers et puces. Ces objets sont aujourd'hui en cours de développement, et leur caractérisation est donc d'un grand intérêt, qu'elle soit électrique, mécanique, ou morphologique, à la fois pour mieux comprendre les mécanismes qui se produisent pendant leur fabrication, et pour limiter la défaillance du produit fini. Dans cette étude, nous nous intéressons en détails à ces objects, et plus particulièrement aux pads de cuivre de quelques micromètres de large, ainsi qu'aux copper pillars de quelques dizaines de micromètres de diamètre.

Pour caractériser de tels objects, des tests électriques et mécaniques peuvent être réalisés. S'ils permettent d'obtenir une information sur la fiabilité du composant, ils ne fournissent que peu d'informations sur l'origine d'une éventuelle défaillance. L'imagerie quant à elle permet d'obtenir une information sur la morphologie de chaque objet, celle-ci pouvant être corrélée à son fonctionnement. En pratique, l'observation de trous à l'interface de collage entre deux pads de cuivre, ou au sein de piliers de cuivre est cruciale pour le suivi du procédé de collage. Pour être pertinentes sur le long terme, de telles études doivent fournir une information statistique et donc être réalisables de manière routinière.

En micro-électronique, la caractérisation morphologique est communément réalisée par microscopie électronique, sur un microscope électronique à balayage (MEB) ou à transmission (MET). Cependant, la technique de caractérisation doit s'adapter à la géométrie de ces nouveaux objets. En effet, l'imagerie de composants utilisés dans l'intégration 3D est assez contraignante, et ce pour plusieurs raisons. (i) Les techniques telles que le MEB et le MET, bien qu'atteignant de hautes résolutions (quelques nanomètres et quelques angstroms, respectivement) ne fournissent qu'une information concernant une faible épaisseur de l'échantillon, typiquement moins de 100 nm. Les objets considérés sont cependant tridimensionnels, et la technique de caractérisation doit donc l'être également. (ii) Des méthodes d'imagerie 3D, telles que les tomographes de laboratoire, existent et peuvent être appliquées à l'industrie. Cependant, leur résolution est aujourd'hui souvent limitée au micromètre. Dans le cas de l'intégration 3D, les défauts recherchés mesurent typiquement quelques dizaines de nanomètres, les plus petits faisant jusqu'à quelques nanomètres [2]. La technique d'imagerie doit permettre d'obtenir de telles résolutions. (iii) Comme mentionné précédemment, les objets observés sont relativement grands : ils peuvent mesurer quelques dizaines de micromètres. Des techniques d'imagerie 3D à haute résolution, telles que la tomographie électronique par exemple, imposent des échantillons de moins de 50 nm de diamètre, et ne s'appliquent donc pas ici. Des techniques destructives de type Slice and View, implémentées dans un FIB/SEM, sont quant à elles souvent limitées à des régions d'intérêt de 10 μm de côté. Elles atteignent donc également leurs limites ici. (iv) Du fait du context industriel de cette étude, la technique d'imagerie choisie devra fournir des informations statis-

tiques, soit à travers un champ de vue large, soit grâce à un procédé automatisé. Plus généralement, il est crucial que l'information obtenue le soit de manière aussi automatique que possible, et soit facilement exploitable.

Le but de ce travail de thèse est de développer de nouvelles méthodes d'imagerie 3D, adaptées à l'intégration 3D. Les principaux objets étudiés sont les piliers et les pads de cuivre, et le développement sera orienté vers une utilisation routinière et automatique des techniques de caractérisation. Comme expliqué précédemment, ceci requiert une technique d'imagerie 3D associant un large champ de vue (100 μm) à une haute résolution ($<$ 100 nm), et dont le procédé d'analyse complet, allant de la préparation d'échantillon au résultat final, peut être automatisé. Ce travail a été réalisé à des fins industrielles, et les expériences réalisées ont été adaptées à des échantillons en constante évolution. Il s'agit de ce point de vue d'un travail assez exploratoire, d'autant plus qu'il est basé sur des techniques très récentes, qui n'ont souvent pas pour but originel une utilisation routinière.

Les principales techniques étudiées dans ce travail datent de seulement quelques années. Parmi elles, les lignes de lumière ID16A et ID01 de l'ESRF (European Synchrotron Radiation Facility), ont été construites durant la première phase du programme "Upgrade" de ce synchrotron, qui a eu lieu entre 2009 et 2015. Elles bénéficient donc des dernières avancées faites dans de nombreux domaines, qui ont fourni par exemple de nouvelles optiques pour les rayons X, des détecteurs rapides, une puissance de calcul pouvant gérer de grandes quantités de données, ou des moteurs ultra-précis pour le positionnement des échantillons. Grâce à un faisceau pouvant être focalisé jusqu'à 200 nm, la ligne ID01 offre la possibilité de mesurer localement les déformations dans de grands échantillons (des zones d'intérêt de 100 x 100 μm^2 peuvent être observées). Durant cette thèse, il a été possible de réaliser des expériences sur cette ligne. La ligne ID16A est la première ligne de rayons X durs dédiée à la nano-tomographie. Elle vise une résolution 3D de moins de 50 nm, pour des échantillons pouvant aller jusqu'à 100 μm de diamètre. La plupart des expériences réalisées durant cette thèse ont été faites sur cette ligne, avec pour but de l'adapter aux besoins de l'industrie. Des mesures ont également été réalisées sur une troisième ligne de lumière de l'ESRF, ID19, plus ancienne et orientée vers l'industrie. Elle offre la possibilité d'acquérir des données de tomographie et de laminographie. La préparation des échantillons a été réalisée au sein d'un PFIB (Plasma Focused Ion Beam), qui est une machine commercialisée depuis seulement quelques années. Une technique d'imagerie Slice and View a aussi été développée dans ce PFIB, originellement prévu pour la préparation d'échantillons.

Comme on peut le voir, des échantillons et des techniques de caractérisation de dernière génération ont été accessibles durant cette thèse, grâce à un contexte particulier. Elle a en effet été réalisée dans le cadre du programme *Grands Instruments* de l'IRT (Institut de Recherche Technologique) Nanoelec, qui vise à rapprocher les grand instruments tels que les synchrotrons (et en particulier l'ESRF) du monde de l'industrie. Dans ce cadre, un iLTP (innovation-led Long Term Project) a été monté par trois acteurs : l'ESRF, le CEA, et ST Microelectronics, tous situés dans les environs de Grenoble (voir carte en Figure 4). Ce iLTP garantit un temps d'accès

aux trois lignes de lumières présentées précédemment : 71% du temps a été alloué à ID16A, 17% à ID19, et 12% à ID01. Cet accès privilégié à l'ESRF, ainsi que l'utilisation des équipements de la PFNC (PlateForme de NanoCaractérisation du CEA), ont permis d'obtenir les résultats présentés dans ce manuscrit.

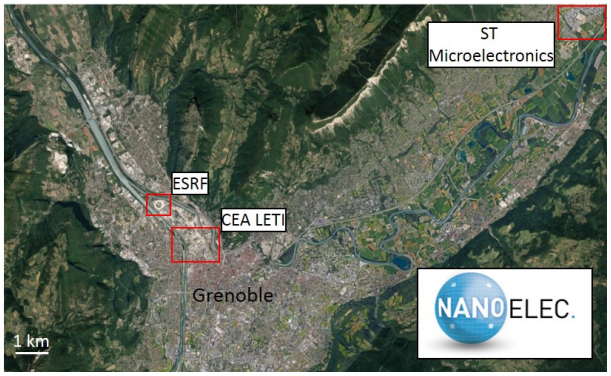

Figure 4: Les acteurs (académiques et industriels) impliqués dans ce travail : le CEA, l'ESRF, et ST microélectronique.

Les trois premiers chapitres de ce manuscrit présentent le contexte de ce travail. Un premier chapitre introduit les principes de l'intégration 3D, et les principaux objets étudiés. Leurs besoins en termes de caractérisation et les réponses possibles sont décrits. Dans un second chapitre, les microscopes électroniques et ioniques sont présentés. Leurs principes de fonctionnement communs et spécifiques sont décrits, ainsi que deux applications possibles, utilisées durant cette thèse. Enfin, les techniques de caractérisation par rayons X utilisées dans le cadre de ce travail sont présentées dans le chapitre 3. Les sources de rayons X de laboratoire et synchrotron sont détaillées, de même que les dispositifs expérimentaux permettant l'imagerie et les mesures de déformations.

Les trois chapitres suivants présentent les principaux résultats obtenus pendant ce travail de thèse. Le chapitre 4 est dédié au développement de l'imagerie 3D par Slice and View au sein d'un PFIB. L'automatisation de l'acquisition elle-même, ainsi que le post-traitement des données, sont décrits. Les possibilités, limites, et éventuelles améliorations futures d'un tel dispositif sont détaillés.

Le travail mené sur ID16A est présenté au chapitre 5. Le procédé complet original y est détaillé, ainsi que les différentes stratégies mises en place pour faire de cette technique une méthode d'imagerie routinière pour l'industrie. Une discussion est menée sur le temps gagné par l'utilisation de ces stratégies. Quelques exemples d'applications sont donnés, supportés par des résultats obtenus par d'autres moyens d'imagerie, à des fins de comparaison.

Le chapitre 6 illustre les possibilités de la ligne ID01 pour l'intégration 3D au moyen de deux études, visant respectivement à observer les déformations dans les

couches de silicium d'un empilement fonctionnel, et à mesurer les déformations dans une couche de cuivre pleine plaque, prévue pour du collage direct.

Enfin, une conclusion reviendra sur tous les résultats obtenus au cours de ce travail, avec pour but l'évaluation des différentes techniques utilisées. Quelques perspectives concernant la caractérisation appliquée à l'intégration 3D seront présentées et discutées.

Chapter 1

Characterization for 3D integration

Contents

1.1 Towards 3D integration 12
1.2 Objects of interest 15
1.2.1 Through Silicon Via (TSV) 16
1.2.2 Wafer-to-wafer (W2W) bonding 16
1.2.3 Copper pillar (CuP) 18
1.3 Characterization methods 20
1.3.1 Characterization needs 20
1.3.2 Strain measurement method 20
1.3.3 Imaging methods 20

Any microelectronics device is based, on the smallest scale, on transistors, that can be as small a several tens of nanometers. From this scale to the macroscopic one we are able to manipulate, several intermediate objects play a role, such as dies, chips, and packaged integrated circuits (IC). The latter usually contains a die, placed inside a plastic packaging. The die itself is a piece of silicon wafer on which a network of transistors, resistors, capacitors, is fabricated. The network itself is made of gold or copper and is usually edited on the chip itself. Transistors, which are the very base of microelectronics, are components that regulate the current or voltage flow in the circuit, and can therefore act, when combined together, as logical gates. A complex network of connections, with a large variety of spatial scales, connects the transistors, that can be as small as several tens of nm, to the final package, which is several centimeters large.

To limit the size of the whole chip, the main strategy since the 1970s has been to decrease the size of the transistors themselves, together with their connections. In 1971, the first microprocessor contained 2300 transistors, while in 2010 the number of transistors on a microprocessor was about 10^9. Between those two dates, the expansion was exponential, as the number of transistors per microprocessor has doubled every 2 years - this is the so-called Moore's law. This was made possible mainly by the improvement of precision in circuit editing.

However, this strategy reaches its limits, and Moore's law is said to be impossible to follow by 2020. There are several reasons for that. First, as the final transistors became smaller, the connections became thinner and more numerous. This rose issues regarding Joule heating, increasing the resistivity of the connections and thus

the signal propagation time. This is today answered by new materials, such as copper connections instead of aluminum ones, and low-k materials replacing the $Si0_2$ insulator. Moreover, the miniaturization of transistors itself reaches its limits. In fact, although transistors of 9 nm have been shown to work [3], some of the manufacturing steps are impossible to achieve in an industrial context. Moreover, from a quantum physics point of view, the miniaturization is assessed to reach its limits by 2036 [4].

1.1 Towards 3D integration

One path for further development of microprocessors is therefore to increase the density of transistors, while limiting the connections length, which will allow for a reduction of the power consumption. The global footprint of the circuit is to be taken into account as well. As the direct diminution of transistors size is not a solution anymore, a new geometry of the global circuit is to be developed. To some extent, Systems on Chips (SoC) answer the problem of the connection length, as they concentrate several types of elements on a single chip: the connections are therefore shorter (see left hand side of Figure 1.1). However, the issue of connections between dies still remains, so does the footprint and power consumption.

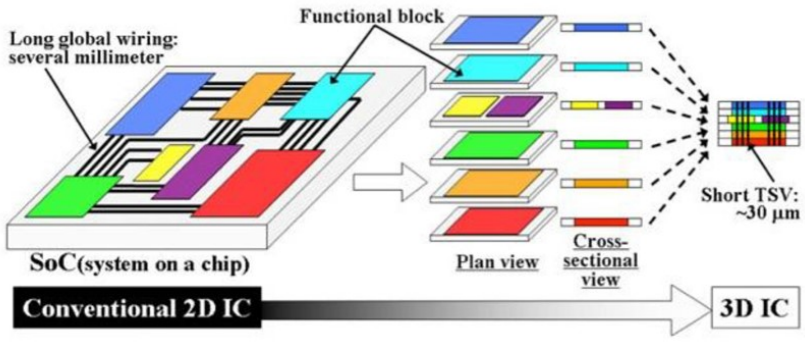

Figure 1.1: Principle of 3D integration. In SoC, heterogeneous structures are present on a single chip. This allows to reduce the length of connexions. To further reduce the connections, and limit the footprint as well, 3D integration is being developed. *Image source: http: //www.athenis3d.eu/technology.php*

The Package on Package (PoP) is a good strategy to answer those needs (see right hand side of Figure 1.1). It relies on vertical connections between dies inside the same package or chip. They allow for a gain of footprint, while allowing for the stacking of heterogeneous units inside a package. Two bonding systems are used today inside such devices: the wire bonding and the flip-chip, both illustrated in Figure 1.2. The wire bonding simply uses wires (usually made of copper or gold) to connect one part of the upper die to another part of the lower die inside the package, while the flip-chip technique relies of the rotation of the upper chip, in

order for its active layer to face the active layer of the lower chip. The connection is made using solder bumps or balls, which can be made of an alloy of SnPb or SnAg. Those two techniques can be combined, as illustrated in Figure 1.2c, and can reduce the interconnection length by 40% in a 4 active layer stack [5].

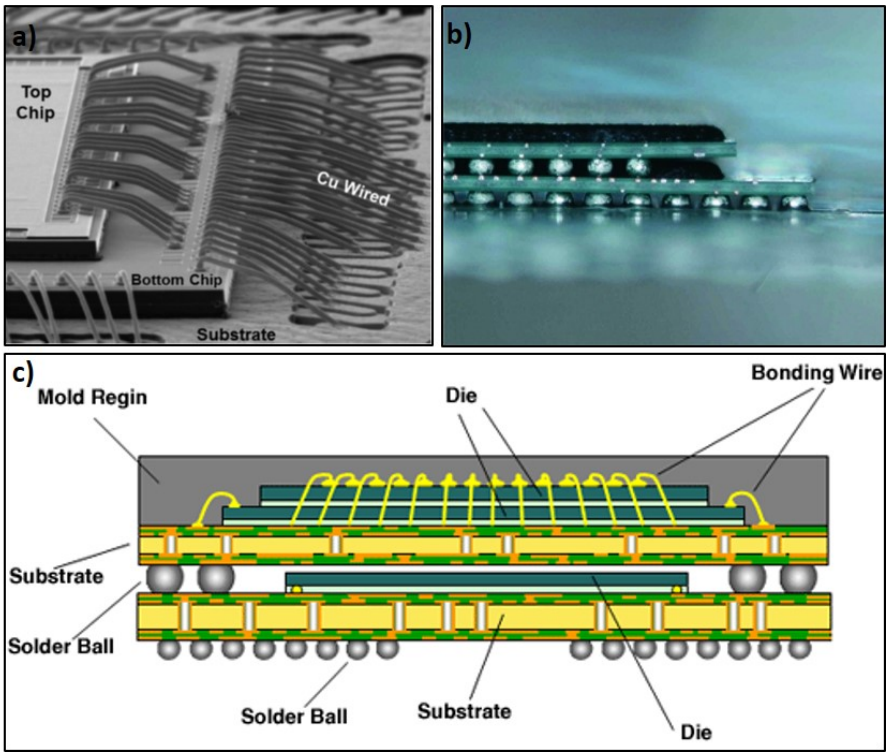

Figure 1.2: Images of two bonding technologies used in the System in Package a) wire bonding (image source: [6]) b) flip-chip (image source: http://www.tresky.com) . c) Schematic of the two technologies used together (image source: electronics.stackexchange.com).

This first 3D geometry, called 3D IC packaging, paves the way for actual 3D integration. The passage was made possible by the development of Through Silicon Vias (TSV) [6]. Those objects, first imagined in 1956, are today of high interest. They are several tens of micron large cylinders, filled with copper or tungsten, and going through an entire thinned wafer in the vertical direction (up to 100 μm). As such, they allow for an electric signal to cross the wafer, making vertical communication possible. 3D integration can be separated into 3D IC integration, where dies are stacked together, using both TSVs and solder bumps, and 3D Si integration, where wafers are bonded together using TSV only. Figure 1.3a offers an overview of 3D packaging and integration technologies, with their use of TSVs and their maturity in 2014. 3D packaging is today commercialized, especially for mobile applications such as smartphones and tablets, while 3D integration is today still in a development phase [7].

Several microelectronics industry actors are currently working on 3D IC integra-

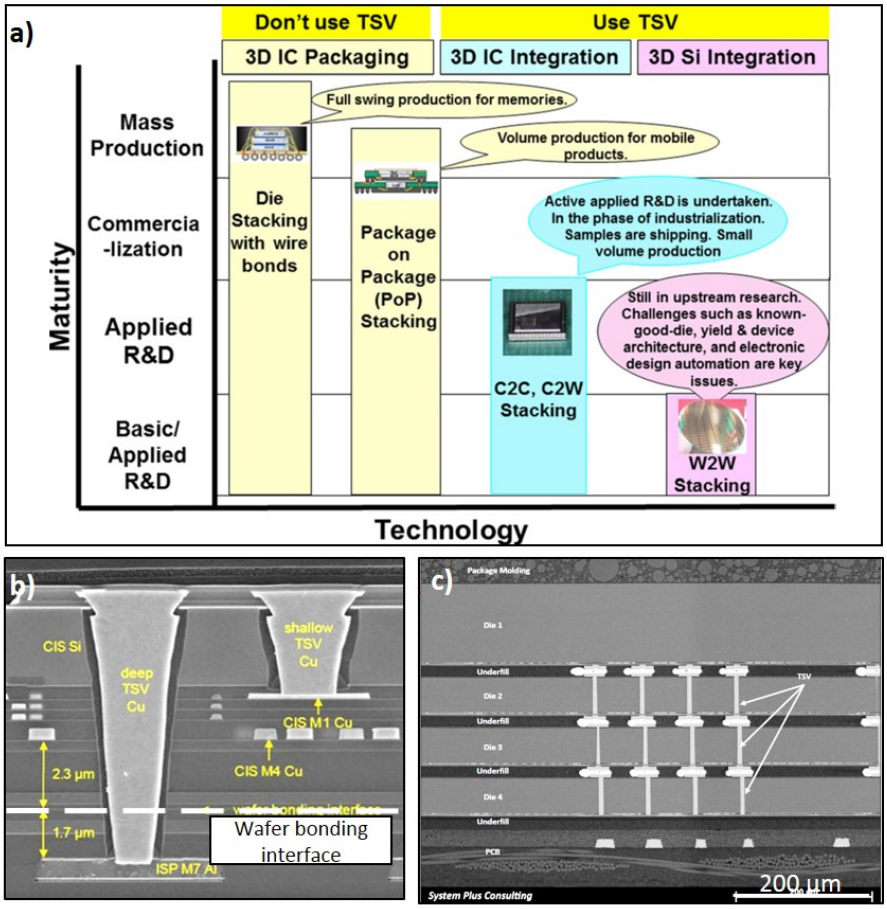

Figure 1.3: a) 3D integration technologies and their maturity regarding industry in 2014. *Image source: [6].* b) Cross section view of the Sony imaging sensor containing TSVs. In this stack, TSVs ensure the connection between the top and bottom layers. (Image source: [8]). c) Cross section of Samsung DDR4 DRAM, with TSVs conneting opposite sides of dies and pillars connecting dies together (Image source: [9]).

tion [1], and some commercialized devices already contain TSVs [10]. Sony released in 2013 an imaging sensor based on TSVs, where the bonding itself was made by direct SiO_2/SiO_2 direct bonding, as can be seen in Figure 1.3b [8]. Such a sensor allows for the signal processing unit to be closer to the pixels, and therefore to obtain better images. It is today used in Sony Xperia XZs smartphones for example. In this device however, TSVs connect electrically two layers of the stack, and not two faces of the same wafer. Further development of 3D integration leads to electrical connections at the interface itself, using hybrid bonding for example, as will be described in section 1.2. 3D integration has also been implemented for other applications, such as high performance computing units, in which digital and analog functions of a product are manufactured separately and connected with copper pillars and TSVs [11]. Dynamic Random Access Memories (DRAM) were also investigated [12], and are already commercialized by Samsung, in the 64 Gb DDR4 model, illustrated in Figure 1.3c [9].

When compared to 3D packaging, it is clear that 3D integration offers higher electrical performances, a lower power consumption due to shorter connections, a higher density and a lighter weight. The two technologies are however complementary and can be applied together [7]. Here we focus on 3D IC integration, as it rises most challenges today. Next section is dedicated to the description of several objects of interest used in 3D IC integration and thoroughly analyzed during this PhD. The issues they face, together with their characterization needs, will also be discussed [13]. In a second section, conventional characterization methods will be assessed in the case of 3D integration. Characterization methods proposed and developed during this PhD thesis will be introduced and their use justified.

1.2 Objects of interest

As mentioned previously, 3D integration relies on the stacking of dies or wafers in the vertical direction. The connections between two faces of a die or wafer are made by TSVs. The bonding is called Wafer to Wafer and noted W2W. It can be performed by using an additional material between the surfaces. This indirect bonding can be performed using a polymer, or a eutectic alloy. It can also be made with no intermediate layer between metals, oxides, or dielectrics. It is then called direct bonding [14]. Hybrid bonding will occur when direct bonding is performed on a surface containing two types of materials, for example a metal and a dielectric [2]. In the case of 3D IC integration, the connections between dies are performed at different scales, depending on the level of the connection. Solder balls are placed close to the substrate, while smaller solder bumps are situated further away. To improve both the density and the quality of connections, copper pillars, later noted Cups have been developed for upper levels.

In this section, insight will be given into some specific objects of interest used in 3D integration. TSV will be briefly described, as they play a huge role in 3D integration, although they were of little concern during this PhD. Goals, fabrication

processes, and characterization needs will be provided for direct and hybrid bonding, as well as for copper pillars. This section voluntarily contains very generic information about processes and features of interest inside the objects. When needed, more specific information will be provided along the manuscript about the manufacturing process of given samples and their characterization needs. A word will be given about how the samples can be handled after the manufacture, as this will have an impact on possible characterization and on sample preparation.

1.2.1 Through Silicon Via (TSV)

Through Silicon Vias (TSVs) are high form factor (or depth to diameter ratio) structures inside a silicon wafer. Basically, they are several μm wide cylindrical holes in the wafer, filled with a conductive material such as copper or tungsten. Depending on their role inside the circuit, their shape and filling material differ. Their diameter ranges from 3 to 80 μm, while their form factor ranges from 1 (for large TSV) to up to 10 (for smaller ones).

Their manufacturing process is today well-understood, and they were not studied in this work.

1.2.2 Wafer-to-wafer (W2W) bonding

Direct and hybrid bonding are wafer to wafer bonding techniques with no use of additional bonding layer. To achieve a good quality bonding, the surface may be polished using CMP (Chemical Mechanical Polishing) before bonding, and the bonding can be assisted by thermo-compression. Inside a circuit, direct bonding can link copper pads together, as illustrated in Figure 1.4a.

During this PhD, a widely studied bonding type is the hybrid bonding, which bonds metal pads and dielectric material ($Si0_2$) areas together, as illustrated in Figure 1.4b. More specifically, daisy-chain structures were studied. They are electrical test structures, that create back and forth connections between two levels of the stack, using 5 μm wide copper pads and via matrices, as illustrated in Figure 1.4c. One possible manufacture process for hybrid bonding pads is presented in Figure 1.5.

Several challenges occur during this process. A first consideration is that for patterned structures, pads must be well-aligned to maximize the current flow. This alignment must therefore be controlled [16, 17]. Furthermore, voids can appear at the bonding interface, for two main reasons. First, the copper can contain vacancies in its structure. During the reflow, those vacancies migrate and aggregate, creating voids. A second origin is in the process itself. A small layer of oxide can appear on the wafers surfaces, before the bonding. This will also generate voids [18, 19]. Such voids are illustrated in the case of a full-sheet Cu-Cu bonding and a copper pad in Figures 1.6a and 1.6b, respectively. Their size ranges from several nanometers, up to several tens of nanometers [2]. Contrary to not-bonded areas of wafers, in the case of small voids the bonding still exists and provides an electrical and mechanical connection. As the smallest connections at this level are 350 nm wide vias, voids

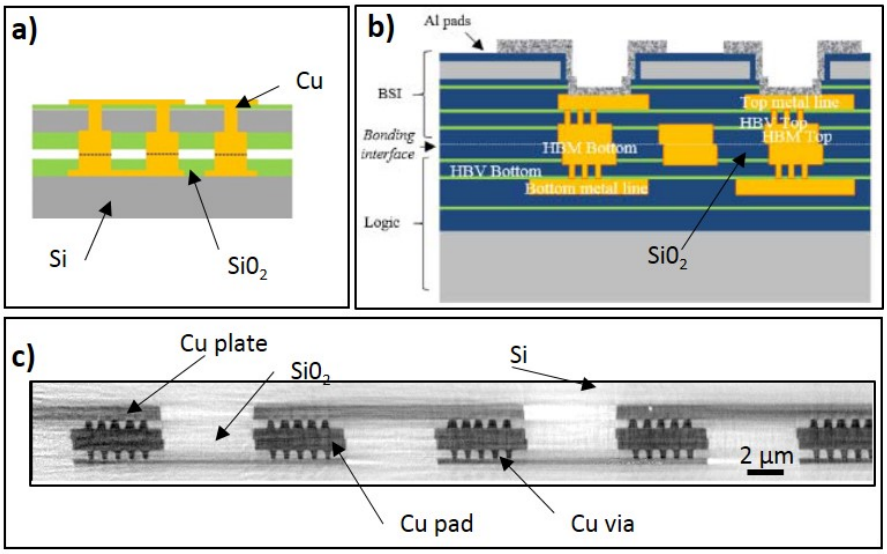

Figure 1.4: Profile illustration of a) direct bonding. *Image source: [15]*; b) hybrid bonding. *Image source: [2]*. c) Profile view of the daisychain structure, obtained with x-ray tomography.

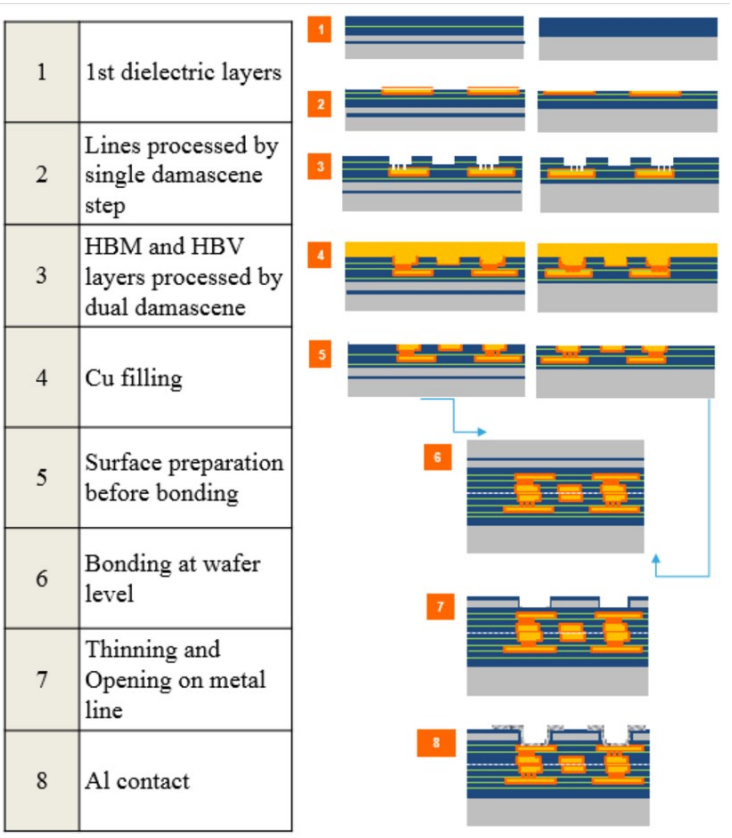

1	1st dielectric layers
2	Lines processed by single damascene step
3	HBM and HBV layers processed by dual damascene
4	Cu filling
5	Surface preparation before bonding
6	Bonding at wafer level
7	Thinning and Opening on metal line
8	Al contact

Figure 1.5: Simplified hybrid bonding process. *Image source: [2]*

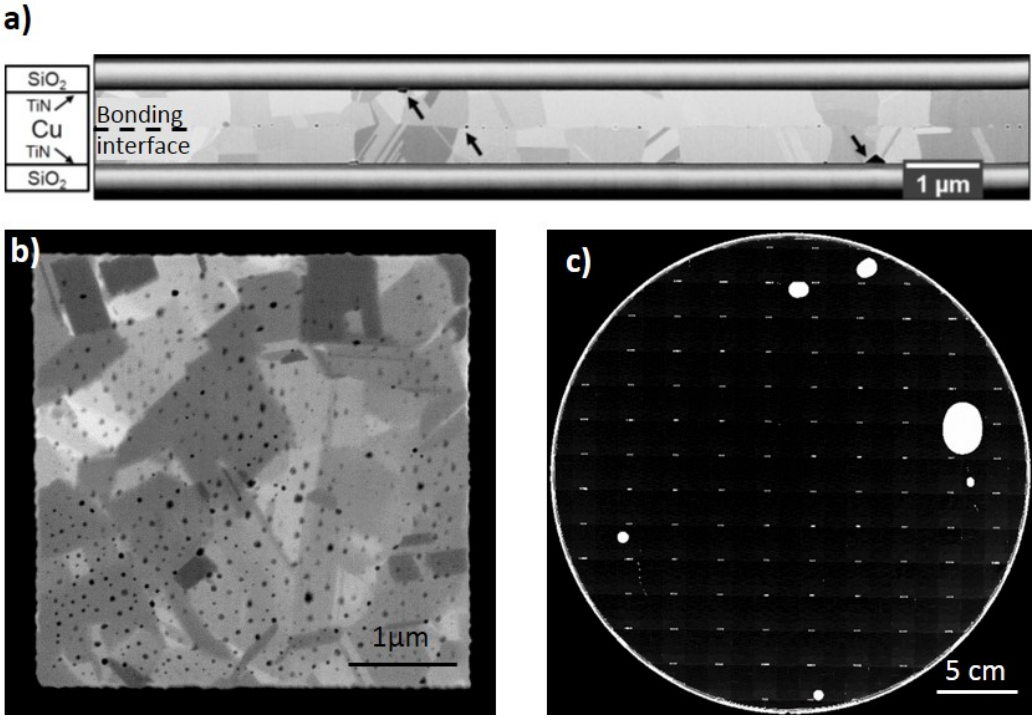

Figure 1.6: a) SEM image of voids at the interface of a full-sheet Cu-Cu bonding, obtained with a SEM [20]; b) TEM image of voids (in black) at the interface between two copper pads [21]. c) Scanning Acoustic Microscope (SAM) image from a whole 300 mm wafer. The white areas are ill-bonded

smaller than 50 nm are unlikely to be an issue. It is however of great importance to monitor their size, in order to assess new fabrication processes.

When they exit the manufacturing process, samples are still 300 mm large wafers stacked together. Most of the time, the upper wafer is thinned down to a thickness of 3 to 10 μm. The bottom wafer is 750 μm thick. The wafers can be sawn and cleaved quite easily, and can undergo a PFIB (Plasma Focused Ion Beam) sample preparation.

1.2.3 Copper pillar (CuP)

Connections between chips are made by solder bumps, balls, or copper pillars (CuPs) [22]. Similarly to TSVs, their shape and size varies according to their position in the stack and their purpose. In this study, the focus has been set on copper pillars, which are copper cylinders of typically 10 to 50 μm in diameter, surmounted by an alloy usually made of copper, silver, and tin (called SAC for SnAgCu), as illustrated in Figure 1.7. Since their materials behavior still rises questions, especially in the case of smaller CuPs (10 μm), their morphological characterization is today of high importance.

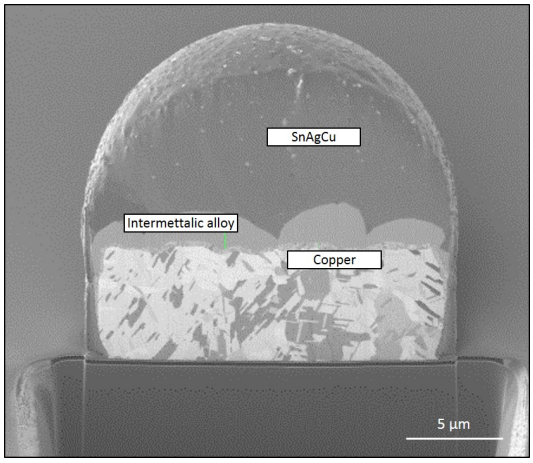

Figure 1.7: SEM Profile view of a 20 μm wide copper pillar.

Several fabrication processes coexist when it comes to copper pillars [23, 24], and one of them is illustrated in Figure 1.8. Copper and SnAgCu alloys are usually deposited by electrodeposition in regions delimited by a resin, creating cylinders (the SnAgCu alloy being deposited on top of the copper). The resin is then removed chemically, and a reflow gives the final copper pillar shape. This reflow creates intermetallic alloys and voids at the interface between copper and SnAgCu, as well as Ag precipitates in the bump. This is all the more significant since the layers are stacked one after the other, which means pillars situated at the bottom of the stack will undergo multiple reflows. Those features are likely to influence the electrical and mechanical behaviors of the pillar [25, 26, 27, 23]. As such, we here focus on the morphological observation of copper pillars, mainly regarding the possibility to observe voids and intermetallic alloys et the interface between the copper cylinder and the bump.

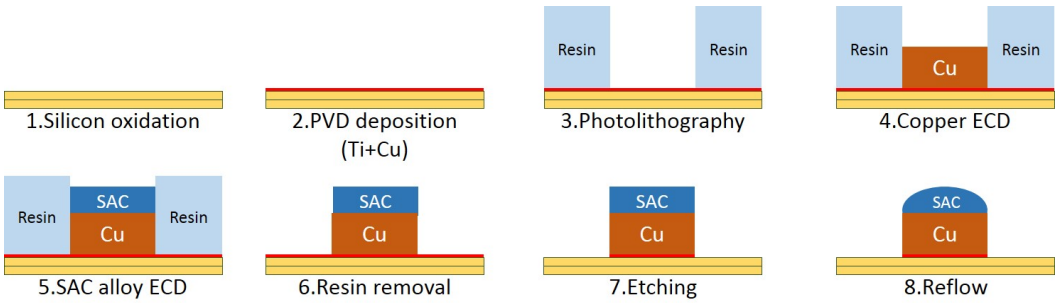

Figure 1.8: Illustration of the fabrication steps of copper pillars.

After the growth, copper pillars are situated on the top of 300 mm large and 750 μm thick wafers and are organized into matrices on the wafer surface. They are therefore quite sensitive, and the sample preparation must not require any contact

with the top part of the wafer. The wafer cleavage and sawing is possible, while FIB or PFIB preparation requires a protective deposit.

1.3 Characterization methods

1.3.1 Characterization needs

Here we summarize the characterization demands for copper pillars and wafer to wafer bonding, together with the characterization tools susceptible to answer them.

As presented in the previous section, voids and intermetallics can have an impact on the electrical and mechanical behavior of W2W bonding and copper pillars. A first characterization can be made by characterizing the conductivity of the features, and their mechanical resistance [28, 23]. Those techniques offer statistical information, and are quite fast to set. However, they offer a very global information, with little information about the causes of the problem.

1.3.2 Strain measurement method

A study of strain inside the samples can also be performed, in order to isolate the areas subject to failure. As the areas to explore are several μm^2 wide, TEM characterization is not well adapted, while lab x-ray diffraction offers resolution of several tens of microns, which often does not allow to discriminate areas within a given die.

A local strain information can be obtained with a focused synchrotron x-ray beam. Diffraction patterns are recorded for every point of a scanned region of interest (ROI), and strain can be deducted in this ROI. Diffraction can be performed in a transmission geometry (Laue diffraction) or a reflective one (Bragg diffraction). The limit of resolution is therefore set by the focus size (which can be a few hundred of nm in modern beamlines), and the field of view is determined by the time available for the scan. In the case of monochromatic Bragg diffraction, a fast scanning acquisition system has been implemented in the ID01 beamline at ESRF. Given the possibility to acquire data from 100 x 100 μm^2 areas within an hour, and the fact that silicon used in wafers is a monocrystal (thus does not require a polychromatic beam to be analyzed), strain measures were performed on ID01 during this PhD. A more detailed presentation of this beamline is provided in chapter 3, while results of the experiments are displayed in chapter 6.

1.3.3 Imaging methods

As explained in the previous section, the observation of different features is interesting is the case of copper pillars and pads. For the former, the observation of voids, for monitoring purposes, is of value. For the latter, both voids and intermetallic alloys will be observed, for a better understanding of the behavior of CuPs, from a material science point of view. To obtain those information, imaging is a suitable solution. It also offers information about a possible misalignment of pads

in the case of hybrid bonding. In the case of W2W bonding, Scanning Acoustic Microscopy (SAM) is an appropriate imaging technique, in which acoustic waves are projected on the sample, and are reflected by interfaces. Voids therefore appear in white, as can be seen on the SAM cliché from Figure 1.6c. Ill-bonded areas are clearly visible, and a whole wafer can be imaged within minutes. This technique however lacks resolution, which is limited to several tens of μm [20].

High resolution tools can be applied to the imaging of both CuPs and bonding interfaces, such as Scanning Electron Microscopy (SEM) and Transmission Electron Microscopy (TEM). Those techniques are well-established and widely applied in the microelectronics field. They offer a good observation of voids, as has already been shown in Figures 1.6 a and 1.6b. However, they offer a quite narrow field of view, which reduces the statistical information one can get from an analysis. Besides, those imaging technique only offer a 2D information, while the objects are three-dimensional.

3D imaging tools are also available. Lab tomographs aimed for industry offer the possibility to image in three dimensions objects up to several centimeters in width. The complete analysis is realized in a few hours, which is compatible with the industry requirements. Their resolution is however often limited to about 1 μm in commercial equipments [29]. Tomography performed in a TEM offers high 3D resolution but, as in the 2D case, has a very limited field of view (50 nm). In this work, x-ray tomography performed in a synchrotron was investigated for 3D integration, in two different imaging beamlines, that are ID16A and ID19. They are dedicated to nano- and micro-tomography respectively, with resolutions reaching 500 and 700 nm. Their specificities will be given in chapter 3, while results obtained on those beamlines will be presented in chapter 5.

In order to achieve a high resolution, Slice and View techniques can be performed in a FIB/SEM instrument. They offer resolutions of several nanometers, but require long data acquisition times, which limit the analyzed volume to about 10 μm^3 [30]. During this PhD, a Slice and View method has been implemented inside a Plasma-FIB (Focused Ion Beam), in order to reduce the data acquisition time and increase the imaged volume. A more detailed description of the Slice and View techniques will be given in section 2.4, while the development of this technique inside a Plasma-FIB will be presented in chapter 4.

Caractérisation pour l'intégration 3D
Résumé du chapitre

Ce premier chapitre introduit les principes de l'intégration 3D en micro-électronique. L'augmentation des performances des composants de micro-éléctronique passe jusqu'à aujourd'hui par la diminution de la taille des transistors. Cette approche atteignant ses limites physiques et techniques, une nouvelle géométrie, appelée intégration 3D, est en cours de développement. Elle consiste en l'empilement des différents éléments des circuits intégrés. Ceci peut être réalisé au niveau du packaging ou des puces elles-mêmes. Dans cette étude, nous nous intéressons à ce second cas, qui est actuellement en cours de développement.

Pour cela, différents objets tels que les TSV (Through Silicon Vias), les piliers de cuivre (copper pillars), et les pads de cuivre (copper pads), sont développés dans l'industrie. La caractérisation des deux derniers, dont les mécanismes ne sont pas encore parfaitement connus, font l'objet du présent travail. Leurs besoins en termes de caractérisation sont définis. D'une part, le suivi du procédé de fabrication de ces objet nécessite une information morphologique sur les trous à l'interface entre deux pads, ainsi que sur les trous, les alliages intermétalliques, et les précipités d'argent au sein des piliers de cuivre. L'imagerie de ces objets nécessite une technique permettant un large champ de vue (quelques dizaines de micromètres) et une haute résolution (quelques dizaines de nanomètres). D'autre part, la mesure des déformations au sein de telles structures permet de comprendre et prévenir d'éventuelles défaillances. Ici aussi, la méthode de caractérisation doit pouvoir couvrir de larges zones d'un échantillon (typiquement 100 x 100 μm^2) et fournir une information locale (500 nm). Dans les deux cas, pour satisfaire les besoins de l'industrie, la caractérisation doit pouvoir être faite de manière automatique et routinière, afin d'obtenir des données statistiques.

Quelques méthodes classiquement utilisées pour de telles analyses sont évoquées, et les solutions proposées et développées au cours de ce travail sont introduites. Il s'agit, pour les mesures de déformation, de la ligne ID01 de l'ESRF, et, pour l'imagerie 3D, des lignes ID16A et ID19 de l'ESRF, ainsi que d'une procédure Slice and View implementée dans un PFIB (Plasma Focused Ion Beam).

Chapter 2

Electron and Ion based microscopes

Contents

2.1 General overview and relevant values 24
2.2 Sources of electrons and ions 26
2.2.1 Electron guns 26
2.2.2 Ion guns 28
2.3 Objects/matter interactions and applications 30
2.3.1 Milling 32
2.3.2 Matter deposition 35
2.3.3 Imaging 35
2.4 Applications of Focused Ion Beam microscopes 37
2.4.1 Slice and View procedure 37
2.4.2 Sample preparation: lift-out procedures 40

Scanning Electron Microscopes (SEM) are today widely used in a variety of fields, as they represent fast solutions for surface imaging and provide a large panel of information, including topology, chemistry, and crystalline orientation. What is usually called FIB (for Focused Ion Beam) is a scanning ion microscope. Ion sources have been developed in the 50s, together with the electron guns, but their application was restricted for a time to broad beams, aiming at global etching. Focused Ion Beam sources, which allow for scanning microscopy and therefore local etchning and imaging, are more recent: FIB microscopes have mainly been developed since the 1980s. Their mainstream area of application is today the sample preparation for Transmission Electron Microscopy (TEM), particularly for the microelectronics industry.

Both types of microscopes rely on the same basic principles and physic phenomena, although their practical characteristics vary. In both cases, a charged beam is focused and accelerated towards the surface of a sample. The interactions between the beam and the sample emits new charged particles, that can be captured by detectors and analyzed: they will provide a panel of information, be it topological, chemical, or crystalline. Moreover, for heavy and energetic objects such as ions, the sample itself is altered: matter can be removed from the surface, making the ion gun a milling tool as much as an imaging tool.

In this chapter, a general overview of such microscopes is presented, with a strong focus set on three versions: the SEM, the gallium FIB, and the xenon PFIB (later

noted PFIB), aiming at a layout of their similarities and differences. The PFIB was extensively used in this work, while the FIB and SEM came as side tools. As they fulfill different yet close purposes, we here choose to present the three machines.

In a first section, the main parts constituting such microscopes are presented. A detailed description of the existing sources is given in section 2.2, while the sample-objects interactions, with a focus set on their properties and the consequences on the microscopes' applications, are examined in section 2.3. Finally, two applications of ion microscopes are introduced: Slice and View procedures and sample preparation.

2.1 General overview and relevant values

Here we present the general principle and instrumentation for an electron or ion based microscope. Data provided for electron microscopes are mainly taken from [31], while the physics of ion microscopes were investigated with the support of [32] and [33]. References for specific information and values are given along the text.

The electron and ion microscopes are made of three main components, shown in Figure 2.1. As their designs may differ, the basics components or the different microscopes are quite similar. First, electrons or ions are extracted from a source cathode and accelerated using an anode. In the case of an electron source, the cathode can be a hairpin or a field emission gun; ions can be extracted using Liquid Metal Ion (LMIS) or plasma sources.

The beam then enters the column, in which it is focused and its energy selected. According to the original beam and the column settings, a wide panel of spot sizes and energies can be obtained. The beam is accelerated towards the sample, which is placed down the column and mounted on a stage with 5 degrees of liberty: X, Y, Z, tilt and rotation. For each machine, a computer is connected to the system and a software allows the user to control the machine. As we will see, the different setups do not answer the same needs, they have their own assets and drawbacks when it comes to resolution, sputtering rate, sample damage etc. It is therefore relevant to combine the tools together. Dual beam microscopes are commercialized today, allowing for simultaneous FIB and SEM applications on a given sample, in order to combine their advantages.

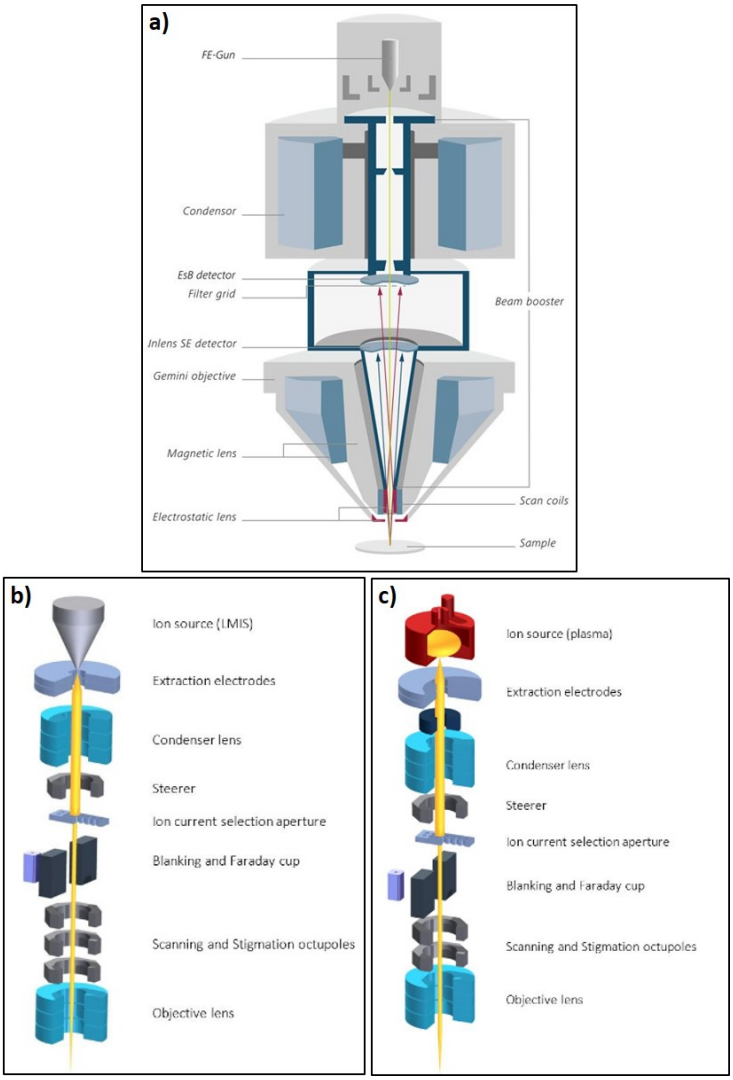

Figure 2.1: Illustrations of columns for a) a SEM (source: Zeiss Gemini) b) a FIB with a Ga^+ Liquid Metal Ion Source (Ga) c) a FIB with a Xe^+ plasma source (source: Orsay Physics).

2.2 Sources of electrons and ions

Here we describe the basic principles of the extraction of electrons and ions from a metallic material. For the emission of electrons, the thermionic effect and the field effect will be described, followed by their respective applications. As ion gun can rely on either Liquid Metal Ion Sources (LMIS) or Plasma Induced Ion Sources, these two phenomena will be described, together with the sources designs they lead to.

Electron and ion microscopes can be described by many quantitative features. Some relevant features are presented in table 2.1, both for electron and ion guns. To characterize ion and electron sources alone, one of the most often used is the reduced brightness β_r [34]. It relates to the amount of objects (electrons or ion) that exit the source, per solid angle, per cathode surface unit, and per energy unit: it determines the maximum current in a spatially and temporally coherent beam. As such, it summarizes several source characteristics such as the source size, the total intensity exiting the cathode, the angular intensity, the current density of the cathode, and the energy spread of the source.

2.2.1 Electron guns

In a metallic material, electrons have a high energy but are confined to the material. Their energy levels fit in a range, and the highest reached energy level is called the Fermi level E_F. To escape the material, an electron needs an energy E, defined by $E = E_W - E_F$, with E_W the work function of the material. To obtain electrons, one has to provide enough energy to the material for some electrons to reach the energy level E. This can be done by providing thermal energy to the material (the thermionic effect) or through an electric field (the Schottky effect).

The thermionic effect occurs when a metallic material is heated to the point were some electrons can overcome the work function energy barrier. The cathode current density J_C is given by the Richardson's equation:

Value	**Electron Guns**		**Ion Guns**	
	LaB_6	**Schottky FE**	**Ga^+ LMIS**	**Xe^+ ICP**
Reduced brightness $(A \cdot m^{-2} \cdot sr^{-1} \cdot V^{-1})$	10^5	$1.2 \cdot 10^8$	10^6	$9.1 \cdot 10^3$
Source size (μm)	5	15	0.05	13
Energy spread (eV)	1.5	0.4	5	6
Emission current (μA)	80	200	1-3	> 20
Angular density $(\mu A \cdot sr^{-1})$			15	18 000
Minimum Spot Size (nm)	1	40	5	25
Sample Current	60 pA	60 pA	1pA - 20 nA	1 pA - 2 μA
Sputtering rate $(\mu m^3 \cdot s^{-1})$			5.4	300

Table 2.1: Some relevant values for the assessment and comparison of electron and ion sources.

$$J_c = A_C \cdot T^2 \cdot e^{-(\frac{E_W}{k.T})} \tag{2.1}$$

Where A_C is the constant for thermionic emitters, with a value of 120 $A \cdot nA^{-2}$. T(K) is the emission temperature, while k is the Boltzmann's constant ($8.6{\cdot}10^{-5}$ $eV \cdot k^{-1}$) and E_W(eV) the work function of the material. To maximize the electron emission of the gun, one either has to lower the work function, or to increase the temperature. However, a higher temperature can lead to material evaporation and therefore shortens the lifetime of the source. The emitter material therefore has to feature a low work function combined with a high melting temperature. A good compromise can be found by using tungsten, as its work function value is 4.55 eV for a melting temperature of 3670 K. This material was used in the first electron sources, called tungsten hairpin electron guns. As shown in Figure 2.2a, a thin (100 μm) tungsten filament (the cathode) is curved in a V-shape and heated to about 2700 K. The temperature is chosen at a plateau of electron emission, where a small change in temperature does not change the current much. The electron emission occurs at the highest curvature point, and an anode extracts them using a voltage ranging from 0.1 to 300 kV. The source thus created measures from 30 to 100 μm and has a typical current density of 3.4 $A \cdot nA^{-2}$, with an energy spread of 3 eV.

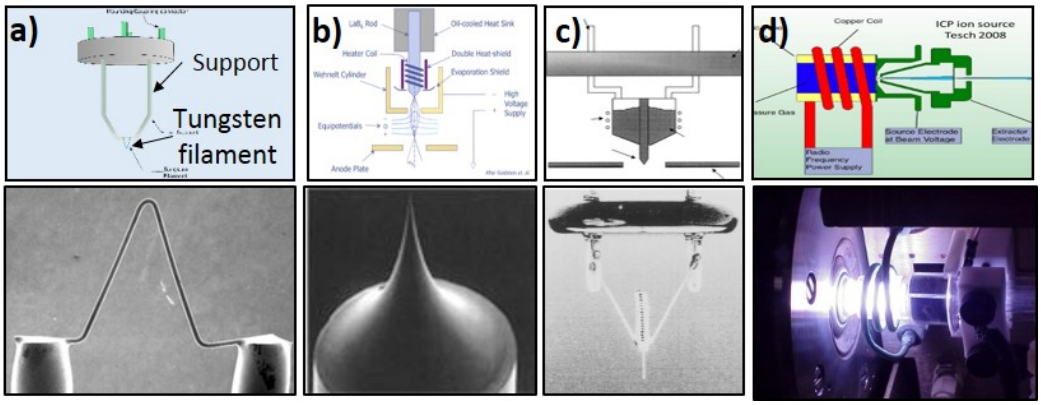

Figure 2.2: Illustrations and actual pictures of a) W filament electron source (source: nanoscience.com), b) a field emission gun (FEG) (nanoscience.com), c) the LMIS (source: Orsay Physics), and d) the Inductively Coupled Plasma (ICP) source (source: elementalanalysis.com).

To increase both the current density and lifetime of the source, other materials can be used as an cathode. A popular material is the Lanthanum hexaboride (LaB_6). It presents a lower work function than tungsten (2.5 eV), which allows for a similar or even higher density with a lower temperature. For example, to obtain the current density provided by a W cathode at 2700K, a LaB_6 cathode only needs to be heated to 1600 K. Its typical working temperature is however 1800 K, for which it provides a current density of $40A \cdot nA^{-2}$. The typical source size is 5 μm and the energy

spread close to 1.5 eV. Other materials such as the Cerium Hexaboride (CeB_6) have also been used as electron gun cathodes.

Another manner to allow the escape of electrons from the material is to set the cathode, in that case a wire with a sharp point (about 100 nm in diameter, as presented in Figure 2.2b) to a negative potential of 3 to 5 kV and to use the field effect thus created. The electric field at the top is strong and narrows the potential barrier for the surface electrons: that is the Schottky effect. The electrons can tunnel through the barrier, with no supplementary energy. The Cold Field Emission (CFE) gun was the first used and features a current density of $10^5 A \cdot \ nA^{-2}$ with a small source of 5 nm in width. It however presents a high emission angle (20°). Several improvements have been made on the FEG (Field Emission Gun), by increasing the working temperature or changing the cathode material. The most advanced gun today is the Shottky Field Emission (SFE) gun [35]. It combines the field emission phenomenon, together with thermionic emission. A <100> oriented tungsten tip is covered with a ZrO layer that lowers the work function of W from 4.5 eV to 2.8 eV [36, 37]. These allow for a high current density (5300 $A \cdot \ nA^{-2}$). It is moreover combined with a relatively small source (15 nm), which altogether leads to a high reduced brightness of $10^8 A \cdot m{-}2 \cdot sr^{-1} \cdot V^{-1}$[38, 34]. Although this type of sources has been developed since 1964, several phenomena occurring during the emission process are still unexplained and there is still ongoing research [39].

2.2.2 Ion guns

In an ion gun, a voltage is applied to a cathode, which will become the ion provider. As soon as the process provides an energy higher than the first ionization potential of the matter, ions are created. Moreover, the matter is put in a state (liquid or gas) that enables the ions to escape.

A first and most classic model of ion sources is the Liquid Metal Ion source (LMIS). In this type of sources, a needle (usually made of tungsten) with a diameter of 2 to 5 μm is placed under a reservoir filled with another metal (usually gallium). The reservoir is heated and the metal wets the needle surface. An electric field is applied to the top of the needle: the balance between the surface tension forces and the electrostatic forces is changed, forcing the gallium cone on top of the needle to change its shape. It forms a Taylor cone. Once it reaches the equilibrium, the tip of the cone is small enough for the field to extract Ga ions from the needle.

Several reasons make the gallium a good candidate for these sources. First, it features a low melting point (30°), which means it is easy to design and operate at room temperature. Due to its super-cooling properties, gallium stay molten weeks after it has been melted. Its low vapor pressure ensures a low evaporation rate, which increases the lifetime of the source. The wetting of gallium on tungsten is quite good, and the low operating temperature ensures no reaction occurs between the two metals. A typical Ga^+ LMIS source is today about 50 nm wide, with a final spot size of 5 to 400 nm (resp. at 1 pA and 20 nA). Their energy spread is quite low (5 eV) and they offer an overall reduced brightness of $10^6 A \cdot m^{-2} \cdot sr^{-1} \cdot V^{-1}$.

Such a source however presents some limitations ([40]). The sputtering yield it can offer is of several $\mu m^3 \cdot s^{-1}$ ([40, 33]), which allows for typical removed volumes below 10^4 μm^3. For some FIB applications however, including microelectronics, much large volumes have to be milled. Simply increasing the beam current is not a solution, as the spot size increases drastically for currents above 5 nA, as presented in Figure 2.3. This is due to the relatively low angular density of LMIS sources (10 $\mu A \cdot sr^{-1}$) together with their large emission angle (20°). In fact, the repulsion force between the positively charged particles widens the beam, which makes it difficult for the optics to focus the beam.

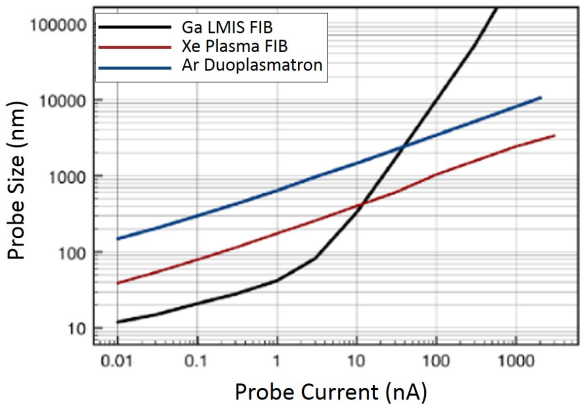

Figure 2.3: Probe size vs probe current for three different types of ion sources: the (Ga^+) LMIS, the (Xe^+) Plasma FIB, and the (Ar^+) duoplasmatron.

Other solutions, such as plasma sources and the different ion species they allow, have been considered over the last 40 years, aiming at increasing the current with little increase of the spot size. Up to the 2000's, the most popular commercially available plasma source was the duoplasmatron. It is made of a cathode filament which emits electrons when heated, as in an electron source. A gas (often argon) is introduced into the chamber with a very low pressure. As this gas is ionized by the free electrons of the cathode, it becomes a plasma. It can therefore be accelerated by a charged electrode, creating an ion beam. Although their spot size remained quite stable with the increase of current (see Figure 2.3), those sources presented low reduced brightnesses (1130 $A \cdot m^{-2} \cdot sr^{-1} \cdot V^{-1}$), low angular densities and too large spot sizes for a scanning technique. Besides, their lifetime was very low (about 250-500h [40]). Duoplasmatrons were therefore mainly used for surface cleaning, depth profiling in AES and XPS, and as primary ion sources for SIMS applications, using Ar^+ ions [41].

In 2005, Keller et al. patented a new type of plasma ion source, called ICP (Inductively Coupled plasma) sources, where the current was inductively set into a plasma [42, 40, 33]. Its general principle is presented in Figure 2.2d. A similar source, based on electron cyclotron resonance (ECR), was also introduced, with similar final characteristics. Here we focus on the ICP sources. A reservoir containing

a low pressure gas is surrounded by a coil antenna. A radio frequency power supply provides an alternating current in this antenna, which induces a time varying magnetic field in the gas. By the Faraday's law of induction, this generates a time varying electric field in the gas, and therefore a time varying current. The frequency is chosen to be above the electrons resonant frequency and below the ion resonant frequency, which results in a high density plasma (10^{13} cm^{-3} for xenon sources) since the electrons are given high thermal energy while ion thermal energy remains low. Those sources were first used with O^+ ions to replace the Ar^+ duoplasmatron for SIMS applications, as they offered an increased current density, a higher depth resolution and a smaller spot size.

As summarized in table 2.1, Xe^+ ICP sources offer a much higher emission current than Ga^+ LMIS ones with a similar energy spread. They suffer from a large virtual source (13 μm compared to 50 nm), which they compensate for with their quite parallel beam: their angular density is much higher than the one obtained with LMIS (10 $mA \cdot sr^{-1}$ compared to 15 $\mu A \cdot sr^{-1}$, with respective emission angles of 1° and 20°). Those features allow the Xe^+ ICP sources to reach a typical reduced brightness of 10^4 $A \cdot m^{-2} \cdot sr^{-1} \cdot V^{-1}$). As we will see later, this leads to much higher sputtering rates than those obtained with LMIS.

During the work presented here, sample preparation was mainly performed on a ICP PFIB, as the considered samples were quite large (about 100 μm in diameter). The machine used was a Vion single beam Xe^+ PFIB from FEI. For punctual requirements, a Strata dual beam Ga^+ FIB from FEI was also used.

2.3 Objects/matter interactions and applications

After the electron or ion beam exits its column, it is focused and aims at the sample surface. The beam itself is characterized by four main features: its spot size (d_p), its convergence angle (α_p), its current (e.g. how many object are projected on the surface, i_p), and its accelerating voltage (e.g. how fast the objects are going towards the surface, V_p). Its interaction with the sample will depend on those features, as well as the type of objects it carries, the nature of the sample, and the incidence angle.

Once the beam reaches the sample, several phenomena can occur. All phenomena come from the interactions between the arriving electrons and/or ions and the target electrons and/or ions. Those interactions can be elastic, with almost no energy loss in the beam, or inelastic, where the electrons or ions from the incoming beam lose energy. Particles resulting from those interactions, together with their microscopy-related applications, are illustrated in Figure 2.4.

In the case of an electron aiming at a target atom, the negative charge of the atom electrons can repulse the incident electron. It will therefore be deflected, with little loss of energy. After being deflected several times, the electron can find its way back to the surface and leave the sample. It can therefore be captured by a detector, which detects its high energy and labels it as a backscattered electron. If

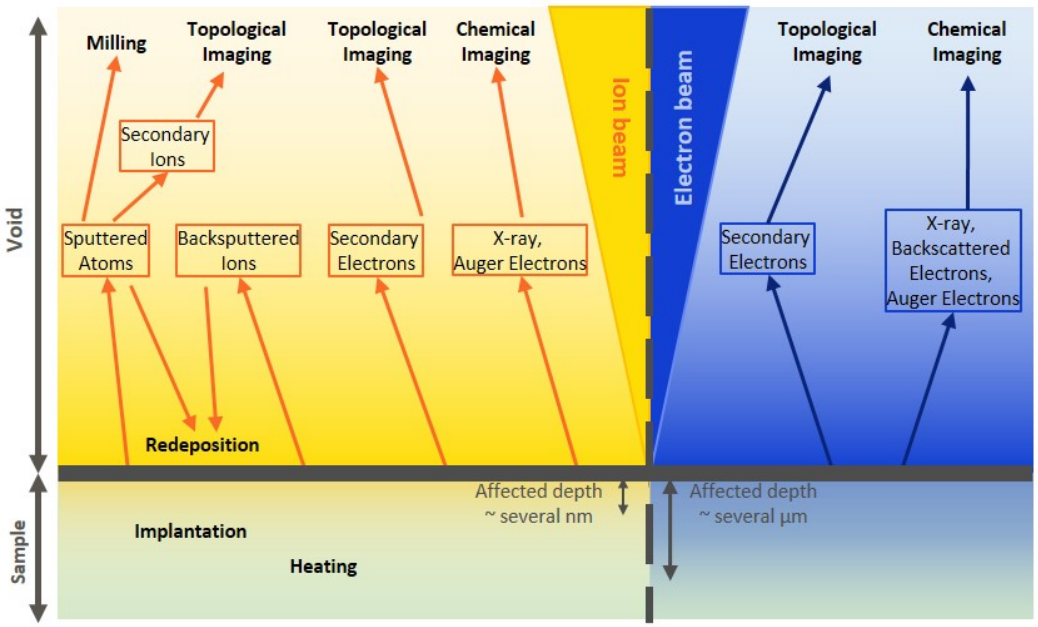

Figure 2.4: Different phenomena of interest occurring between an ion or electron beam and the sample surface.

the kinetic energy of the incident electron is high enough, it can remove a low energy electron from an atom orbit, creating a secondary electron. The obtained electron has a low energy, and is therefore used for topology imaging if it can exit the surface of the sample and be captured by a detector. The distinction between backscattered and secondary electrons is made using an energy filter, with a limit arbitrarily set to 50 eV [31]. With electrons with even higher energies, inner electrons of atoms can be removed, triggering either the emission of a photon or an Auger electron. The former provides the user with a general chemical information and leads to EDX analysis, while the latter provides the chemistry of the very surface of the sample (several nm), through Auger spectrometry. Although many imaging techniques are available inside a FIB microscope, only secondary electron imaging will be detailed in this study (see section 2.3.3).

Most of these interactions products (Auger electrons, secondary electrons, and x-ray) are observable both in the case of scanning electron microscopy and scanning ion microscopy, as they come from the direct interactions between the electrons from the beam and the electrons from the sample. In the case of an ion beam however, other mechanisms can add up, given the relatively high mass of the ions compared to the electrons (the electrons are 10^5 times lighter than gallium ions and $2 \cdot 10^5$ times lighter than xenon ions). Typically, for an 30 kV acceleration voltage, a gallium ion's momentum is 360 higher than an electron's one. This energy makes it possible for ions to eject surface atoms from the sample, resulting in sputtering of

the matter. Secondary ions can therefore be created and used for imaging. However, the capability of ion beams to sputter matter makes it above all a well suited tool for sample preparation. Parameters must be adapted to maximize the milling while limiting the redeposition of matter close to the milling area, as will be explained in section 2.3.1. The final sample can suffer from other several side effects occurring during this process. The material is heated by the ion beam, and amorphization can occur. Moreover, ions can remain in the sample and become implanted ions, and stress can be generated by the sample preparation process. Whether those side effects are critical or not on the sample will depend on the further analysis to be performed on it.

Finally, the ion or electron beam energy and its ability to break some junctions can be exploited for matter deposition, by Electron/Ion Beam Induced Deposition (EBID or IBID), as will be presented in section 2.3.2.

2.3.1 Milling

The capability of a given ion to eject an atom from the sample is linked to whether, during the collision, it transfers enough momentum to the atom for it to overcome the surface binding energy (SBE) of the material. Whether the sputtering happens or not will therefore depend on the sample material, the ions nature, their velocity and direction. It can be described by the sputtering yield Y, which is defined as the mean number of sputtered target atoms per incident ion. A basic intuitive model is that the sputtering yield, for a given target, at a normal incident and for a given acceleration voltage, would be proportional to the momentum M_{ion} of the incident ion. Let's compare the values of momenta for gallium and xenon ions, accelerated at the same voltage. In both cases, the ions kinetic energy is equal to $e \cdot \Delta V$, which leads to:

$$Ec_{Ga^+} = Ec_{Xe^+} \tag{2.2}$$

$$\frac{1}{2} \cdot m_{Ga^+} \cdot v_{Ga^+}^2 = \frac{1}{2} \cdot m_{Xe^+} \cdot v_{Xe^+}^2 \tag{2.3}$$

$$\frac{v_{Xe^+}}{v_{Ga^+}^2} = \sqrt{\frac{m_{Ga^+}}{m_{Xe^+}}} \tag{2.4}$$

The comparison of momenta rises:

$$\frac{M_{Xe^+}}{M_{Ga^+}} = \frac{m_{Xe^+} \cdot v_{Xe^+}}{m_{Ga^+} \cdot v_{Ga^+}} \tag{2.5}$$

$$= \frac{Ec_{Xe^+}}{Ec_{Ga^+}} \cdot \frac{v_{Ga^+}}{v_{Xe^+}} \tag{2.6}$$

$$= \sqrt{\frac{m_{Ga^+}}{m_{Xe^+}}} \tag{2.7}$$

As the values of gallium ions and xenon ions are known and worth $1.2 \cdot 10^{-25} kg$ and $2.2 \cdot 10^{-25} kg$ respectively, we obtain $M_{Xe^+} = 1.35 \cdot M_{Ga^+}$. Using this simple

model, one obtains $Y_{Xe^+} = 1.35 \cdot Y_{Ga^+}$. Sigmund et al. presented in 1977 the Linear Collision Cascade theory to explain conditions for sputtering happening [43]. The theory relies on the successive interactions between primary ions and sample atoms, the interaction series possibly ending in providing energy and momentum to an atom close to the surface, which can then escape from the sample. When comparing the values provided by this theory for gallium and xenon on a silicon target with an acceleration voltage of 30 kV, one obtains $Y_{Xe^+} = 5.2$ and $Y_{Ga^+} = 4$, which rises a ratio of 1.3.

Thus, the choice of xenon ions for large volume milling is motivated by the intrinsic sputtering yield of xenon ions, 1.3 times bigger than the gallium one. Combined with this feature, xenon ions can be extracted from a plasma source, as explained previously, which allows for a 2 μA current reaching the target (compared with 20 nA with Ga^+ LMIS). This means the sputtering happening during a given duration is 100 times higher with ICP than with LMIS. This leads to higher sputtering rates attainable by Xe^+ ICP ion beam (more than 100 $\mu m^3 \cdot s^{-1}$ compared to 5.4 $\mu m^3 \cdot s^{-1}$)
.

After leaving the sample surface, sputtered atoms have a quite low energy (3 to 5 eV). They can be ionized and, as charged particles, they can be attracted by a grid and hit a detector. They can therefore be used for imaging (secondary ions imaging), although they are much less numerous than secondary electrons (10 to 1000 times less [32]). Most of ejected atoms remain in the area of the milling zone, as their low energy prevents them from leaving. They will likely redeposit on the surface. Redeposited matter is mainly spotted on the side walls, where it can have a width of 170 nm for a Ga^+ milling on Si [44]. The redeposition phenomenon is to be taken into account when milling, since it adds matter in the area supposed to be milled. Enough space must therefore be allowed for redeposition to happen far enough for the milled area, and currents must be adapted for milling to prevail on redeposition. Redeposited matter has been shown to contain up to 12% at. of Ga, and to change conductivity of the surface. This will have an impact not only on the milling and the imaging of the sample, but also on the conductivity of the final sample.

Due to inner repulsive interactions between positively charged ions, it is hard to focus the whole ion beam, which will have a cone shape. Even if the top of the cone is highly focused as quite small, the tail of the beam will be much larger. Therefore, in the case where a deep milling occurs (several microns in the case of FIB, several tens of microns for PFIB), as the beam scans the sample discretely, vertical line can appear on the cross-section, as illustrated in Figure 2.5. This is all the more true when the sample is made of several materials with different sputtering yields. This side effect is critical for imaging, as the vertical lines make image interpretation difficult. Several strategies have been developed to overcome this issue. They can rely on the addition of an amorphous protective layer on top of the surface, which will randomize the direction of ions and reduce the curtaining [45, 46]. Processes based on a rocking curve around the horizontal direction are also studied. The sample is tilted during the milling, in a plane coplanar with the incident ions, so

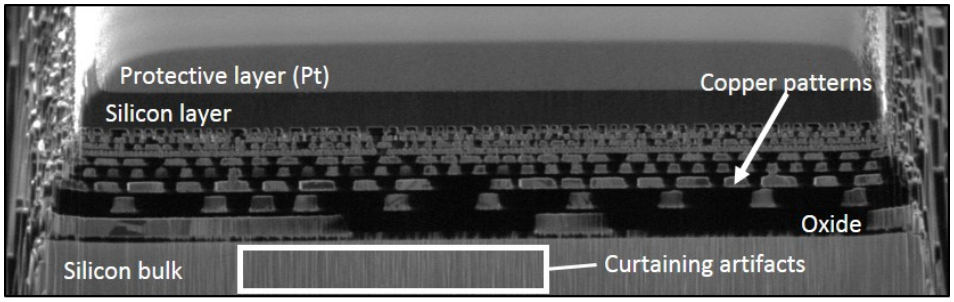

Figure 2.5: Illustration of curtaining artifacts: surface imaging of a copper stack inside an oxide matrix, cut and imaged with a Xe^+ PFIB. *Image: Ion-induced secondary electron image acquired in a PFIB.*

that the ions do not come from the same direction during the whole process [47, 48]. Curtaining is mainly an issue for further imaging of the milled cross-section, for example in the case of Slice and View procedures or for very thin lamellae made for TEM observations.

Furthermore, the FIB preparation damages the sample around the milling or imaging area. On the bottom wall of the milled area, heating occurs in the material. For a gallium FIB, the increase in temperature is less than 10°K for gallium FIB [49]. Several definitions of FIB damages can be found in the literature. It can be defined as a change in the sample morphology outside of the milling area, or the decrease of the electrical properties of the sample [50].

Two main problems of FIB preparation, especially in the case of thin samples aimed for TEM observation, are amorphization and implantation. Amorphization occurs because of the substrate atoms recoil, coming from the interaction between atoms and ions. The lattice order is then destructed and a part of the crystalline substrate becomes amorphous. Moreover, as incident ions lose energy with every collision inside the lattice, they may remain in the material, as implanted ions. Charged substrate ions can also be implanted in the material (self-implantation). For a silicon substrate and gallium ions accelerated at 30 kV, the thickness of amorphous material next to the side walls is 30 nm, while it is 56 nm next to the bottom wall. The implantation of Ga^+ ion occurs on 13 nm next to the side walls (36 nm for the bottom wall), while the self implantation is present on 26 nm near side walls (58 nm for the bottom wall) [44]. The use of xenon ions seems to reduce the amorphization of the substrate, as its thickness near side walls has been evaluated to only13 nm with Xe^+ accelerated at 30 kV [30]. Those two phenomena must be taken into account when setting parameters for a milling, as for low doses of ions, they prevail upon milling, and induce swelling of the sample [50].

When defining the damaged zone as the electrically modified one, the thickness of the affected areas is however much higher and can reach up to several microns [50, 51]. This can be explained by beam broadening and diffusion. In x-ray tomography experiments presented here, the samples were several tens of microns

wide. Therefore the regions of interest did not suffer from damages caused by the PFIB during sample preparation.

2.3.2 Matter deposition

The secondary electrons and ions created by the interactions of the beam with the sample have a lower energy than the primary beam. As such, they have a higher cross-section and are more likely to interact with any particle present in the sample environment. This phenomena, together with the heat the interactions generate, is used for matter deposition. For this, a precursor molecular gas containing the wanted material atoms is introduced in the chamber through a Gas Injection System (GIS), near the sample. It is adsorbed on its surface. The ion or electron beam is then directed towards the surface, drawing a pattern. The secondary electrons and ions reach the gaz molecules close to the interaction point, and separate their two parts: the gas itself leaves the area, while the material to be deposited stays on the surface of the sample and builds layers. Depending on the used beam, this process is called EBID (Electron Beam Induced Deposition) or IBID (Ion Beam Induce Deposition). Several processes are therefore competing during the procedures. An equilibrium has to be found in order to provide the right amount of gas for the adsorption to happen layer after layer and the right current to separate the gas molecules without milling the sample.

EBID and IBID are used for several purposes. First, for any extracting procedure, as will be presented in section 2.4.2, metal joints (typically Pt) are created between the selected region of interest and a micromanipulator, allowing for the displacement of the future sample. Insulator can be deposited to separate two conductive zones, while conductive patterns or grids, or even circuits, can be designed and realized using metal local deposition. The deposition of a thick (several microns in the case of PFIB) layer of an adapted material can also serve as a protection of the sample surface, either to reduce its damage, either to counter the curtaining artifacts.

2.3.3 Imaging

Here, only secondary electron imaging is considered, as it is the most commonly used. Secondary electrons are emitted after an electron from the incident beam has ejected an electron from one sample atom. Once it exits the sample surface, it is attracted by a cathode and detected, typically using a Everhart-Thornley detector. As the secondary electrons come from an inelastic interaction, they have a low energy. The information they provide therefore comes from the region close to the surface (typically a few nanometers), with little sensitivity to the chemistry: they provide a topological information.

The electron are first attracted by a positive potential grid (at about 400 V), and accelerated towards a scintillator (using a 2 kV voltage), which converts the electronic signal into light. This signal generates the final image: for every scanned

point, the more electrons reach the scintillator, the brightest the equivalent image point. The SE yield is defined as the number of SE detected per incident object and highly depends on the incidence angle [52]: the topology is therefore easily visible in the obtained images.

In this process, the spot size d_p will determine the lateral resolution of the final image, while the voltage V_p will play a role on the penetration of ions or electrons in the sample. The signal to noise ratio will be linked to the current i_p together with the exposure time. The depth of focus will come from the value of the convergence angle α_p. Due to the relative values of electron and ion sources size, emission angles, and emitted intensities, the reachable spot sizes vary in a large range. Generally, the smallest probe sizes are obtained for SEM, with spot sizes smaller than 1 nm [53]. Ga^+ LMIS sources allow for spots as small as 5 nm, while Xe^+ ICP sources reach 25 nm large spot sizes. This induces higher imaging resolutions for SEM than for LMIS FIBs, and ever higher than for ICP FIBs.

As mentioned earlier, topological contrast in SE images comes from the difference in SE yield depending on the orientation of the surface. When it comes to polycristalline materials, this effect allows the visualization of grains using SE: the SE yield will depend on the orientation of both the surface and the cristalline planes. This effect is called channeling [54]. As ions have a smaller penetration depth in the material than electrons [32] and thus a higher sensitivity to orientation, they offer a higher sensitivity to the channeling effect [55]. This high orientation contrast has been shown to allow for quantitative analysis, giving results close to the ones obtained by EBSD (Electron BackScatter Diffraction) imaging, provided the adequate post-processing [56].

An important effect to be taken into account when imaging a surface, and especially an insulator, is also the charging effect. When imaging the sample with electrons, if the electron cannot flow through the material towards the ground, they remain trapped at its surface, close to the impact location. By their negative charges, they will deviate any supplementary electron arriving at the surface, resulting in artifacts (mainly extremely bright regions) on the final image. This effect also occurs for positive ion imaging: as they cannot flow through the sample, positive charges will accumulate on the surface. In addition to the deviation of incoming ions, if SE are created, they are attracted back to the surface, resulting in dark areas in the final image.

Several solutions are deployable when dealing with charging effect. First, the conduction of charges can be assured by a conductive coating or contact, together with a good grounding. When performing the observation in a FIB column, secondary ion imaging can be used, as ions will not be attracted back to the sample. Furthermore, a neutralizing electron flood can suppress the remaining positive charges and allow the imaging (for a time).

Finally, one has to keep in mind that when imaging with ions, all the problems encountered when milling are present. Thus, imaging whith ions can lead to ion implantation, swelling of the surface, and sputtering when it come to fragile materials.

2.4 Applications of Focused Ion Beam microscopes

FIB microscopes offer a large set of tools that allow to sputter and deposit matter, as well as to image a given sample. They are today used in various fields, ranging from biology to the semi-conductor industry [57]. Here, two applications of interest are reviewed, as they have been extensively used during this PhD. Sample preparation using the lift-out technique allows to select a region of interest (ROI) from a piece of wafer, and to install it on top of a support for further observations such as tomography. Slice and view procedures are used to directly image a volume inside a dual beam or single beam focused ion beam microscope.

2.4.1 Slice and View procedure

Slice and view (SaV) is a destructive 3D imaging method which relies on the sequential slicing of the sample with a regular step, and the imaging of the newly created surface at each step. After acquiring a large number of such cross-sections, one can obtain a 3D rendering of the analyzed region of interest, assuming an interpolation between slices leads to an accurate enough estimation of the object. The slicing can be done using microtomy [58], focused ion beam (FIB) [59], or polishing [60], while imaging can be performed with all available 2D techniques, using light, electrons, ions, or x-ray for example [61, 62, 63].

Observable volumes and achievable resolutions obviously depend on the chosen slicing and imaging tools. In 3D integration, observed volumes can measure up to $100^3 \mu m^3$. The resolution should be below 100 nm. Given these constraints, ion slicing, together with ion and electron imaging, are particularly relevant. In this section, a general workflow of Slice and View procedures is presented, together with four slicing/imaging tools couples, chosen among electrons, Ga^+ ions, and Xe^+ ions.

2.4.1.1 Slice and View workflow

Although the slicing and imaging tools used for Slice and View procedures can differ, the workflow itself remains similar. It is illustrated in Figure 2.6.

When performed inside a focused ion beam chamber, all procedures demand a preparation step, during which deep trenches (typically 10 to 100 μm deep) are milled around the region of interest (ROI). This step is necessary in order to reduce future redeposition. The data acquisition simply relies on the successive slicing of a cross-section and its imaging. Depending on the type of implementation (whether the slicing tool is the same as the imaging one or not), a change of current values and of sample position can occur between those two steps, as will be presented in section 2.4.1.2. Once all the slices have been acquired, they are aligned with one another and a volume is obtained by stacking them together. In ion and electron imaging, the 2D cross-sections pixel size is usually much smaller than the slicing step (up to 3 times smaller for FIB/SEM or PFIB/SEM). In order to obtain isotropic voxels, the post-processing step may include a resampling step.

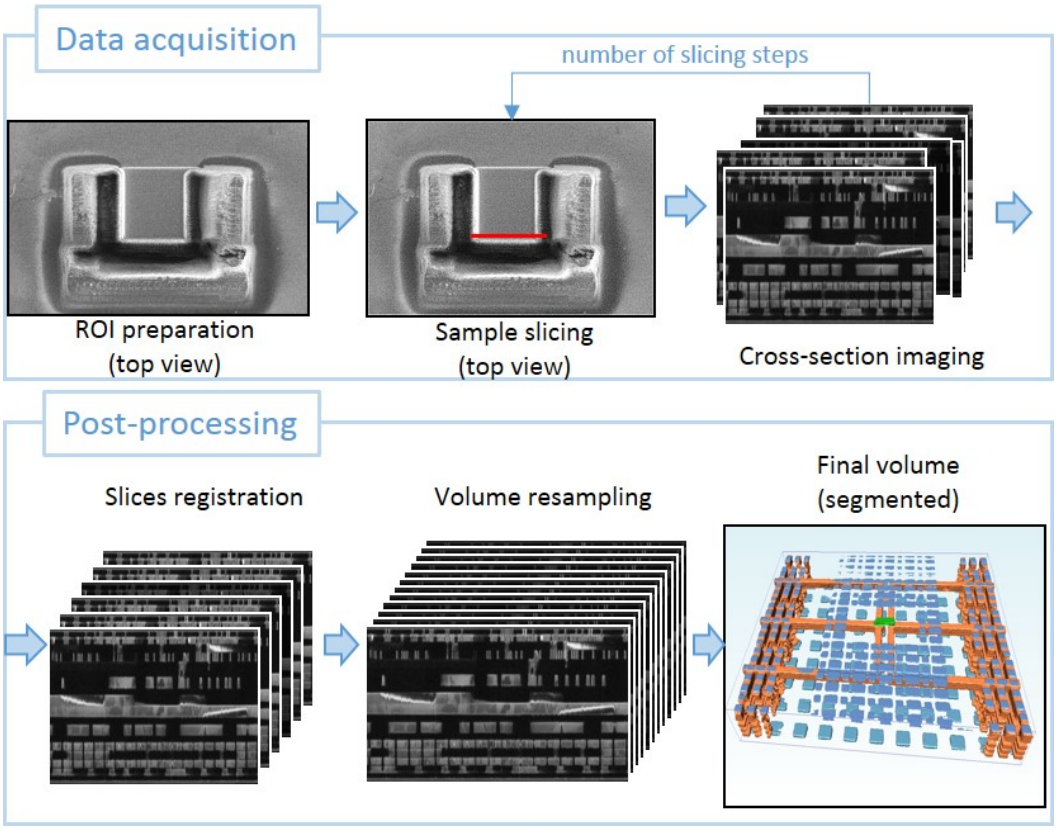

Figure 2.6: Illustration of the Slice and View (SaV) procedure workflow. *Images: Ion-induced secondary electron images acquired in a PFIB.*

2.4.1.2 Different implementations

Here we present most common implementations of the Slice and View technique for resolutions and volumes compatible with 3D integration samples. Figure 2.7 presents typical voxels sizes and analyzed volumes as found in the literature for those techniques.

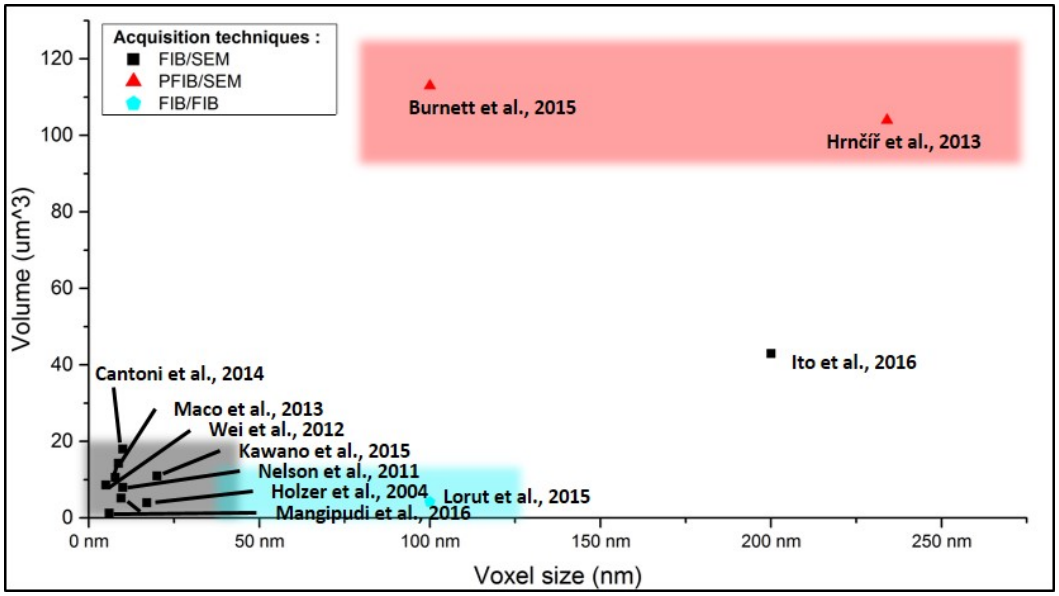

Figure 2.7: Comparison of reachable volumes and pixel sizes for Slice and View procedures.

The most common implementation of SaV procedures is performed in a FIB/SEM dual beam microscope. It was introduced in 2004 [59] and has been used in many fields since [64, 65]. The slicing of the sample is performed using Ga^+ ions, while the imaging is made with the electron column. No movement of the sample is necessary between the slicing and imaging steps, as the two column form an angle of 52°. The image pixels however are not square-shaped and a resampling step is usually necessary. As the secondary electron imaging offers high resolution, the slices pixel size are typically 5 nm wide, while the slicing step can be as small as 10 nm. Using this technique, volumes of $10^3 \mu m^3$ can be imaged in about 30 hours.

As presented in section 2.3.3, ions are more sensitive to channeling than electrons. Better orientation differentiation can therefore be obtained by inducing secondary electrons with ions. For given applications, a FIB/FIB procedure si therefore relevant [66, 67]. It applies perfectly to the distinction of intermetallic compound inside a copper pillars, for example. The data acquisition is performed using only the ion beam: therefore, the sample must be rotated and the current value changed between slicing and imaging.

Although FIB slicing allows for small voxel sizes, it also limits the observable

volumes to about 10^3 μm^3. To achieve larger volumes, SaV procedures in a dual beam PFIB have recently been developed. While the imaging is still performed using electrons, the slicing step is made using Xe^+ ions, which reduces the time needed for this step. Volumes of 100 μm^3 have been observed [68, 30]. The time needed for the analysis ranges from a few hours to 65 hours, depending mainly on the slicing step.

During this PhD, an implementation of a PFIB/PFIB Slice and View procedure has been designed and set on a single column PFIB. The details of these hardware and software developments are presented in section 4.

2.4.2 Sample preparation: lift-out procedures

Ga^+ Focused Ion Beam microscopes offer the possibility to mill and manipulate objects smaller than 10 μm^3, and to extract them from pieces of wafers. They are extremely well adapted for sample preparation for TEM, which require a lamella whose thickness is below 100 nm. To perform this sample preparation, FIB lift-out techniques [69, 70] have been developed and are currently extensively used, especially in the field of microelectronics [71]. The method was further adapted for electron tomography [72, 73], atom probe tomography [74, 75], and x-ray tomography [76, 77]. To overcome the limit in time and volume fixed by the FIB milling, the technique has also been implemented in a PFIB [48, 78].

As will be presented in section 3.3, the samples needed for x-ray tomography (in the case of the ID16A and ID19 beamlines) have a typical width of several tens of micrometers. The PFIB, combined with a lift-out technique, is therefore relevant for their preparation, and is illustrated in Figure 2.8.

The lift-out technique forms into several steps:

a) First, the region of interest is coated with a protective layer of Pt and the region around it is milled at a high beam current ($2\mu A$).

b) One side of the cylindrical sample is partly cut using the ion beam. The sample is then rotated by 180° in order to access the other side.

c) A micromanipulator (EasyLift) is approached to the region of interest together with a Gas Injection System (GIS). A Pt join is deposited between the ROI and the micromanipulator using the IBID method presented in section 2.3.2.

d) The sample is released from the wafer using a second cut, performed at a high current (typically $2\mu A$). The micromanipulator is lifted together with the sample.

e) The micromanipulator, on top of which the sample is attached, is placed close to the sample support.

f) A Pt deposition solders the sample to the support.

g) An ion abrasion releases the micromanipulator from the sample.

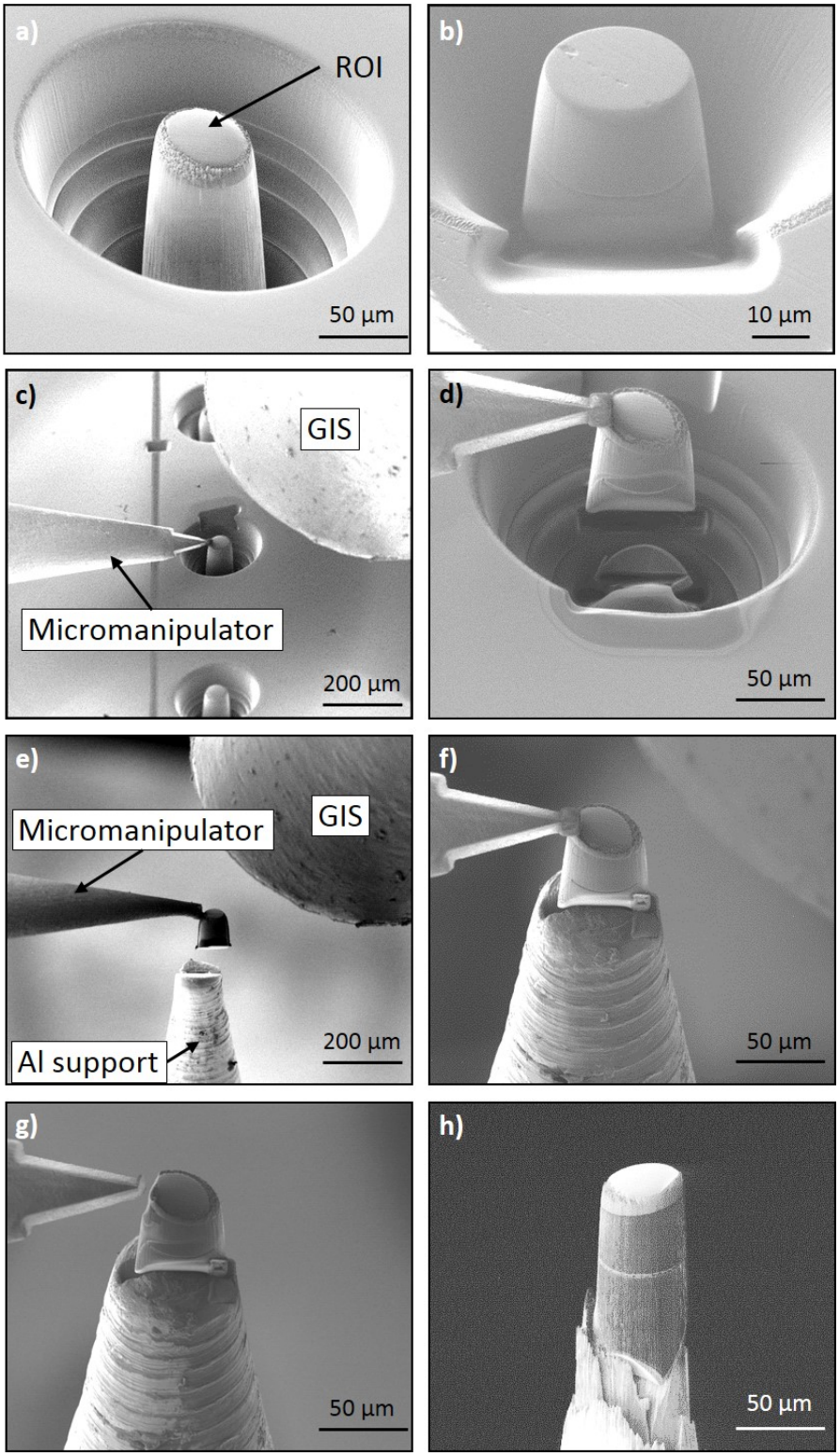

Figure 2.8: Illustration of the lift-out procedure performed in a PFIB microscope. *Images: Ion-induced SE images acquired in a PFIB.*

h) An optional annular milling gives the final sample. The ion current is set to a lower value (typically 59 nA) in order to obtain a cylindrical shape while limiting the damaged area around the sample.

The first circular milling was originally performed using concentric circle-shaped patterns, as shown in Figures 2.9a and 2.9c. The successive patterns were triggered using the iFast FEI software. A typical milling of a 50 μm wide sample took about 4 hours. During the time of this PhD, a new and more efficient milling method was developed in the laboratory, and has been routinely used since. It is described in details in [78] and illustrated in Figure 2.9. It relies on an ellipse-shaped pattern and a new dwell time management throughout the pattern, aiming at a more efficient milling. This new milling method takes about 1 hour and allows for the extraction of the sample with only one cut (instead of two). The remaining steps stay the same as in the original method.

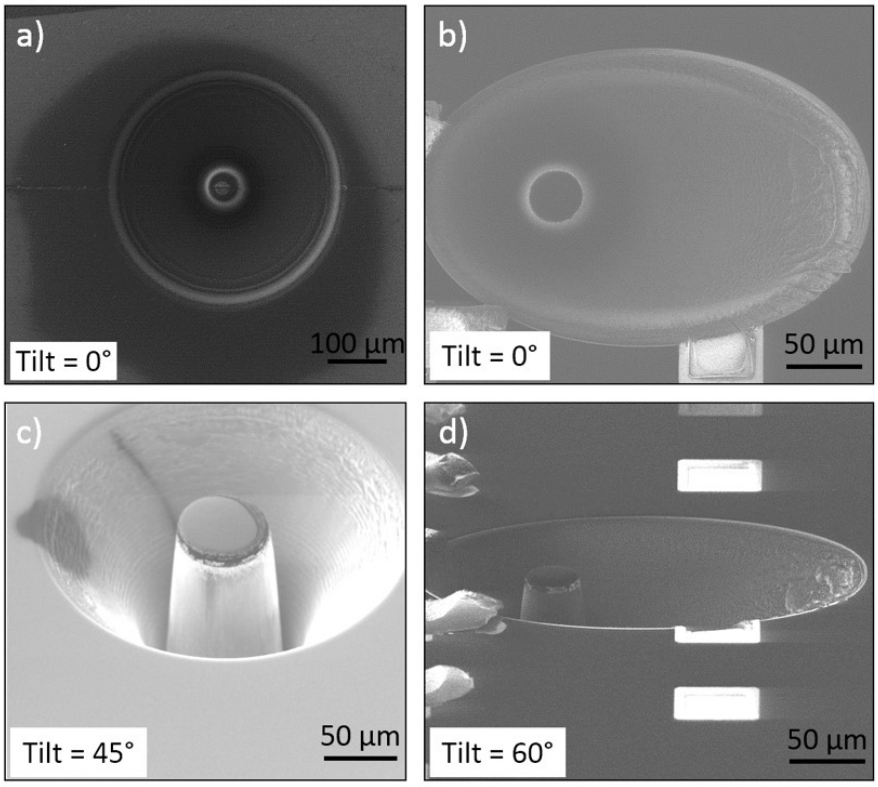

Figure 2.9: Illustration of the originally used circular milling method (with a) tilt=0° and c) tilt=45°) and the improved ellipse-shaped milling method (with b) tilt=0° and d) tilt=60°). *Images: Ion-induced SE images acquired in a PFIB.*

Microscopes électroniques et ioniques
Résumé du chapitre

Dans ce chapitre, les microscopes électroniques et ioniques sont présentés et décrits. Les différentes sources d'électrons et d'ions sont présentées, avec leurs caractéristiques. L'utilisation de sources plasma d'ions xénon est justifiée par leur fort taux d'abrasion de la matière, bien supérieur à celui des sources gallium classiques. Le PFIB (Plasma Focused Ion Beam) est donc choisi comme outil pour la préparation de grands échantillons (100 μm de diamètre) comme ceux utilisés dans ce travail.

Les différentes interactions possibles entre les faisceaux de particules chargées (électrons ou ions) et la matière sont passées en revue. Les différentes actions possibles au sein d'un tel microscope, provenant de ces interactions, sont décrites. Il s'agit de l'abrasion de matière, du dépôt de matière sur l'échantillon, et de l'imagerie (ici uniquement par électrons secondaires).

Enfin, deux applications spécifiques de microscopes à faisceau d'ions, utilisées pendant ce travail de thèse, sont introduites. Tout d'abord, les procédures dites Slice and View, techniques d'imagerie 3D destructives, sont détaillées. Il s'agit de méthodes consistant à découper des tranches successives de l'échantillon considéré, et d'imager à chaque étape la surface nouvellement créée. Trois implémentations déjà utilisées sont présentées : le FIB/SEM, le FIB/FIB, et le PFIB/SEM. La technique de préparation d'échantillons nommée lift-out est également présentée, puisqu'elle a été utilisée sur bon nombre d'échantillons au cours de ce travail. Il s'agit d'une technique consistant à détourer une zone d'intérêt grâce à un faisceau d'ions, puis de fixer cette zone à un micromanipulateur. L'échantillon ainsi formé est alors fixé à un support, que l'on pourra manipuler pour une analyse future.

Chapter 3

X-ray imaging methods

Contents

3.1 Elements of x-ray physics 46
3.1.1 Obtaining an x-ray beam 46
3.1.2 X-ray/matter interactions 53
3.2 Experimental setups 57
3.2.1 ID16A: a nano-tomography beamline 58
3.2.2 ID19: a versatile tool for coherent imaging and diffraction . . 60
3.2.3 ID01: Local strain measurement 61
3.3 X-ray transmission 3D imaging 62
3.3.1 2D image formation 62
3.3.2 Obtaining a 3D reconstruction 70
3.3.3 Sample Preparation 74
3.4 Strain measures by Bragg diffraction 76
3.4.1 Monochromatic Bragg Diffraction 76
3.4.2 The ID01 workflow 78
3.4.3 Sample Preparation 82

As seen in the previous chapter, electrons offer great features for imaging, as they can be focused and participate in high resolution scanning imaging techniques. They can also be used for diffraction measures, although their penetration depth remains below the micrometer. On the contrary, x-ray offer high penetration depth, and wavelength compatible with the size of crystalline lattices in matter. In fact, their energy is comprised between 124 eV and 124 keV, for wavelengths comprised between 0.01 nm to 10 nm. X-ray have consequently widely been used for diffraction measures. With the improvement of focusing X-ray optics and sources, it is also possible to perform condensed matter imaging using X-ray, as will be shown in this chapter. Moreover, hard x-ray (defined as having an energy above 5-10 keV) can penetrate into several millimeters or even centimeters of condensed matter, offering the possibility to analyze the inside of quite large samples. To exploit those advantages, many experimental setups have been designed, depending on the wanted information and the analyzed material. They can be implemented in a lab instrument or in a synchrotron.

Although some techniques rely on similar physics principle, the characteristics of the beam they use will have a critical impact on the type and precision of information they allow for. The beam characteristics, such as its energy, its monochromaticity and shape for example, can be tuned according to the given experiment. This is all the more true in a synchrotron, as will be presented later on. Such a beam

interacts with the sample, be it by absorption, scattering, or refraction, and exits it. A detector then allows to record the exiting signal, and a post-processing step hopefully provides the wanted information.

This chapter provides an introduction to the x-ray characterization methods used in this work. A first section provides the main elements of x-ray physics exploited here, including the generation of x-ray and their interaction with matter. The focus is set on the versatility of x-ray sources, and more specifically of synchrotron ones. A section is dedicated to the presentation of the characteristics of the beamlines used here. Finally, a mode detailed description of x-ray imaging and strain measurement is provided.

3.1 Elements of x-ray physics

In this section, largely based on [79], the main steps of the experimental part are depicted. First, we will present the different ways to obtain an x-ray, in a lab instrument or in a synchrotron, and the different features it can be given. The main interactions of x-ray with matter will then be described, as they will give the reader an insight on the characterizations x-ray can provide.

3.1.1 Obtaining an x-ray beam

Several processes allow for the creation of an x-ray beam. Two types of x-ray sources are depicted here: laboratory sources and synchrotron ones. The common principle is that x-ray are emitted when a charged particles, such as an electron beam, is accelerated or decelerated. In lab sources, the beam is decelerated when approaching a target cathode, while in synchrotron sources, the deviation of trajectory of the electrons by magnets produces the x-ray beam.

In this section, a more detailed presentation of those sources is provided, together with some relevant characteristics of an x-ray beam (see table 3.1). It is noticeable that the notion of source is ambiguous in the case of a synchrotron. As will be presented in section 3.1.1.3, several types of devices (bending magnets or insertion devices) allow for the generation of photons. Moreover, for a synchrotron beam, many filters and optics occur between the source and the sample, changing its characteristics. In the case of an experiment, relevant values are the one concerning the beam that interacts with the sample. Therefore, in table 3.1, only values of the final beam are given, for three ESRF (European Synchrotron Radiation Facility) beamlines where experiments were carried out: ID16A, ID19, and ID01. In the case of a lab source, the general principles apply to any source, but values given in this chapter apply more particularly to the Xradia tomograph, which was used in this work. The characteristics given here for x-ray sources can be linked to the values provided in table 2.1 (see chapter 2) about characteristics of electron and ion sources.

Value	Lab source	Synchrotron source		
	Rotating anode (Xradia)	**ID16A**	**ID19**	**ID01**
Brilliance ($ph./s/mrad^2/mm^2/0.1\%BW$)	10^8	$> 2.10^{12}$		
Flux ($ph./s.$)	10^6	10^{13}		10^9
Source size (μm)	2	0.03	125 x 25	0.065 x 0.056 to 6000 x 1000
Energy (keV)	polychromatic	17.05; 33.6	26.5	8; 9
Energy spread	polychromatic	10^{-2}	10^{-3}	10^{-4}

Table 3.1: Some relevant features of x-ray sources, for one lab source (the Xradia tomograph) and three ESRF beamlines: ID16A, ID19, and ID01. The given values are the ones obtained near the sample, during this experiments presented in this work.

3.1.1.1 Relevant features of an x-ray beam

When comparing x-ray beams from different instruments, the mainly used parameter is the brilliance B. It is somewhat equivalent to the reduced brightness presented for electron and ion beams (see chapter 2). Brilliance is defined as:

$$B = \frac{photons}{second \cdot mrad^2 \cdot (mm^2 sourcearea) \cdot 0.1\%BW} \tag{3.1}$$

It represents the number of photons of a given wavelength produced by the source per second, in a surface unit area and for an angle unit divergence. The higher the brilliance, the more photons of similar energy will reach the sample per second. Although brilliance summarizes the main features of an x-ray beam, it can be broken down into simpler characteristics, also relevant for the comparison of x-ray beams. Their descriptions are given here, and their values for classic sources are provided in table 3.1.

The flux of the beam, expressed in photons/second ($ph./sec.$), is a critical parameter for the speed of an experiment. A high flux will allow for statistical or even in-situ experiments. Moreover, a high flux will allow the filtering of the beam in energy while keeping enough photons for the actual experiment. In the same order of ideas, the global divergence of the beam makes the filtering possible or not: if the beam is too wide, focusing optics' angular acceptance will be too small to capture and focus the whole beam, and a large fraction will be lost. Since the manufacturing of large x-ray optics remains a challenge, obtaining a low divergence beam is very important for further filtering and focusing.

The energy spread $\frac{\Delta E}{E}$ and the source size define the beam coherence. Coherence of the beam relates to the ability of interferences to occur in the beam, and is useful for phase-contrast imaging and coherent diffraction. The coherence of a source is defined by the longitudinal and transverse coherence lengths, as well explained in [79]. In simple models of propagating waves, the source is often considered punctual and monochromatic, which is never the case. To illustrate the notion of coherence, a real source can be modeled as two source points (the source is not punctual) which emit two waves with different wavelengths (the source is not monochromatic). This leads to the two situations illustrated in Figures 3.1a and 3.1b. In the first one, two waves are emitted in a same direction with a slightly different wavelength. Their

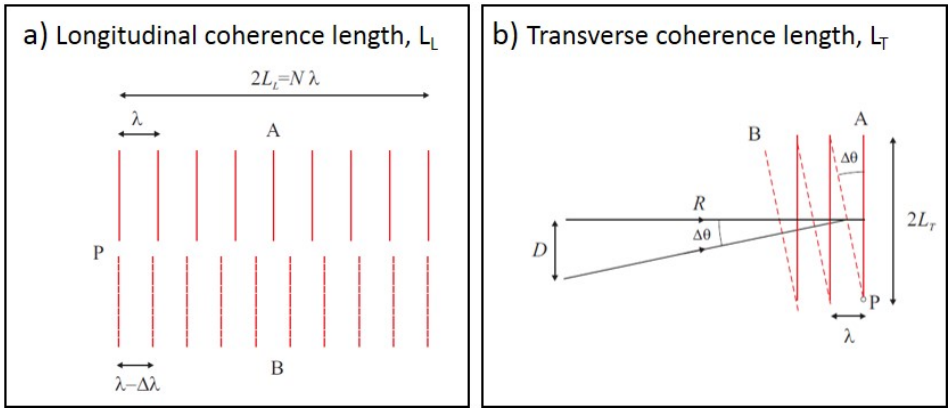

Figure 3.1: Longitudinal and transverse coherence lengths. (a) Two plane waves with different wavelengths are emitted in the same direction. For clarity we have shown the waves displaced from each other in the vertical direction. (b) Two waves with the same wavelength are emitted from the punctual ends of a finite sized source of height D. *Image source: [79].*

wavefront coincide at the origin (P), and the longitudinal coherence is defined as the distance needed for the wavefronts to coincide again. It is also given by the expression 3.2.

$$L_L = \frac{\lambda^2}{\Delta\lambda} = \lambda\frac{E}{\Delta E} \tag{3.2}$$

where $\Delta\lambda$ (resp. ΔE) is the difference between the two wavelengths (resp. energies) and λ the central wavelength (resp. energy). The longitudinal coherence refers to how monochromatic the source is. In the second situation, two monochromatic and punctual sources, separated by a distance D, emit waves at a wavelength λ. The waves are observed from the point P. From its point of view, the two waves arrive from two slightly different directions, separated by a angle $\Delta\theta$. The transverse coherence length is defined by the distance from the source where the wavefronts will coincide (where the source will appear punctual). Its expression is given by equation 3.3.

$$L_T = \lambda\frac{R}{D} \tag{3.3}$$

with R and D defined in Figure 3.1 and λ the wavelength of the beam. The transverse coherence refers to the size of the source, as seen from the target point of view. The longer those two characteristic distances, the more coherent the source. From those equations, we can see that to improve the coherence of the source, one can reduce its wavelength amplitude, reduce its angular divergence, and/or set the observation further away. Consequences of this remark will be discussed in section 3.2.

3.1.1.2 Laboratory sources

First laboratory x-ray sources, called Coolidge tubes and first commercialized in 1912, were simply made of a metallic anode, typically tungsten, towards which an electron beam was accelerated. The beam obtained this way is composed of two parts, as can be seen in Figure 3.2 (in blue). First, the deceleration of electrons creates a bremsstrahlung radiation, which presents a continuous spectrum whose maximum energy is the kinetic energy of the incident beam. In addition, much more intense sharp peaks appear on the spectrum. They are fluorescence peaks: when an energetic enough photon reaches the target material atoms, it can eject an inner electron, creating a hole. An external electron fills the gap, and this desexcitation releases a photon, with an energy specific to the material. As the interaction between the electron beam and the anode generates heat, the cathode must be water-cooled.

Since the 1960s, in order to dissipate heat more efficiently, rotating anode sources have been commercially available. The principle of such sources is illustrated in Figure 3.3a. The typical brightness obtained with such sources is B=10^8 $ph./s/mrad^2/mm^2/0.1\%BW$, with a flux of 10^6 $ph./sec.$ and a source size of several microns. As the source size is defined by the sphere of interaction between the electrons and the cathode, further studies aim today at focusing the electron beam on nanowires. The source size obtained this way is sub-micronic [80].

All those sources however lack flux when it comes to selecting specific energies for monochromatic experiments for example, and generally lead to low signal to noise ratios. They imply long acquisition time (60 sec for a radiograph), which prevents any time-resolved experiment or statistical study. As presented in Figure 3.4, synchrotrons sources offer much higher brilliances (typically 10^{20} $ph./s/mrad^2/mm^2/0.1\%BW$), which implies they are a much more versatile tool.

3.1.1.3 Synchrotron sources

The principles presented in this section are valid for any third generation synchrotron, as they are based on the same architecture. Their precise features are however not exactly the same. Each synchrotron is best suited for a set of applications. In this section, examples which are provided illustrate the ESRF.

ESRF, as any third generation synchrotron, is composed of several parts, illustrated in Figure 3.5. First, a 100 kV triode Field Emission Gun provides an electron beam which is injected and accelerated inside a linear section (called LINAC) thanks to a series of radio-frequency cavities, until it acquires an energy of 200 MeV. The electron beam is then transferred to a circular booster, where it is accelerated until it gets an energy of 6.04 GeV. Once this energy is reached, the electron beam is transferred into the storage ring, which has a circumference of 844 m and is under ultra high vaccum ($<10^{-8}$ mbar, in order to avoid collisions). The electrons will travel inside the ring several hours. The storage ring, despite its name, is actually a polygon, with successive linear sections. At each submit of the polygon, a bending magnet (BM) ensures both the deviation of the electrons, in order to keep them

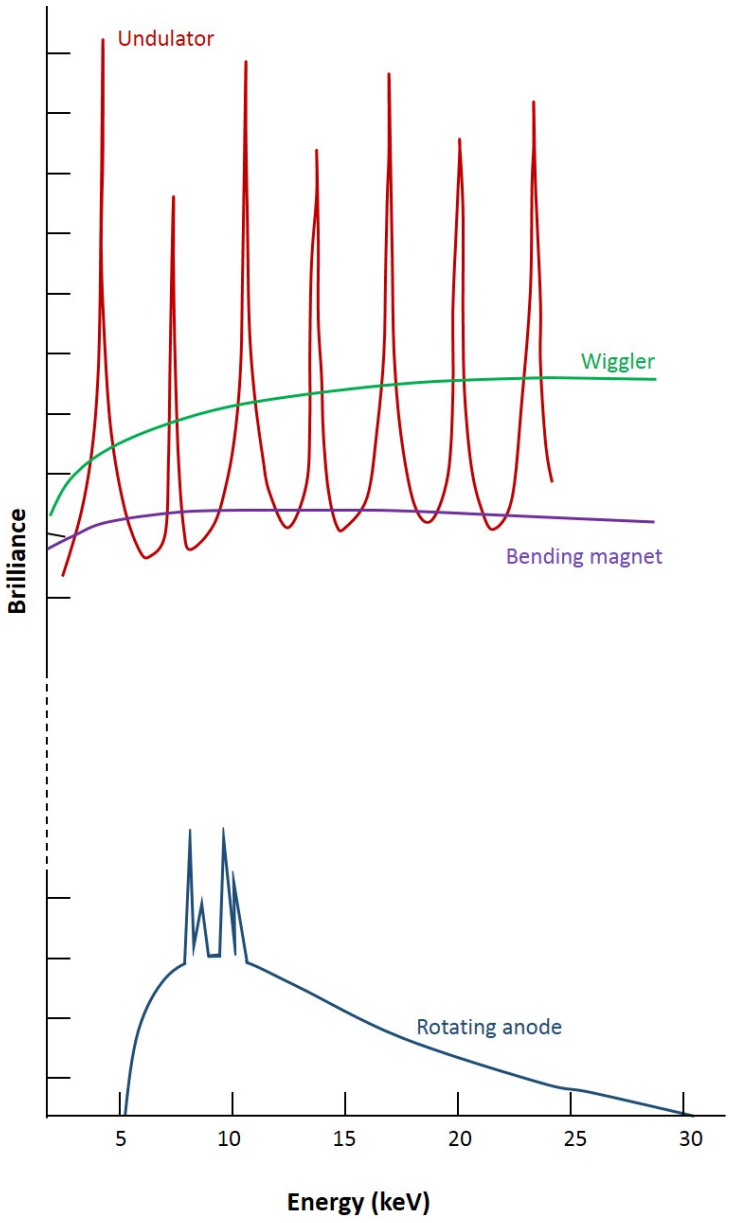

Figure 3.2: Typical spectrum obtained with different types of x-ray sources: a rotating anode (in blue), a bending magnet (in purple), a wiggler (in green), and an undulator (in red).

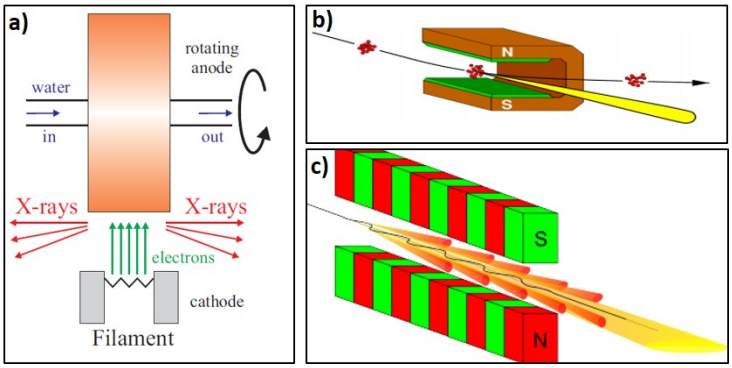

Figure 3.3: Schematics of a) a rotating anode source; b) a bending magnet *(source: http: //uspas.fnal.gov)*; c) an undulator *(source: http: //uspas.fnal.gov)*.

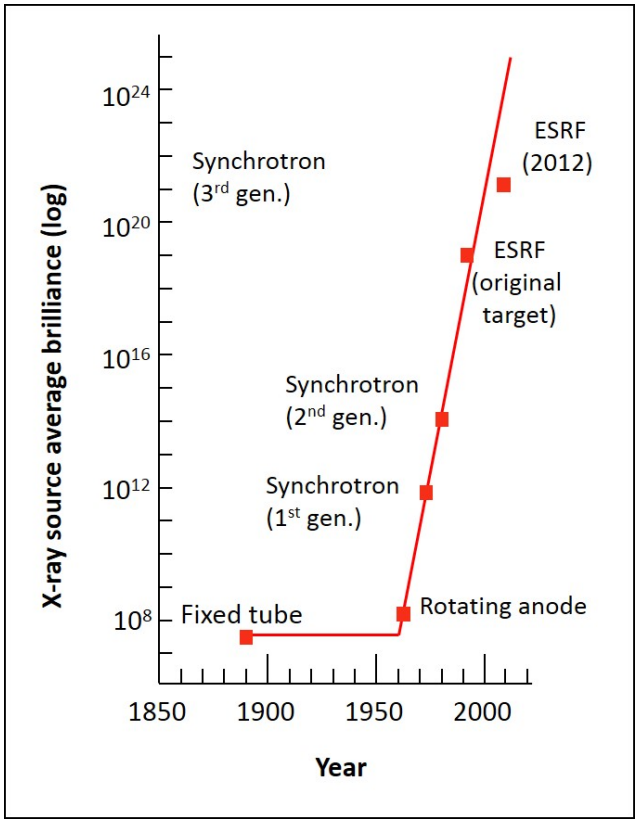

Figure 3.4: Typical brilliance of lab and synchrotron x-ray sources.

inside the loop, and the creation of x-ray, due to the said deviation. In the linear sections, devices that can produce x-ray without changing the electrons' global direction can be inserted. They are called insertion devices (ID), and can either be undulators or wigglers.

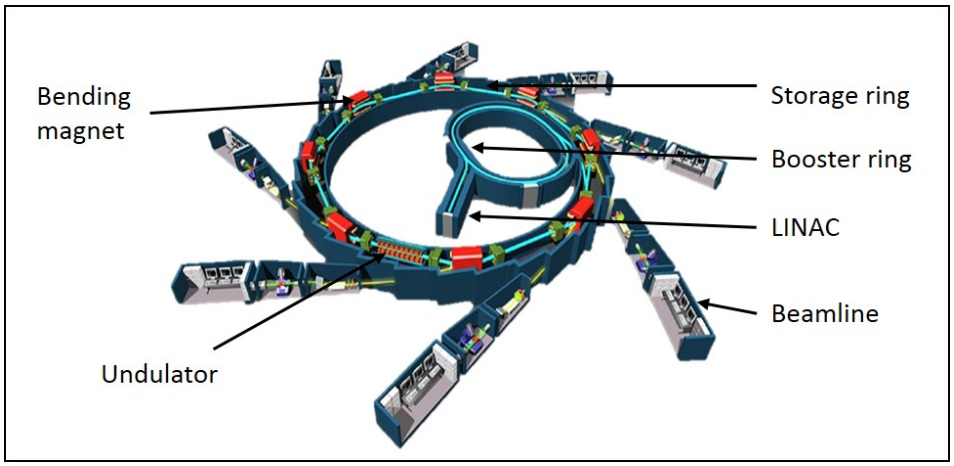

Figure 3.5: Schematic view of a typical third generation synchrotron. *Image source: wikipedia.org*

Bending magnets are used for two purposes. First, they maintain the electron beam inside the storage ring. By doing so however, they modify the electrons velocity and therefore generate x-ray. A bending magnet is illustrated in Figure 3.3b and its typical spectrum is presented in Figure 3.2. The energy spectrum of the x-ray it produces is continuous and covers a broad spectral range. The critical wavelength λ_c is defined as the wavelength that separates the emitted power in two equal parts. For the radiation emitted by bending magnets, it is defined (in nm) by equation 3.4 [81]:

$$\lambda_c = 0.599\frac{R}{E^3} = \frac{1.865}{B}{E_e}^2 \tag{3.4}$$

E_e is the electrons energy in GeV, R the curvature in meters, and B the magnetic induction of the bending magnet in Tesla. λ_c is representative of the x-ray energies reachable with a given synchrotron, and therefore the analyses that can be carried inside. At the ESRF, the electrons have an energy of 6.04 GeV, and the bending magnets produce a 0.8 T magnetic field. This leads to a critical wavelength of 0.06 nm (or an energy of 21 keV): the ESRF is optimized for hard x-ray.

Insertion devices are placed in the straight regions of the storage ring and are made of a number N of magnets. In undulators (see Figure 3.3c), electron are deviated periodically in the horizontal plane by weak magnetic fields. The emitted spectrum is made of several harmonic peaks, since the contribution of x-ray from every period add coherently. Wigglers on the contrary contains periodic strong magnets. The trajectory of electrons inside the wiggler is not perfectly sinusoidal, and the contributions add incoherently: the emission is continuous, similar, although

more intense, to the one in bending magnets. Typical spectra from those three devices are presented together in Figure 3.2.

The shape of the emitted beam also varies from one device to another. Let us define γ as the ratio between the electrons energy and the rest mass energy: $\gamma = \frac{E_{e^-}}{E_r}$, with the rest mass energy $E_r = m_{e^-}c^2 = 0.511$ MeV. The cone of emission for a bending magnet has a half-angle of $\theta = \frac{1}{\gamma}$, while the cone coming from a wiggler is much larger. Finally, the cone for an undulator is much sharper, and depends on the number of magnets N it is made of. It is defined by $\theta = \frac{1}{\gamma \cdot \sqrt{N}}$.

Let's now focus more specifically on the interactions occurring between the x-ray beam and the matter, and what information can be retrieved from them.

3.1.2 X-ray/matter interactions

When an x-ray beam encounters matter, many interactions can occur. Much information can be obtained from the result of these interactions. This section does not aim at an exhaustive description of the interactions occurring between x-ray and matter, it is far beyond the scope of this work. We here present generally the possible interactions, and focus on those leading to transmission imaging and strain measure, as they are the techniques used here. A larger panel of interactions is depicted in [79], while many applications of synchrotron radiation are well presented in [81].

X-ray based strain measurement

Let's imagine a situation where a monochromatic photon beam propagates along direction z, and encounters a sample. In addition to being a group of photons traveling in the same direction, an x-ray beam can be described as an electromagnetic planar wave of wavelength λ. As such, the x-ray beam can be diffracted by features of the same size as its wavelength, typically several tens of angstroms in the case of x-ray. More specifically, it will be diffracted by crystalline structures in matter, and for a beam coherent enough interferences will occur after the beam leaves the sample. Those will create diffraction patterns, that can be recorded on a detector. Whether the interferences are constructive or destructive depends on the incident angle, as illustrated in Figure 3.6. For every crystalline structure and material, the incident angles causing constructive interference are given by the Bragg law (see eq. 3.5). If θ is the incident angle of the beam (between the surface and the incident beam), the diffracted beam will form an angle of 2θ with the original direction of the beam.

$$2d \cdot \sin\theta = m \cdot \lambda \tag{3.5}$$

where θ is the angle between the sample surface and the incident beam, λ the wavelength of the beam, d the interplanar spacing, and m a positive integer. The apparition of the diffraction pattern is highly dependent on the incident angle and the interplanar spacing d: a compression or dilatation of the lattice can be seen on

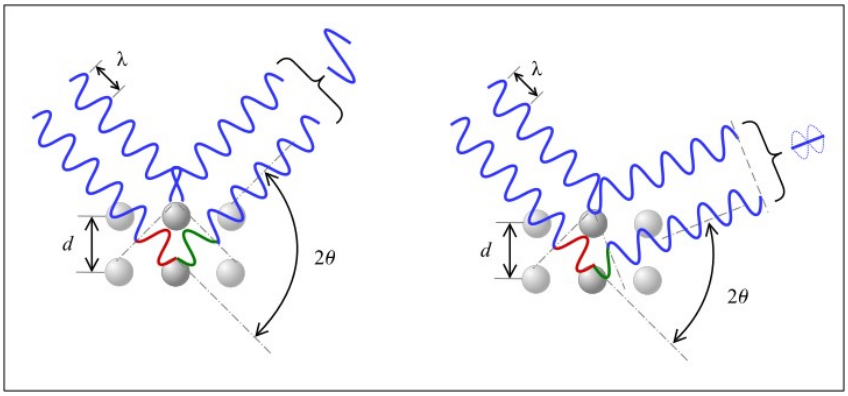

Figure 3.6: Illustration of the constructive and destructive interference occurring after a crystalline structure, depending on the incident angle of the beam, on which the value of the phase shift relies. *Image source: Wikipedia.*

the diffraction pattern. Since λ is close to d, x-ray diffraction is a well-adapted tool for strain measurement inside crystalline structures and has given rise to a variety of techniques, including Laue diffraction, made in transmission, and Bragg diffraction, performed in reflection.

In this study, only Bragg diffraction with a monochromatic beam will be studied. The experimental setup, together with the analysis principles, will be presented in section 3.4.

X-ray based imaging

X-ray attenuation in matter can be described by four main effects: the photoelectric effect, the Rayleigh scattering, the Compton effect and pair production. According to the atomic number of the sample and the photons energy, one or another will be predominant, and some can be neglected. For energies and materials considered in this work, the photoelectric effect is predominant, as presented in Figure 3.7.

The photoelectric effect occurs when a photon is fully absorbed by an atom, and ejects an inner electron, which is called a photoelectron, ioninzing the atom (see Figure 3.8a). In order for the atom to become stable, an electron from an outer layer will replace the ejected electron. The energy released by such an operation will be ejected in the form of a photon, which energy will be equal to the energy gap between the two layers. This is called fluorescent emission and is illustrated in Figure 3.8b.

The x-ray beam being a planar wave, if traveling in vacuum, it can be described by its wavenumber k, linked to its wavelength by $k = \frac{2\pi}{\lambda}$. In a medium, for a wave propagating along direction z, the front wave becomes:

$$\phi(x, y, z) = exp(ikn(x, y, z)z), \tag{3.6}$$

where n is the complex refractive index of the medium, defined for each (x,y,z)

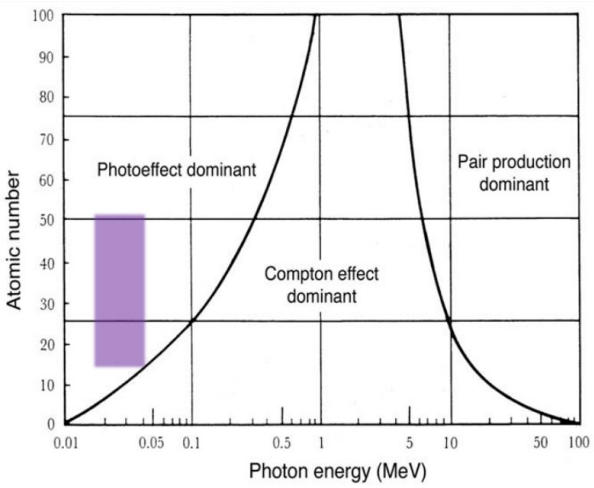

Figure 3.7: Regions of relative predominance of the three main forms of photon interaction with matter. The purple region represents the energies used for imaging in this study (17 keV and 33.6 keV), and the considered materials: Si (Z=14), Cu (Z=29), Ag (Z=47), and Sn (Z=50) [82].

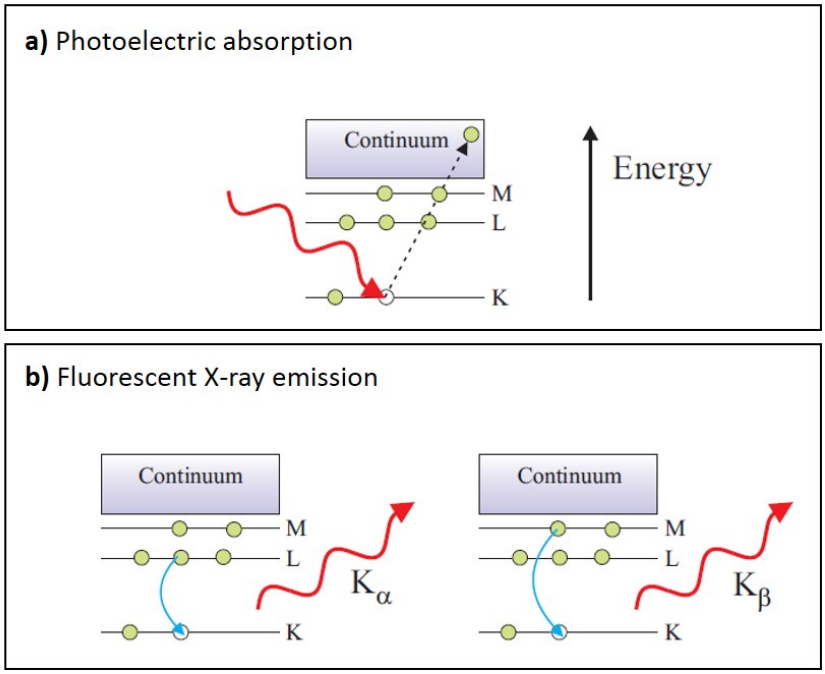

Figure 3.8: Illustration, at the atomic scale, of the absorption and fluorescence phenomena.

point of the medium by equation 3.7. n forms into a real part, $1-\delta$, with δ the refractive index decrement, and an imaginary part β, the absorption index. δ is usually very close to zero (10^{-5} in solids and 10^{-8} in air) and positive, which makes the real part of the refractive index inferior to 1 for x-ray. δ relates to the phase shift that the wave undergoes inside a medium. β describes the decrease of amplitude of the beam while going through the medium. Those two effects, in the case of the beam going through a sample, are illustrated in Figure 3.9.

$$n(x,y,z) = 1 - \delta(x,y,z) + i\beta(x,y,z) \tag{3.7}$$

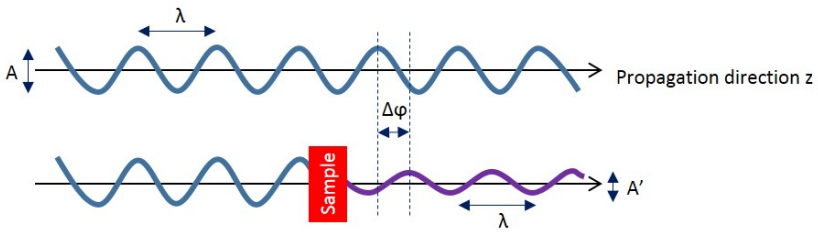

Figure 3.9: Illustration of the absorption and the phase shift phenomena when an x-ray beam goes through a sample.

As the beam travels inside the material, its total phase shift and the attenuation of its amplitude are proportional to the length it has covered in the said material. Let's assume the beam is monochromatic, of energy E_0. For the amplitude, if we define $N_0(E_0)$ the number of photons arriving at the sample, and $N_t(E_0)$ the number of photons present after a length t along the propagation direction z, the Beer-Lambert law provides:

$$N_t(E_0) = N_0(E_0) \cdot \exp(-\int_{path} \mu(z, E_0)dz) \tag{3.8}$$

with μ being defined as the linear attenuation coefficient, linked to β by eq. 3.9.

$$\mu(x,y,z) = \frac{4\pi}{\lambda}\beta(x,y,z) \tag{3.9}$$

The Beer-Lambert law describes the fraction of photons which are neither absorbed or scattered by the sample per length unit, and is characteristic of the material, as it is proportional to its atomic number Z. Therefore, measuring the ratio between incident photons and exiting ones provide information about the sample. Absorption imaging techniques use this property to image the inside of objects. It is widely used in the medical sector, where it provides high contrast between bones and surrounding materials. Most of lab tomographs aimed for industrial imaging also use absorption imaging.

δ is also characteristic of the material, and can even be linked to the local

electronic density ρ_e by eq. 3.10 (where r_c is the classical electron radius).

$$\delta = \frac{r_c \lambda^2}{2\pi} \rho_e \tag{3.10}$$

The value of δ would therefore provide information about the composition of the sample. The measurement of the phase is however not direct, as a detector is only capable of measuring the intensity. For a coherent enough beam however, interferences can occur after the beam exits the sample. Interference fringes that can be captured by a detector: they will be observable on the raw radiographs. Several experimental setups exist to make those interferences happen, and, in many cases, provide much better contrast than absorption imaging, as will be presented in section 3.3.1.2.

As presented in this section, many interactions occur between the x-ray beam and condensed matter. Depending on the information one wants to obtain (morphology, strain, etc.), constraints on the beam features will be different. Next section presents the beam obtained inside a typical lab tomograph, followed by the description of three ESRF beamlines, together with the demands they are designed to meet.

3.2 Experimental setups: tuning the x-ray path and the detection system

Depending on the final experimental setup, the requirements for the x-ray beam reaching the sample will not be the same. A lab source such as the Xradia tomograph offers a continuous large spectrum propagating in every direction of space (including towards the sample). The relevant part of the beam is cone-shaped, and the source size depends on the interaction sphere between the original electron beam and matter. Usually, the detection of photons is made using a scintillator, followed by visible light optics that allow for further magnification, before the beam reaches a CCD (Charge Coupled Device) detector.

As mentioned previously, synchrotron sources offer more latitude for beam adjustments to a given use, due to their high flux combined with relatively low divergence. In the next sections, three ESRF beamlines are presented, with their original specifications, the main optics chosen to fulfill those requirements, and the detectors used to perform the experiments. ID19 and ID16A are two long beamlines, aimed for high resolution imaging, respectively at pixels sizes below the micron and below 50 nm. ID19 aims at fast data acquisition and post-processing for industrial applications. ID16A's experiment setup implies longer acquisition and post-processing, as it aims for higher resolution. ID01 is also a long beamline, designed for diffraction analysis. It is quite versatile, and only its capacity to locally measure strain with coherent Bragg diffraction was used during this work.

Among those three beamlines, ID01 and ID16A were built during the first phase of the ESRF upgrade, that has run from 2009 to 2015. All three are long beamlines, that exploit the coherence of the beam. They benefit from state-of-the-art developments in various fields linked to x-ray. In fact, the source itself is a third generation

synchrotron, optimized for hard x-ray, as explained in 3.1.1.3. X-ray optics include monochromators and Fresnel plates that use latests technologies developed originally for the microelectronics industry, in particular for surface preparation. Stages are precisely controlled via piezoelectric motors, while detectors have been improved in order to increase the resolution and the read-out time, to make the most out of the incoming beam. Finally, as will be presented in the next part, algorithms have been written to acquire and exploit the data from those beamline, making the experiments as efficient as possible. Those beamlines, among other newly-constructed ones, are the outcome of many years of engineering and physics, performed in various fields.

3.2.1 ID16A: a nano-tomography beamline

ID16A is a newly-built beamline, as first experiments were conducted at the end of 2014. Its goal is high resolution 2D and 3D imaging for biology, medicine, and nanotechnology. To achieve this, a small source, together with high flux and coherence, are necessary. From eq. 3.2 and eq. 3.3, it has been deducted that improving the coherence of the beam implies either improving the monochromaticity, or setting the observation point far away from the x-ray source (or both!). To achieve its coherence goal, ID16A is a long beamline: 185 m separate the original x-ray source from the sample. Figure 3.10 provides a very simplified view of the optical path between the original x-ray source and the beam interacting with the sample. This optical path is described hereafter.

Figure 3.10: Simplified view of the optical path in the ID16A beamline. The beam's trajectory goes from left to right. Upper scheme shows the top view of the beam, where only the KB (Kirkpatrick-Baez) mirror is present. The lower scheme, showing the profile view of the beam, features the monochromator, the slits, and the KB (Kirkpatrick-Baez) mirror. The sample is placed after the final focus.

Two in-air revolver-type undulators set in series produce the x-ray. Depending on the chosen magnet period, they provide either x-ray with an energy of 17 keV (with a period of 18.3 mm) or 33.6 keV (with a period of 22.4 mm). The emission brilliance at this point is $8.2 \cdot 10^{19}$ $ph./s/mrad^2/mm^2/0.1\%BW$ at 17 keV and $2.5 \cdot 10^{19}$ $ph./s/mrad^2/mm^2/0.1\%BW$ at 33.6 keV [83]. After the x-ray generation, the general idea is to limit as much as possible the number of optics present on the optical path, in order to preserve the coherence of the beam. The original x-ray source measures 22 μm in the vertical direction (with a divergence of 7.4 μrad), and 940 μm in the horizontal one (with a divergence of 25 μrad). It is therefore possible to let the beam propagate freely in the vertical direction, but the source must be demagnified in the horizontal direction, otherwise most of the beam will be lost in the focusing process to come. Moreover, the beam has to be monochromatized before it reaches the experimental hutch. At 28 m from the source, the beam therefore encounters a mutli-layer monochromator. Its goal is twofold. First, the different layers covering the spherical mirror it is made of aim at selecting, using Bragg condition, one harmonic of the beam, improving its monochromaticity. In addition, its spherical shape focuses the beam in the horizontal direction. This, combined with slits, creates a 50 μm wide horizontal secondary source, at 40 m from the original one. The beam is then monochromatic with $\frac{\Delta E}{E} = 10^{-2}$, which is rather modest for a synchrotron, but the use of such a monochromator (instead of a crystal monochromator for example) is justified by the will to save the flux of the original beam.

After propagating along 185 m from the x-ray source, the beam reaches the experimental hutch. There, it is focused in both horizontal and vertical directions, using a pair of Kirkpatrick-Baez (KB) mirrors [84], as illustrated in Figure 3.11. They are a curved substrate, coated with a multilayer deposit, and a pair of those mirrors (one in each direction) has been designed for each energy (17 keV and 33.6 keV). Such a setup allows to focus the beam down to 13 nm [85, 86]. This focus size is mainly used for scanning applications, such as ptychography and fluorescence; during the experiments performed in this work, the focus was measured to be 38 x 27 (horizontal x vertical) at 17.5 keV (in February 2015) and 27 nm x 21 nm (horizontal x vertical) at 33.6 keV (in July 2015).

The KB mirrors are placed inside a vessel under vacuum, where the sample stage is also located. After interacting with the sample, the beam can be captured by several types of detectors. For the acquisition of holo-tomography projections, the detector uses a semi-transparent scintillator allowing the beam to propagate towards a FReLoN CCD (Fast Readout Low Noise) image sensor. It measures 2048 pixels x 2048 pixels with an effective pixel size of 1.1 μm.

As the beam is focalised, it is cone-shaped while interacting with the sample, and the recorded images are magnified when reaching the detector. This allows for an improvement of the resolution: by setting the source-to-sample and sample-to-detector distances, one can choose a magnification of the object.

At the ID16A beamline, it also possible to perform fluorescence scanning imaging. The sample is then placed in focus, and the exiting beam is captured by two

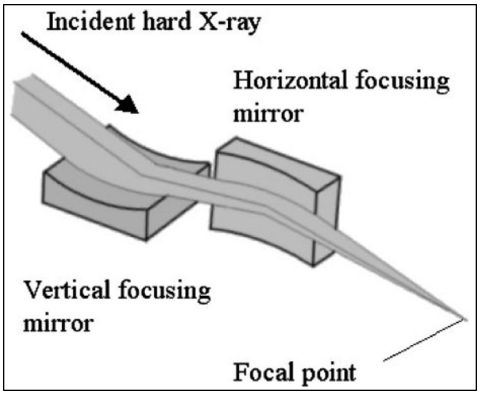

Figure 3.11: Illustration of the x-ray beam focusing using a pair of KB mirrors. *Image source: http: //www.spring8.or.jp*

six elements silicon drift diode detectors.

During this work, one experiment at the ID16A beamline was performed at 17 keV. The other 5 were performed at 33.6 keV. Coherence lengths can be calculated for the beamline, using eq. 3.2 and eq. 3.3. Given the features of the beam, one obtains a longitudinal coherence length of 7.3 nm at 17 keV and 3.6 nm at 33.6 keV .The traverse coherence length is (horizontal x vertical) 14.4 μm x 611 μm at 17 keV, and 7.3 μm x 310 μm at 33.6 keV.

3.2.2 ID19: a versatile tool for coherent imaging and diffraction

ID19 is also based on coherent imaging and is therefore a long beamline: the experimental hutch is placed 145 m away for the x-ray source. However, it is aimed at being more versatile than the ID16A beamline. It allows for fast tomography, laminography, and diffraction measures. 4 undulators and 1 wiggler are available on ID19. One of them is chosen according to the experimental needs, and typically leads to a source size of (horizontal x vertical) 120 μm x 30 μm. They provide a large spectrum beam, ranging from 6 to 250 keV. Both multilayer and crystal monochromator are available, leading respectively to a monochromaticity of 10^{-2} and 10^{-4} . Slits allow the selection of the inner and coherent part of the beam, which leads to a parallel beam reaching the sample.

During the experiments presented here, x-ray were provided by a U13 short-period permanent-magnet undulator, with a period of 13 mm, which offered an energy of 26.5 keV (with $\frac{\Delta E}{E} = 10^{-4}$). Along the optical path, an 2.8 mm Al filter was used, and the beam was collimated using 10 Be lenses.

As for the ID16A beamline, the detection of photon is indirect, a scintillator first converts photons to visible light. In this case however, a deflection mirror is placed after the scintillator and directs the beam towards the CCD camera. Moreover, objective lenses are placed between the scintillator and the mirror, in order to add a magnification to the obtained projections.

At 26.5 keV, the longitudinal coherence length at ID19 is about 47 nm (using a crystal monochromator), while the transverse coherence length is about (horizontal x vertical) $109\mu m$ x 42 μm.

3.2.3 ID01: Local strain measurement

ID01 is meant for coherent diffraction. It has been upgraded in 2014 and is now a long beamline, as 118 meters separate the x-ray source from the experimental hutch. Many experiments can be performed on this beamline, including small-angle x-ray scattering (SAXS), grazing-incidence diffraction (GID) and grazing-incidentce small angle x-ray scattering (GISAXS). We here focus on the optical path leading to Bragg coherent diffraction experiments.

To generate x-ray, electrons pass through three undulators set in series. This allows the beamline to tune its energy from 5 keV to 60 keV, by changing the gap between the magnets of the undulators. The horizontal divergence of the beam is then reduced by a white beam mirror, which also directs it towards the monochromator, which is a Si(111) Bragg monochromator. This elements provides a monochromatic beam, with $\frac{\Delta E}{E} = 10^{-4}$. Further away from the source, a transfocator using 58 Be lenses focuses the beam vertically, while increasing the flux density. At that point, the size of the x-ray beam is bigger than its coherence length. To perform the experiments, only the coherent part of the beam must be selected: mobile horizontal and vertical slits are usually placed right before the sample, and the open area between them is below the theoretical transverse coherence lengths (several tens or hundred of μm). In order both to have a local information and to increase the flux focused on the sample, focusing optics are then used. In this case, Fresnel Zone Plates are used, as they offer the smallest focus size. The current focusing optics are optimized for an energy of 8 keV, and then allow for a focus size of about (horizontal x vertical) 300 nm x 200 nm. The flux finally reaching the sample is about 10^9 $ph.s^{-1}$ [87].

The 2D detection, which is the only one performed during this work, is made with a 2D MAXIPIX [88]. It is a photon-counting system, with 516 pixels x 516 pixels, the pixel size being 55 μm.

In this work, two experiments were carried on the ID01 beamline. One was performed at an energy of 8 keV, and the second at an energy of 9 keV. Given the features of the beamline (size of the x-ray source, length of the beamline, together with the energy bandwidth), equations 3.2 and 3.3 provide a value of 1.4 μm (resp. 1.55 μm) for the longitudinal coherence length at 9 keV (resp. 8 keV). The transverse coherence length is (horizontal x vertical) 125 μm x 812 μm at 9 keV (resp. 140 μm x 912 μm at 8 keV).

Interactions between x-ray and matter generate much information that can be used to characterize samples. Moreover, x-ray sources can be highly adaptable to the experimental needs, as illustrated with 3 ESRF beamlines. In the two next sections, we will focus on the experimental setups and post-processing leading to x-ray 3D imaging and strain measurement, respectively.

3.3 X-ray transmission 3D imaging

Based on the interactions of x-ray with matter, several imaging techniques have been developed. Here we present the experimental setups used in this study and the imaging techniques they lead to. They can be based on the illumination of the whole sample, as in absorption and phase contrast imaging, or be performed by scanning the sample placed inside the focus. This last setup is used in fluorescence imaging, to obtain local information on the sample chemistry. Those 2D imaging techniques are presented in the first section (3.3.1).

As will be shown, the 2D images obtained are projections of the sample characteristics along the x-ray beam propagation direction. As such, several images taken from different angles can be combined and form a 3D digital reconstruction of the object. The specific setups to do so, together with several reconstruction algorithms, are presented in section 3.3.2.

Each experimental setup has its limits and constraints. In particular, the requirements for the sample shapes and size will differ from one to another. A summary of these requirements, together with the sample preparation methods used to answers them, is provided in section 3.3.3.

Several experimental setups, with different techniques and parameters, were used in this work. For a clearer further reading, table 3.2 summarizes those features.

	Absorption contrast tomography	**Phase contrast tomography**	**Absorption contrast laminography**	**Fluorescence tomography**
ID16A	Possible	17 keV; 33.6 keV Cone beam	Not possible	33.6 keV Focus size <30 nm
ID19	19 keV; 26.5 keV Parallel beam	Possible	26.5 keV Parallel beam	Not possible
Xradia	70 kV Cone beam	Not implemented	Not implemented	Not possible

Table 3.2: Experimental 3D transmission imaging techniques and experimental setups used in this work.

3.3.1 2D image formation

Here we present two types of imaging experimental setups: the transmission imaging, where the sample is placed in the propagating beam, and scanning imaging, where the sample is placed inside the focus of the beam. The former will be illustrated by fluorescence imaging, while the latter will lead to absorption and phase contrast imaging. The expression of the complex refraction index is reminded in eq. 3.7, as it leads both to absorption and phase contrast imaging. Figure 3.12 provides the notations used in this section regarding the space coordinates. This figure can be seen as the follow-up of fig 3.10 picturing ID16A's optical path. As those notations are common to 2D and 3D imaging, an angle θ is already present in this figure and in the next equations, as they foresee a sample rotation.

$$n(x, y, z) = 1 - \delta(x, y, z) + i\beta(x, y, z) \tag{3.11}$$

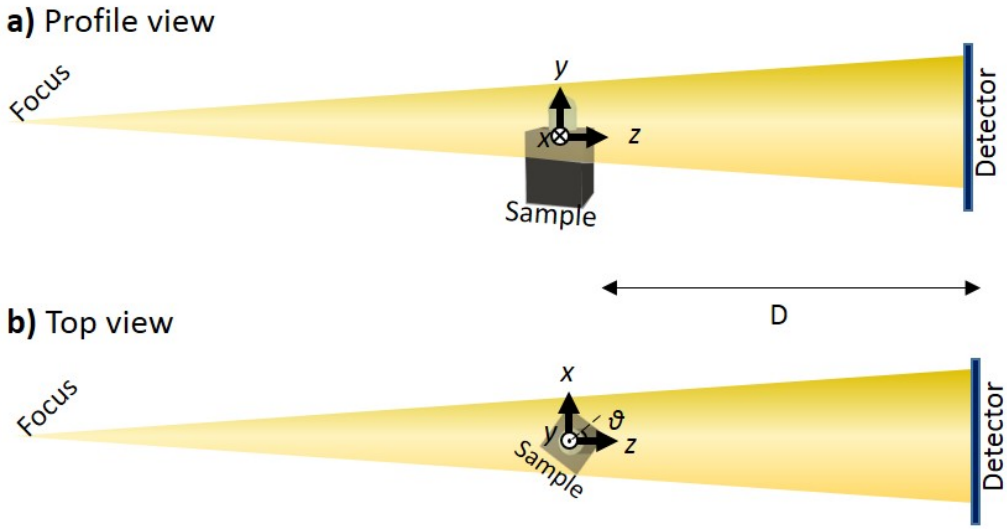

Figure 3.12: Notations regarding the space coordinates used in this section. The x-ray beam propagates along direction z, and the projection planes are (x,y). The distance between the end of the sample and the detector is noted D.

3.3.1.1 Absorption contrast imaging

As presented in section 3.1.2, when an x-ray beam travels through a sample, along direction z, its amplitude is reduced, and its phase shifted. When a detector captures the exiting beam, the recorded intensity on the detector is proportional to the square of the wave modulus. The interaction between the wave and the sample, for a rotation angle θ, can be described by a transmittance function T_θ, defined as:

$$T_\theta = exp(-B_\theta(\mathbf{x}) + i\phi_\theta(\mathbf{x})) \tag{3.12}$$

where $\mathbf{x}$ is the projection plane (x,y), and B_θ and ϕ_θ the projections along the sample of the absorption index and the refractive index decrement, respectively. They can be written as:

$$B_\theta = \frac{2\pi}{\lambda} \int \beta(\mathbf{x}, z)dz \tag{3.13}$$

$$\phi_\theta = -\frac{2\pi}{\lambda} \int \delta_n(\mathbf{x}, z)dz \tag{3.14}$$

Let's now imagine the projection plane is situated right after the sample (D=0 in Figure 3.12). Then, if the incident wave front is u_{inc}, the wave front reaching the detector is:

$$u_{0,\theta} = T_\theta(\mathbf{x}) u_{inc}(\mathbf{x}) \tag{3.15}$$

Therefore, the intensity measured by the detector is:

$$\begin{aligned} I_{0,\theta} &= |u_{0,\theta}(\mathbf{x})|^2 && (3.16)\\ &= |T_\theta(\mathbf{x}) u_{inc}(\mathbf{x})|^2 && (3.17)\\ &= |e^{-B_\theta(\mathbf{x})}|^2 \cdot |e^{i\phi_\theta(\mathbf{x})}|^2 \cdot |u_{inc}(\mathbf{x})|^2 && (3.18) \end{aligned}$$

As ϕ_θ is a real number, $|e^{i\phi_\theta(\mathbf{x})}| = 1$. Moreover, by definition $|u_{inc}(\mathbf{x})|^2 = I_0$. Hence:

$$\begin{aligned} I_{0,\theta} &= I_0 |e^{-B_\theta(\mathbf{x})}|^2 && (3.19)\\ &= I_0 \cdot e^{-2B_\theta(\mathbf{x})} && (3.20) \end{aligned}$$

The last line corresponds to the Beer-Lambert law for absorption imaging, stated in eq. 3.8. Obtaining the projected value of β is however not direct, since the detector often presents a dark current. Materials can still be distinguished by the grey levels of the image, as can be seen in Figure 3.13a: the copper the sample is made of can be distinguished from the silicon it stands on. This technique is largely used in lab tomography setups and medical imaging, but encounters limits for materials with close atomic numbers or weakly absorbing materials.

This technique is largely used in lab tomography setups, for example in the Zeiss Xradia tomograph used in this study.

3.3.1.2 Phase contrast imaging

As presented in the previous section, imaging contrast can be obtained by measuring the absorption underwent by the beam when crossing the sample. However, this method reaches its limit for close atomic numbers or low absorbing materials. Phase-contrast imaging is based on the beam phase-shift occurring in the sample and the scattering of the beam. It is directly linked to the value of δ. Figure 3.14 represents the ratio $\frac{\delta}{\beta}$ in function of the energy for copper and silicon. For hard x-ray, δ is several orders of magnitude higher than β. Obtaining a phase map (representing δ) rather than an absorption map (representing β) would therefore provide high sensitivity images.

Unfortunately, the value of the phase shift is not directly accessible on the acquired projections. Phase contrast techniques must be implemented in order to encode enough information on the radiographs, on which a phase retrieval algorithm must then be applied.

Several experimental setups allow to capture phase-contrast on a detector, such as crystal interferometry [90], analyzer-based phase imaging [91], grating-based phase imaging [92], or the edge-illumination technique [93]. The simplest method

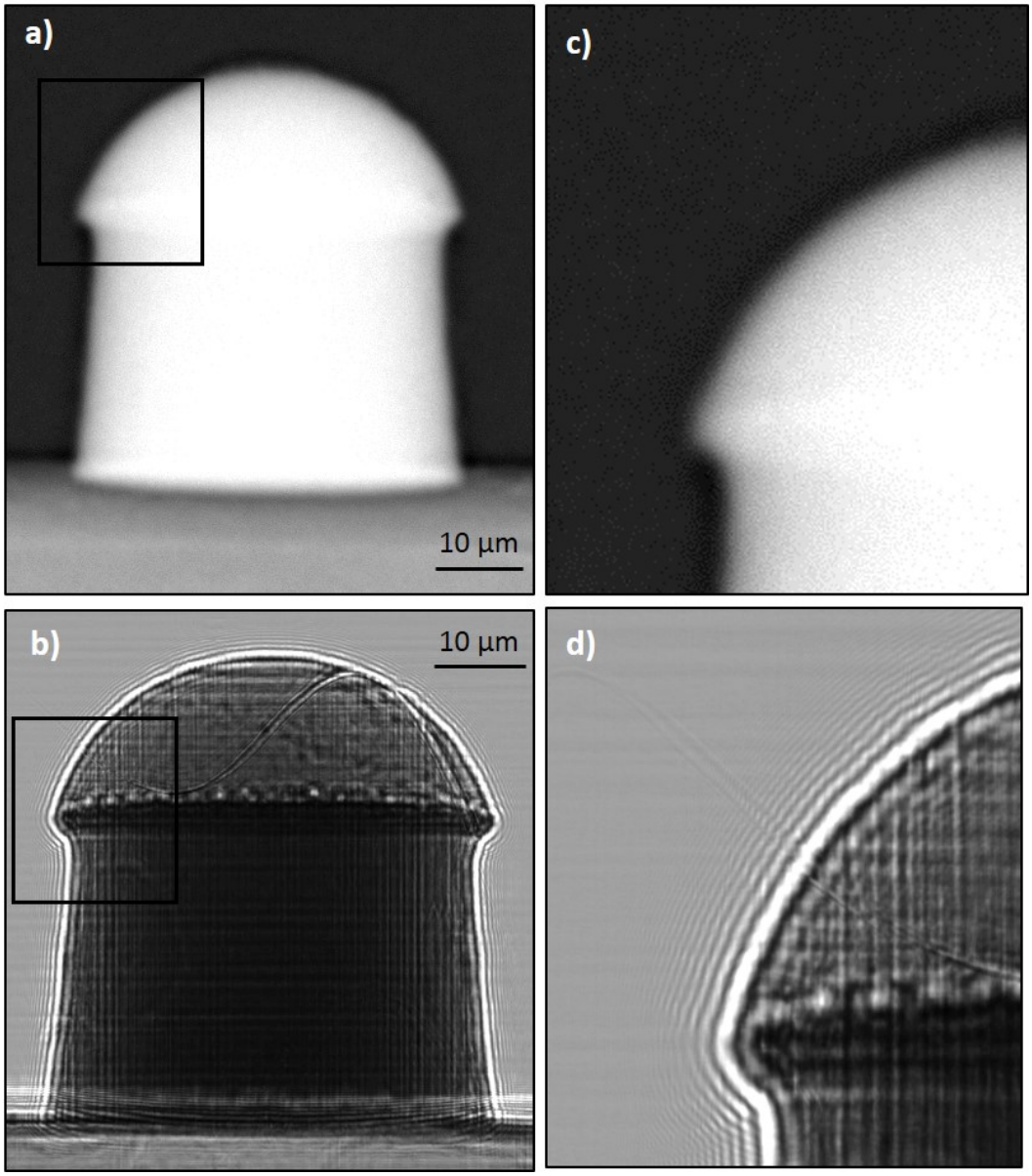

Figure 3.13: Radiographs of a 50 μm wide copper pillar, obtained with two different techniques. a) Absorption contrast imaging obtained on the Xradia lab tomograph. b) phase contrast imaging on ID16A. c) zoomed-in view of image a. d) zoomed-in view of image b, where interference fringes are clearly visible.

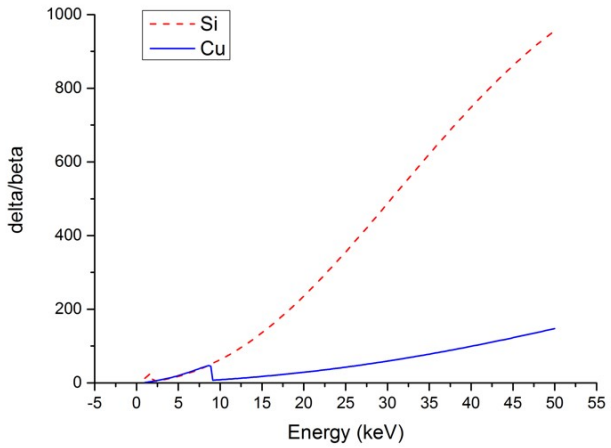

Figure 3.14: δ/β ratio of copper (in blue) and silicon (in red dashed line), as a function of the energy. Data source: Xop software [89]

to obtain such contrast is propagation-based phase contrast imaging, or free space propagation phase contrast imaging. It relies on the propagation of a spatially coherent beam in the space between the sample and the detector. To obtain higher phase contrast, the distance between the sample and the detector is simply increased. In practice, on the ID16A beamline it is done by changing the focus-to-sample distance (while the focus-to-detector distance remains the same), while in ID19 the sample remains at the same position and the detector is moved.

In the case where a further free propagation is allowed after the sample (D>0), a Fresnel transform must be added to the obtained wave front. It requires the use of a propagator noted P_D, which form is given in eq. 3.21 (where λ is the monochromatic beam wavelength and D the propagation distance) [94].

$$P_D(\mathbf{x}) = \frac{1}{i\lambda D}\exp(i\frac{\pi}{\lambda D}|\mathbf{x}|^2) \tag{3.21}$$

Assuming $u_{inc}(\mathbf{x}) = 1$, the wave front on the projection plane $\mathbf{x}$ is the convolution of the transmission function inside the sample and the propagator along distance D after the sample:

$$u_{\theta,D}(\mathbf{x})(T_\theta * P_D)(\mathbf{x}) \tag{3.22}$$

This leads to the expression of the intensity on the detector, expressed here in the Fourier domain [95]:

$$\tilde{I}_D(\mathbf{f}) = \int T_\theta(\mathbf{x} - \frac{\lambda D\mathbf{f}}{2})T_\theta^*(\mathbf{x} + \frac{\lambda D\mathbf{f}}{2})\exp(-2i\mathbf{x}.\mathbf{f})dx \tag{3.23}$$

The collected intensity is linked quantitatively to the phase shift of the wave. In practice, interference fringes appear on the radiographs, as can be seen in Fig-

ure 3.13b and d. The propagation is a direct process, and retrieving the phase shift from the radiographs is the corresponding inverse problem. As it is quite complex, several approximations and linearizations of the problem have been developed [96, 97]. The Contrast Transfer Function (CTF) is well-adapted to slowly varying phase and weakly attenuating objects and has been mainly used here. In this approximation, the transmission function is developed to the first order, raising $T_\theta(\mathbf{x}) = 1 - B(\mathbf{x}) + i\phi(\mathbf{x})$. This leads, when substituting this expression in eq. 3.23, to a new expression of the intensity (still in the Fourier domain):

$$\tilde{I}_D(\mathbf{f}) = \delta(\mathbf{f}) - 2cos(\pi\lambda D|\mathbf{f}|^2)\tilde{B}(\mathbf{f}) + 2sin(\pi\lambda D|\mathbf{f}|^2)\tilde{\phi}(\mathbf{f}) \tag{3.24}$$

where δ is the impulse function, $\tilde{B}(\mathbf{f})$ and $\tilde{\phi}(\mathbf{f})$ are the Fourier transforms of the absorption and the phase, respectively. This expression can be solved both for the absorption B and the phase ϕ, but present the drawback of having zero crossings for given frequencies $\mathbf{f}$ of the Fourier domain. To overcome this issue, radiographs can be acquired at different sample-to-detector distances and compiled to provide one projection. The distances will have to be chosen such as the zero crossings do not occur for the same frequencies. Another approximation, the Transport of Intensity Equation (TIE) [98], is more adapted to parallel beams and small propagation distances. A mixed approach between the two offer the possibility to retrieve the phase from absorbing materials, such as the ones encountered in 3D integration, placed in a cone beam.

The method consisting in the acquisition of four different projections, when combined with tomography, is called holo-tomography [99, 100]. It is illustrated in Figure 3.15b. Figures 3.16a-d present an example of four radiographs acquired by holo-tomography, and the final projection obtained after the phase retrieval procedure.

As presented in this section, phase contrast is observable on absorption radiographs, provided a coherent enough source and a sufficient distance of propagation between the sample and the detector. Those are conditions achievable both on the ID16A and ID19 beamlines. Radiographs obtained on ID16A are usually acquired using the four-distance scheme and used after a phase retrieval procedure. The focus-to-detector distance was typically 1 meter, while the focus-to-sample distances were kept around 1 nA. The radiographs obtained on ID19 were directly used during this work. In such projections, the phase contrast mainly appears on the edges of materials, as the scattering is higher. The radiographs can therefore be considered as absorption projections, with an edge enhancement due to the phase contrast. This improves the imaging of voids in copper pillars and copper pads for example.

3.3.1.3 Fluorescence imaging

As depicted in section 3.1.2, the absorption of an incident photon by an atom can trigger the emission of another photon, which energy will be characteristic of the atom. This gives rise to the fluorescence technique, illustrated in Figure 3.15c. The

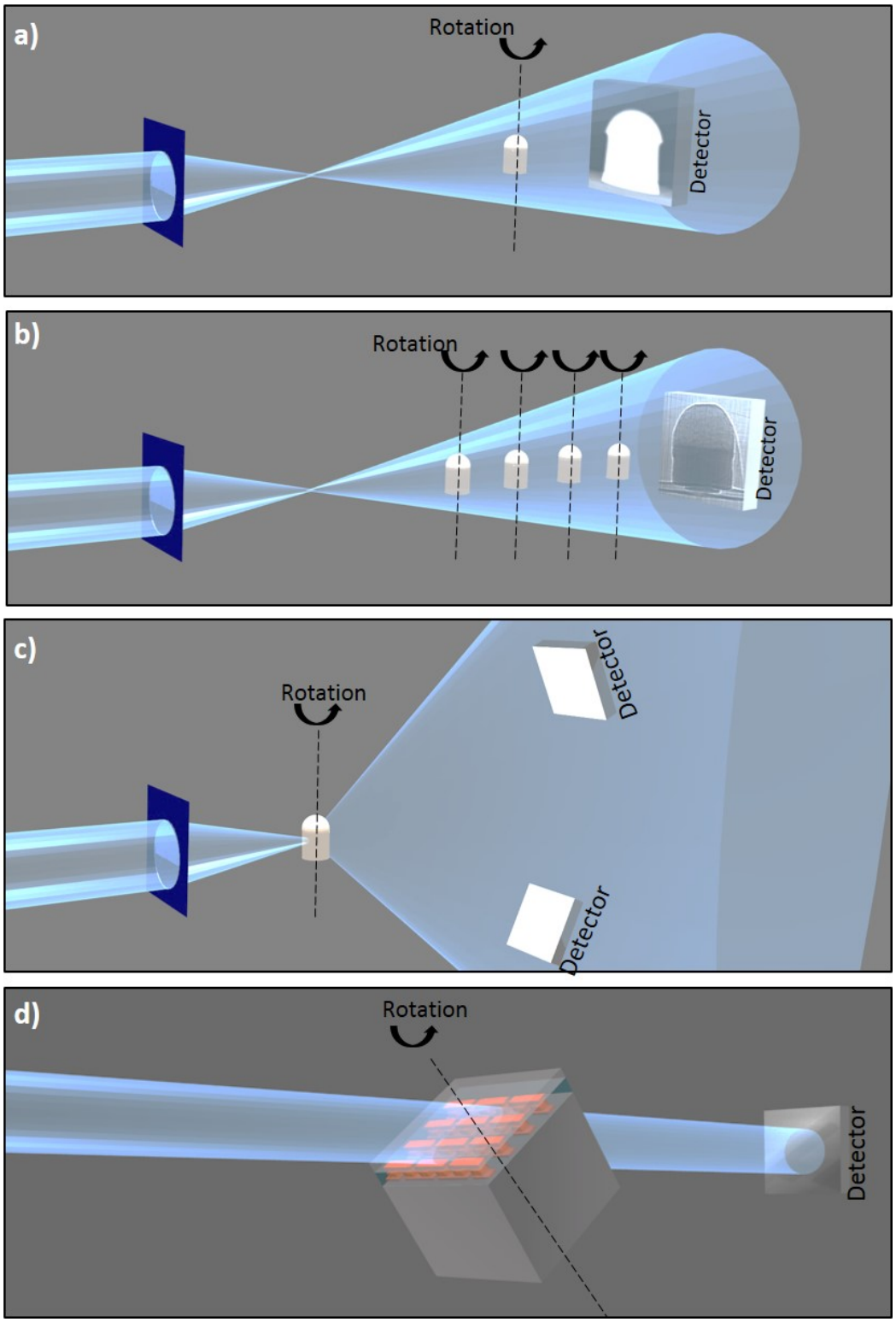

Figure 3.15: Illustration of the 3D imaging setups presented in this section. a) Absorption-based tomography. b) Holotomography (propagation-based phase contrast imaging). c) Fluorescence tomography. d) Laminography.

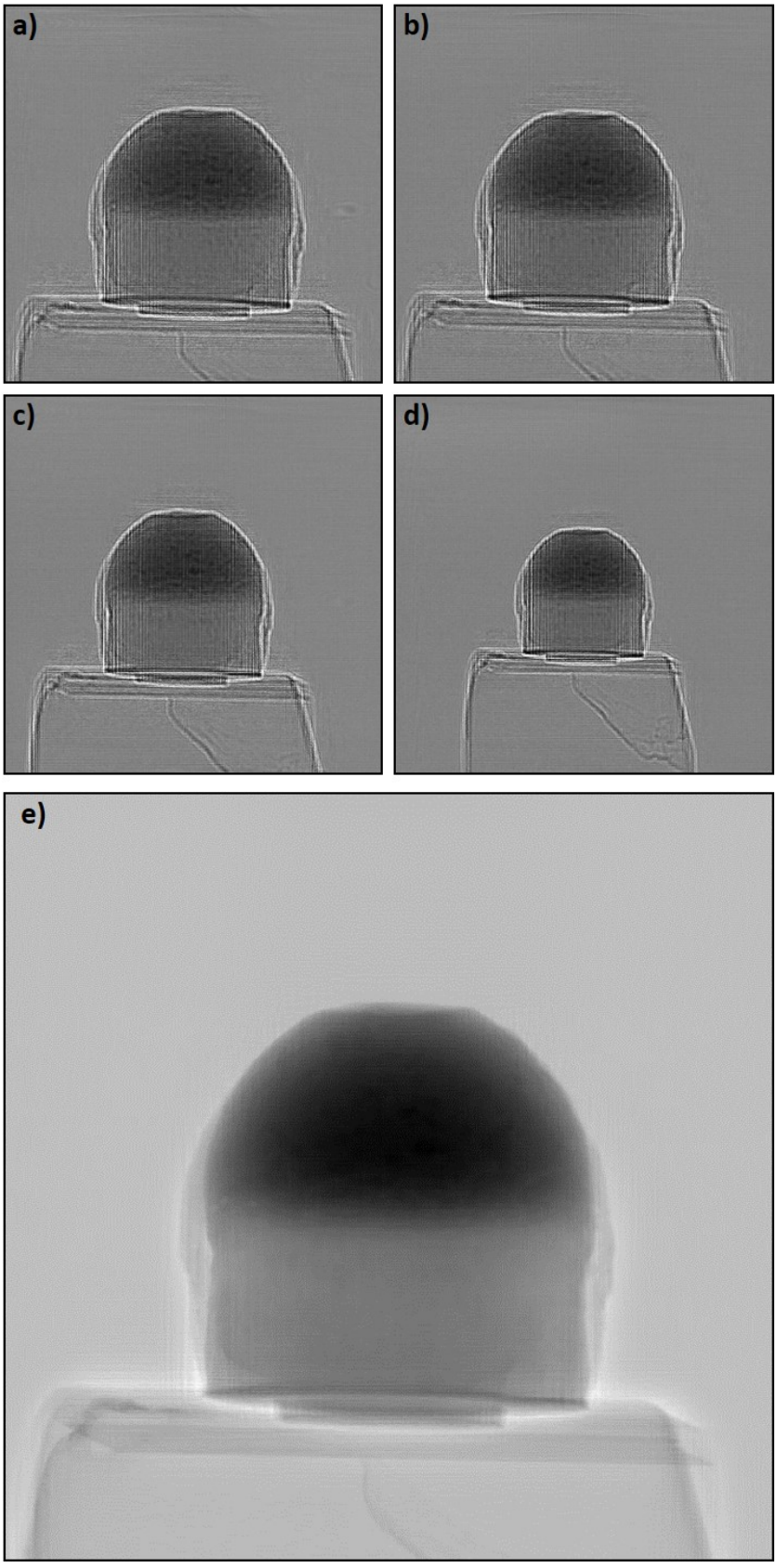

Figure 3.16: a-d) Raw radiographs on a copper pillar obtained on the ID16A beamline, at four different distances. e) Projection obtained after the phase retrieval procedure, combining images a, b, c, and d.

idea is to illuminate the sample with the x-ray beam and to detect the exiting photons. By selecting them by their energy, one obtains a spectrum presenting all the present elements. A fitting process, where peaks of the spectrum are linked to their origin material, provides an information on the chemistry of the sample in the area illuminated by the beam. The pixel size is limited by the size of the beam cross-section on the sample. In a synchrotron, it is possible to focus the beam down to several tens of nanometers. This allows one to obtain a chemical map of the sample, by shifting it inside the focus, in a plane (x,y) orthogonal to the x-ray beam. Specific fitting tools are implemented to obtain an accurate distribution of elements. In fact, several side effects must be taken into account, among which the re-absorption of emitted photons by the sample itself. In addition to re-absorption numeric models that improve the fitting, for the measure to be considered quantitative, the sample must be small enough to limit re-absorption.

The fluorescence acquisitions realized in this work were performed at the ID16A beamline. Two detectors collect the exiting photons. They are placed on opposite sides of the sample, in order to collect as many photons as possible. The vessel in which the samples are placed is under vacuum, which improves the quality of the analysis as it reduces absorption.

From a data set of the 2D projection images, one can reconstruct an accurate enough 3D volume, provided some conditions on the setup geometry, the number and distribution of the acquired projections, and the use of an adapted reconstruction algorithm. All those features are described in the next section.

3.3.2 Obtaining a 3D reconstruction

In the previous section, several ways of obtaining a 2D projection of a sample were explained and illustrated. Those projections can be combined together in order to obtain a 3D reconstruction of the object. Here we present two experimental setups to do so - tomography and laminography. They are illustrated respectively in Figure 3.15a-c and 3.15d. Reconstruction algorithms are also presented and discussed in this section.

For a clearer visualization, all examples are presented for a 2D reconstruction with acquisitions made with a parallel beam. Notations from the previous section are kept: the x-ray beam propagates along z, and the imaged object is defined in the plane (x,z) by a function f. f is usually taken as μ, but it has been shown the equations given here also apply to δ [101]. The sample's orientation in the plane is defined by the angle θ, as given in Figure 3.12. The 1D detector is therefore defined by a line z=constant. They can be easily adapted to a 3D situation.

The Radon transform, here noted R, defines the relationship between the function f and the signal obtained on the detector. The transform, when applied to the function f and for a projection along a path of length L, is defined as:

$$Rf = \int_L f(x,z)dz \tag{3.25}$$

It can be shown that this transform is directly linked to the Fourier transform of the object. In fact, the Fourier slice theorem states that the 1D Fourier transform of an object's projection at an angle θ is equal to the 2D Fourier transform of the object along a line forming an angle θ with the abscissa and passing through the origin. Therefore, the Radon transform offers a sampling of the object in the Fourier domain. And since the Fourier transform is bijective, by acquiring enough projections (at different angles θ) of the object, on can reconstruct the object in the Fourier domain, and then in the real space.

3.3.2.1 Experimental setups: tomography, holo-tomography, and laminography

To obtain a reconstruction of the object, projections must be acquired regularly, with evenly distributed angles θ along 180° or 360°. To do so, a first experimental setup is the tomography one, illustrated in Figure 3.15a. The sample is placed in the x-ray beam, and is rotated around the axis y, orthogonal to the beam. In the case of holo-tomography, this procedure will be adapted: the whole rotation will be performed at 4 focus-to-sample distances, as illustrated in Figure 3.15b. For those setups, it is possible to perform local (or zoom-in) tomography. It consists in placing the sample such as it is larger than the field of view. This allows to improve the resolution without thinning the sample, but may also trigger some artefacts [102]. Fluorescence tomography can also be performed using the tomography setup, by placing the sample in the focus (see Figure 3.15c).

For those experimental setups, an issue rises in the case of a laminar sample (typically a piece of wafer). A 2D sample defined by dimensions E and F is called laminar when one of its dimensions (for example E) is much smaller that the other (here, F). For given angles, when direction F is parallel to the x-ray beam, the beam will be highly absorbed, much more than when the direction F is orthogonal to the beam. Their will be a lack of information, called missing wedge, coming from this (those) angle(s), which will reduce the resolution of the reconstruction. To avoid this, a second setup can be set for laminar samples. It is called laminography and is illustrated in Figure 3.15d. The rotation is made around an axis which is slightly tilted from the y axis, in the (yz) plane. This way, projections can be acquired without reaching the situation of missing wedge described earlier.

In this work, tomography has been performed on the Xradia tomograph, and on the ID16A and ID19 beamlines. Laminography was also performed in ID19. The 3D reconstruction algorithms rely on the same principles for all setups. They are presented in next section.

3.3.2.2 Reconstruction algorithms

Analytical methods A first reconstruction algorithm can be directly deducted from the Fourier-slice theorem [103]. It states that the 1D Fourier Transform of the projection at angle θ of an object is equal to the 2D Fourier transform of the said

object, evaluated on a line passing through the origin and forming an angle θ with the X axis. Therefore, it is possible to reconstruct the object in the Fourier domain, and apply an inverse Fourier transform. Unfortunately, this requires to perform an interpolation in the Fourier domain, which leads to serious distortion.

However, the theorem expression also leads to a more intuitive reconstruction algorithm, called the Filtered Back Projection (FBP) algorithm. Each projection is first filtered, and back-projected. The addition of all back-projections provides the final image, as can be seen in Figure 3.17. The back-projection process implies to pass from polar coordinates (r,θ) to cartesian ones (x,y). This tends to highlight low frequencies. A filter (typically a ramp one) ensures all the frequencies are equally represented in the final reconstruction.

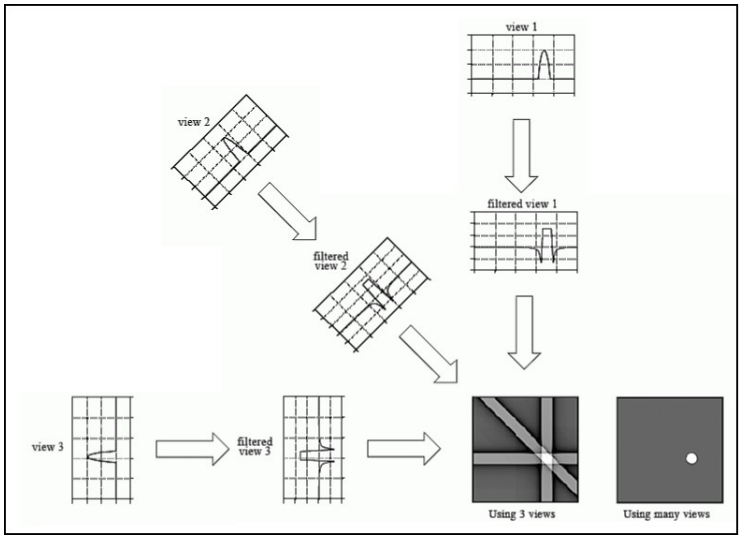

Figure 3.17: Schematic view of the Filtered Back Projection reconstruction process. Image source: adapted from [104]

As FBP relies on the sampling of the Fourier domain, it abides by sampling rules and demands many projections. In fact, as the projections are a sampling of the Fourier domain, and if the detector pixel size Δr is considered the resolution limit, then the angular step between projections should be $\Delta\theta \cdot \delta r$. On a half-circle rotation, this raises:

$$N\Delta\theta = \pi r \tag{3.26}$$

with N the number of acquired projections and r the object radius. For an object imaged on a detector having M pixels, r can also be written as $r = \frac{\Delta r(M-1)}{2}$. The theoretical value of N is therefore given by:

$$N = \frac{\pi}{2}M \tag{3.27}$$

For a 2048 pixel large detector, the number of projections should therefore be $N = 3200$. With this amount of projections, the FBP algorithm is considered to

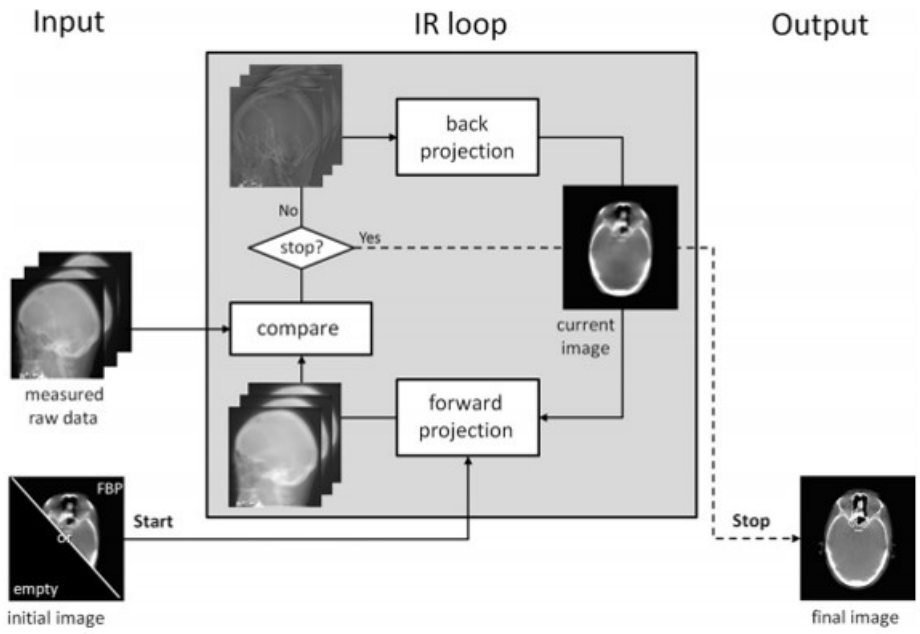

Figure 3.18: Schematic view of the iterative reconstruction process. *Image source: [105].*

provide an accurate reconstruction of the object. In practice, 3200 projections are indeed acquired on ID19, while reconstructions on the ID16A beamline were based on 2000 projections or even 1500.

In order to limit the number of projections needed (and also to limit the reconstruction sensitivity to noise), other reconstruction algorithms, known as iterative, have been developed.

Algebraic iterative methods FBP is an analytical method, since the discretization of the data occurs when implementing the reconstruction. On the contrary, algebraic methods such as iterative ones directly use discrete data. They rely on the discretization of the space and the sample. The sample is no longer defined by a function f(x,y), but by a set of discrete values f_i, called pixels. The Radon transform is represented by a projector matrix R, and the acquired projection P can be written as:

$$P = Rf \tag{3.28}$$

Provided the geometry of the experimental setup (in particular the shape of the beam), the matrix R can be known. The direct inversion of the matrix R, in order to obtain f from P, is theoretically possible, but given the size of the matrices, impossible to implement. Iterative minimization methods are therefore applied, only using the knowledge of R and the implementation of the forward projection it leads

to. At the first iteration, the function f^0 is usually taken as the null matrix. At each iteration, the matrix f will be calculated relatively to its value at the previous iteration [106]:

$$f_i^{(n+1)} = f_i^{(n)} + \lambda^{(n)} \Delta f_i^{(n)} \tag{3.29}$$

Where $\lambda^{(n)}$ is a relaxation parameter, and $\Delta f_i^{(n)}$ the calculated normalized difference between the current reconstruction forward projection and the actual experimental data, as illustrated in Figure 3.18. The way this difference is calculated is the main distinction between the existing iterative algorithms. It will have an impact on the convergence criterion of the algorithm, and on the number of iterations needed. Many iterative algorithms exist, here only the ones used in this work are presented.

In the ART (Algebraic Reconstruction Technique) algorithm, the distance is calculated for each pixel, projection after projection. Each pixel is therefore modified several times during one iteration. As every pixel is dealt with separately, the ART algorithm is little robust to noise. SIRT (Simultaneous Iterative Reconstruction Technique), on the contrary, compares the whole acquired projections with the ones generated from the current reconstruction. This makes the algorithm slower than ART, but more robust. The CG-LS (Conjugate Gradient - Least Square) algorithm is very similar to SIRT, but calculates distances using the L_1 norm instead of L_2. The SART algorithm modifies the reconstruction after back-projecting all the pixels (like SIRT) from one projection (like ART). The SART algorithm therefore benefits from the stability from SIRT and the fast calculation of ART.

As mentioned earlier, iterative algorithms have mainly been developed for electron tomography, and have been applied to x-ray tomography since [107, 105, 108]. In this work, some of them have been tested on ID16A data. The results are presented in section 5.3.

3.3.3 Sample Preparation

Here we present the constraints on the samples shapes and sizes linked to the experimental setups. A first constraint comes from the penetration depth of x-ray inside the sample. Transmission imaging relies on the fact that the photons -at least some of them- are able to exit the sample and reach the detector. A too absorbing material or a too low energy will lead the a low signal to noise ratio and poor reconstructions. Given a material and an energy, the size of the sample must be adapted. The second origin for those constraints is the field of view reachable by a given experimental setup. This is directly linked to the setup geometry and the size of the detector.

Let's first focus on the energies and penetration depths. The x-ray attenuation length L_p is defined as the distance in the sample after which the proportion of non-absorbed and non-scattered photons is e^{-1}. Table 3.3 provides the values of the x-ray attenuation length L_P for silicon and copper, at the energies used in the experimental setups from this section. The values of β are obtained using XOP

software [89], and μ are derived from them (see eq.3.9). The Beer-Lambert law then rises $L_p = \frac{1}{\mu}$.

	17keV	**19 keV**	**26.5 keV**	**33.6 keV**
Copper	21	29	66	140
Silicon	599	826	2174	4000

Table 3.3: Values of x-ray attenuation length L_p (in μm) in silicon and copper, for energies used during this PhD.

From table 3.3, it is visible that for the considered energies, sample must be quite small. Depending on the amount of copper, an experiment at 33.6 keV (as performed today at ID16A) may require samples below 200 μm for example. For an experiment at ID19 conducted at an energy of 26.5 keV, samples should be below 100 μm for tomography.

As mentioned previously, in the case of fluorescence, since re-absorption is possible, one has to take into account not only the incident beam energy, but also the emitted photons energy. The size of the sample may have to be reduced in order to allow the photons emitted inside the sample to reach the detector. Photons can be emitted from differents shells of the electronic layer (K, L, or M). However, the brightest is usually the $K\alpha_1$ emission, and it is the one considered here when dimensioning a sample for fluorescence imaging. Table 3.4 summarizes the $K\alpha_1$ emission energies for the materials looked for during this work. Although silver and tin emit at rather high energies (22 keV), silicon, copper, and nickel demand a rather small sample ($< 20\mu m$). Moreover, the smaller the sample, the more quantitative the data will be, as re-absorption will be smaller. In this work, 2D fluorescence images were acquired with a 1 μm thick sample, while 3D acquisitions where acquired on a 7 μm large copper pillar.

	Si	**Cu**	**Sn**	**Ag**	**Ni**
$K\alpha_1$ (keV)	1.74	8.05	25.3	22.2	7.48

Table 3.4: Values of the $K\alpha_1$ emission energies for materials usually imaged in this work.

The field of view that can be acquired by a given setup is a further constraint. In the case of the ID16A beamline, given the setup geometry, experiments are typically performed with a pixel size of 25 nm. As the detector is a 2048 pixels x 2048 pixels one, the sample should be about 50 μm large to fit the field of view. On ID19, several optics can be chosen to reduce the pixel size, which has an impact of the final field of view. Typically, for a pixel size of 165 nm, the field of view will be of 420 μm (using a 2560 pixel large 2D detector).

To obtain samples below 50 μm for ID16A experiments, the PFIB was used, applying the lift-out procedure presented in section 2.4.2 to set the sample on a aluminum pin. This method was adapted to statistical analysis during this PhD, as will be detailed in 5.2.

	Absorption contrast tomography	Phase contrast tomography	Absorption contrast laminography	Fluorescence tomography
ID16A		PFIB or FIB		FIB
ID19	Cleavage/PFIB		Cleavage	
Xradia	Cleavage/PFIB			

Table 3.5: Preparation techniques used in this work, for the different experimental setups.

For tomography performed on ID19, limitations linked to the penetration depth are similar to the ones on ID16A. The field of view however is larger in the conditions of our experiments, as the pixel size was larger. Sample prepared for ID16A are therefore perfectly suitable for tomography on ID19, where larger samples can also be imaged. For example, 2 mm wide chips could be cleaved and imaged. The same thoughts apply to the Xradia tomograph, which is designed for samples of several cm^3.

In the case of laminography, performed on ID19, only the thickness of the sample, that the x-ray will have to cross, will have an impact. For laminography measures of wafers, the typical sample will measure less than 2 mm in width, in order to get a high enough signal to noise ratio. The dimensions in the plane are of less importance. In order to be placed and fixed into the setup, they could be cleaved (typically to a 15 nA x 15 nA square).

For the imaging setups presented here, the sample preparation methods used are summarized in table 3.5.

3.4 Strain measures by Bragg diffraction

As presented in paragraph 3.1.2, x-ray can be diffracted by a crystal. The diffraction patterns that result from such an interaction can be captured by a detector. They lead to crystallographic information about the sample. Several techniques have been implemented in order to retrieve such information. Here we focus on monochromatic Bragg diffraction, that allows to measure the interplanar distance inside a crystal, and therefore obtain an information about strain in a sample. It has been applied here to silicon and copper stacks.

3.4.1 Monochromatic Bragg Diffraction

A perfect crystal can be seen as a periodic layout of a given lattice, described by three dimension parameters and three angles, as illustrated in Figure 3.19a. Here, the considered materials are silicon and copper, which both have a cubic lattice, so $a = b = c$ and $\alpha = \beta = \gamma = 90°$. The lattice is therefore only defined by a, called the lattice spacing. Any 3 points inside the lattice define a plane, as illustrated in Figure 3.19b. The plane can be described by the Miller indices (hkl). A family

of equivalent planes (parallel and equidistant) is written $\{hkl\}$. The interplanar distance is noted d_{hkl} and, for a cubic lattice, is calculated by eq. 3.30.

$$d_{hkl} = \frac{a}{\sqrt{h^2 + k^2 + l^2}} \tag{3.30}$$

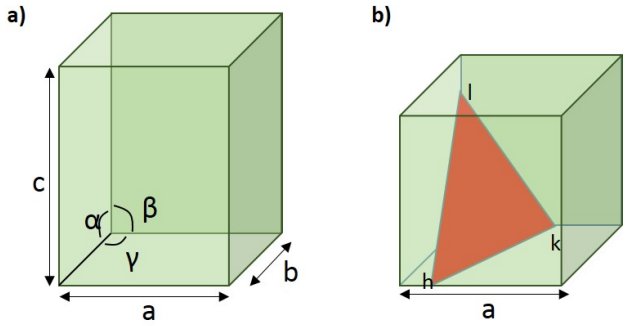

Figure 3.19: a) Lattice parameters of a crystal. b) Illustration of a crystallographic plane inside a crystal, together with its Miller indices (hkl).

In real crystals, atoms can be shifted with respect to their ideal position. This is interpreted as strain inside the material, and can be due to the presence of defects inside the crystal, such as dislocations, grain boundaries, or stacking faults, or to an applied external force, such as a mechanical stress, an electric field, or a change of temperature. The out-of-plane strain, whatever its origin, is defined for a given family of planes by eq. 3.31:

$$\varepsilon_{hkl}(\%) = \frac{d_{hkl} - d_{ref}}{d_{ref}} \cdot 100 \tag{3.31}$$

where a is the lattice spacing of the material, and d_{ref} is a reference value for the interplanar distance, obtained by calculation or measured on an unstrained region of the material. Strain measurement therefore relies on the measurement of the interplanar distance, for a given family of planes.

Let's now consider an x-ray beam forming an angle θ with a crystalline sample's surface, as presented in Figure 3.20. It is here assumed that the surface is parallel to the plane family of interest. As explained in section 3.1.2, Bragg law provides: $2d \cdot \sin\theta = \lambda$ with d the interplanar distance, and λ the x-ray wavelength: x-ray diffraction is therefore sensitive to the interplanar distance. Bragg diffraction can also be described using the propagation vectors. $\mathbf{k_i}$ is defined as the propagation vector of the incident beam, and $\mathbf{k_f}$ as the propagation vector of the scattered beam towards the detector position. By definition, $|\mathbf{k_i}| = |\mathbf{k_f}| = \frac{2\pi}{\lambda}$. The momentum transfer vector si defined as $Q = k_f - k_i$. Diffraction being an elastic process, Bragg law can be written as:

$$|\mathbf{Q}| = |\mathbf{k_f} - \mathbf{k_i}| \tag{3.32}$$
$$= 2 \cdot \sin(\theta) \tag{3.33}$$
$$= \frac{2\pi}{d} \tag{3.34}$$

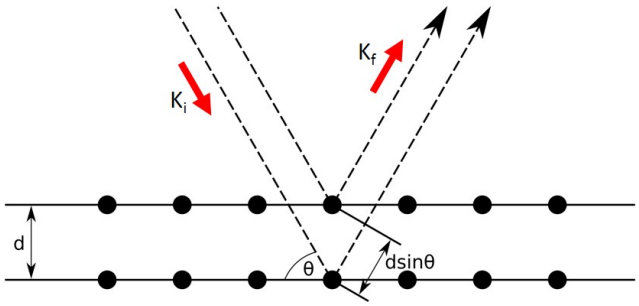

Figure 3.20: An illustration Bragg law, expressed with propagation vectors $\mathbf{k_i}$ nad $\mathbf{k_f}$

By changing the angle θ, one can therefore access different interplanar distances and probe the reciprocal space. This conclusion leads to one of the experimental setups used in ID01. It relies on Bragg law and is performed with a monochromatic wave (with $\Delta E/E = 10^{-4}$). The idea is to tilt the sample around the theoretical Bragg angle value and to observe the displacement of the Bragg peak on the detector. The fitting of these displacements provide the interplanar distance for the considered planes, and therefore the strain underwent by the material.

3.4.2 The ID01 workflow

3.4.2.1 Experimental setup: the K-map scanning technique

To set this idea in practice, an experimental setup such as the one shown in Figure 3.21 is implemented. The sample is placed in the focus of the x-ray beam. It can be tilted, so the angle η created between the beam and the sample can be adapted to the observed material and plane. An hexapod allows the sample to stay in focus while doing so. In the case where the observed planes are parallel to the sample surface, one obtains $\eta = \theta$. The detector is placed on a rotable arm, and can be set at an angle 2θ so it captures the diffraction patterns.

To obtain a strain map of the sample, it is scanned in the X and Y real space direction. For each point, the diffraction pattern is recorded on a detector. The 2D MAXIPIX ultra-fast detector, recently developed, makes it possible to acquire the data fast enough to realize such an experiment [88]. The sample is tilted along a rocking curve around the theoretical Bragg angle and scanned for each angle. Bragg angles and some relevant values are given in table 3.6 for the materials and planes studied and energies used during this work.

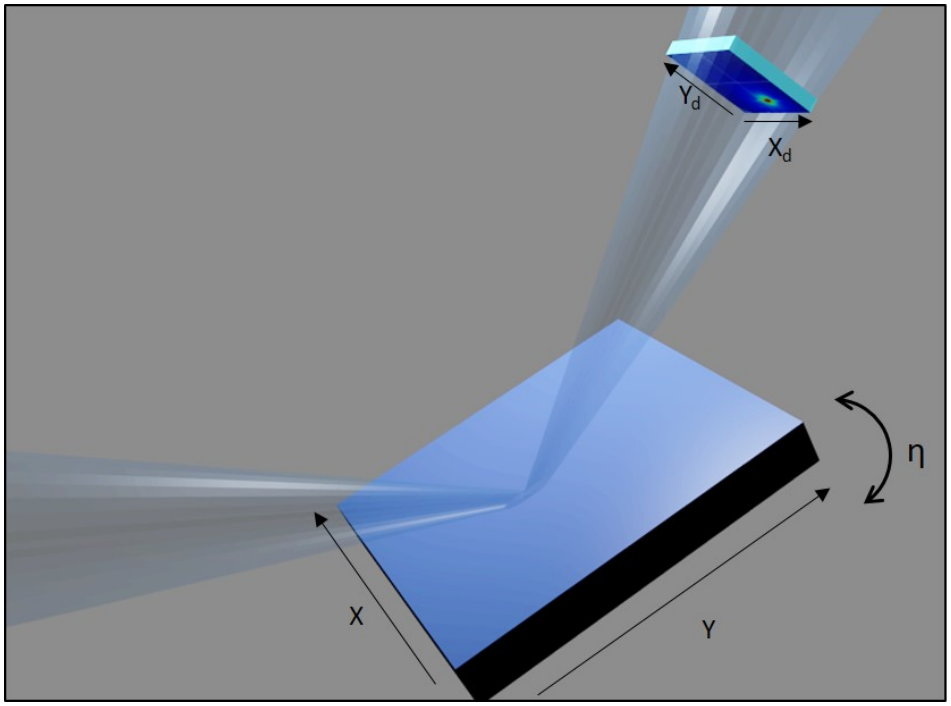

Figure 3.21: Experimental setup for x-ray Bragg diffraction experiments, aiming at strain measures. X and Y are the real space dimensions of the scan, η is the angle between the incident beam and the sample surface (here supposed to be parallel to the observe plane family), and X_d and Y_d are the coordinates on the 2D detector.

	d_{hkl} (nm)	q_0 (Å^{-1})	η (°)	
			8 keV	9 keV
Cu_{222}	0.105	6.03	48.80	41.81
Si_{004}	0.543	4.63	34.81	30.50

Table 3.6: Relevant values for Si_{004} and Cu_{004} planes observation

In order to perform the scan and the rocking curve of the sample in a reasonable time, a scanning technique called K-map (quicK mapping) was developped in ID01. It is fully described in ref. [87] and is based on the continuous acquisition of data, thus saving time on the hardware communication of data. Final scan times can be reduced by as much as 2 orders of magnitude.

This technique generates a tremendous amount of data. A typical acquisition can cover a 30 μm x 30 μm area with scanning steps of 300 nm, and with a rocking curve containing 30 points. This leads to 300 000 2D diffraction patterns. To deal with this quantity of data, a software called X-SOCS, for x-ray Strain Orientation Calculation Software, was developed and implemented in ID01 (https: //gitlab.esrf.fr/kmap/xsocs). The next section describes its main features, while further details can be found in [87].

3.4.2.2 Post-processing: the X-SOCS software

The process described in the previous section generates 5 dimensional data. In fact the scanning in the X and Y directions are two dimensions, to which θ adds a dimension. All acquired data are 2D images (with dimensions X_d and Y_d), thus bringing 5 dimensions. This allows for an unambiguous determination of the lattice strain and orientation (tilt). In this section, only the strain maps generation is described.

For each point (X,Y) of the sample, the rocking curve generates a 3D volume in the reciprocal space, which is defined by directions Q_x, Q_y, and Q_z expressed in Å^{-1}. Such a volume, showing a Bragg peak obtained for a Si_{004} observation, is presented in Figure 3.22. The main part of the post-processing is to find the coordinates of the Bragg peak for every point of the sample. Once this is done, one obtains maps such as the ones presented in Figure 3.23a-c, showing respectively Q_x, Q_y, and Q_z for every point of the analyzed sample. Finally, the out-of-plane strain ε_{hkl} is obtained by eq. 3.35. By including this formula into eq. 3.31, the software provides a strain map, such as the one presented in Figure 3.23d. During the experiments performed here, patterns covered the whole wafer surface. There were no unstrained regions, therefore theoretical values were taken as d_{ref}. Their values are given in table 3.6. It is noticeable that the obtained strain maps are highly dependent on the chosen reference value, and the values they contain should therefore be considered as relative.

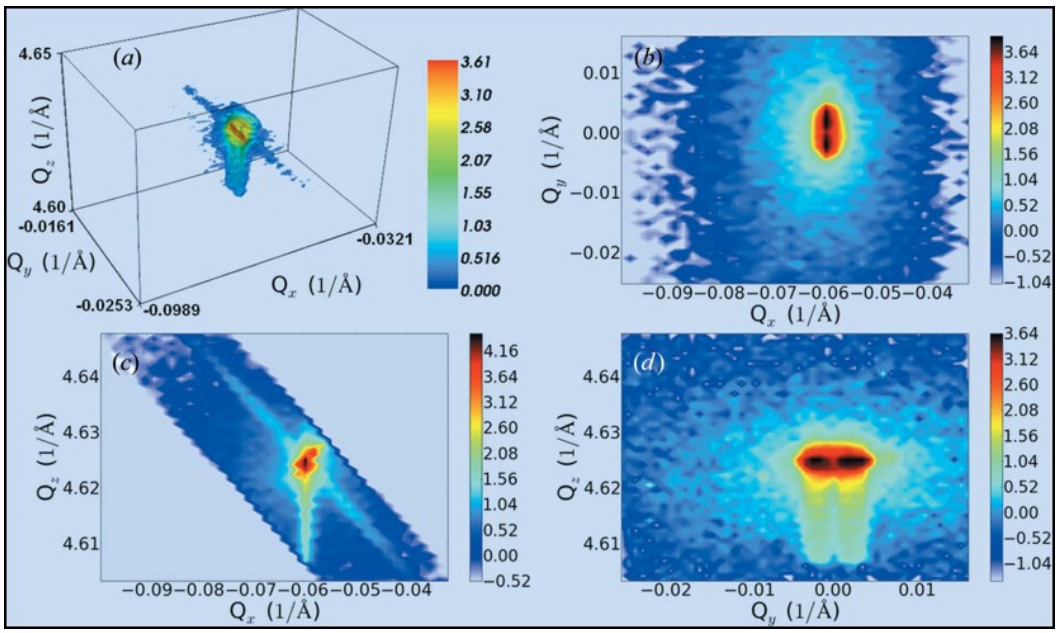

Figure 3.22: (a) Three-dimensional representation of the Si 004 Bragg peak for a given real space position on the sample. Two-dimensional cuts of the Bragg peak in reciprocal space as a function of Qx and Qy (b), Qx and Qz (c), and Qy and Qz (d). *Image source: [87]*

$$d_{hkl} = \frac{2\pi}{|\mathbf{Q}|} \tag{3.35}$$

$$= \frac{2\pi}{\sqrt{Q_x^2+Q_y^2+Q_z^2}} \tag{3.36}$$

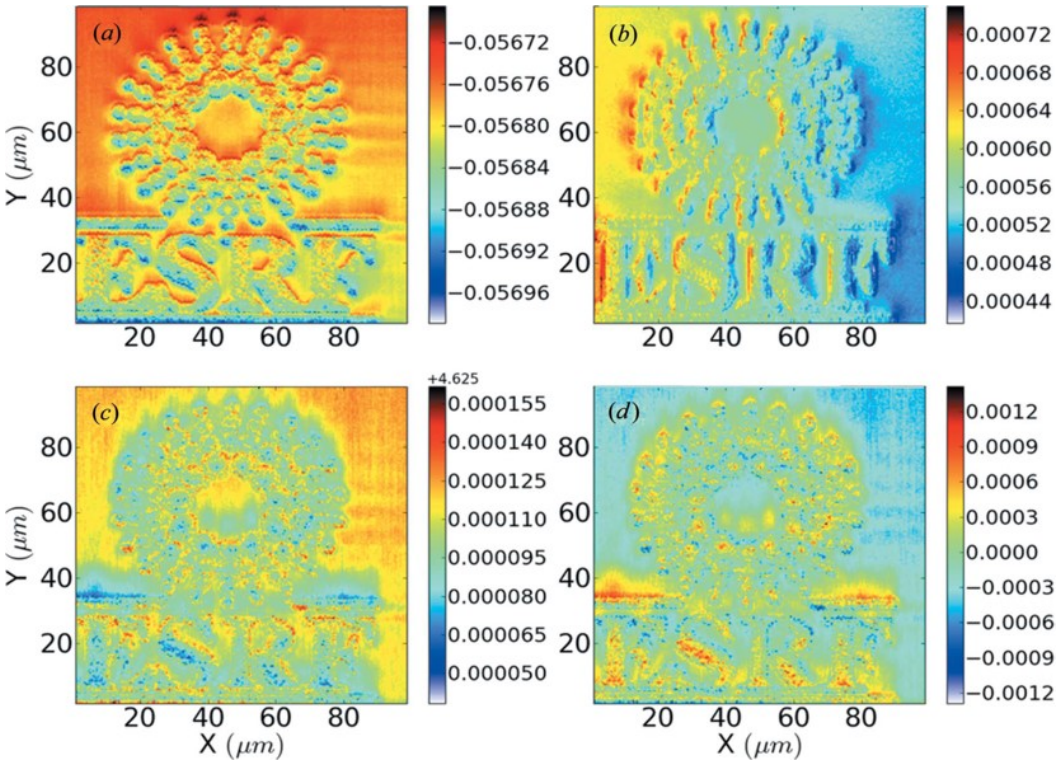

Figure 3.23: Scattering vector coordinates (a) Qx, (b) Qy and (c) Qz, and (d) out-of-plane strain as a function of real beam position on the sample. *Image source: [87]*

Two resolutions must be discussed when referring to the k-map technique. First, the spatial resolution. It is limited by the footprint of the beam on the sample, and is therefore linked to the size of the focus, thus the size of the source. Typically, the spatial resolution achievable on this beamline is about 200 - 800 nm. It must also be taken into account that the obtained value is averaged through the depth reached by the beam. At 8 keV, if not limited by the thickness of the sample itself, this depth will be about 70 to 100 μm in silicon. The strain and tilt sensibility is the resolution in the reciprocal space. It is linked to the divergence of the beam, and can go down to $\frac{\Delta\varepsilon}{\varepsilon} = 10^{-5}$.

3.4.3 Sample Preparation

As presented in this chapter, the experiments are carried by diffraction, in a Bragg (reflection) configuration. It does not require specific sample dimensions, as the

beam does not have to go through the sample. However, one of the advantages of using x-ray is their penetration depth, and the fact that buried structures can be observed. In the case were such objects are to be analyzed, the sample must be thinned in order for enough photons to reach the structures, be scattered by them, and exit the sample. For example, as will be presented in chapter 6, here silicon and copper stacks were analyzed. For the 8 keV beam to reach the lower layer of the stack, absorption had to be taken into account, and the upper layer of the stack had to be thinned down to 3 μm.

Méthodes d'imagerie par rayons X
Résumé du chapitre

Ce chapitre présente en détails quelques possibilités des rayons X pour la caractérisation de matériaux, et les dispositifs expérimentaux associés. Comme dans le chapitre précédent, quelques sources de rayons X sont décrites, avec leurs principales caractéristiques. Les deux types majeurs sont les sources de laboratoire et les sources synchrotrons, bien plus versatiles. Ces dernières sont détaillées, en prenant comme exemple l'ESRF (European Synchrotron Radiation Facility), où les expériences présentées ici ont été réalisées. Les différentes interactions possibles entre les rayons X et la matière sont décrites, avec un intérêt particulier pour celles exploitées pendant cette thèse.

Les dispositifs expérimentaux permettant l'imagerie par rayons X sont également décrits. Notamment, trois lignes de lumières de l'ESRF sont présentées, et leur caractéristiques spécifiques mises en avant.

L'imagerie 3D par rayons X (par tomographie ou laminographie) est ensuite présentée. Les différentes techniques d'imagerie 2D compatibles sont décrites. Il s'agit de l'imagerie d'absorption, de l'imagerie par contraste de phase, et de l'imagerie par fluorescence, permettant d'obtenir une information chimique.

Finalement, les principes et la mise en pratique de la mesure de déformation, basée ici sur la diffraction de Bragg, sont présentés. Cette description est supportée par le principe de fonctionnement de la ligne ID01.

Chapter 4

Development of 3D imaging in a single column PFIB

Contents

4.1 Automation of the data acquisition 86
4.1.1 The iFast software 86
4.1.2 Data acquisition workflow 88
4.2 Data post-processing 94
4.2.1 Calculation of the actual slicing step 96
4.2.2 Slices registration 96
4.2.3 Volume re-sampling 98
4.3 Results 99
4.4 Limits of the technique and possible improvements 104
4.5 Conclusion 107

Slice and view techniques, described in section 2.4.1.2 have been used for a long time and are still under development. Although they offer great insight into the matter, and the possibility to image selected regions of interest at resolutions reaching several nm, their implementation in dual beam FIB/SEM microscopes shows some limits. The main one is the quite low sputtering rate of Ga^+ ion beams (5.4 $\mu m^3.s^{-1}$). To overcome this issue, dual beam PFIB/SEM, originally developed for large sample preparation, have been applied to Slice and View imaging [30, 68]. They offer the possibility to image volumes as large as 100^3 μm^3 with a voxel size of 100 nm.

Similarly to FIB/FIB techniques described in section 2.4, it is possible to implement a PFIB/FPIB Slice and View procedure. A single beam PFIB benefits from the high abrasion rate of the xenon plasma ion beam (300 $\mu m^3.s^{-1}$), and would therefore allow for higher imaged volumes than FIB/SEM and FIB/FIB procedures. This machine is however originally designed exclusively for sample preparation, and a number of adjustments are required for it to be compatible with 3D imaging.

In this chapter, we present the development of such a procedure, implemented inside a single-beam Plasma FIB. A first section is dedicated to the automation of the data acquisition inside the FEI Vion Plasma-FIB. In a second section, the post-processing script, written specifically for these data, is described and explained. Finally, results obtained with such a setup are presented and discussed. The technique is illustrated throughout the chapter using images acquired on the PFIB, all of them having been obtained in the frame of this PhD thesis.

4.1 Automation of the data acquisition

The Slice and View procedure was implemented on a single column FEI Vion Plasma FIB. This microscope offers 5 degrees of liberty to the sample. The stage is able to move the sample in the X,Y, and Z directions, as illustrated in Figure 4.1. Furthermore, a rotation around axis Z and centered on any sample point can be applied. A tilt around axis X, ranging between -12° and 60° can also be used. Figure 4.1 also presents the features defining the region of interest (ROI) to be imaged. The ROI is considered to be a rectangle, defined by dimensions X_{ROI} and Y_{ROI}, and which center is called P_0. In this chapter, directions X, Y, and Z are defined regarding the sample: at a 0° tilt, discussed directions are X and Y, while the acquired images are defined in the (XZ) plane.

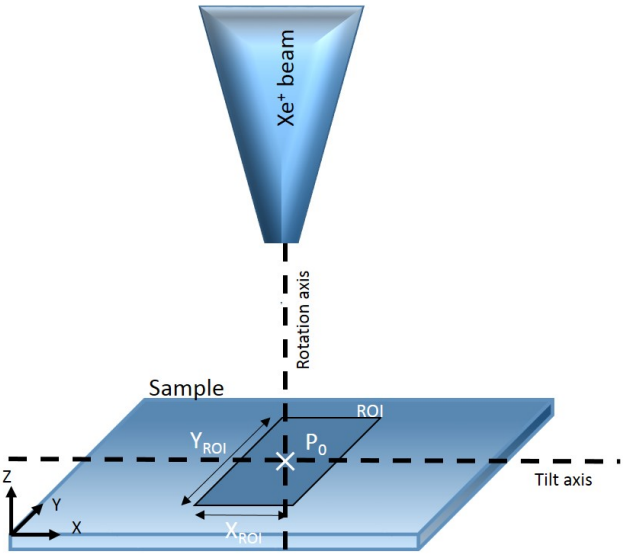

Figure 4.1: Notations used in this chapter to designate the degrees of liberty (X, Y, Z, rotation, tilt) allowed by the single column PFIB, and the notations regarding the sample itself. The ROI to be imaged is considered to be a rectangle, defined by its dimensions X_{ROI} and Y_{ROI} and its center P_0.

4.1.1 The iFast software

The whole data acquisition was automated using the FEI iFast software [109]. It is a visual scripting software which enables the triggering of successive actions on the PFIB, without human intervention. The programming of actions consists in connecting graphic boxes together, as presented in Figure 4.2 which illustrates some functionalities of the software. More generally, the actions programmable using iFast include:

Stage movements Stage movements can be defined with absolute or relative coordinates. The final position is accurate up to several tens of nanometers.

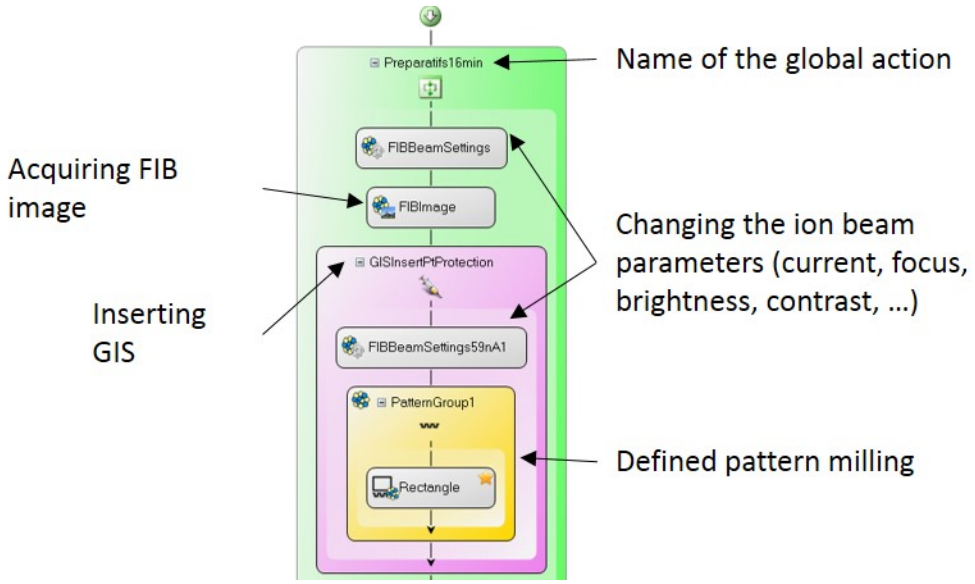

Figure 4.2: Example of a visual script produced in iFast. It this script, named "Preparatifs16min", the beam parameters (current, focus, brightness, contrast) are first set, and an image is acquired. Then, a GIS (Gas Injection System) is inserted and stays in the chambre until the end. The beam parameters are modified (the current is changed), and a rectangle-shaped pattern is deposited.

Beam shift movements Those movements allow, with no move from the stage, to adapt the imaged area, in the limit of 50 μm in all directions. The final position is accurate up to several nanometers.

Saving of beam parameters Parameters such as the focus, the brightness and contrast, can be saved during the settings, and used later in the experiment.

Imaging The image acquisition parameters, such as the field of view and the acquisition time, can be tuned.

Change of current The change of current can be triggered by iFast.

Milling Milling can be performed with all shapes, currents, and general settings available on the PFIB, and the patterns can be saved.

Matter deposition IBID is available, the insertion of gas being also triggered by the iFast software.

Pattern recognition The iFast software is able to compare a reference image previously saved with a newly acquired one. It then aligns the two images, and moves (by beam shift or stage movement, depending on the user choice) towards the position at which the original image was taken.

4.1.2 Data acquisition workflow

4.1.2.1 Main issues and answers

Compared to classical dual beam setups, the single beam requires the sample to move between the slicing and imaging steps. This rises issues regarding the sample alignment and the time needed for the whole procedure. Here we present the difficulties met, the solutions brought in the case of PFIB/PFIB imaging, and the final workflow they led to.

Between the milling and imaging steps, the sample must be moved regarding the beam. Two possibilities exist. First, the sample can be simply tilted. It is a quite easy to implement solution, that does not need any specific tool. However, as the tilt of the PFIB is limited to 60°, the imaging is not performed orthogonally to the cross-section: acquired cross-sections have to be re-sampled for the dimensions to be correct in both directions. A second possibility is to set the sample on a 45° pre-tilted support. The slicing is then performed at a PFIB tilt of 45°, so that the beam arrives orthogonally to the sample surface. For the beam to image the cross-section, the sample is tilted back to 0° and rotated by 180°. The imaging is then performed at 45°, which allows to image the cross-section orthogonally. In this study, the first solution, as it was simpler and did not require supplementary sample support, was chosen. Besides, as will be presented in the post-processing description, a re-sampling is needed in most cases after a Slice and View procedure, and is performed in dual beam solutions, since the two beams do not form a 90°

angle. The re-sampling required by the data acquisition made at 60° occurs at little supplementary computation cost.

As the stage is moved between two successive slicing procedures, a second challenge is to ensure the slicing step remains constant through the whole SaV procedure. To do so, at the beginning of each successive step, the PFIB stage is programmed to go to point P_0, situated at the center of the ROI. As mentioned before, this stage movement is not very precise. To improve the location of the reference point, an alignment step is needed. To do so, an alignment cross is milled at the top of the ROI, at a distance D of the ROI edge, as illustrated in Figure 4.3a. The center of this cross is the reference point: at the beginning of every iteration, the pattern recognition algorithm implemented in iFast sets the center of the image on the center of the cross, using only beam shift. Actually, this procedure is done twice, with two different fields of view. The first procedure is realized with a large field of view image (typically 130 μm) such as the one presented in Figure 4.3a. The large field of view ensures the cross can be found on the acquired image. After this first step, a more precise alignment, based on a smaller field of view image (typically 20 μm), is applied. A typical reference image for this smaller field of view is presented in Figure 4.3. Once the center of the image is aligned with the center of the alignment cross, a final beam shift moves the center of the image to the edge of the previously-sliced cross-section. Moreover, control images are acquired during the procedure. They allow for the measurement of the actual slicing step during the post-processing procedure. This will be detailed in section 4.2.

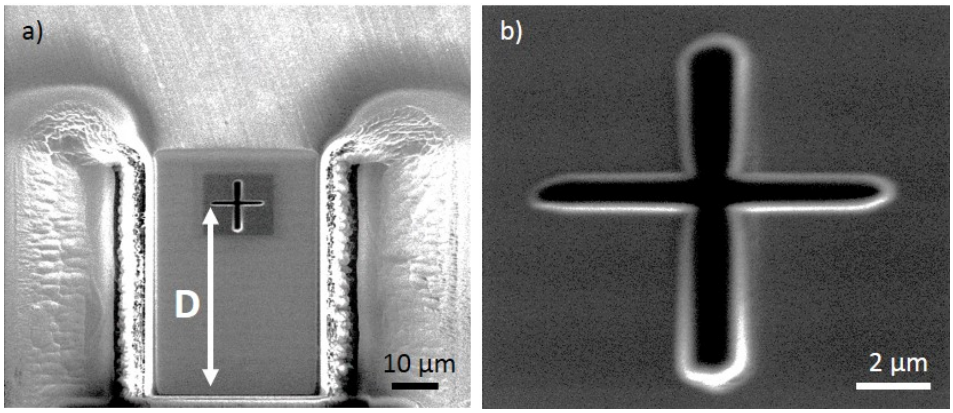

Figure 4.3: Typical reference images, containing the alignment cross, used for the alignment step. a) Image with a large field of view (100 μm; b) image with a smaller field of view (13 μm).

Finally, a supplementary difficulty is to keep the region of interest (usually parallel to the sample surface) inside the field of view imaged during the procedure. A first step to do so is to adapt the Z position of the sample for the ROI to be on the tilt axis, as illustrated in Figure 4.4a. By doing so however, the region of interest tends to drift towards the top of the imaged area along the successive Slice and View steps, as shown in Figure 4.4b. This is due to the fact that the stage is still

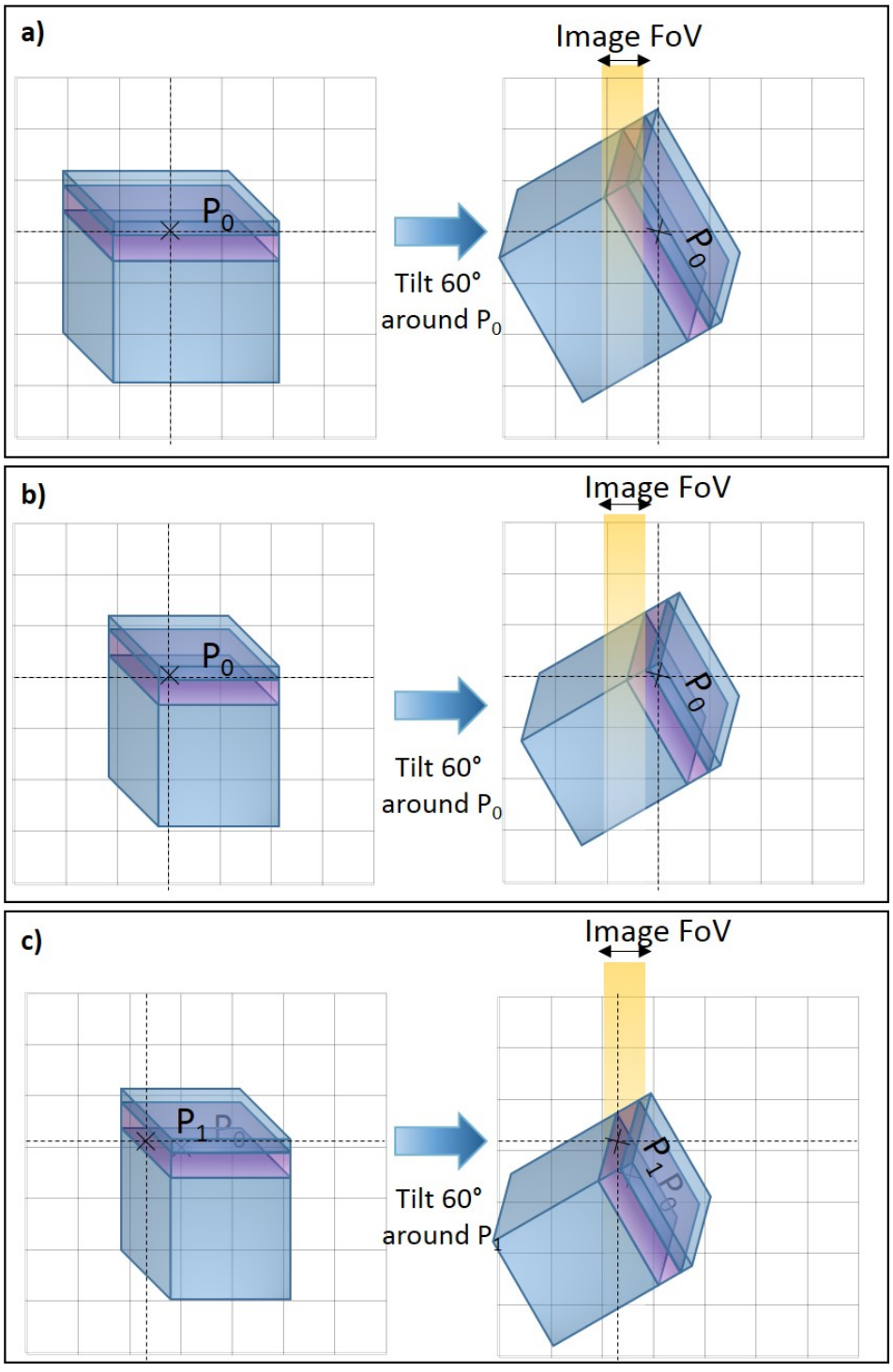

Figure 4.4: Imaged regions of the ROI during the SaV procedure, depending on the tilt axis. The purple layer of the sample is the region ot be imaged. a) The tilt is realized around an axis passing through point P_0, at the begining of the procedure. The imaged area is adapted to contain the purple layer. b) After several iterations, the tilt around the same axis P_0 does not guaranty the purple layer to be in the imaged area. c) The sample is tilted around a parallel axis, passing through the point P_1, situated on the edge of the ROI. The purple layer is imaged. The tilting axis must therefore be changed along the SaV procedure, and always contain a point from the edge.

centered on point P_0, and not on the edge, since only beam shifts have been performed. To overcome this issue, the last beam shift is replaced, after the end of the cross-section milling, by a stage movement of the same amplitude. On Figure 4.4c, the tilt is performed around point P_1, situated on the edge. As illustrated, this ensures the region of interest is always placed at the center of the imaged region. For some samples, a further beam shift (triggered by an image alignment algorithm or user defined) could also be applied after the shift in order to set the cross-section region of interest on the center of the imaged region.

4.1.2.2 PFIB/PFIB acquisition workflow

ROI preparation Before beginning the acquisition of data, a preparation of the region of interest is necessary. The ROI preparation steps are summarized and illustrated in Figure 4.5. First, a protective Pt layer of typically 3 to 5 μm thickness is deposited on a region containing the ROI (cf 4.5a), using the Ion Beam Induced Deposition method described in section 2.3.2. Then, large trenches are milled around the ROI, in order to limit future redeposition. A first milling step is made a high ion current (typically 2 μA), using a regular cross-section pattern (cf 4.5b). Then, a softer pattern (cleaning cross section, cf 4.5c) is applied, at a lower current (0.18 μA). Finally, the edge of the ROI is defined by a soft cleaning cross section (performed at a 59 nA current), and the alignment cross is milled (cf 4.5d).

Acquisition preparation Once the preparation step is over, the data acquisition must be configured. The number of Slice and View steps is defined by the number N, and each iteration is designated by its number n. The slicing step required by the user is noted p. Figure 4.6 presents the general workflow for any iteration n of the process. The user realizes the first iteration manually, while setting the parameters for the automatic data acquisition.

First, the user adjusts and saves the focus, brightness, and contrast parameters for imaging at 0°. These values will be used throughout the whole process. This ensures that the images always look similar, and therefore ensures the success of the pattern recognition algorithm to come. The distance D is then measured and input into the software. Then, the two reference images, at large and small field of view, are recorded and saved. After the alignment step, a beam shift of D is applied. More generally, at each iteration, the movement from the center of the cross to the edge of the ROI will be defined by distance D-np in the Y direction. The milling pattern can then be defined by the user, as a cleaning cross section that is to be placed on the edge of the ROI, as shown in Figure 4.6d. The user then tunes the Z position of the sample, for the region of interest of the cross section to be in the center of the imaged area after the 60° tilt. The user can also add and save a beam shift that will be applied at each iteration, for a better image. The sample is then moved back to a 0° tilt, and the P_0 position can be saved into the software, given the new value of Z. If needed, the focus, brightness and contrast parameters at 0° can be updated.

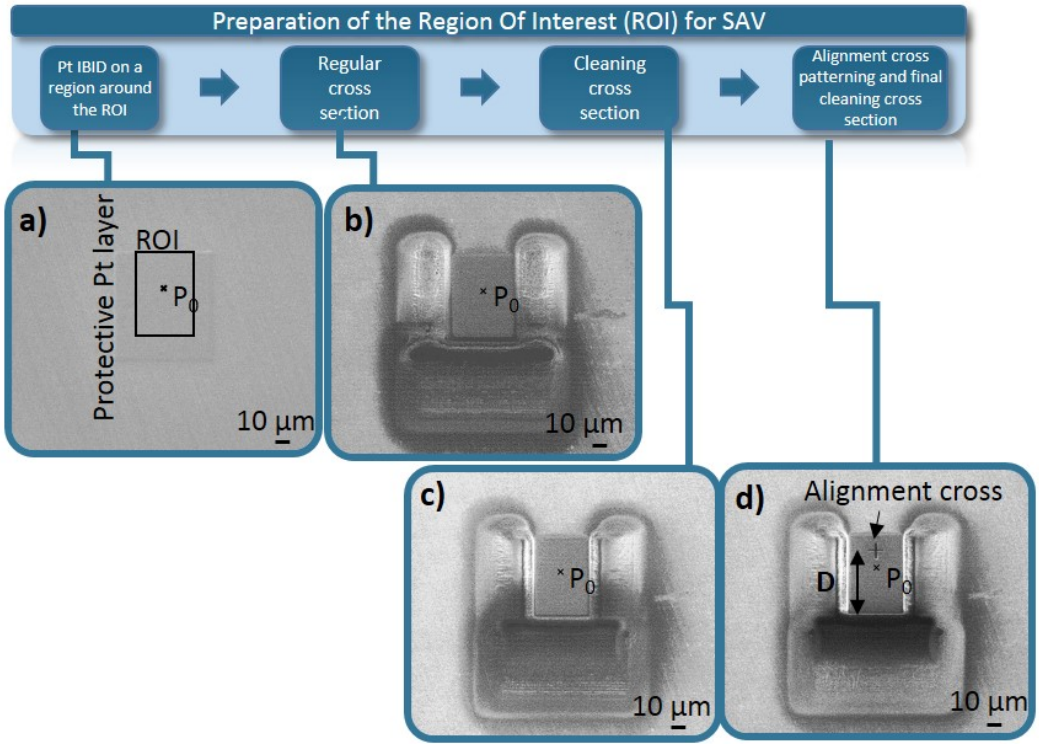

Figure 4.5: Steps of the ROI preparation for the SaV procedure. a) Deposition of a protective layer on the ROI. b) Regular cross-section milling around the ROI. c) Cleaning cross-section milling around the ROI. d) Alignment cross and final cleaning cross section milling.

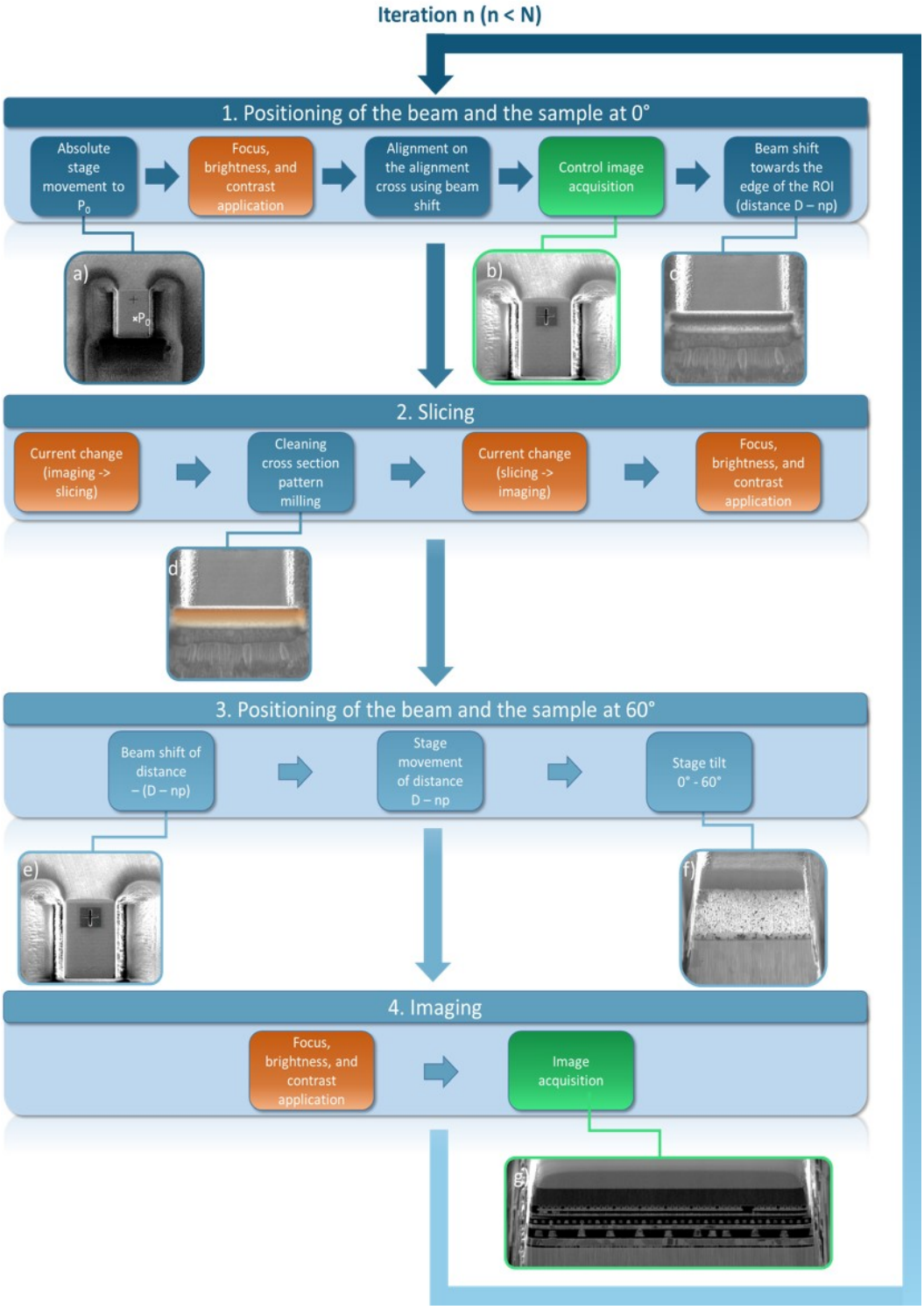

Figure 4.6: Automatic Slice and View actions occurring during a step (noted n). The actions related to beam parameters appear in orange, while imaging appears in green.

Automatic acquisition After the setting of all the parameters, it is possible to launch the Slice and View procedure for a number N of successive steps. Each step n consists in several actions, depicted and illustrated using different samples in Figure 4.6. In this figure, actions referring to beam parameters appear in orange, while imaging procedures, be it for control purposes or the actual imaging of the ROI, are presented in green. As illustrated, each step can be separated into four sub-steps:

1. **Positioning of the beam and the sample at 0°** The first action of the procedure is to move the stage towards P_0 (see Figure 4.6a). The positioning of the beam then relies on the application of previously saved beam parameters, together with the alignment of the beam on the center of the alignment cross. A control image (see Figure 4.6b) is acquired then. This first alignment allows to set the beam on the edge of the sample (see Figure 4.6c).

2. **Slicing of the sample** The slicing is performed using the milling pattern previously defined, situated on the center of the image (see Figure 4.6d). After the slicing step and a change of current, saved beam parameters are applied.

3. **Positioning of the beam and sample at 60°** As explained previously, before tilting the sample, the last beam shift is suppressed (see Figure 4.6e) and replaced by a stage movement. The tilt is then realized (see Figure 4.6f).

4. **Imaging the cross-section** Finally, after applying beam parameters, the wanted image of the cross-section can be acquired (see Figure 4.6g).

4.2 Data post-processing

After the data acquisition, two sets of data are available. They are illustrated in Figure 4.7. The control images (see Figure 4.7a) allow to retrieve the actual value of the slicing step. Their dimensions in pixels are noted $X_{control}$ and $Y_{control}$, and N of them have been acquired. The N cross-sections dimensions in pixels are noted X_{im} and Z_{im}. The pixel sizes in the X and Z directions are noted p_X and p_Z, respectively. Figure 4.7b features the raw volume and two orthogonal views obtained by simply stacking those N images together.

As can be observed on the YZ (red) orthogonal view of the volume, the cross-sections are not perfectly aligned with one another, which leads to planar interfaces that do not appear as such in the reconstruction. In order to obtain the final volume, the cross-sections therefore have to be registered.

Moreover, let us note p_X and p_Z the pixel sizes of the cross sections in the X and Z directions. Since the cross-sections are not imaged orthogonally, p_X and p_Z are not equal. Additionally, the slicing step p_Y is set independently from those two values, and is therefore not equal to them. To obtain a final volume, with cubic voxels, a re-sampling step is therefore needed, preceded by the calculation of the actual slicing step p_Y.

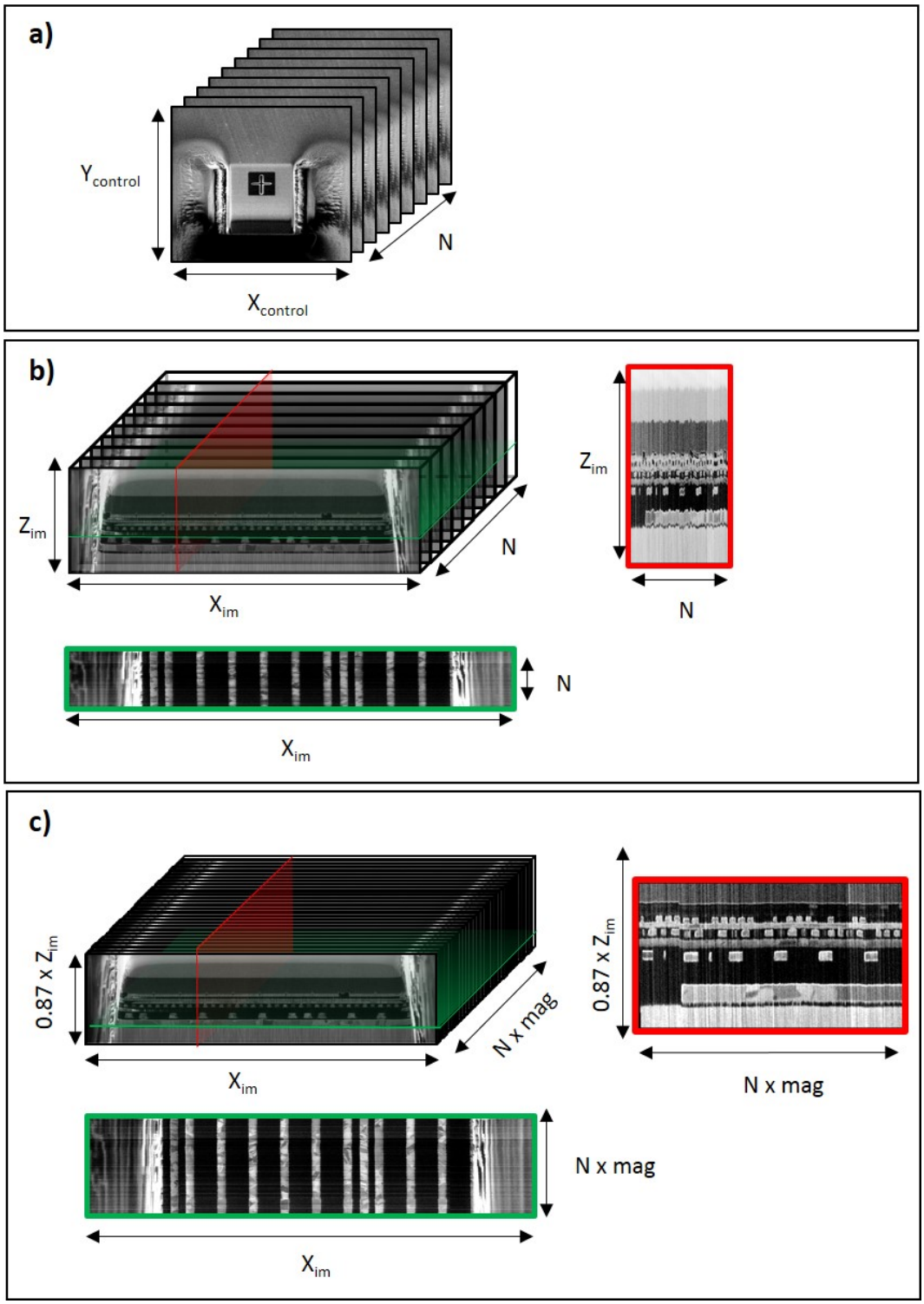

Figure 4.7: Data obtained after the data acquisition and the post-processing, respectively. a) Control images acquired for slicing step calculation. b) Raw volume generated by stacking cross-sections. c) Final volume, obtained after the post-processing. The slices have been registered, and the volume re-sampled in order for the dimensions to be isotropic.

The following sections aim at describing the post-processing steps leading to a well-registered, isotropic reconstructed volume. The main steps are presented in Figure 4.8.

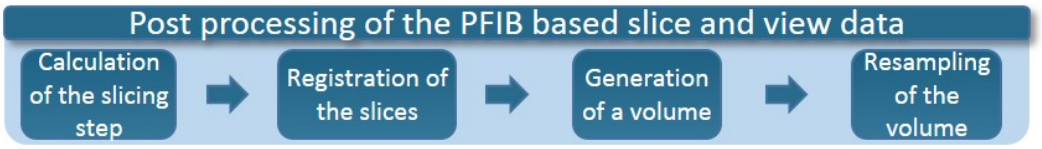

Figure 4.8: Steps of the data post-processing developed for PFIB SaV data.

4.2.1 Calculation of the actual slicing step

The first step of the post-processing is to retrieve from the data the actual value of the slicing step, noted p_Y. To do so, the script uses the control images. The control images are centered on the alignment cross. As shown in Figure 4.9, the edge of the ROI gets closer to the alignment cross with the iterations. What the script measures is the position Y of the edge in the image for each iteration, and therefore its advance in pixels and later in nanometers.

As the edge appears as a very bright horizontal line in the image, its position can be found using the profile of the image in the vertical direction, possibly calculated on a ROI (identical for all slices and manually defined). Figures 4.9d, e, an f show such profiles, calculated on the ROI defined on images a, b, and c, respectively. In this example, the maximum value corresponds to the edge of the sample and allows to follow the slicing step throughout the procedure. Depending on the sample, the calculation of the profile's gradient can provide better results, as it will help spotting the sharp change of grey level that is the edge, and leave out the other possibly bright features of the image. This method is illustrated in Figures 4.9g, h, and i. The choice of the method and of the ROI are up to the user. Once the edge position is known for all the slices, the script draws a graph presenting the evolution of the position vs the number of the slice. The graph should represent a line, which slope provides the slicing step, as will be presented in section 4.3.

At the end of this step, the value p_y of the slicing step is known and expressed in pixels. As the pixel size of the control image is known, the conversion to a slicing step in nanometers is straightforward.

4.2.2 Slices registration

A second step in the post-processing is to read all the slices, to register them with one another, and to stack them into a volume. Although the shifts between the different slices are quite small, due to the efforts made during the data acquisition step, the slices have to be perfectly or registered for the volume to be of good quality.

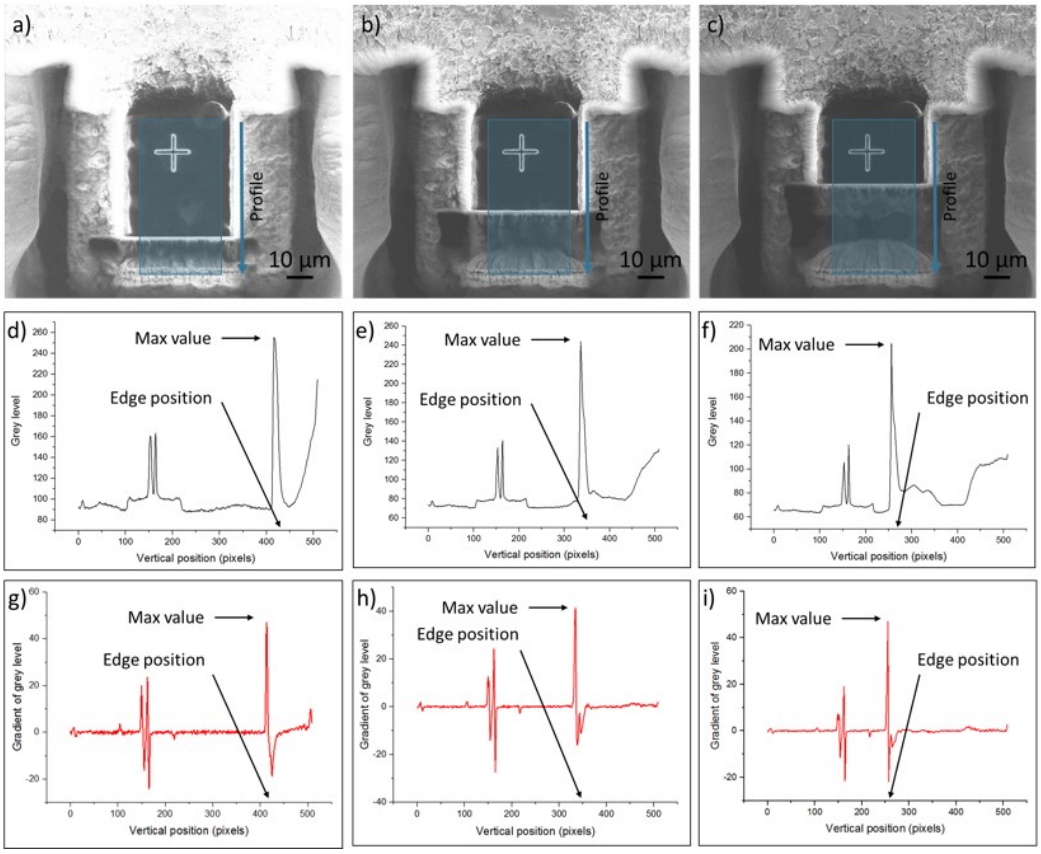

Figure 4.9: Control images acquired during a Slice and View procedure, after a) 100 iterations; b) 300 iterations; c) 500 iterations. The slicing step was set to 50 nm. d, e, f) profiles calculated on the ROI respectively shown on a, b, and c. g, h, i) gradients of profiles d, e, and f, respectively.

The script calculates and applies shifts to the slices in directions X and Z. It allows for different options:

- Two different registration methods are available. The first one is the *register_translation* function from the *skimage.feature* package from Python. The second one relies on the same profile calculation as the slicing step evaluation. It is faster than the registration function, but only works for very specific samples, having a bright spot that can be identified through the sample.
- The alignment is either performed on all slices regarding the first one, or for all slices regarding the previous one. This second method is less precise, and often leads to a linear shift throughout the volume, but allows to minimize the impact of possible high magnitude shifts during the acquisition.
- The alignment can be performed on a given ROI of the acquired image, manually defined.
- In most cases, no or little movement occurs in the horizontal (X) direction. It is possible then to limit the registration calculation to the vertical (Z) direction. This is advised when the chosen registration method is the profile-based one.

For all the sets of possible options, the script draws a graph showing the calculated shifts. During the tests performed on this experimental setup, these different options were implemented on the go, in order to adapt to the tested samples. As will be presented in the next sections, it allowed to image a wide panel of sample types. The set of options must be adapted to the studied sample, and no parameters have been found to work on every sample.

While registering the slices, the script reads them, shifts them in the X and Z direction, accordingly to the shift values found, and normalizes their contrast. It can then stack them into a volume. This volume has to be re-sampled, in order for the voxels to be cubic and the measures to be accurate in all directions.

4.2.3 Volume re-sampling

In the setup presented here, two re-sampling actions are needed. The horizontal cross-section pixel size p_X is taken as reference, and the other pixel sizes are adapted to it. First, all slices are distorted given the acquisition setup: since the imaging is done at 60° instead of 90°, a first re-sampling must be made in the Z direction (by a factor $sin(30°) = 0.87$). This allows to obtain isotropic cross-section, of pixel size p_{XZ} (typically 30 nm for an imaging field of view of 60 μm). The slicing step p_Z is however typically of 50 nm, or even 100 nm. A second re-sampling must then be performed in the Y direction, by a factor mag defined as $mag = \frac{p_Y}{p_{XZ}}$. These procedures are performed using the *zoom* function from the Python *scipy.ndimage.interpolation* package, and render an isotropic volume.

The final volume, obtained after all the post-processing steps, is illustrated in Figure 4.7c. Slices have visibly been aligned, since the interfaces now appear as

clearly planar. The re-sampling is also visible, on the cross sections (which are smaller in the Z direction), and on the orthogonal views: *mag* is here taken superior to 1 (which will usually be the case), which enlarges the volume in the Y direction.

4.3 Results

For the PFIB/PFIB Slice and View technique to be reliable, it is critical that the data acquisition step can be performed automatically. The acquisition being quite long, the process must remain stable for several tens of hours. This has been achieved, mainly by saving the imaging parameters at 0°: this made the pattern recognition step more robust. The experiment setup is now able to acquire data for tens of hours uninterrupted: 40 hours of unsupervised data acquisition were achieved so far. The process could last even longer, if needed.

The experimental setup presented here did allows for the reconstruction of various samples of different natures, with different slicing steps, imaging pixel sizes, and fields of view. As an illustration of the presented setup, figure 4.10 presents three examples of samples imaged on this setup: a stack containing several layers of copper, a copper pillar, and ceramics used in Solid Oxide Fuel Cells (SOFC). More generally, Figure 4.11 presents the volumes and voxel sizes of some samples analyzed on this setup, together with the type of material studied. The voxel size in this case was chosen to be the slicing step, as it is the limiting factor to the resolution. As can be seen, the PFIB/PFIB imaging allows to increase the analyzed volume compared to FIB/SEM imaging, since the analyzed volumes reached 50^3 μm^3, with a typical slice size of 60 x 20 μm^2 for stacks.

The previously detailed script automatically provides the slicing step value in a few minutes. Figure 4.12a) presents such a graph, for a demanded slicing step of 50 nm acquired on a stack sample such as the one presented in Figure 4.10a. The relationship between the iterations and the position of the edge is clearly linear, and was fitted by a line of coefficient -0.399 pxl/iteration, with a coefficient of determination $R^2 = 99.94\%$. Therefore, the slicing step is found to be 50.7 nm and quite regular. This regularity was also found for the other samples and slicing steps. The slicing steps mainly tested were 50 nm, 100 nm, and 200 nm. The 50 nm slicing step, combined with an image acquisition made with a FoV of 100 μm, offered the advantage to render volumes that needed little re-sampling to be isotropic.

For most samples, the slice registration can be made automatically in about 10 minutes. Figure 4.12b shows typical movements applied to the slices during the registration process for a stack sample such as the one shown in Figure 4.10a. As can be seen, the movements of the sample are quite small (below 10 pixels), but still need to be corrected: the data acquisition setup ensures the ROI remains in the imaged area, but does not provide a perfect alignment of the slices.

However, it is worth noticing that the registration software works very well on stacks, but is less efficient on copper pillars for example. For these samples, a manual registration using other tools such a the Fiji StackReg plugin can be required. In

that case, the post-processing is more likely to require about one hour per sample.

The data acquisition time itself varies with the slicing step, the imaged volume, and the slicing current. Figure 4.13a shows some of the times needed for the imaging of various samples tested in this study. The acquisition time varies from 7 hours (for the imaging of 19^3 μm^3) to 42 hours (for an imaged volume of 54^3 μm^3). On average, the time per slice is of 4.5 minutes. The PFIB allows for fast milling, and the slicing time is only of 60 seconds on average, which represents 20% of the step time. Figure 4.13b presents the average contribution of every action performed during a Slice and View step. As can be seen, high resolution ion imaging requires a long time (about 1.5 minutes), and takes about one third of the overall time. Moreover, the two main actions during a step (imaging and slicing) only account for 55% of the time, the rest being spent in changing the current, setting the beam and stage parameters, and tilting the sample.

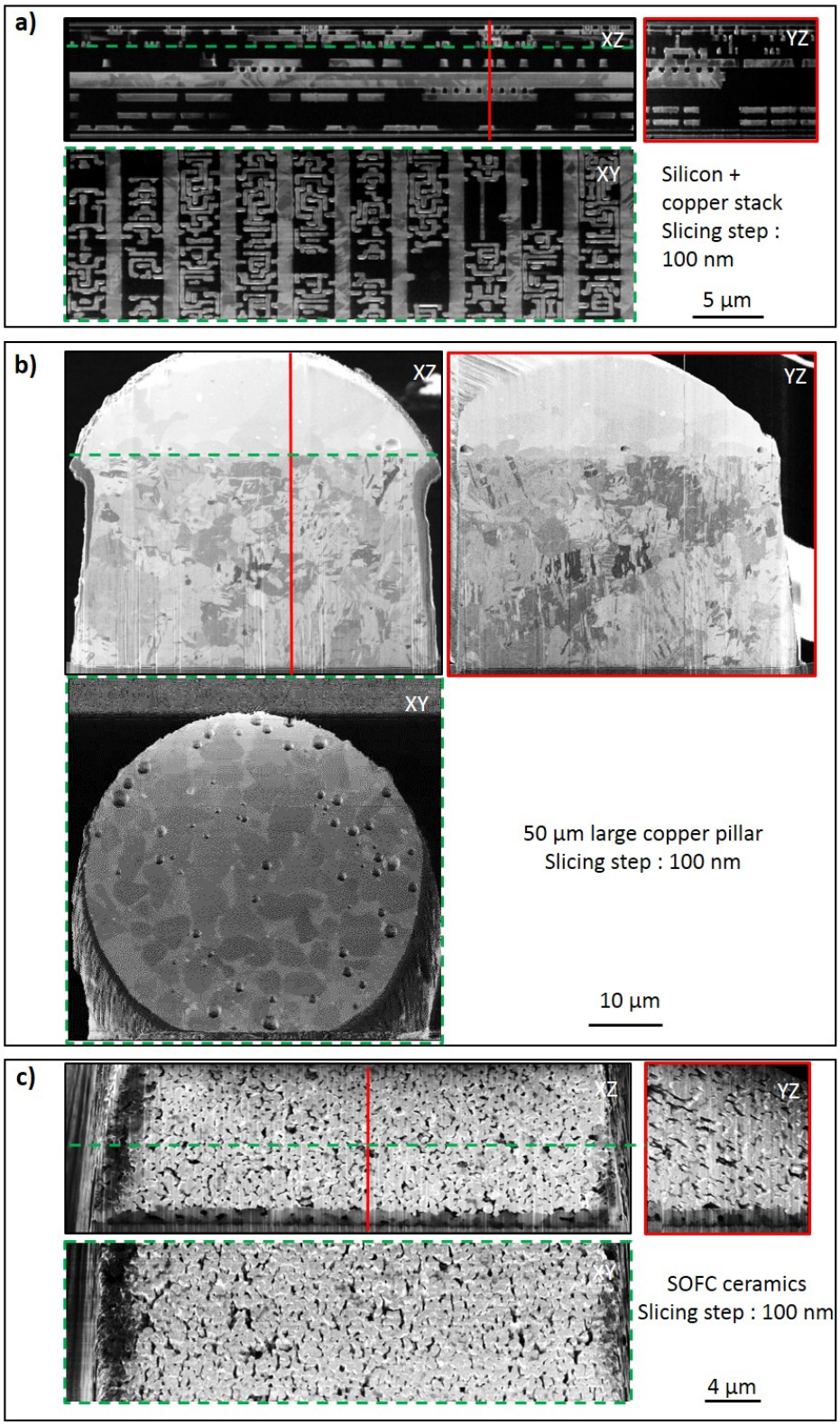

Figure 4.10: Results obtained by PFIB/PFIB 3D imaging. All results are presented through one XZ view (the imaged cross section) and two orthogonal views (XY and YZ), obtained from the final reconstructions. a) A copper + silicon stack; b) A 50 μm large copper pillar; c) A ceramic for SOFC (Solid Oxide Fuel Cells).

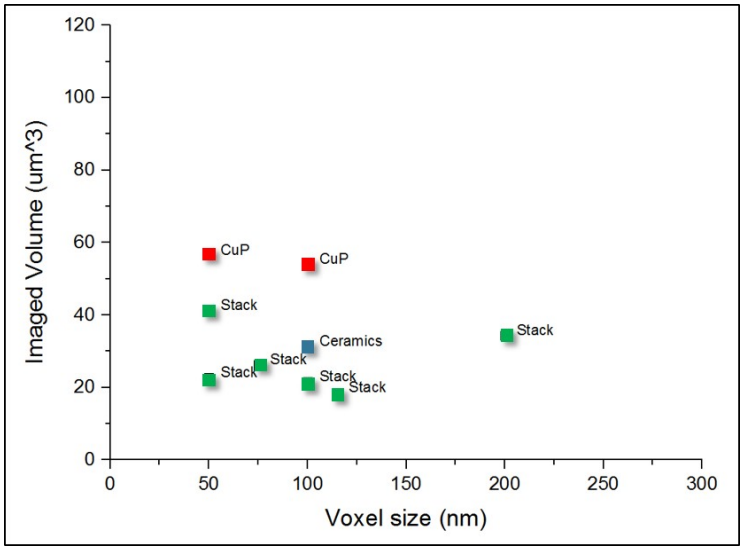

Figure 4.11: Imaged volumes and voxels sizes obtained for various samples analyzed in this study.

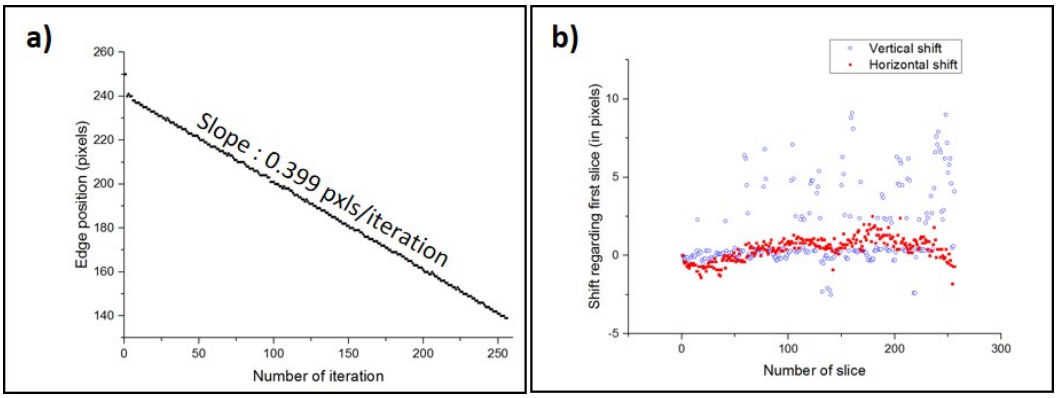

Figure 4.12: Graphs shown during the post-processing of the SaV data acquired from a hybrid bonding stack, which programmed slicing step was 50 nm. a) The graph showing the position of the edge regarding the number of the iteration. The slope coefficient is -0.399 (calculated with a coefficient of determination of 99.94%), which leads to a slicing step of 50.7 nm. b) The graph showing the shift applied to every slice, in the horizontal and vertical directions.

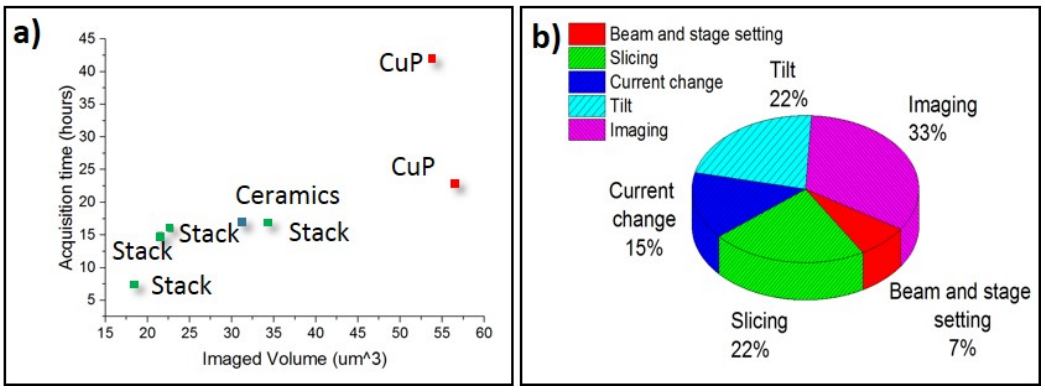

Figure 4.13: Time considerations regarding the PFIB/PFIB data acquisition. a) Acquisition times vs imaged volumes for various samples. b) Relative time needed for every action during a Slice and View step.

4.4 Limits of the technique and possible improvements

As discussed previously, the data acquisition and post-processing have been designed and implemented to demand little user intervention. A step further in the development of this setup would be to improve its automation. The data acquisition itself is fully automatic, but requires the user to spend about one hour on average to set the parameters. For known samples, this time could be reduced by the use of saved recipes, adapted to specific materials. Furthermore, the experiments could benefit from a user interface. In such an interface, it would be possible for the user to only set the wanted ROI and the slicing step desired, and the software could set the trenches, the position of the alignment cross etc. However, the setting of the Z position of the sample would still be up to the user, together with the setting of focus. Such an interface should be able to reduce the user intervention to about 20 minutes.

Regarding the post-processing, the automation is more challenging. As mentioned previously, the registration of slices does not work on all samples, and in any case the choice of the method and the ROI on which the registration is made are left up to the user. The post-processing software could however benefit from the implementation of other registration methods, such as SIFT (Scale Invariant Features Transform), which is based on the recognition of features, for example. The user would therefore still have to make choices during the post-processing, but would be provided with more options.

As observed previously, the data acquisition still requires much time. Although the use of xenon ion plasma source allows for very fast milling, the other steps of the procedure require more time than in a classic FIB/SEM setup for example, since the sample has to be tilted and the current changed. Moreover, as the machine was not meant for imaging originally, the detector requires long acquisition times to produce a high quality image. The data acquisition time could therefore be reduced by acting on those parameters. Although the use of a dual beam microscope or a better detector could solve some of these problems, we here present solutions applicable with the given single beam microscope, as it is able to provide valuable results with no hardware change.

After the slicing step, the current is changed, and the stage is tilted. Those two steps require almost one minute together. The iFast software does not allow the two to happen simultaneously. If this was made possible, 30 seconds could be saved per iteration. Moreover, the tilt itself could be improved by changing its speed parameters in the PFIB software. A 3D post-processing de-noising step could also allow to acquire image of less quality, thus saving time. Combining these different features, it should be possible to reduce the time per slice to 2.5 minutes.

The resolution and field of view could also be improved without increasing the acquisition time. In fact, the PFIB is able to operate a -12° tilt. If the sample was sliced at a stage position of -12°, the cross-section would be imaged at an angle of 72° instead of 60°. This would increase the image quality, as the further resampling would be of lower amplitude. However, the implementation of this idea

would require new techniques to maintain the region of interest in the imaged zone: the cross section would not be orthogonal to the sample surface anymore. This could be done inside the software: since the angle of the pre-tilt is known, the software can compensate for it by moving the stage or the beam. An even simpler way would be to place the sample on a 12° pre-tilted support. This way, the cross-section would be orthogonal to the sample surface, even when slicing the sample at a -12° tilted stage position.

The imaged volume is, as of today, limited in the Y direction to 100 μm. In fact, the workflow relies on the fact that the movement between the center of the alignment cross and the edge of the ROI is performed by the beam shift. On the PFIB, the vertical beam shift is limited to 50 μm in both directions (positive and negative values of Y). The distance D between the center of the alignment cross and the edge must therefore be inferior to 100 μm. The point P_0 is placed on the center of the ROI precisely to maximize the accessible region. It is worth mentioning that 100 μm was more than enough in the samples studied here. However, if a higher length is needed, it should be easy to implement a data acquisition in several parts, with several alignment crosses aligned on the Y axis and used one after the other. With such a technique, the length of the imaged volume should be virtually infinite.

The PFIB/PFIB imaging presents a drawback encountered in FIB/FIB imaging, but avoided in FIB/SEM imaging. As explained in chapter 2 (section 2.3.3), if the positive charges cannot escape the sample (e.g. the area is an insulator or surrounded by an insulator), they will accumulate at the surface, preventing any charge arriving in this area to leave the surface. Therefore, the area will appear in black. If a sample contains conductive areas (copper pads for example) that are isolated from other conductive zones (for example in the case of dummies), they will not appear on the acquired volume. This phenomenon is illustrated in Figure 4.14. In fact, on the top view presented in Figure 4.14a, obtained by milling a rectangle pattern from the surface of the sample, different structures are visible. Among them, pads covering a grid pattern can be observed. Figure 4.14b presents a YZ view of the reconstruction and two XY orthogonal views, acquired on the PFIB/PFIB setup. On the one labeled 1, the pads are clearly visible and the area from figure a is clearly identified. However, the grid pattern is not visible. When exploring the sample is the Z direction, this pattern does not appear, as illustrated by the slice labeled 2. This is due to the fact that during the ROI preparation step, the milling of trenches around the ROI cut the grid from the rest of the wafer. Their imaging was no long possible. To overcome this issue, negative charges should be projected on the surface. This is only possible in a dual beam microscope.

Finally, the PFIB-based Slice and View procedure encounters all the typical issues of Slice and View procedures. Since the imaging technique is sensitive to crystalline orientation, the segmentation can be difficult: a polycrystalline material will feature several grey levels. Moreover, as for every SaV procedure, the segmentation of porous materials is very hard. An example is given in Figure 4.15. It presents an histogram calculated on a subvolume of data acquired by PFIB/PFIB from a 50 μm copper pillar (see Figure 4.15a). The subvolume was taken around

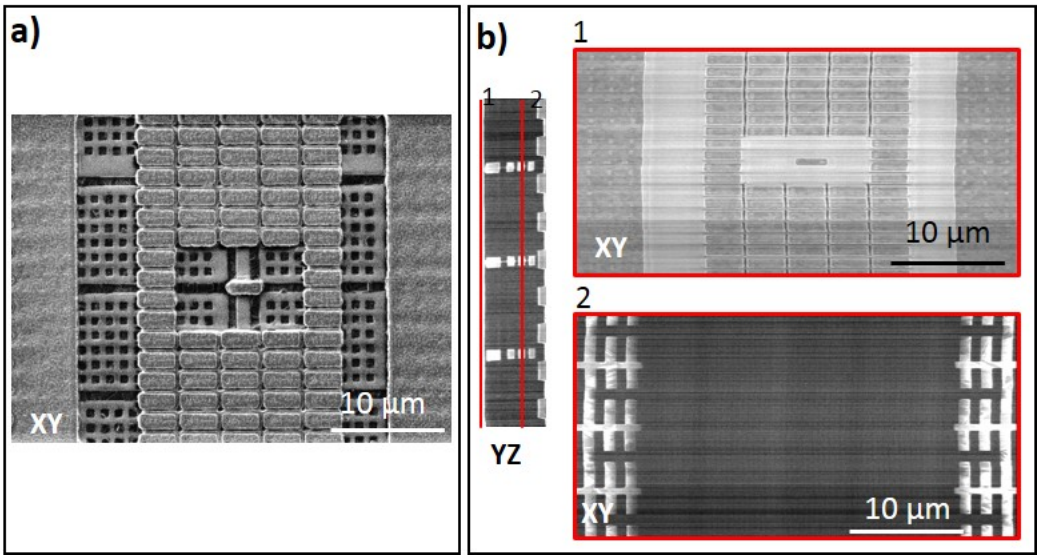

Figure 4.14: Illustration of the consequences of charge accumulation on the PFIB/PFIB imaging. a) Top-view of a silicon + copper stack, acquired on the PFIB and featuring pads on the whole surface. b) Reconstructed slice, using the PFIB 3D imaging, where the central pads cannot be seen.

the interface, which means it contains all the voids. The histogram is quite smooth, and does not allow for a direct segmentation based on a threshold, as shown in Figure 4.15b: a threshold level set at 57 leads to a selection (in red) that does not contain all the voids, whereas a 98 threshold level leads to selecting intermetallic alloy and a part of copper, while the voids are still not completely segmented. This issue was also encountered when imaging porous ceramics such as the one shown in Figure 4.10c. It is a well-known problem [110], inherent to Slice and View procedures. Although some solutions are being found, it remains a challenge in the case of porous media [111, 112]. The difficulty mainly relies on the high depth of field of the 2D imaging techniques. Indeed, a deep enough void will appear as a black spot, since the secondary electrons created in it will not be able to come back at the surface and hit the detector. After a few slices however, when the void is shallower, some secondary electrons will come back to the detector and the void will appear in a lighter grey level. After the volume creation, the obtained void will not appear in a uniform grey level. The segmentation will require advanced tools and several hours per sample.

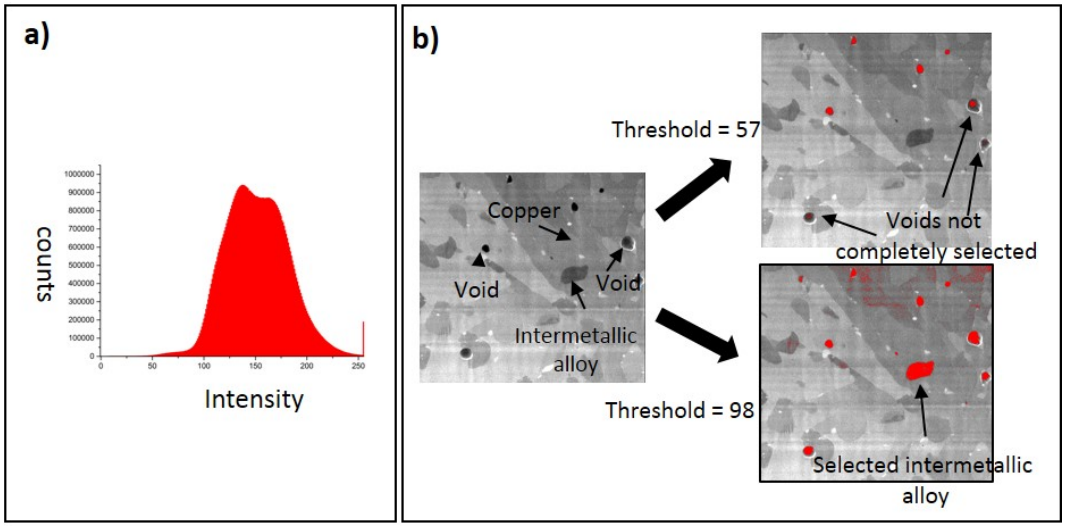

Figure 4.15: a) Histogram of a ROI of a copper pillars, containing intermetallic alloys and voids. b) Two attempts for the segmentation of voids (in red) inside this ROI, using two different threshold levels.

4.5 Conclusion

In this chapter, the implementation of a Slice and View procedure inside a single column PFIB has been presented. The main goal of such an implementation was to increase the achievable imaged volume by a Slice and View procedure, using the high sputtering rate of a xenon plasma ion source.

As the PFIB machine was originally designed for sample preparation, its application to 3D imaging rose several issues. They have been identified and answered in this chapter, and the implementation they led to has been presented: a complete workflow, including ROI preparation, data acquisition, and post-processing, has been provided and detailed. As a result, the setup now allows for the 3D imaging of various samples, as illustrated throughout the chapter. The acquisition process has been shown to be stable and reliable, as it could run unsupervised for 40 hours. The post-processing provides the user with information on the slicing step, and renders a registered and re-sampled reconstructed volume for most samples. Limits of the setup, including those regarding the acquisition time, have also been discussed.

As expected, the achievable volumes are higher than the ones acquired in FIB microscopes: xenon slicing allows to obtain cross-sections of 40 x 30 μm^2 in less than one minute, leading to imaged volumes between 15^3 and 50^3 μm^3. As the microscope only features one column, time is lost in current change and tilt operations, which leads to longer acquisition times than those obtained with dual beam PFIB. Given this analyses and the experiments realized during this work, Figure 2.7, presenting the volumes and voxel size achievable by Slice and View techniques (and presented in section 2.4), has been updated. A new version is provided in Figure 4.16: results

of PFIB/PFIB imaging, implemented for the first time during this PhD, offer fields of view and voxel sizes placed between the ones offered by FIB-based SAV and by dual beam PFIB procedures.

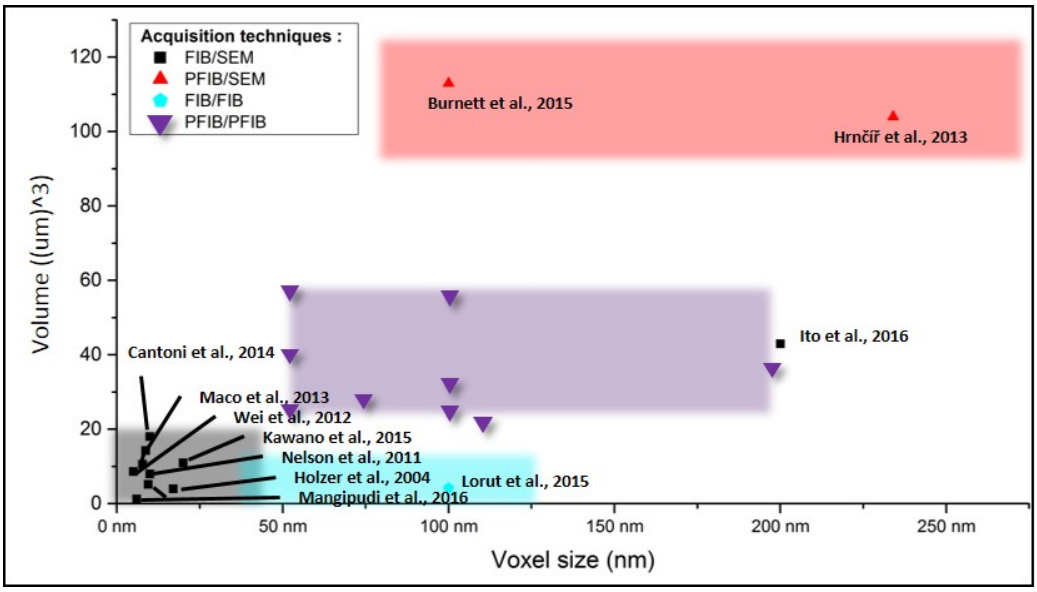

Figure 4.16: Updated version of Figure 2.7, presenting the achievable volumes and voxel sizes using different Slice and View techniques: FIB/SEM (in black), FIB/FIB (in light blue), PFIB/SEM (in red), and PFIB/PFIB (in purple and acquired in the frame of this PhD).

It is worth mentioning that the setup presented here offers voxel sizes (50 nm) and fields of view (50 μm) which are not only compatible with the 3D integration requirements, but also similar to the ones obtained on the ID16A beamline of the ESRF. The techniques are of course very different, and so are the obtained results. However, a comparison between those techniques remains interesting and is made possible by those similarities.

Développement d'une technique d'imagerie 3D dans un PFIB
Résumé du chapitre

Dans ce chapitre, nous présentons le développement d'une technique d'imagerie 3D destructive, implémentée au sein d'un PFIB à une seule colonne. Cette techniques est basée sur l'imagerie Slice and View, typiquement implémentée dans un FIB/SEM. Les difficultés liées à la présence d'une seule colonne et à l'automatisation de l'acquisition des données sont décrites une à une, et des solutions sont proposées. La procédure d'acquisition des données en résultant est décrite et justifiée. Le script de post-traitement écrit pour cette procédure, et les différentes étapes le constituant, sont ensuite décrits.

Les résultats obtenus grâce à cette technique, tant au niveau de l'implémentation elle-même que des matériaux imagés, sont ensuite fournis. L'acquisition des données est un procédé aujourd'hui stable, qui peut tourner plusieurs dizaines d'heures sans intervention humaine. Le post-traitement permet d'obtenir automatiquement (pour la plupart des échantillons) un volume aligné et reconstruit. Il fournit de plus une mesure du pas effectif de découpe. Les matériaux testés incluent des piliers de cuivre, des empilements à plusieurs niveaux de cuivre et de silicium, et des céramiques poreuses.

Enfin, les limites et possibles améliorations de la technique sont discutées. Les limites portent principalement sur le temps d'acquisition des données, aujourd'hui assez long. Des solutions sont proposées, telles que l'utilisation d'un microscope comportant deux colonnes, et l'optimisation des paramètres du microscope utilisé, comme le mouvement de l'échantillon. Une discussion plus large sur les problèmes rencontrés par les procédures Slice and View est menée. Elle porte notamment sur l'imagerie des matériaux poreux, toujours difficile.

Les possibilités d'imagerie du PFIB/PFIB sont enfin mises en relations avec celles d'autres implémentations similaires, telles que le FIB/SEM, le FIB/FIB, et le PFIB/SEM. Cette étude est basée sur la littérature et les résultats obtenus au cours de ce travail. Le PFIB/PFIB permet comme espéré d'augmenter les volumes imagés, par rapport au FIB/SEM ou au FIB/FIB. Il est bien sûr, en contrepartie, limité par sa résolution. Comparé au PFIB/SEM, il est moins rapide, donc les volumes atteints sont moins importants. La taille de pixels qu'il propose (30 nm) en imagerie 2D est cependant assez compatible avec son pas de découpe (50 nm), ce qui en fait une technique essentiellement 3D.

Chapter 5

Contribution to the ID16A workflow for 3D integration

Contents

5.1 Original ID16A workflow 112
5.2 New sample preparation scheme 114
5.2.1 New sample supports 115
5.2.2 Making the most of the sample preparation and installation . 115
5.3 Reduction of the number of projections 123
5.4 Automation of the post-processing 126
5.5 Time gain and discussion 128
5.6 Application to 3D integration imaging 130
5.6.1 Imaging of a large number of post-electromigration samples . 130
5.6.2 Morphology study on copper pillars 133
5.6.3 Towards a larger field of view 137
5.7 Conclusion 139

As explained in section 3.2.1, the ID16A beamline of the ESRF is a recent beamline, built during the first phase of the ESRF upgrade. It is meant for sub-50nm resolution 3D imaging, and is the first hard x-ray nano-tomography beamline. As of today, it offers the possibility to perform holo-tomography, fluorescence tomography, and ptychography, on samples ranging from biology to microelectronics.

In this chapter, we mainly focus on the holo-tomography technique, and more particularly on strategies allowing to increase the sample throughput on this beamline, in order to perform statistical studies for the industry. To do so, a first section will be dedicated to the original analysis workflow on ID16A, going from the sample preparation to the data acquisition and the data processing. The three next sections describe solutions to reduce the overall time of the whole procedure, using a new sample preparation scheme, the reduction of the number of projections, and the automation of the post-processing, respectively. The new workflow thus obtained is also discussed. Finally, a section presents those results in the larger context of 3D integration characterization, by placing them next to results obtained on other well-established 3D imaging techniques, such as the FIB/SEM or the ID19 beamline of the ESRF (presented in section 3.2.2).

Sample-based examples are given throughout the chapter, in order to illustrate the different steps of the procedure and the obtained results. Unless specified oth-

erwise, those images were acquired in the frame of this PhD thesis[1].

5.1 Original ID16A workflow

The complete workflow of an experiment on ID16A goes from the original sample in the form of a wafer to the final reconstructed volume. As one can expect, it forms into many steps. In this section, the main ones are presented, from a user point of view, together with the time they require.

Sample preparation As explained in section 3.3.3, the ID16A is quite demanding in terms of sample dimensions, as they should be below 50 μm in width to fit the field of view (for a pixel size of 25 nm). The original workflow to do this, in the case of microelectronics samples, is to prepare the sample inside a PFIB and place it on top of an aluminum pin, using the lift-out procedure described in section 2.4.2. The aluminum pin is then placed inside a brass cylinder (a Huber pin), that can be introduced inside a holder which is specific to the beamline.

The sample preparation step requires about one hour of milling, which is performed without human intervention, after a user-performed setting that takes about half an hour. The extraction of the sample requires about half an hour as well. Placing the aluminum pin inside the Huber pin takes about five minutes.

Data acquisition Once the sample is mounted on the holder, it is placed under vacuum, in a sample changer. An automatic arm gets it and puts it inside the beam. The stage is then moved, for the sample to be inside the field of view during the rotation. After the data acquisition, the sample is replaced outside of the beam, in the sample changer, and the next one can be fetched.

The time between the end of one acquisition and the begining of the next one is counted by adding the time to retrieve the first sample, place it back inside the sample changer, to fetch the second one, place it in the beam, and to align the stage. It is estimated to about one hour.

Data acquisition relies on the acquisition of reference images (dark images, with no beam, and reference images, with no sample in the field of view) and radiographs for a number N_{proj} of angles, for four different focus-to-sample distances. Here, each radiograph will be designated by the couple (d_{rad}, n_{rad}), with $d_{rad} < 4$, and $n_{rad} < N_{proj}$. Typically, $N_{proj} = 2000$, for an exposure time of 0.5 seconds. This leads to an acquisition time of four hours per tomography, including the time of stage stabilization and camera read-out.

Post-processing The post-processing of the data is made of several steps, each one set and triggered by the user:

[1] The changes brought to the ID16A workflow described in this chapter have been the object of two contributions to the ISTFA conference, in 2016 and 2017 [113].

1. For each angle n_{proj}, the corresponding radiographs (d_{rad}, $n_{rad} = n_{proj}$) must be aligned together. First, they are resampled, for the sample to measure the same size on all of them. This resampling is made knowing four focus-to-sample distances, and therefore the magnification applied to the sample. The actual registration can be made in real space or Fourier space. It is usually made every 100 angles, and the movements of the radiographs are fitted for the remaining angles. This procedure requires about 30 minutes for 2000 angles. This step must be triggered by the user, but is quite transparent to them: the user only chooses the registration method and checks manually if the radiographs are well-aligned. For some samples, different registration methods can be applied successively for better precision.

2. Once the projections are registered, the phase can be retrieved for each angle. Each projection obtained then is characterized by the number n_{proj} (n < N_{proj}). Several phase retrieval algorithms are available, among which the CTF (Contrast Transfert Function), the TIE (Transport of intensity equation), and a mixed approach between them (see section 3.3.1.2 for a description of those algorithms). In the case of 3D integration samples, the CTF method was the most often applied. This procedure requires about 8 hours for 2000 acquired angles.

3. After the phase retrieval, the rotation axis is manually calculated. To do so, the first projection of the data set is registered with the last one, flipped horizontally. The shift found this way is noted s. The rotation axis is then provided by the formula: $RotationAxis = 1024 - \frac{s}{2}$. Usually, the user reconstructs one slice of the sample with a range of rotation axis around this value, and compares the results visually, in order to select the better suited rotation axis. This requires about 20 minutes of human intervention.

4. Finally, the volume can be reconstructed, using the FBP (Filtered Back Projection) algorithm. This requires less than one hour, in the case of 2000 projections, each one measuring 2048 x 2048 $pixels^2$. The obtained volume is a 2048 $pixels$ wide cube.

Figure 5.1 summarizes and illustrates all the steps depicted in this section, together with their time contribution during the workflow. Those times are given based on the experience acquired along this work. Of course, computation times depend widely on the considered machine. In the case of experiments performed on the ID16A beamline, phase retrieval and reconstruction steps are performed on ESRF clusters, managed by the OAR batch scheduler [114]. The global computation time can of course vary, depending on the availability of the machines and their performances, and the given values are mean ones.

It is worth mentioning that although the overall time from wafer to volume is important, the reduction of some steps is more relevant than others. In fact, in the frame of this work, the focus was set on limiting mainly the beam time and the

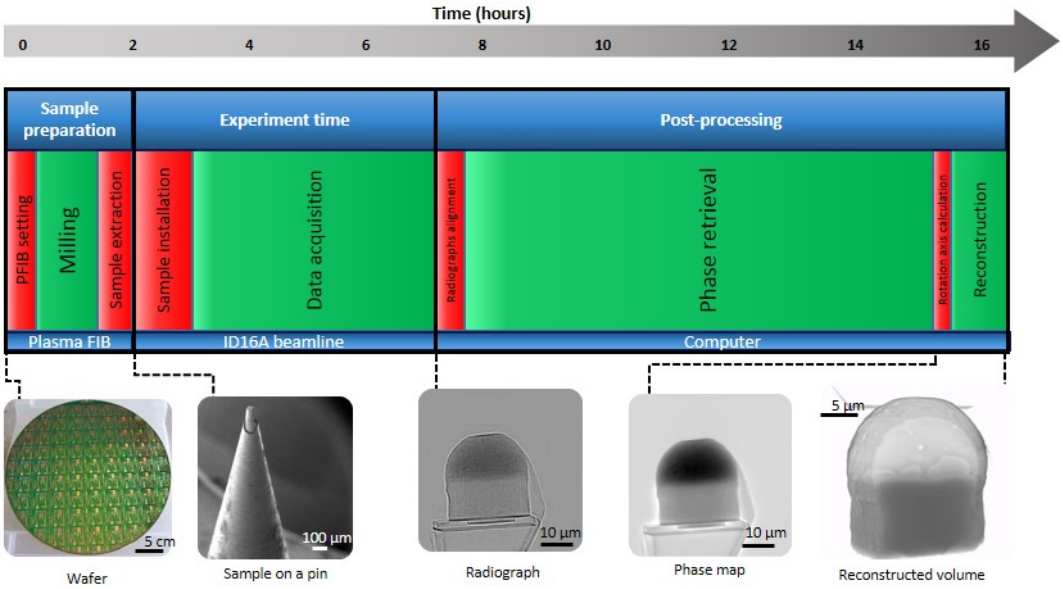

Figure 5.1: The ID16A workflow and the time needed for each step, in the case of a data acquisition of 2000 projections.

human intervention time. To limit the beam time, two strategies are possible. The first one would be to decrease drastically the acquisition time per projection. This is done on several beamlines, and can even lead to ultra-fast acquisitions and possibly to in-situ measures [115]. However, this decrease in time comes at the cost of the resolution. Here, the goal is to maintain the resolution, and make the most out of the beam time. To do so, the applied strategy is to automate as much as possible the workflow. For clarity purposes, the human intervention time is represented in red in the figure, while long enough (one hour and more) automatic procedures appear in green. Given the previous goals, three strategies have been set in place and tested on the ID16A beamline, as will be presented in the next sections. As the high resolution reached by the ID16A beamline is quite demanding, little change has been brought to the technique itself, and the main focus was to limit the time of the surrounding actions without decreasing the resolution of the final reconstructions.

5.2 New sample preparation scheme

As can be seen in Figure 5.1, the sample preparation and installation require quite some time, and are mainly made manually. A first approach therefore focuses on those two steps.

5.2.1 New sample supports

As mentioned in the workflow presentation, after the sample preparation, the aluminum pin has to be placed into a Huber pin and glued to it, as illustrated in Figure 5.2a. More importantly than the time taken by this step, the issue is that there is a risk to damage the sample while doing this. To avoid this step, new sample supports were therefore designed. The new sample supports feature the exterior aspect of Huber pins, in order to fit the ID16A beamline. Instead of being hollow however, they feature a pin on which the sample can be placed, as shown in Figure 5.2b. This allows for a small gain in time, and more importantly decreases the risk to lose the sample during the sample preparation. Those samples support have been successfully tested on the ID16A beamline.

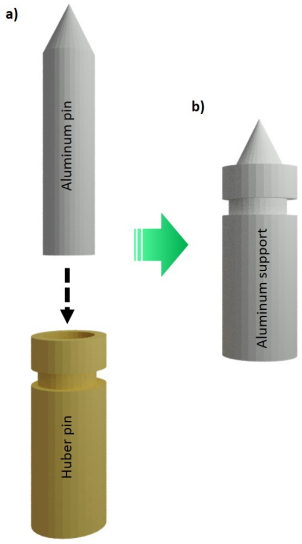

Figure 5.2: Sample support designs for the ID16A beamline. a) An aluminum pin on which the sample is mounted, which has to be placed inside a Huber pin. b) A new design of sample support, already featuring the external dimensions of the Huber pin.

5.2.2 Making the most of the sample preparation and installation

In order to automate the installation of the sample inside the beam, several beamlines have been equipped with robots which automatically change the sample. This is the case of the BM05 and ID19 beamlines at the ESRF. This solution is however expensive, and introduces an additional risk of failure. At ID16A, an articulated arm allows for the change of sample without opening the experimental bowl placed under vacuum. This action however still requires a human action. The strategy developed here is to limit the number of times this manipulation has to be done during an experiment. It is therefore to make the most out of every sample installation, by putting a large number of samples on every support. Successive tomography can

be launched by a macro on the ID16A beamline, and the stage allows a vertical movement (Z direction) of 5 mm, which makes the imaging of many successive samples possible. To do so, different sample preparation methods have been developed, depending on the type of sample to be imaged.

For tomography experiments, copper pillars are usually isolated and mounted on an aluminum pin using a FIB. The final configuration is shown in Figure 5.3a. In the case of copper pillars statistical analysis, the chosen strategy is here to saw a 100 μm large support out of the wafer supporting the copper pillars. Such a configuration is presented in Figure 5.3b. Once in the beam, the copper pillars are imaged one after the other, with only an automatic shift in the Z direction between the tomography acquisitions.

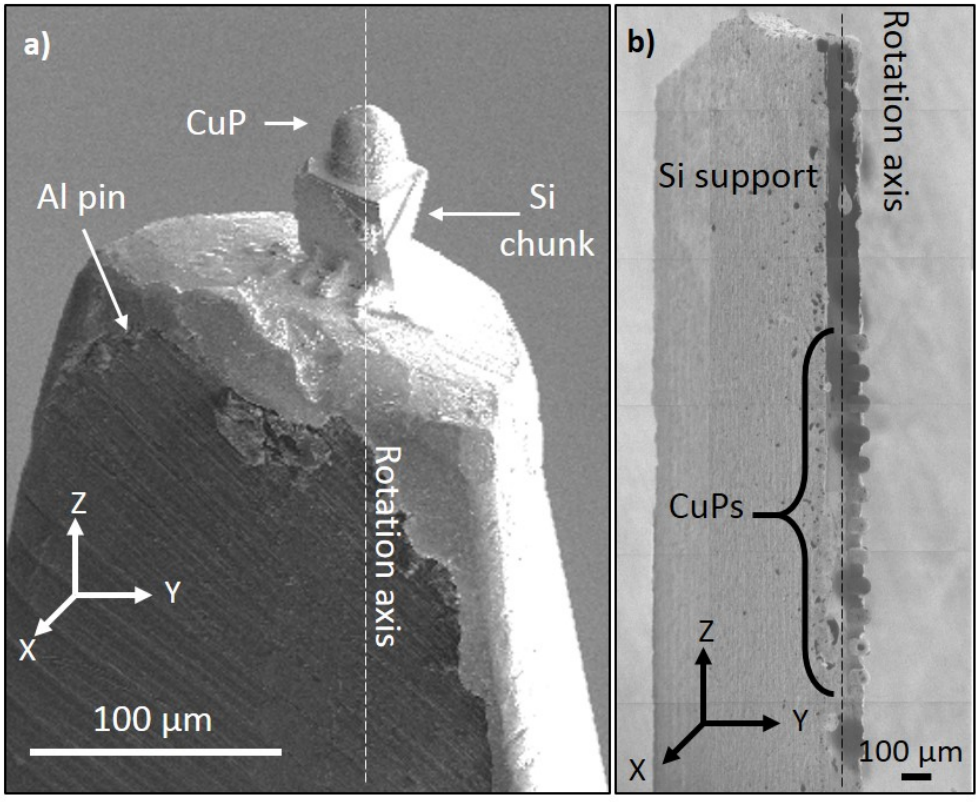

Figure 5.3: Two sample organizations for copper pillars. a) A copper pillar placed on an Al pin. b) 12 copper pillars placed on a sawn silicon lamella.

A comparison between the imaging of a copper pillar placed on a pin and on a multi-sample support has been performed on 25 μm wide copper pillars, fabricated with the same process. Results are shown in Figures 5.4a, b, and c (resp. d, e, and f) for a copper pillar placed on a pin (resp. on a sawn support). For each, an XY slice reconstructed by the algorithm is shown (Figures 5.4a and 5.4d, respectively), together with a XZ orthogonal view (Figures 5.4b and 5.4e, respectively). Figures

5.4c and 5.4f are zoom-in views of the interface between the copper cylinder and the bump.

As shown on this figure, the main features to spot can easily be identified in both samples. Attention can be brought here on the zoom-in views, and the voids appearing on them. In Figure 5.4c, voids appear a little star-shaped. Those are movement artifacts and make the further segmentation of the voids difficult. On Figure 5.4 however, voids appear perfectly round. This can be explained by the orientation of the projections and thus the reconstruction: the star-shaped artifacts are born by the originally reconstructed slices, those being orthogonal to the beam during the experiment: for a copper pillar placed on a pin, the artifacts will therefore appear on slices of interest (the interface), whereas for a copper pillar on a silicon support, they will be present on one of the orthogonal views (namely Figure 5.4d). By placing the copper pillar samples of a vertical support, more than one hour per sample is saved during preparation, as the silicon support is only sawn, and about 1 hour per sample in installation, as this procedure is done once for all samples. Furthermore, no loss in resolution is noticeable by doing so, and even an improvement can be seen in the slices of much interest.

For samples which are ROIs taken from a wafer, two samples preparation schemes, adapted from the classic lift-out procedure, have been developed. In the case of stacks presenting different regions of interest situated next to one another, it is possible to adapt the previously shown technique and to prepare large samples (100 μm large for example), which contain several ROIs. The goal here is twofold. First, a large sample allows to obtain a large field of view image of the ROI, at a lower but still below 100 nm resolution. A more resolved acquisition of the same area can also be obtained using local tomography, which focuses on one area of the sample.

To test this sample preparation, a parallelepiped-shaped sample was extracted and placed on a pin, using a lift-out technique close to the one used for cylindrical samples. The steps of the sample preparation are illustrated in Figure 5.5 in the case of a hybrid bonding sample, in which the interface between copper pads was to be observed.

The two sample preparation schemes described so far can save time during the sample preparation and installation. However, they only apply to the imaging of regions of interest (here, the copper pillars) situated next to one another on the original wafer. For ROI situated far way from one another, a second method has been developed. A sample support is first prepared, by applying an annular milling to the top of an aluminum pin, using the PFIB. A cylinder of several hundred of micrometers, such as the one illustrated in Figure 5.6a, is obtained in about half an hour. The sample is isolated and extracted exactly as previously. The deposition of the sample on the support is quite similar, although the sample is not mounted on the top of the support, but rather on its side, as shown in Figures 5.6a, b, and c. This procedure can be repeated with other samples, as illustrated in Figure 5.6d, which features a support where 12 samples, extracted from different dies, have been mounted. Similarly to copper pillars, successive tomographies are performed on the samples.

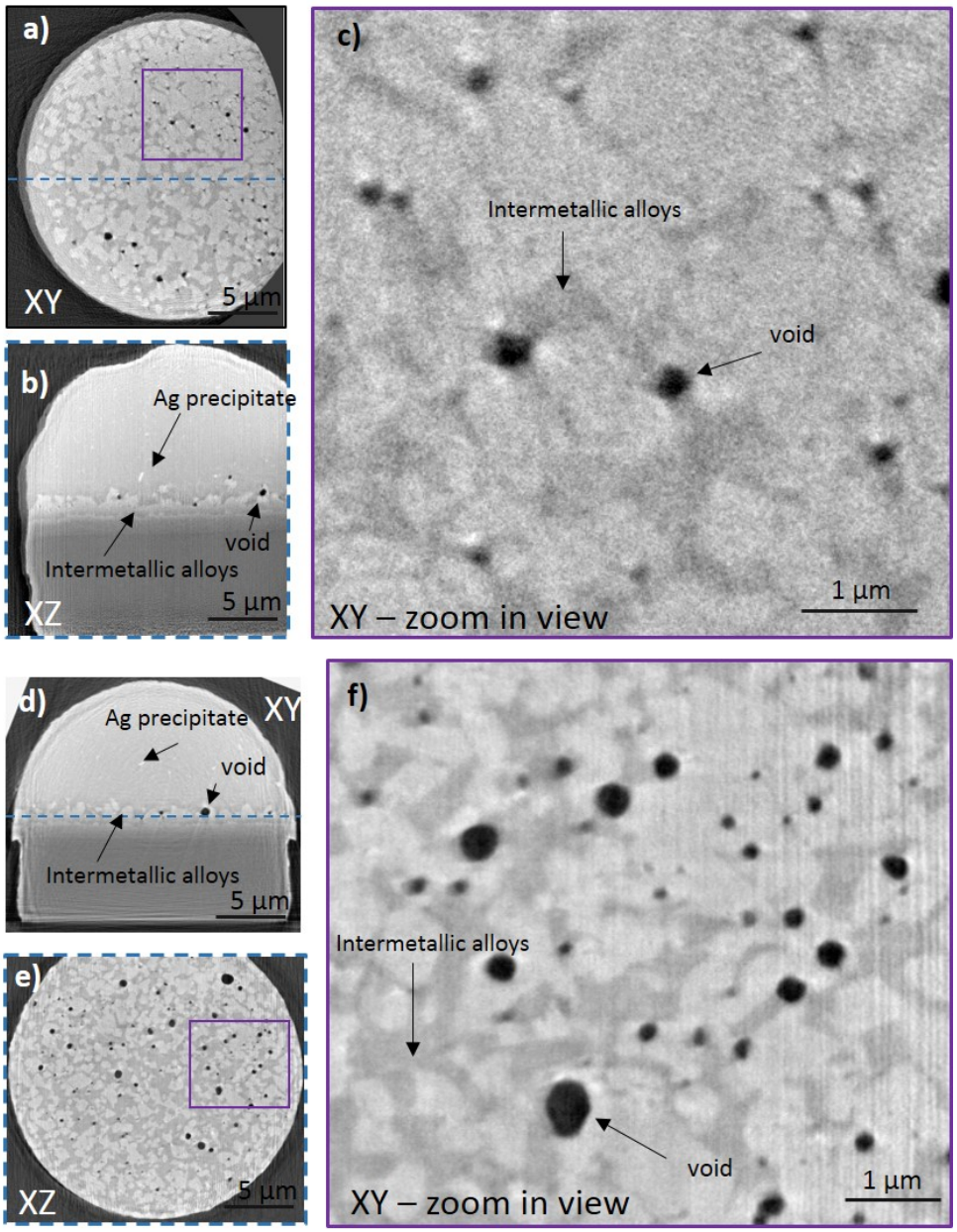

Figure 5.4: Comparison of the results obtained when imaging copper pillars placed alone on an Al pin (a, b, and c) or on a multi-sample Si support (d, e, and f). a) Originally XY reconstructed slice of the pillar, presenting the interface between the bump and the cylinder; b) Orthogonal XZ view of the pillar; c) Zoom-in view of figure a. d) Originally XY reconstructed slice of the pillar, presenting the whole copper pillar; e) Orthogonal XZ view of the pillar, containing the interface; f) Zoom-in view of figure e.

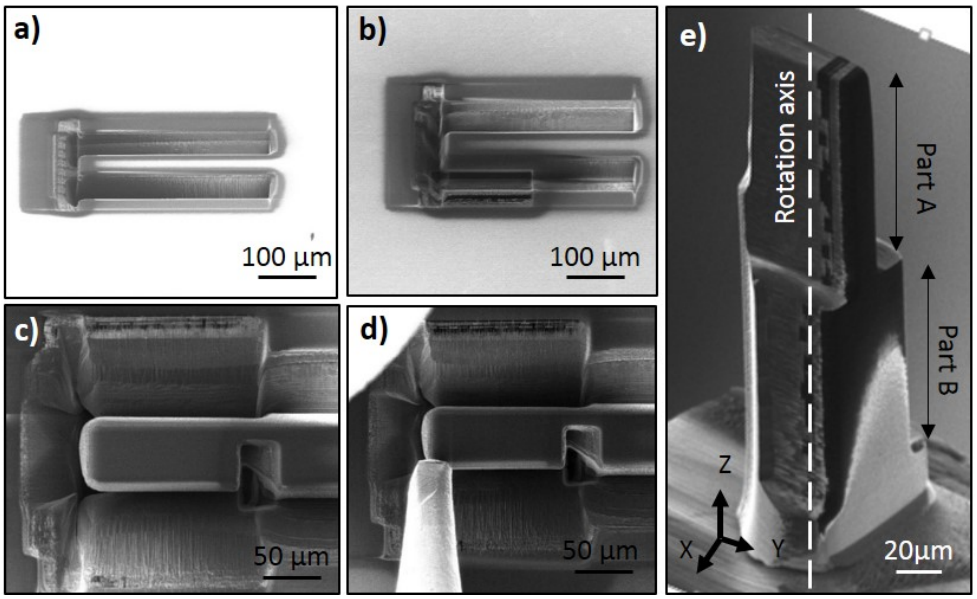

Figure 5.5: Sample preparation allowing for a large sample, containing several regions of interest or meant for large field of view imaging. a) The region around the ROI is milled. b) An area under the ROI is milled. c) The part of the wafer supporting the ROI is partly-milled. d) A micromanipulator is soldered to the ROI. The remaining wafer part supporting the ROI is then milled, and the micromanipulator brings the ROI to an aluminum pin. The ROI is then soldered to the Al pin, and the solder join with the micromanipulator is removed. e) The sample thus obtained.

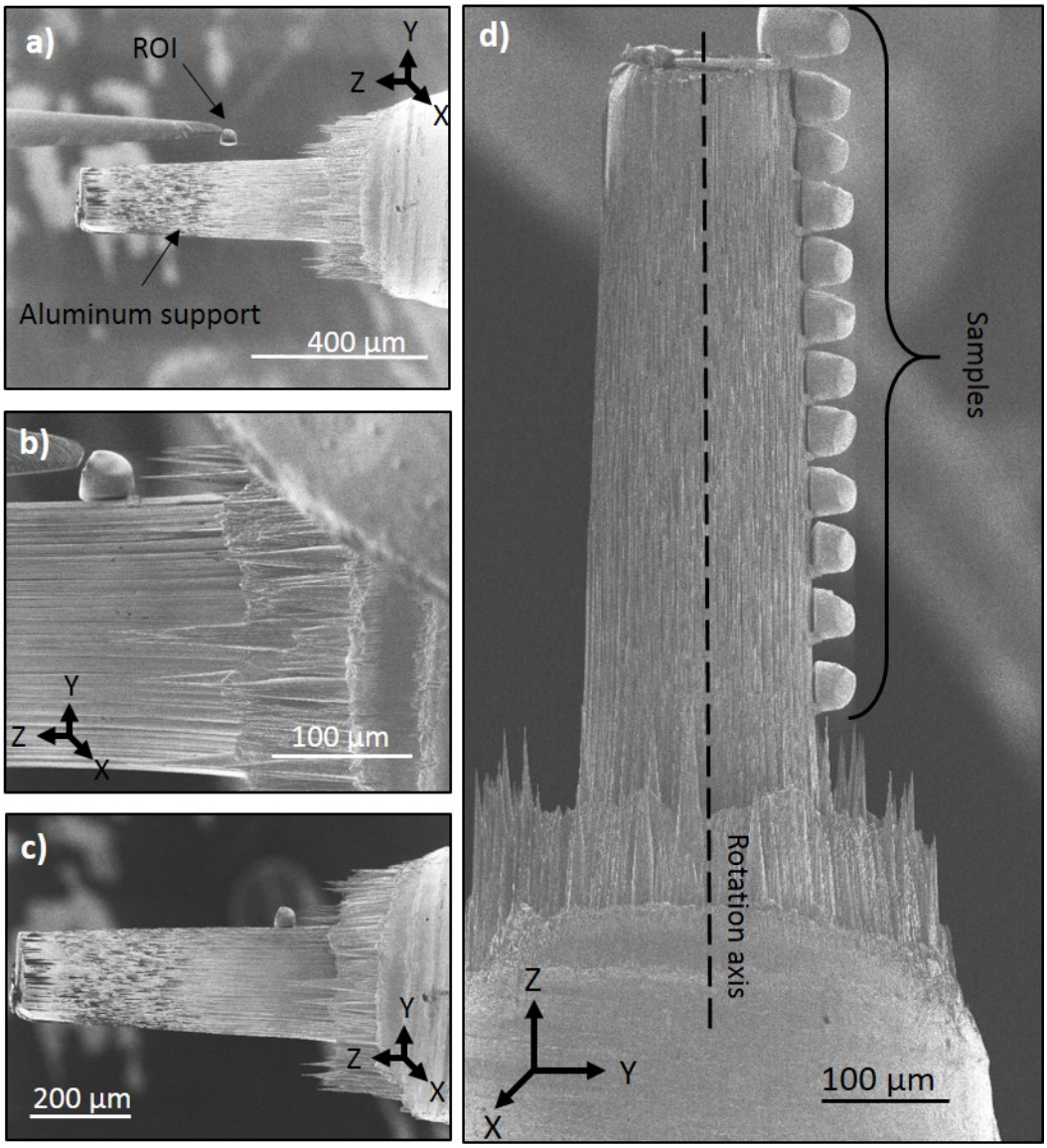

Figure 5.6: Sample preparation scheme, aiming at placing several samples on one single support. The support is an aluminum pin, milled in order to have a cylindrical shape, several hundred of μm wide. The ROI is isolated and soldered to a micromanipulator, as in a classic lift-out technique. a) The ROI approaches the support. b) The ROI is placed on the support and a solder join is deposited between them. The micromanipulator is removed. c) The sample remains on the support. d) The final sample support, after this procedure (a, b, c) has been performed for several (here, 12) samples.

Those PFIB-based samples preparation methods have been tested on hybrid bonding samples. The goal was to compare the techniques, when it comes to imaging the voids at the interface between the copper pads. To do so, a first large sample, illustrated in Figure 5.5e, has been prepared in the PFIB. In this sample, the upper region has been thinned down to 20 μm, in order to image the pads non locally. This upper region is later called Part A, and is the reference region for further imaging. Part B, on the contrary, measures 50 μm in width and is intended both for large field of view and local imaging. Part A, defined in Figure 5.5, has been imaged with a pixel size of 10 nm. Part B has been imaged locally, at a pixel size of 10 nm, and non-locally, at a pixel size of 25 nm. Another sample was also prepared and placed on a support, following the PFIB-based multi-sample support scheme presented previously. In this example, the support was made of a 100 μm wide and 750 μm thick sawn silicon lamella, and the acquisition was made with a pixel size of 25 nm. All acquisitions were made at an energy of 33.6 keV and 2000 projections.

Results of the PFIB-based samples preparation schemes presented here are provided in Figure 5.7, in which a specific slice containing the interface between copper pads is shown. Figure 5.7a is the reference image, acquired with a small pixel size (10 nm) without local tomography. As can be seen in the corresponding zoom-in view (Figure Figure 5.7e), the morphology of the pads, together with some voids, can be observed. In the local tomography reconstructed slice (see Figures Figure 5.7b and Figure 5.7f), the same features can be observed, without any obvious artifact due to the locally-acquired data. In the large field of view slice (see Figures Figure 5.7c and Figure 5.7g), more pads are visible, and their morphology can be assessed. However, the pixel size is too big to spot all the voids spotted using local tomography (as the pads presented in Figures Figure 5.7f and Figure 5.7g are the same, this comparison is straightforward). Finally, the slice obtained from the sample placed on a Si support features clearly visible voids. This technique is therefore shown to provide good results. On all the reconstructions, it is visible that the voids present at the interface between copper pads remain below 50 nm in width. They are still in the acceptance range, from a process point fo view.

As shown in this section, placing several samples on one support allows for an obvious gain in time in the ID16A-based analysis, both during sample preparation and installation. It has also been shown to provide good quality reconstruction, by comparison with samples placed on individual pins. A variety of sample preparation methods has been thought of and are illustrated here. Among these techniques, placing several ROI on a support using a PFIB is the more versatile method, as it does not require regions of interest placed close to one another. It has therefore been used extensively during this PhD, mainly for statistical studies (see section 5.6.1). In the next sections, only this method will be considered when discussing the gain in time of the sample preparation. One must however bear in mind the other methods exist and have been proven efficient. They can be more relevant for other samples, with regions of interest situated next to one another.

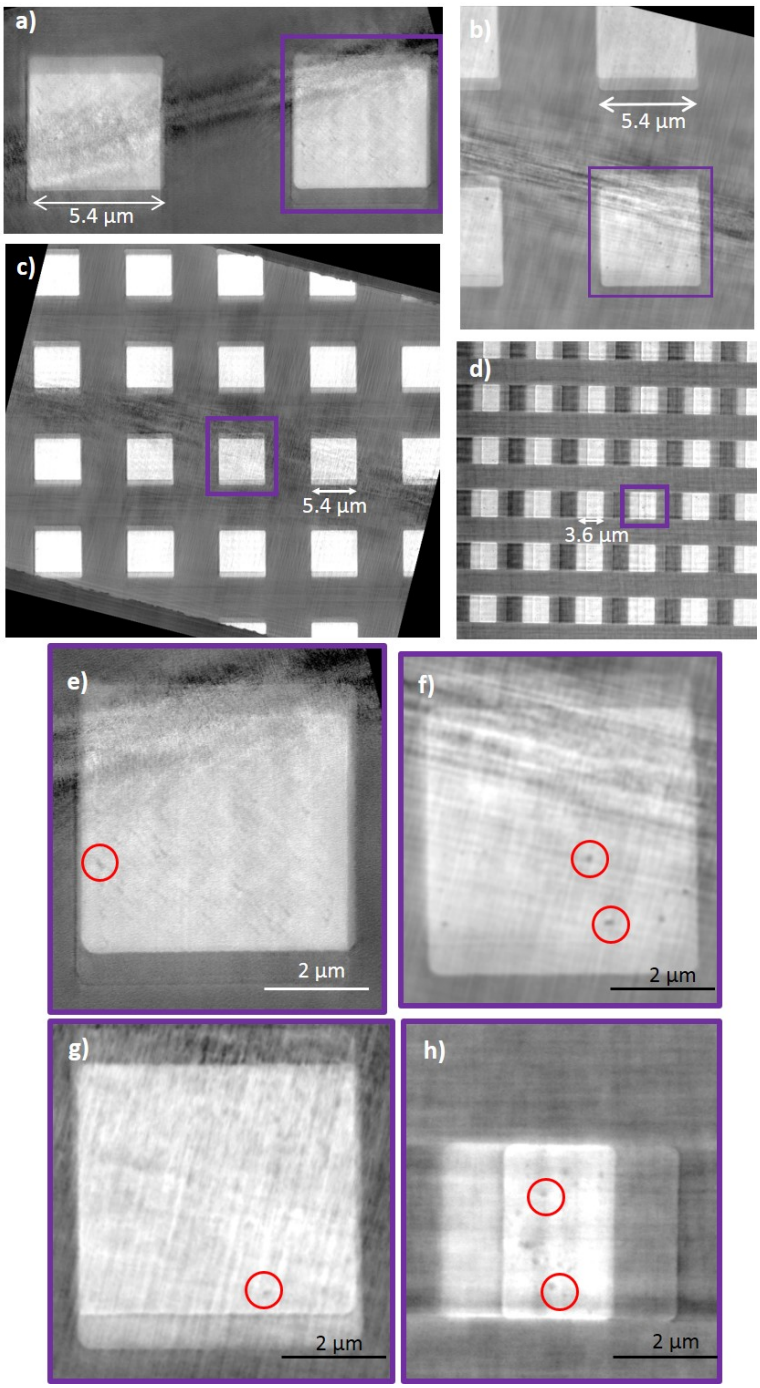

Figure 5.7: Slices at the interface between the dies, obtained with different experimental organizations: a) 20 μm wide sample (part A), pixel size 10 nm, no local tomography (reference image); b) 50 μm wide sample (part B), pixel size 10 nm, local tomography; c) 50 μm large sample (part B), pixel size 25 nm, non-local tomography; d) sample placed on a silicon support, pixel size 25 nm. e),f), g), and h) are zoom-in views of one pad taken respectively from a), b), c), and d), rescaled to make a comparison possible. Voids are circled in red. It should be noted that f) and g) feature the very same pad.

5.3 Reduction of the number of projections

As explained in section 3.3.2.2, the Filtered Back Projection algorithm offers a mathematically exact reconstruction of the imaged object, provided a large number of projections. In our case, 1500 to 2000 projections were typically acquired for every distance on the ID16A beamline. The acquisition of those projections requires several (typically 4) hours. Here, we tried to reduce the number of acquired projections by using iterative reconstruction algorithms [2].

We here tested a number of iterative algorithms on x-ray projections and compared the results to FBP reconstructions. All reconstructions were performed using the Astra toolbox [107]. The study was performed on a slice of a copper pillar, placed on a vertical support such as the one presented previously, with other pillars. A reference reconstruction was made with 2000 projections, using FBP, and all other reconstructions were made from the same set of data. This reference image is shown in Figure 5.8a.

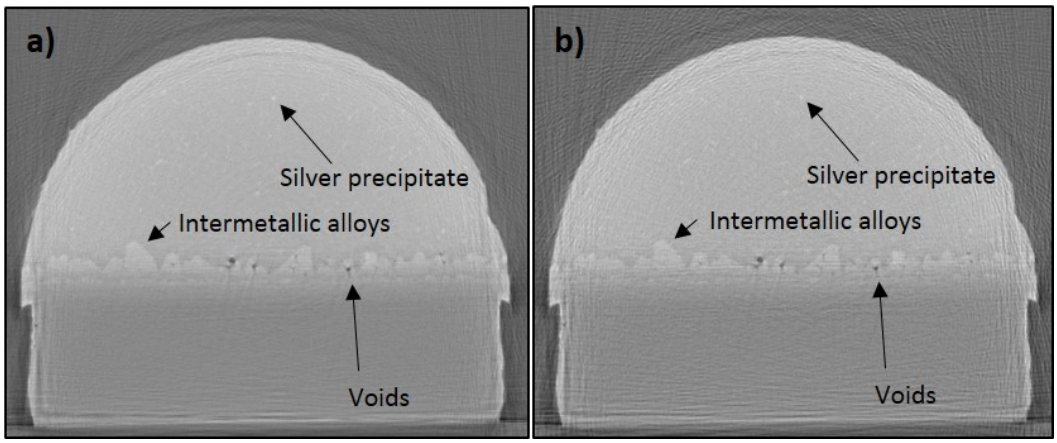

Figure 5.8: Reconstructions of the same copper pillar slice using two different reconstruction algorithms. a) FBP using 2000 projections. b) CG-LS using 500 projections (and 23 iterations). The SSIM value raised by the comparison of those two images is 0.81.

The image quality was assessed by a figure of merit (FoM). Here, the SSIM (Structural SIMilarity) function [117] was used. The main advantage of this function is that the comparison is not local, but concerns general features of the image. As our goal is to distinguish objects in the image, this is of high value. The general expression of the function, for a comparison of two images A and B, is given in equation 5.1.

[2] This work has been made in the frame of an internship realized by Pierre-Olivier Autran [116].

$$SSIM(A,B) = \frac{2\mu_A\mu_B+C_1}{\mu_A^2+\mu_B^2+C_1} \cdot \frac{2\sigma_A\sigma_B+C_2}{\sigma_A^2+\sigma_B^2+C_2} \cdot \frac{\sigma_{AB}+C_3}{\sigma_A^2+\sigma_B^2+C_3} \quad (5.1)$$

$$= l(A,B) \cdot c(A,B) \cdot s(A,B) \quad (5.2)$$

where μ_A (resp. μ_B) is the average value of image A (resp.B), σ_A^2 (resp. σ_B^2) its variance, and σ_{AB} the covariance of A and B. C_1, C_2, and C_3 are constants. The three fractions refer to different characteristics of the images: $l(A,B)$, the luminance, $c(A,B)$, the contrast, and $s(A,B)$, the structure of the images. The parameters of the function (namely, C_1, C_2, and C_3) have been tuned in order to fit the requirements of the copper pillar slices comparison. A comparison of two identical images raises the value 1, and the function is little impacted by a change in overall luminance. A change in contrast, on the contrary, decreases the function drastically. The final function raises values between -1 and 1, -1 being raised when comparing an image with a totally blurred version of itself. All comparisons were then made with the same SSIM parameters, between the reference image (FBP, 2000 projections) and the assessed image.

Figure 5.9a shows SSIM values for FBP reconstructions regarding the number of projections used, together with a ROI of the obtained slices. As can be seen, the SSIM value drops quite fast when the number of projections decreases. For example, the SSIM value for 500 projections is 0.45. As a comparison, figures 5.9b, c, and d present the SSIM values obtained with the SART, SIRT, and CG-LS algorithms, respectively, for various numbers of projections and iterations. As expected, the values for 2000 projections are close to 1, while still remaining below it: iterative algorithms do not rise exactly the same results as FBP. However, the values decrease more slowly than with FBP reconstructions: they all remain above 0.7, even for 250 projections. A ROI of the copper pillar slice is presented for each reconstruction performed, for visual comparison.

As an illustration, Figure 5.8 shows two different reconstructions of the same slice of a copper pillar. The reconstruction 5.8a was performed using the FBP algorithm and 2000 projections (reference image), while the slice 5.8b was reconstructed from only 500 projections, using the iterative algorithm CG-LS. The SSIM value obtained when comparing those images is 0.81. Visually, one can retrieve the same features from the two images: intermetallic alloys are clearly visible, and voids and Ag precipitates can also be spotted. The use of an iterative reconstruction algorithms therefore allows to reduce the number of projections by a factor 4 with little loss of image quality, according to the SSIM figure of merit. The data acquisition time is therefore divided by the same factor, going from four hours of data acquisition to only one.

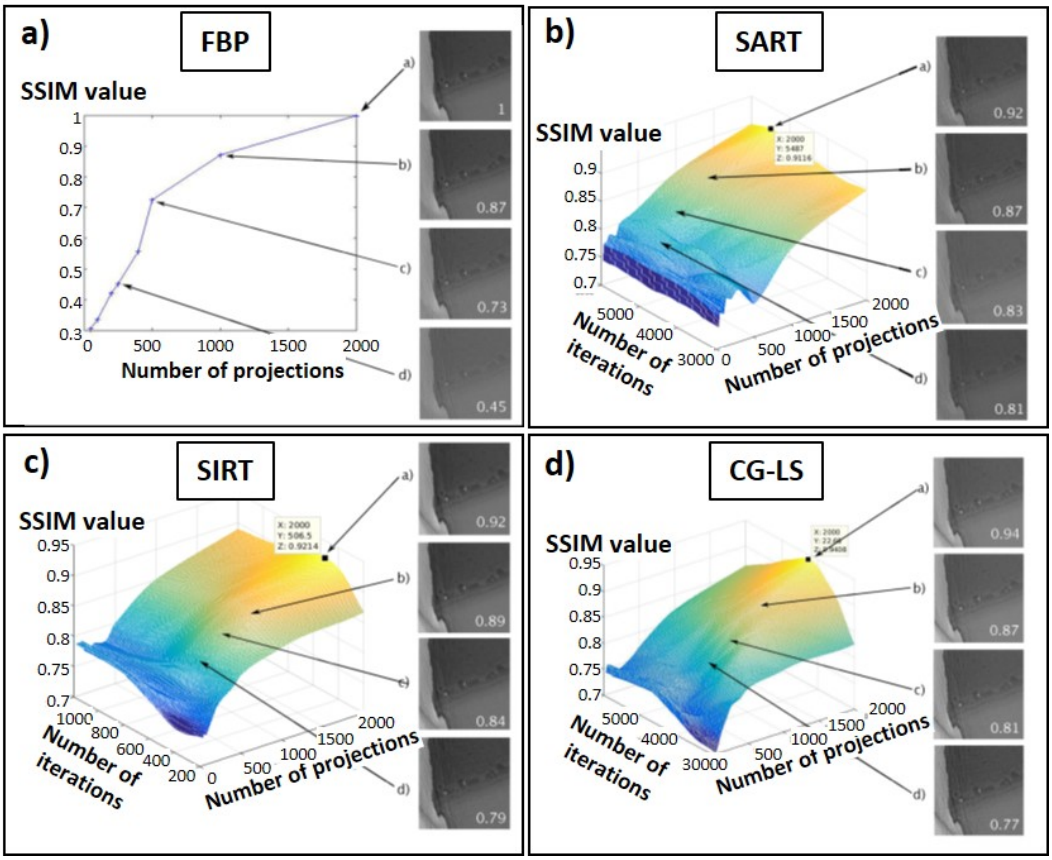

Figure 5.9: SSIM values for different reconstruction algorithms, when comparing the obtained slice with a reference one, obtained when reconstructing the slice with 2000 projections, using an FBP algorithm. a) SSIM values obtained for FBP, regarding the number of projections; SSIM values obtained regarding the number of projections and the number of iterations, for b) SART; c) SIRT; d) CG-LS.

5.4 Automation of the post-processing

In the original workflow, every step is manually set and triggered. When dealing with similar samples (typically copper pillars or silicon+copper stacks), the user often uses the same parameters. Therefore, it is possible to enter those parameters at the beginning of the post-processing, and let the computer trigger the processing steps one after the other.

Here we describe a Python wrapping made around the post-processing algorithms implemented on ID16A. It requires the information listed below:

- Location of the data set, name of the sample
- Number of projections
- Energy of the beam
- Focus-to-Sample distance
- Focus-to-Detector distance
- δ/β ratio for the considered material

As the process aims at being automatic, parameters have been chosen to be the more likely to provide good results. Therefore, the alignment step is made twice, as is usually done manually: the first alignment between radiographs is made in the Fourier domain, and the second one in real space. The rotation axis calculation is performed automatically, following the same principle as in the manual procedure: the first projection is registered with the last one, flipped horizontally, and the rotation axis is provided by the formula: $RotationAxis = 1024 - \frac{s}{2}$, s being the shift found between the two projections.
The script, described here for one sample, can process different data sets in parallel, each data set being processed by an independent thread, which allows for faster results.

The automatic reconstruction of volumes has been implemented and tested with the FBP algorithm. It has shown to be able to post-process a whole batch of samples (a maximum of 12 has been tried so far) without human intervention. The script also provides a report all-along the post-processing, which allows to follow the different steps of the procedure. Such a report, obtained for one sample (with 1500 projections), is shown in Figure 5.10. It also features statistics about the post-processing, by giving the time taken by each step of the procedure.

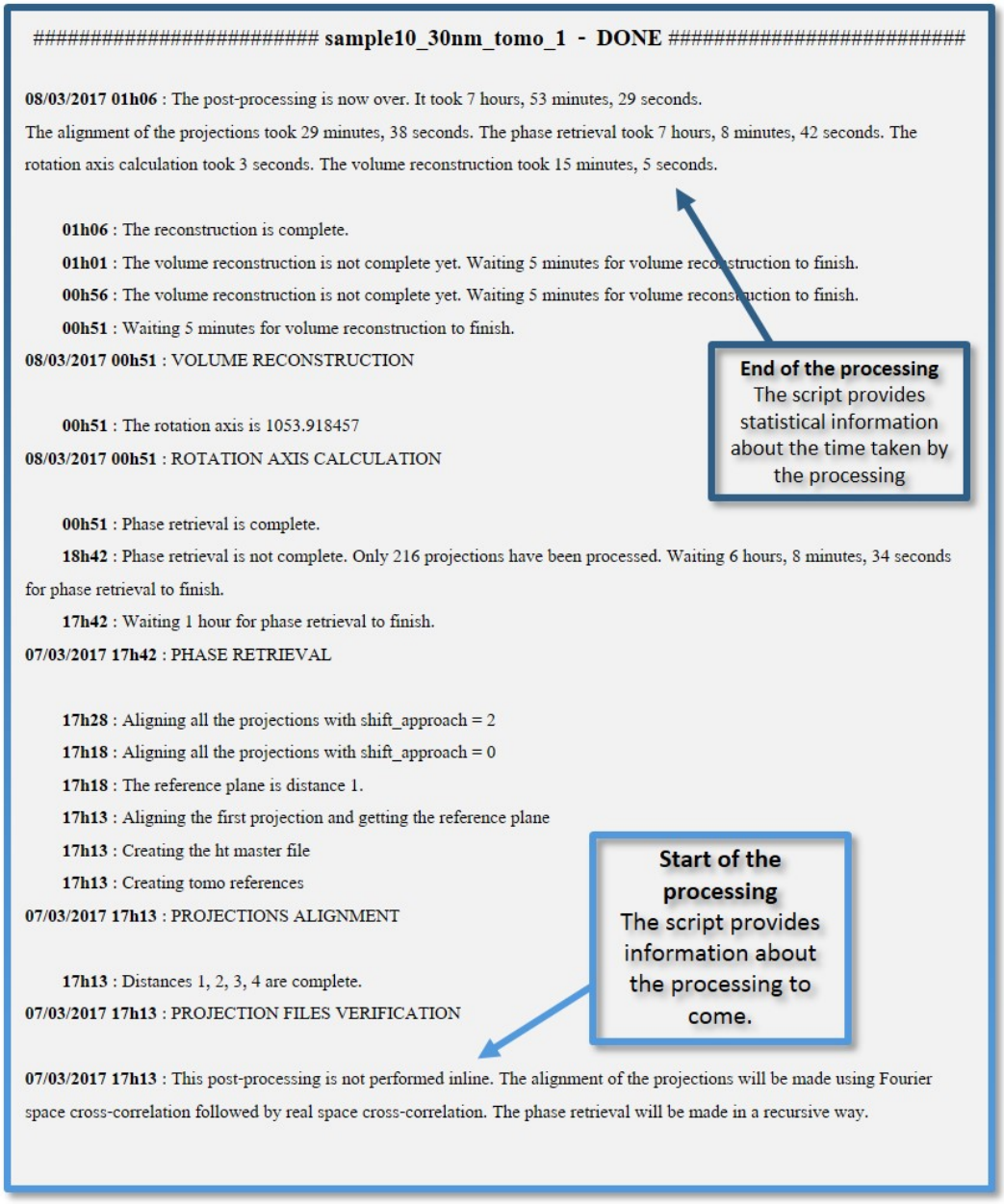

Figure 5.10: Report rendered by the automatic post-processing script during the procedure, obtained for one sample placed on an aluminum multi-sample support. It provides information on the different steps of the post-processing, together with a final assessment of the time they took.

5.5 Time gain and discussion

In the previous sections, different strategies have been set in place in order to reduce the overall time of the tomography setup on ID16A, with a focus on the reduction of human intervention and the beam time. They all have been shown to reduce the analysis time, with no or little loss in resolution. Here, we present an updated version on the ID16A workflow, taking into account those strategies. A discussion on their field of application and their limits is also proposed.

Figure 5.11 presents the updated workflow of ID16A, with the time required for each step. The new values have been calculated with the PFIB-based sample preparation scheme, and a data acquisition based on 500 projections. The figure also assumes an automatic post-processing. The values are given for one sample and calculated as the mean time per sample, assuming the sample is placed on a support containing 10 samples.

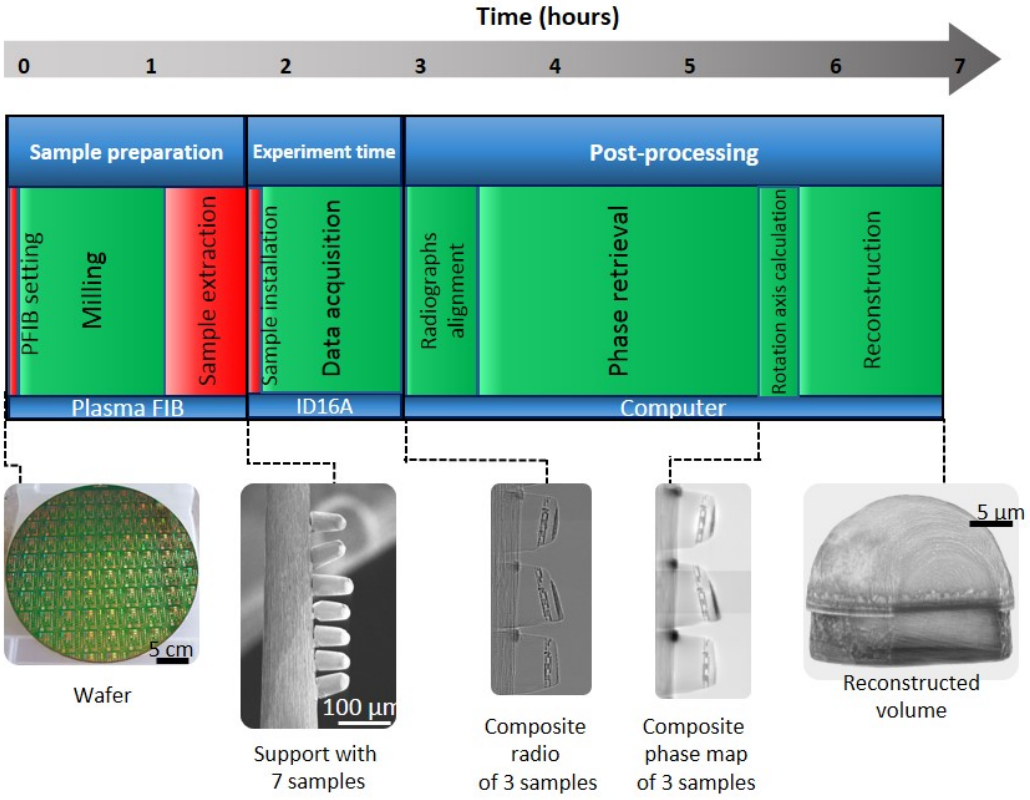

Figure 5.11: Updated version of the ID16A workflow, taking into account the methods aiming at increasing its throughput. The values are average ones, given for 1 sample, assuming it was placed on a support containing 10 samples in total.

It should be noted that the time scale is not the same as in the original figure (Figure 5.1), and the overall time presented is now about 7 hours instead of 16. This

is mainly due to the reduction of the number of projections, which reduces the data acquisition time from 4 hours to 1, together with the phase retrieval time, which passes from 8 hours to 2. Moreover, more steps are now automatic, as compared with the original figure: the whole post-processing therefore appears in green. The sample preparation time is reduced, since the PFIB setting can usually be made for a whole batch of sample. The same applies to the sample installation, which lasts an hour but can be done once for 10 samples. Combined together, these strategies therefore allow for a drastic reduction of the time, especially the one an operator has to spend on the experiment.

It should be reminded that this figure has been realized in specific conditions. Although we believe the methods presented here can apply to many samples and situations, they might not trigger as good results. First, the samples must be absorbing enough. In fact, although the support is made of a low-absorbing material such as silicon or aluminum, it is possible that for low-absorbing samples, the tomography will be considered local (since the support appears on some projections but not all), creating artifacts. In the case of microelectronics and more specifically of copper observation, this issue is not encountered.

When considering the diminution of the number of projections, a number of assumptions have been made. The reconstructions have been made from a data set of 2000 phase maps, from which a number of projections (250, 500, 1000, or 2000) have been used. This means that the original alignment between the four distances was performed using the 2000 x 4 radiograph data set. As the alignment relies on the actual alignment of every 100^{th} angle and a fitting, it is possible that the alignment would be poorer with only 500 projections acquired. However, this issue should be solved by increasing the number of projections the actual registration is based on.

Finally, the complete automatic post-processing has been proven to work so far only with the FBP reconstruction algorithm. It is however likely to work with any algorithm, since it is an independent step of the process. The time value given in fig 5.11 for the phase retrieval is 2 hours, since the number of slices is reduced by a factor 4 and so does the calculation time. The reconstruction time has been (over-)estimated to be 3 times the time needed for an FBP reconstruction, that is to say about one hour. A further investigation of the post-processing time, requiring the implementation of iterative reconstruction algorithms, would be a possible improvement of this study.

Other improvements of the automatic post-processing could be implemented. Since several parameters (such as the positions, energy, and number of projections) are saved in the data acquisition framework, the post-processing script could fetch them, which would limit the number of parameters the user has to enter to the data set location and the δ/β ratio. Moreover, intermediate figures could be shown during the processing, for the user to check its quality before going further. A graphic interface could allow to do so in a user-friendly way.

As seen in this section, the ID16A beamline offers high resolution reconstructions and applies to 3D integration devices. A set of methods, ranging from sample

preparation to post-processing, have been shown to limit the needed time for the complete imaging process, without decreasing the image quality. In the next section, a set of samples from the 3D integration field are shown, in order to illustrate the possibilities of ID16A on such samples, and when possible to compare it with other 3D imaging techniques.

5.6 Application to 3D integration imaging

In this section, three illustrations of the possibilities and limits of ID16A are given, with the help of other 3D imaging results. A first paragraph presents a study on a large number of samples, made possible by the new ID16A sample preparation scheme. A second paragraph is dedicated to the imaging of copper pillars by different tomography setups. A comparison of the different techniques is provided, taking into account not only the obtained resolution, but also the time needed for the imaging process, the retrievable information, and the availability of the equipment. Finally, a discussion is conducted about the possibility to enlarge the field of view of tomography imaging.

5.6.1 Imaging of a large number of post-electromigration samples

Here, we present an illustration of the new ID16A workflow, when applied to a large number of samples, in order to obtain statistical information. The considered samples are hybrid bonding ones [2], with a daisy chain structure. A top view of the structure, acquired by infrared (IR) imaging, is presented in Figure 5.12. The samples are stressed (319 °C/15 mA) until the failure criterion is reached (relative resistance increase of 10 %). The Time To Failure or TTF is then measured. During this test, copper is displaced by electromigration mechanisms, which results in the creation of a void, situated at a location identified in a previous work [118]. This area is circled in Figure 5.12. The goal of the experience is to study whether there is a correlation between the volume of the void and the TTF. Although the location of the void is known, classic imaging methods such as TEM or FIB/SEM only provide 2D information, and the 3rd dimension dimension of the void is in general assumed to be equal to its line width.

By combining the large field of view and high resolution achievable on the ID16A beamline with the new workflow, an actual 3D measure could be obtained for 20 samples, providing statistical information. Two aluminum supports were prepared, and respectively 12 and 8 samples were placed on them, as illustrated in Figure 5.13a and b. The samples of each support were successively imaged by tomography, without any human intervention. The 12 samples on the first support (Figure 5.13a) were imaged with 1500 projections, which led to about 40 hours of unsupervised acquisition. For the second support (Figure 5.13b), 1900 projections were acquired for each sample, and the entire acquisition last for 34 hours. The reconstruction was then performed automatically, once all the acquisitions were over.

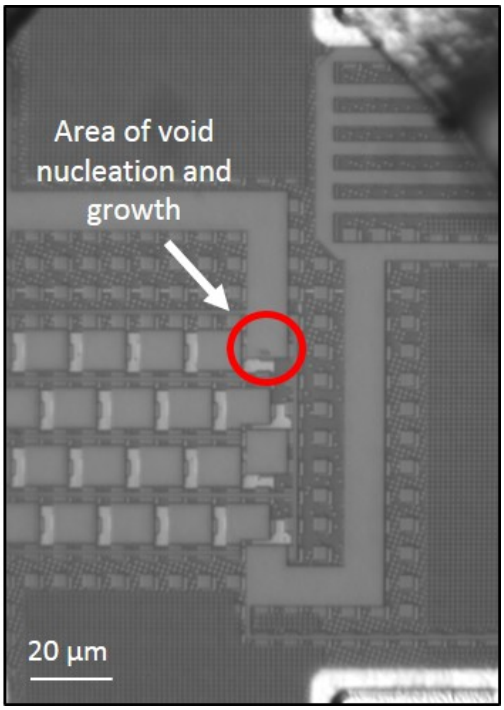

Figure 5.12: Infrared top view of one ROI, where the void due to electromigration appears after an electromigration test. The precise location of the void creation is circled in red.

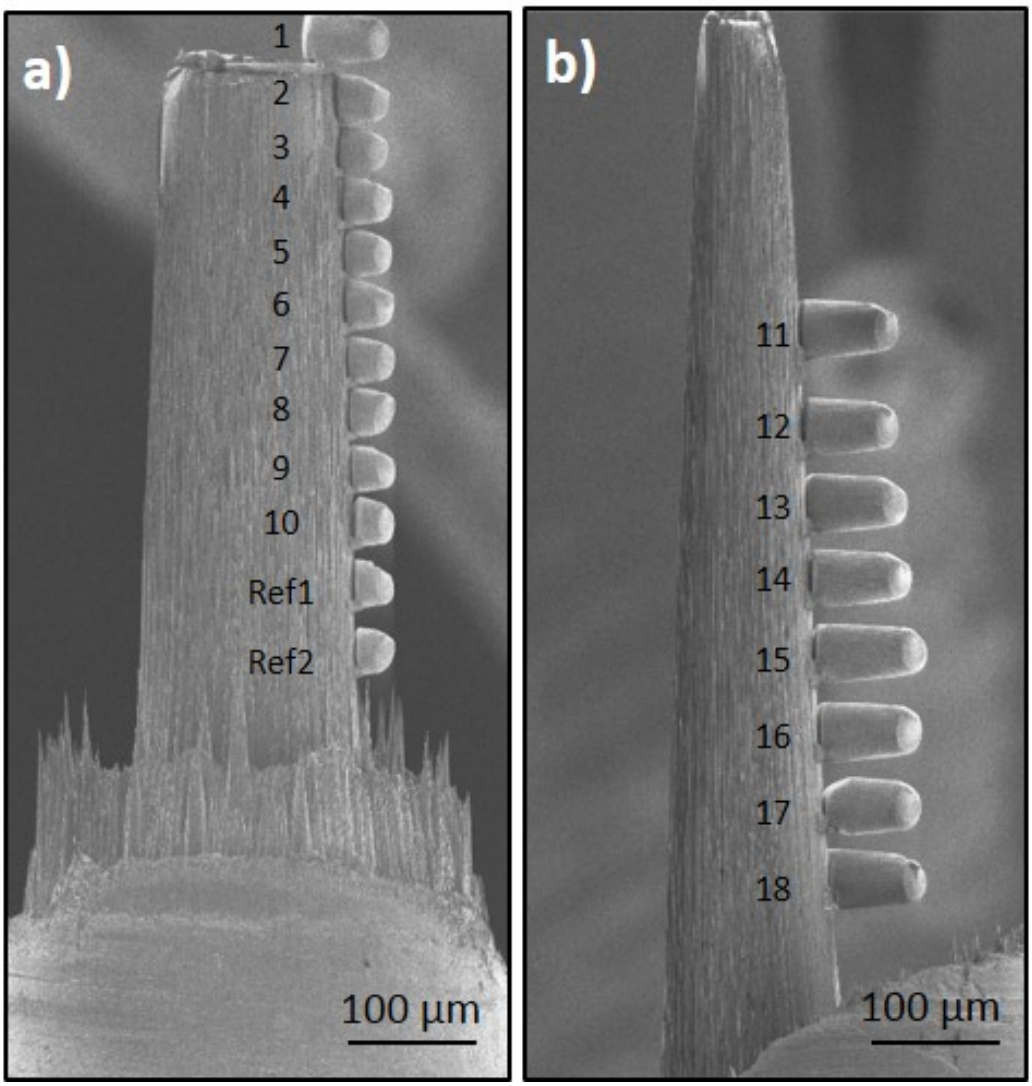

Figure 5.13: Two aluminum supports containing respectively a) 12 and b) 8 samples.

A slice containing the researched void is presented for each sample in Figure 5.14a. The same ROI of the sample can be identified on every slice, and the void appears clearly in black on all (except for the two reference samples, which did not undergo the electromigration test). From those reconstructed volumes, the void can be segmented quite easily, given the high contrast of the reconstruction. One example of such a segmented volume is presented in Figure 5.14b. The segmentation is done independently for every sample with a local threshold tool and takes about 15 minutes per sample, using the Avizo software (and the Magic wand tool). From the segmented voids, the depleted volumes of copper could be measured and compared to the TTF. The result is presented in Figure 5.14c. A clear correlation between depleted volumes and TTF is highlighted thanks to a statistical data analysis. The correlation factor of Pearson is equal to 0.85[3].

The high resolution achievable on the ID16A beamline, combined with a new sample preparation scheme, therefore allowed to perform a 3D statistical study.

5.6.2 Morphology study on copper pillars

During this PhD, copper pillars were imaged with a large panel of techniques. Here, we present the results obtained on 50 μm wide copper pillars, with 3 tomography setups: ID16A, ID19, and a Zeiss Xradia lab tomograph[4]. Those setups have been presented in sections 3.2 and 3.3.

Among the possible setup parameters, preliminary acquisitions have allowed for an optimization of the acquisition setups. For the ID16A beamline, an energy of 33.6 keV was chosen, and the chosen sample organization was a sawn silicon support, on which copper pillars were placed next to one another. The same support was used at the ID19 beamline, where the energy was 19 keV during this experiment. In the case of the lab tomograph, placing the copper pillar on a aluminum pin showed better results than the silicon support. The remaining experimental parameters, such as the pixel size, the number of projections, and the exposure time, are provided in Table 5.1.

Technique	ID16A	ID19	Zeiss Xradia
Pixel size (nm)	40	165	286
Number of projections	1450	3101	801
Exposure time (sec)	0.5	0.2	60

Table 5.1: Experimental conditions for the imagig of copper pillars, using three different tomography setups: ID16A, ID19, and a lab tomograph

A Figure of Merit (later called FoM) is defined in order to approach the resolution and compare the results. It is based on the width of an edge on a 2D image of interest. This easy-to-use method relies on the measurement of the number of pixels

[3] A more detailed version of this study is to be published in 2018.

[4] A more complete study on the imaging of copper pillars, using both tomography and Slice and View techniques, has been submitted to Ultramicroscopy in 2017.

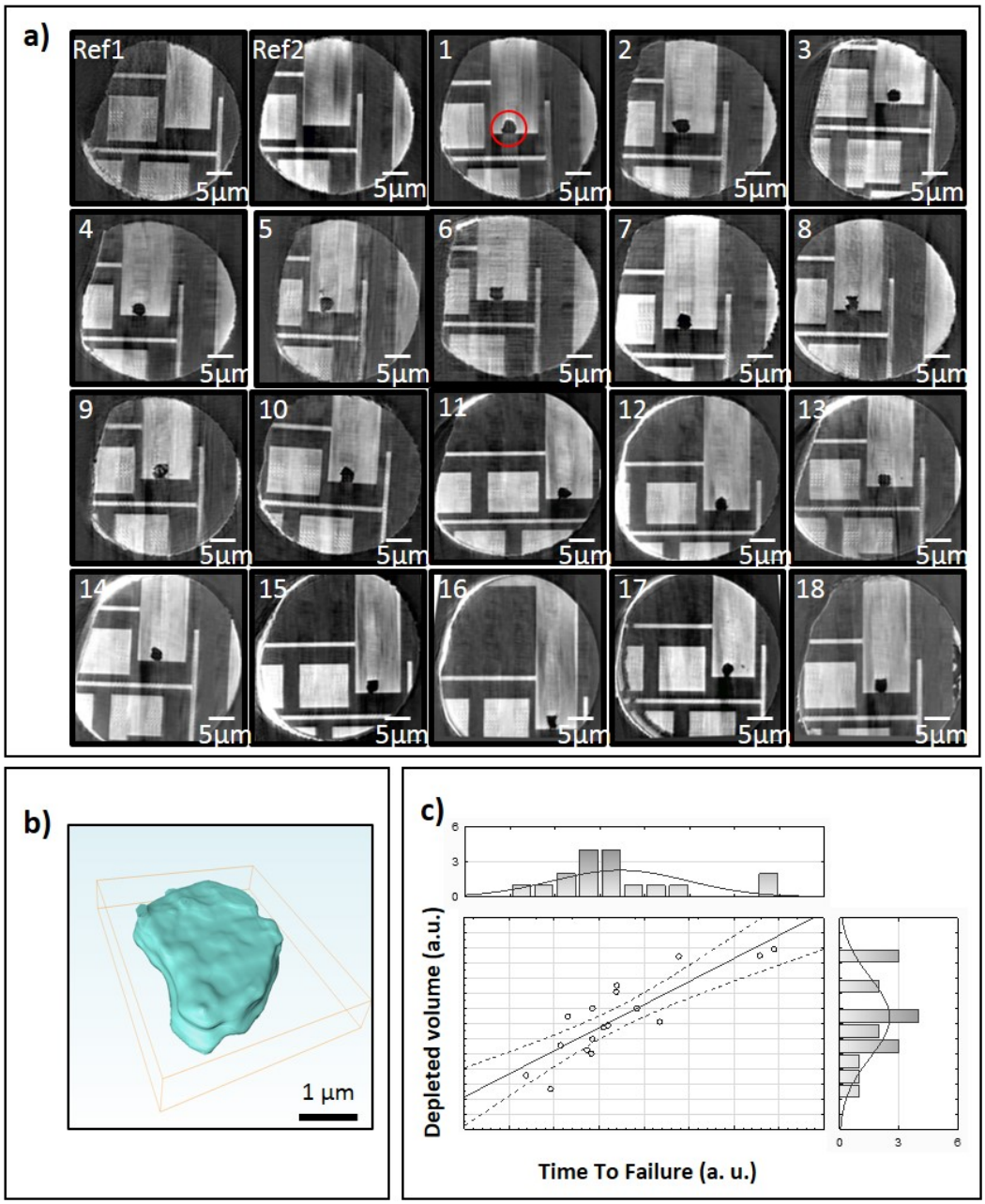

Figure 5.14: a) Slice of interest, containing the center of the depleted volume, for the 20 analyzed samples. The first two samples being references, no copper was depleted. In the other samples, the depleted volume appears in black. b) An example of the segmented depleted volume. c) Values of the depleted volumes regarding the Time To Failure. The plain line is the obtained fit, which is linear (with a correlation factor of 0.85), while the dashed lines define the confidence interval at 95 %.

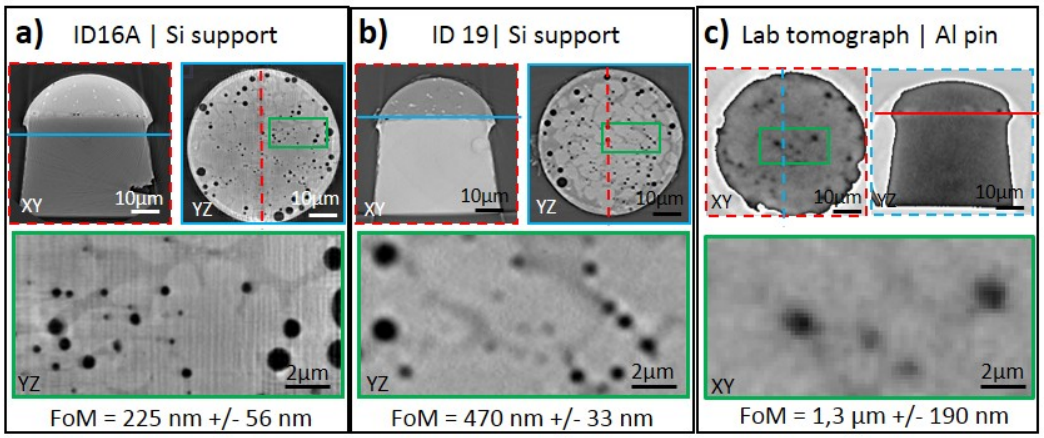

Figure 5.15: Reconstructed volumes of copper pillars, obtained with a) ID16A; b) ID19; c) Lab tomograph. For each setup, a slice reconstructed by the software is shown (XY), together with one orthogonal view (YZ). A zoom-in view of the interface containing the voids is also presented. The obtained FoM value is also provided.

enclosed in an edge of the sample (here the edge of a large enough void). The width of such an edge is obtained by measuring the full width at half maximum (FWHM) of the profile's derivative. This value is then multiplied by the pixel size. This criteria obviously does not provide the resolution, but gives a common ground for imaging techniques comparison: it takes into account the pixel size reachable by the techniques, the sharpness of a drastic contrast change, and to some extent the contrast sensitivity of the technique. In order to limit the impact of the choice of the void, the value is calculated on a number (between 10 and 15) of voids in the whole volume and is given with an error margin.

Figure 5.15 provides selected slices from the obtained reconstructions, together with a zoom-in view of the interface and the calculated FoM. A large range of FoM is visible: while the FoM of the lab tomograph is about 1.3 μm, tomography performed in a synchrotron can achieve FoM of 470 nm (ID19) or even 225 nm (ID16A). It is noticeable that voids even smaller than those values can be spotted (resp. 1.2 μm, 410 nm and 120 nm for resp. the lab tomograph, ID19 and ID16A, those values being calculated with the FWHM value of a void profile). While voids clearly appear on all three reconstructions, the intermetallic alloys are barely visible on the lab tomograph reconstruction. The synchrotron based tomographies, as they are sensitive to phase shifts and therefore more sensitive to edges even between similar materials, allow for a better visualization of those features. On the ID19 microtomography zoom-in view, light circles surrounding voids are visible: they are the effect of phase which enhances the edges and make them more visible. This also affects the FoM value: because of this edge enhancement, the profile seems

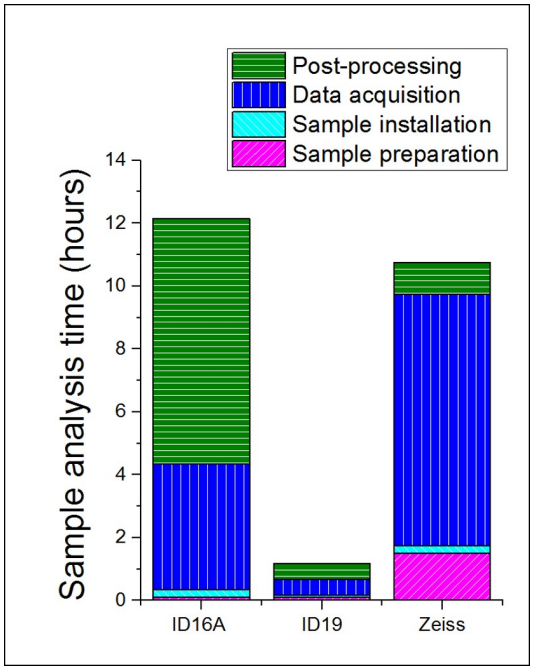

Figure 5.16: Time required for three tomography setups for the imaging of copper pillars, split into their different steps.

sharper than it really is, and the FoM value presented here can be a bit optimistic. Although this image offers high contrast of voids and even intermetallics, better contrast and resolution are provided by the nano-tomography performed on ID16A, as can be seen when comparing the two zoom-in views. It is also worth mentioning that ID16A offers the possibility to adapt the pixel size to the considered sample almost continuously, as it only depends on the position of the sample. ID19 is dependent on the available lenses.

When comparing such characterization techniques in an industrial context, it is important to take into account the time required for the global imaging process. Figure 5.16 presents the time needed for each step of the considered experimental setups. It is noticeable that the values presented for ID16A differ from the ones given earlier (Figure 5.11), because the sample installation differ (here the support is simply sawn), and so does the data acquisition (1450 projections are acquired instead of 500). The ID19 beamline is designed for industrial needs. The data acquisition is made in about 30 minutes, and so does the post-processing. This is enhanced in the case of this experiment, where no phase-retrieval algorithm is applied to the data. This setup, combined with a fast sample preparation scheme, leads to a very quick imaging process. In order to reach resolutions compatible with the copper pillar imaging, the exposure time of the lab tomograph has been increased, together with the number of projections. This leads to a long (8 hours) data acquisition step. Moreover, the chosen sample preparation scheme (FIB lift-out) is a long one, but aims at improving the resolution.

ID19 is a well-established tomography beamline. It indeed offers well-resolved reconstruction in little time (about 1 hour), and is compatible with the new sample preparation scheme proposed here. ID16A offers clearly better resolution and contrast, as discussed earlier, but at the cost of several hours per sample. In fact, even by applying an iterative reconstruction algorithm, which would allow for the acquisition of only 500 projections, the overall time for the ID16A workflow would be about 6 hours. A trade-off must clearly be found between the two beamlines. From Figure 5.16, it is obvious that the lab tomograph cannot compete with the synchrotron beamlines on this particular sample type, neither when considering the resolution, nor the experimental time. However, one must bear in mind that it is a lab equipment, which offers the possibility to image the sample at any moment, which is not the case fo synchrotron experiments. Punctual analysis could therefore be conducted on the lab tomograph, while measurements campaign would benefit from the synchrotron based tomographies, performed on either line, depending on the wanted resolution and available time.

5.6.3 Towards a larger field of view

The new ID16A workflow allows to reduce the analysis time. However, it is still much longer than on ID19, and the field of view remains below 100 μm. Although it offers high resolution, it is not well-fitted for the imaging of complete stacks or packages. For these features, experiments have been conducted on ID19, both in tomography and laminography. Illustrations of the possibilities of this beamline for copper pillar-based stacks are presented here. The imaging experiments primarily aims at spotting voids inside copper pillars.

Using tomography on ID19 with a pixel size of 0.65 μm, complete stacks could be imaged. The sample presented here is a stacking, made by the use of 10 μm large copper pillars. A polymer was then injected in the area remaining between the two wafers, and the top wafer was thinned down to 3 μm. The goal is here to see the voids inside the pillars, and possibly some defects inside the polymer. At this magnification, the ID19 beamline should allow for a field of view of 1.3 mm. However, a method has been implemented on this beamline, in order to increase the FoV: by shifting the rotation axis from the center of the acquired images, and rotating the sample by 360° instead of 180, a larger part of the sample can be imaged. This increases the field of view by 50 %, allowing for 2 mm wide samples. The samples were therefore sawn into this dimension. The tomography acquisition was performed with 5400 projections (to cover 360°), with an exposure time of 0.05 sec. The energy of the beam was 26.5 keV.

Another sample was imaged using laminography. This technique, as explained earlier, presents the advantage of limiting the sample preparation, as it can remain in it original wafer form. The considered sample is also a stack, containing 20 μm large copper pillars. The laminography acquisition was performed at an energy of 25 keV, with a pixel size of 0.65 μm. For each laminography, 3600 projections were acquired, at an exposure time of 0.05 sec.

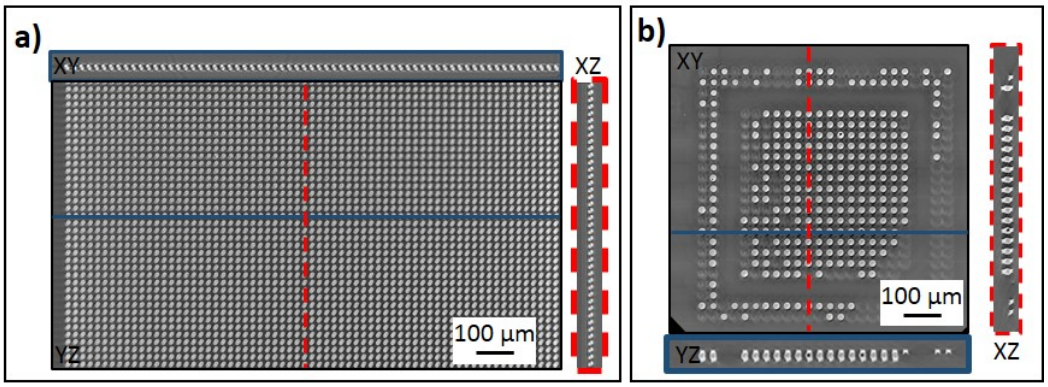

Figure 5.17: Volume reconstructed by large field of view 3D imaging setups: a) Tomography performed at ID19 with a pixel size of 0.65 μm; b) Laminography performed at ID19 with a pixel size of 0.65μm. The figure features one slice reconstructed by the software (XY) and two orthogonal views, all centered on the imaging of copper pillars.

Figure 5.17 presents the volumes obtained by tomography and laminography performed on ID19. For both setups, the acquisition of data requires about 10 minutes. The reconstruction itself takes about 30 minutes in both cases. However, for tomography it is automatic, while laminography today requires manual alignment that last about 20 minutes per sample. As can be seen on the results, the obtained field of view is far larger that the one that can be obtained on ID16A: about 1 mm could be imaged, both by tomography and laminography. This allows for large statistics on copper pillars. This of course has an incidence on the resolution. In both reconstructions, only large voids (about 1 μm) can be imaged. They appear in black and present a good contrast, which means their segmentation is quite easy. It is worth mentioning that for tomography, the resolution is limited by the acquisition method, and is the same is all three dimensions. In laminography however, the resolution is lower in the Z direction, due to a lack of information.

A trade-off between resolution and field of view must then be found, and those two techniques will provide great statistics for large (a few millimeters) objects. Laminography in particular offers the possibility to avoid sample preparation of any kind for thinned stacks. In the experiment conducted here, with the energy of 25 keV, it was however not possible to image a complete packaged die reliably, as the sample was too thick. However, it appears quite clearly that the ID19 beamline (used in tomography or laminography) remains an adapted tool for fast failure localization, especially since it offers fast acquisition and large FoV. However, when it comes to the characterization of small ($<$ 500 nm) defects, the ID16A beamline is better suited, and allows for efficient imaging.

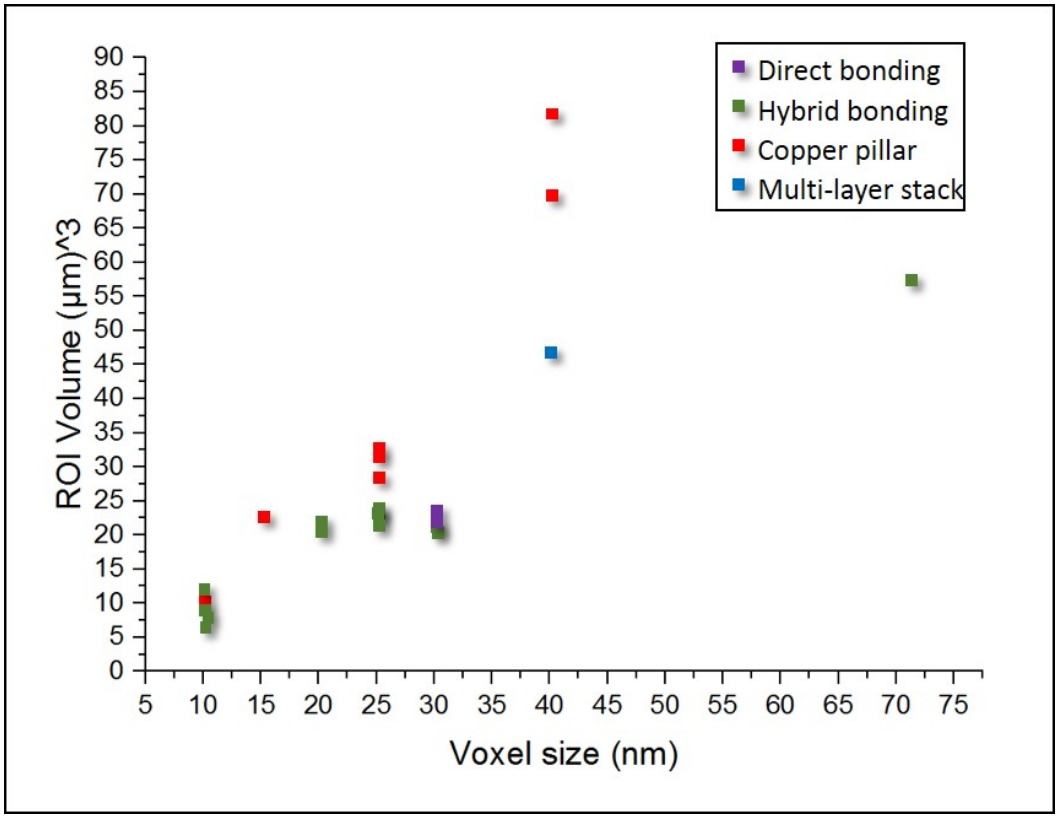

Figure 5.18: Volumes and voxel size of samples analyzed on ID16A during this work, together with their type. The provided volume is the one of the final ROI.

5.7 Conclusion

In this chapter, the ID16A beamline has been presented, in a way it can be used as a routine tool for the 3D imaging of 3D integration devices. The workflow currently implemented on the beamline has been shown and described. A new workflow, relying on a new sample preparation scheme, the reduction of the number of projections, and the automation of the post-processing, has been depicted. It has been shown to work, and allows for the reduction of the overall analysis time by a factor 2. More importantly, it reduces the human intervention time drastically, as the user now mainly acts during the sample preparation and the installation of a whole batch of samples.

In a second part of the chapter, examples of possible applications of the ID16A beamline, combined with the previously introduced workflow, have been given. They include a comparison of different tomography setups applied to the imaging of copper pillars, and a statistical study made possible by the new sample preparation scheme. In order to give an overview of the samples that can be imaged using the ID16A beamline, Figure 5.18 presents the volumes and voxel sizes of a number of samples

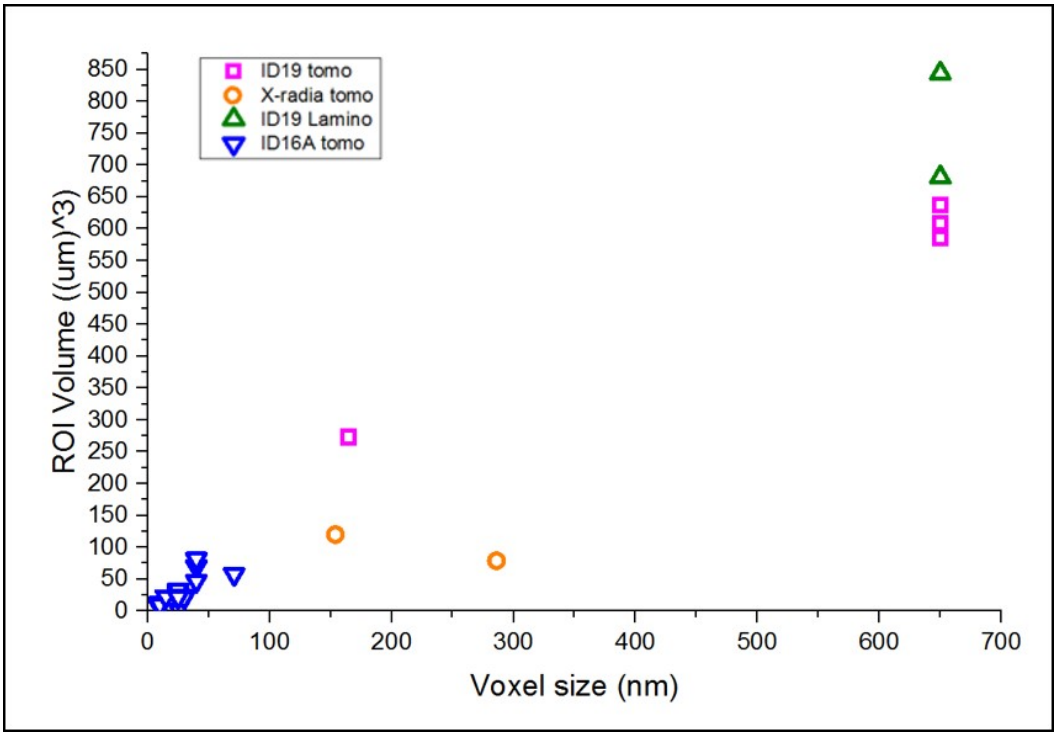

Figure 5.19: Volumes and voxel size of samples analyzed on ID16A, ID19 (tomography and laminography), and the Zeiss lab tomograph during this PhD.

analyzed during this PhD, together with their type. The presented volume is the final ROI volume, and not the volume of the whole reconstructed cube, as this is a more relevant information.

It is worth pointing out that the field of view offered by ID16A is still limited, which is usually the price for high resolution. A last paragraph of the chapter presents ID19 tomography and laminography as ways to increase the imaging field of view, while limiting the samples preparation. It must however be noticed that these positive effects are possible here at the expense of the resolution. In order to compare the possibilities of ID16A tomography to the ones of more established techniques, Figure 5.19 presents a larger selection of samples, imaged respectively on ID16A, ID19 tomography, ID19 laminography, and the Xradia lab tomograph.

It can be seen that ID16 is placed in the left-lower corner, corresponding both to low voxel sizes and quite small imaged volumes. When comparing this image to the one obtained at the end of chapter 4, one can see the tomography performed on ID16A makes the link between the FIB/SEM destructive technique and other, not so well-resolved, non-destructive tomography techniques. A specific set of samples, among which 3D integration basic objects, will therefore highly benefit from this technique. As mentioned before, the goal here is not ultra-fast tomography, and the ID16A beamline is not meant for in situ tomography. However, the processing time

could be reduced, in order to fit some industrial needs.

Contribution à l'imagerie par tomographie sur ID16A appliquée à l'intégration 3D
Résumé du chapitre

Ce chapitre est consacré aux développements menés sur la ligne de lumière ID16A, visant à son utilisation dans un contexte industriel.

Tout d'abord, le procédé global d'analyse de tomographie, pour des échantillons de micro-électronique, est détaillé, depuis la préparation d'échantillons jusqu'à l'obtention du volume reconstruit. Le temps que nécessite chaque étape est donné, basé sur une expérience utilisateur, et séparé en différentes catégories, selon qu'il s'agisse d'un temps nécessitant une machine telle que le PFIB, le faisceau synchrotron, ou une intervention humaine. Les buts de l'étude sont rappelés : il s'agit de limiter le temps global, mais surtout de réduire le temps de faisceau et de maximiser l'automatisation afin de limiter l'intervention humaine.

Pour cela, trois stratégies sont mises en places. Tout d'abord, un nouveau modèle de préparation d'échantillons est développé. Les échantillons sont placés sur des supports verticaux, les uns à côté des autres, ce qui permet de lancer des tomographies successives sans intervention humaine. Le nombre de projections est aussi réduit, grâce à l'utilisation d'algorithmes de reconstruction itératifs. Enfin, un script est écrit afin d'enchainer toutes les étapes du post-traitement automatiquement. Dans ce chapitre, nous montrons que ces stratégies permettent de réduire le temps d'analyse global (d'un facteur 2), le temps de faisceau (d'un facteur 4), et le temps d'intervention humaine (d'un facteur 3), sans perdre en résolution.

Enfin, des exemples d'applications de la ligne de lumière ID16A sont donnés, sur des échantillons d'intégration 3D. Il est montré que le nouveau procédé d'analyse, et notamment la nouvelle préparation d'échantillon, permet de réaliser une analyse sur un grand nombre d'échantillons, avec très peu d'intervention humaine, menant à une information statistique. Une seconde étude, menée sur des piliers de cuivre, compare les performances en temps et en résolution de différents dispositifs de tomographie : ID16A, ID19, et un tomographe de laboratoire. ID19 est adapté pour de grands nombres d'échantillons car l'analyse y est rapide, mais des analyses à haute résolution nécessitent l'utilisation d'ID1A. Le tomographe de laboratoire n'offre dans ce cas ni la résolution ni la rapidité, mais permet de réaliser cette mesure sans délai, contrairement aux lignes synchrotron. Enfin, une réflexion sur le champ de vue, qui reste assez faible sur ID16A, est menée à l'aide de résultats de tomographie et de laminographie obtenus sur ID19.

Chapter 6

Local strain measurements in hybrid and direct bonding stacks

Contents

6.1 Hybrid bonding stack strain measure in silicon 144
6.1.1 Simultaneous observation of two silicon layers 144
6.1.2 Strain maps and morphology correlation 146
6.2 Direct bonding in-situ strain measure in copper 148
6.3 Conclusion 151

In the last two chapters, a panel of 3D imaging techniques has been depicted and shown to apply to 3D integration. Those techniques provide a number of information on the 3D integration objects morphology, that can be correlated with future failure of the device. However, in some cases, the morphology is hard to link directly to the device mechanical behavior. In order to obtain a more complete characterization of 3D integration devices, experiments were carried on ID01, which is a nano-diffraction beamline. The beamline setup was presented in section 3.2.3, while the actual experiment principle and workflow were described in section 3.4. Diffraction is commonly used for microelectronics characterization, and ID01 offers the possibility to obtain a local information, as the beam reaching the sample has a width of 200 nm (at an energy of 9 keV).

Here we present two illustrations of the possibilities of ID01 for the characterization of 3D integration samples. First, the influence of hybrid bonding copper pads on the lower and upper wafers of silicon was investigated. The ID01 beamline allowed for a simultaneous investigation of the two silicon layers, with little sample preparation. The strain results obtained for those patterned samples are correlated with observations of the sample inner morphology, obtained by tomography on ID16A. In a second part, a much simpler sample is investigated, in order to obtain strain maps in copper grains, before and after a 400°C annealing. The sample is only constituted of a silicon wafer, on top of which a full-sheet of copper is deposited[1].

[1] This chapter is a slightly modified version of a paper to be submitted to Microelectronics Reliability under the title "In-situ local strain measurement and morphology correlation in hybrid bonding stacks using nano-focused x-ray and electron microscopy."

6.1 Hybrid bonding stack strain measure in silicon

Here, we present the possibilities of ID01 Bragg diffraction imaging, when applied to a hybrid bonding stack. The considered sample is made of two wafers of (001)-oriented silicon, topped with two layers of patterned copper pads, linked together with copper vias surrounded by $Si0_2$. The wafers are then assembled together, using the back flip bonding, as already illustrated in Figure 1.5 (section 1.2). The considered region of interest in this sample contains a particular structure, called daisychains. Such a ROI is presented in Figure 6.1. The final step of the sample fabrication is the thinning of the top wafer down to 3 μm. It is made by polishing and a chemical attack. Although it is not a sample preparation step, it is however crucial for the experiment, which is performed at an energy of 9 keV,with a beam size of 200 nm x 500 nm (horizontal x vertical). At this energy, the attenuation length of x-ray is 98.2 μm in Si and 3.95 μm in Cu. For the beam to reach the silicon substrate, the original thinning of the top layer is therefore critical. Moreover, the thinning final step is a chemical attack, which allows the assumption that the thinning does not induce supplementary strain.

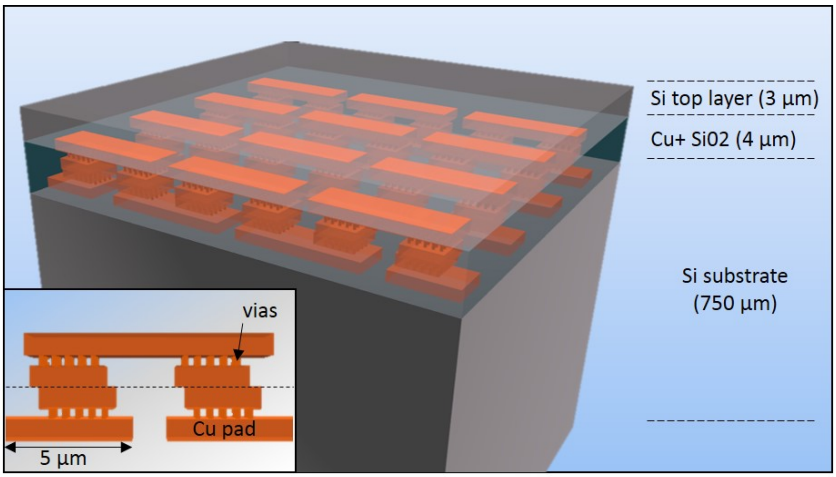

Figure 6.1: a) Stack containing daisy chains. Inset: a view of one unit of the copper design.

A tomography of a similar sample was also realized, in order to correlate the obtained maps with the actual sample morphology. The sample used for this analysis is the one presented in Figure 5.5e (section 5.2.2), imaged at an energy of 33.6 keV. The imaged area is part B, with a pixel size of 25 nm.

6.1.1 Simultaneous observation of two silicon layers

In the hybrid bonding sample, the strain in the two layers of silicon was measured. The thinning of the top layer ensures that the beam reaches both the top layer and the silicon substrate. In this study, the (004) planes of a 100 x 100 μm^2 area were

analyzed (with a sampling step of 500 nm in both directions), the angles of the rocking curve going from 30.47° to 30.97° with a 0.01° step. The sample (X,Y,Z) coordinates are defined such as the x-ray arrive in the XZ plane (see Figure 6.2).

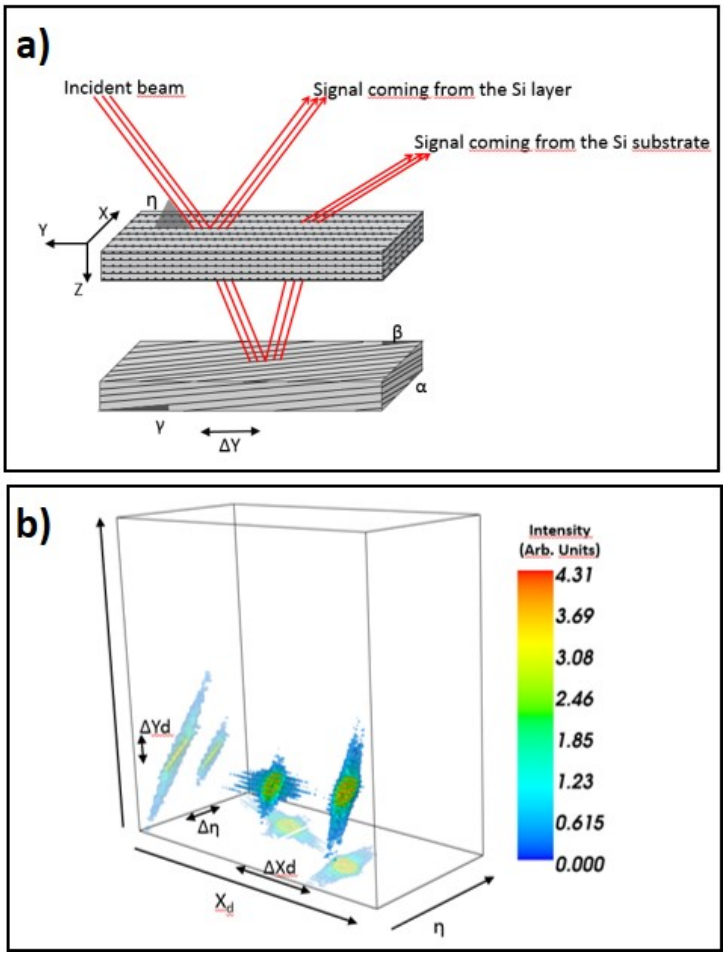

Figure 6.2: a) schematic view of the two silicon layers analyzed in the patterned sample and the trajectory of the x-ray inside it for a given angle η. Inside the top layer, atoms and crystalline directions are represented. For understanding purposes, atoms are not represented in the substrate representation. b) A 3D representation of the detector acquisition, made by stacking the 2D acquisitions for all the angles η.

Figure 6.2a provides a schematic view of the silicon layers of the patterned sample, and more precisely the crystalline planes inside them. From the manufacturing process, the layers are known to be parallel. This has been verified by direct microscopy observation. The (004) crystalline planes from one layer however are not necessarily parallel to the (004) planes of the other layer. In fact, the two wafers that form the top layer and the substrate could be cut from two different Si monocrystals, and the cutting planes are likely to be different from the (001) plane. In

figure 6.2a, the top layer crystalline planes are assumed to be perfectly aligned with the sample based (X,Y,Z) coordinates. The substrate planes however present three angles (α, β, γ) regarding these coordinates. This leads to two different signals on the detector: one comes from the silicon substrate, the other one from the top layer.

Figure 6.2b presents a 3D representation of the obtained data. The 3D view is made by stacking together 2D images of the detector, for all angles η forming the rocking curve. For understanding purposes, projections of the data are given on the planes $(X_d Y_d)$ and $(Y_d \eta)$. As announced, two distinct peaks are observable. They have different shapes, and are separated on the detector by distances ΔX and ΔY. Moreover, they do not appear for the same angle η: they are separated in the 3D representation by a distance $\Delta\eta$. In the case of the patterned sample, the substrate peak appears for $\eta = 30.81°$, while the layer peak appears for $\eta = 30.65°$.

Simple geometry considerations establish qualitative links between the misalignment of the crystalline planes and the relative positions of the peaks. The quantification of those links, which has to take into account the refraction of x-ray inside the sample, is not conducted here. The differentiation between the two peaks is performed using their shape: the larger the layer, the sharper the pattern. This distinction allows for the definition of two ROI on the detector, each corresponding to a silicon contribution.

6.1.2 Strain maps and morphology correlation

The separation of the two layers contribution to the diffracted signal leads to two strain maps, presented in Figure 6.3a with a common color scale. Due to the angle η between the surface and the beam, as well as the actual depth of the different features, originally the two maps are not perfectly aligned in the Y direction: there is a shift between features from the top layer and from the substrate. This is due to the fact that for each map, the (X,Y) point is assumed to be the point where the beam hits the sample surface. For the substrate map however, the value situated at the point (X,Y) relates to information gotten at the point (X,Y+ΔY), as illustrated in Figure 6.2a. For an easier comparison, the presented maps were shifted in the Y direction in order for the features to be aligned. It is noticeable that while the top layer map is directly interpretable, the analysis of the substrate is not so direct, as multiple refraction and absorption effects occur before and after the interaction of the beam with the substrate. The values are therefore rather to be taken as relative values inside each map, instead of absolute values.

The maps show a relatively low and equal out-of-plane strain in silicon in both layers, as the average values for respectively the top layer and the substrate are $< \varepsilon_{zz,layer} >= 0.06\%$ and $< \varepsilon_{zz,substrate} >= 0.07\%$. A higher strain level draws a rectangular shape, that can be interpreted as a large copper pad imprint. The maximum strain is obtained close to those rectangles edges. Figure 6.3b presents slices of the daisy chains reconstructed from nano-tomography experiments. YZ and XZ views show the profiles of daisy chains, while the pads are fully visible on the two XY views, at two different Z levels. Those views show the copper pads close

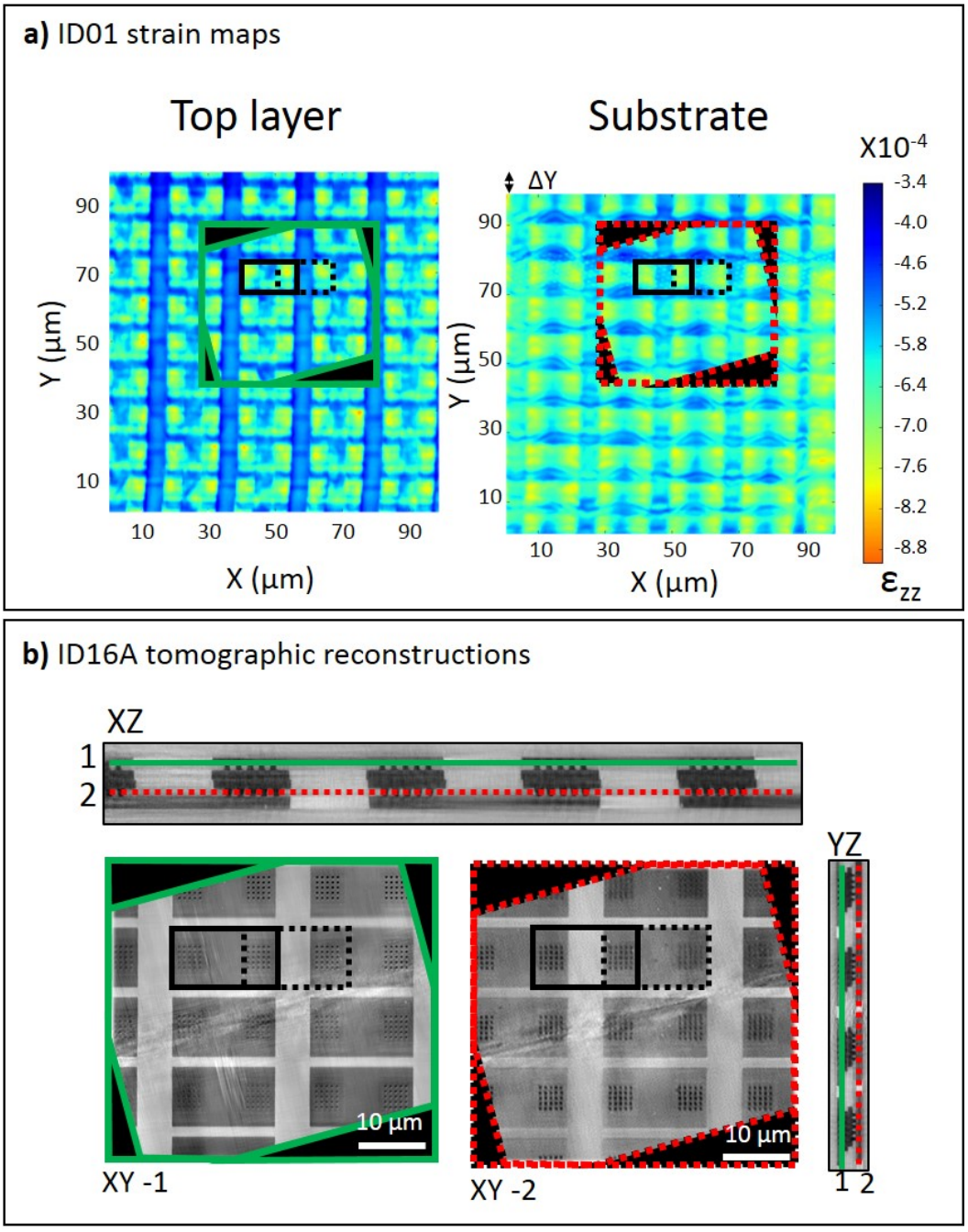

Figure 6.3: Results of the observations performed on the hybrid bonding imager. a) Strain maps of the Si top layer (on the left) and the Si substrate (on the right) with a common color map. The black rectangles draw the shapes of large copper pads. b) Selected slices of the volume reconstructed by nano-tomography. XZ and YZ views of the daisy chains (on the top and on the right), XY slices on the large pads, respectively close to the top layer and the substrate. The shape of the regions of interest presented in Figure b is reported in Figure a for morphology correlation.

to the top layer (on the left, in plain green) and the ones close to the substrate (on the right, in dashed red). As stressed by the frames of figure 6.3b reported in Figure 6.3a, the shapes observed on the strain maps correspond exactly to the morphology of the large pads present on the sample. This confirms the fact that higher strain is observed in the silicon close to large copper pads, and that the highest strain is observed on the pad edges, where the pads are connected to the lower level, using copper vias. The constraint underwent by those small-dimension vias is likely to be the origin of the strain inside the silicon layers.

6.2 Direct bonding in-situ strain measure in copper

In order to measure the strain in copper during the process, and more precisely during annealing, a case-study sample was realized: 500 nm of full-sheet copper were deposited on top of a 750 μm thick silicon substrate, and only a layer of SiO_2 was placed on top of the copper in order to protect it from oxidation. An illustration of such a sample is proposed in Figure 6.4. No sample preparation was needed for the measure of strain.

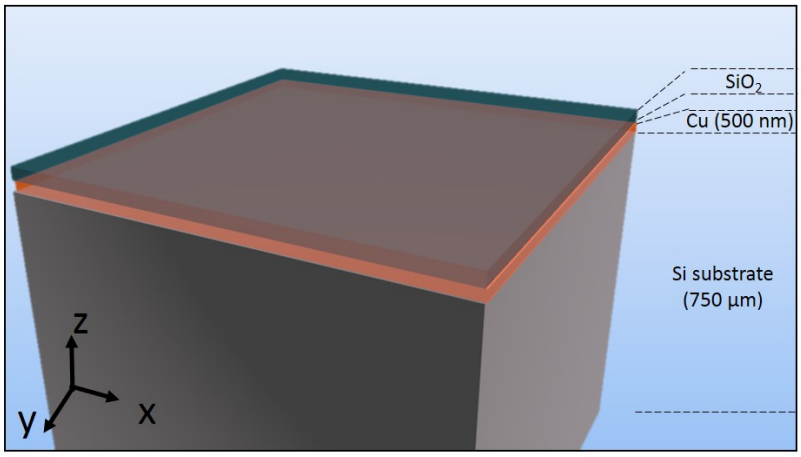

Figure 6.4: Stack made of a silicon wafer topped by a full-sheet layer of copper and protected by a layer of SiO_2.

In this non-functional full-sheet sample, the strain in the copper layer was measured. Planes (444) were observed using the K-Map method at room temperature as well as at 400°C. The sample was placed inside a homemade beryllium dome hot stage [119] in both situations, allowing to heat the sample when needed with little absorption of the x-ray beam. A first experiment was carried out at room temperature (RT) under vacuum. An area of 60 x 100 μm^2 was analyzed, with a sampling of (horizontal x vertical) 428 nm x 714 nm. The angles of the rocking curve were chosen from $\eta = 40.56°$ to $\eta = 41.56°$ with 0.05° steps. Once the experiment was over, the sample was heated progressively up to 394°C, while adapting its Z position in order to keep the same grains inside the field of view. A second strain map of

(444)-oriented grains was then acquired at 394°C, with the same scanned area as previously and a rocking curve going from $\eta = 40.76°$ to $\eta = 41.26°$ with $0.05°$ steps.

Figure 6.5 shows two strain maps of the (444)-oriented grains of the Cu sheet, at room temperature and at 400°C. Individual grains can be observed and it is visible that the same grains have been imaged during the two experiments. The average values from those two maps are $< \varepsilon_{444,RT} >= -0.27\%$ and $< \varepsilon_{444,400°} >= 0.47\%$. Therefore, the annealing induced a strain $\Delta\varepsilon = 0.74\%$. If the strain in copper is only due to temperature (i.e. thermal strain), its theoretical value is given using equation 6.1. With $\alpha = 17 \cdot 10^{-6} K^{-1}$ and $\Delta T = 370K$, it rises $\Delta\varepsilon = 0.63\%$, which is quite close to the experimental data.

$$\Delta\varepsilon = \alpha.\Delta T \tag{6.1}$$

It is noticeable that the analysis was made on a plane (444), so the three directions contribute to the final values of strain. However, when comparing the average values of the components of Q in this case, it appears that Q_Z is predominant for both experiments: the deformation is mainly in the Z direction. The silicon does not constrain the copper in that direction, which means it is normal for the copper to follow its natural behavior during heating. Additional measures in different planes could be interesting and give us more information on the interaction between silicon and copper.

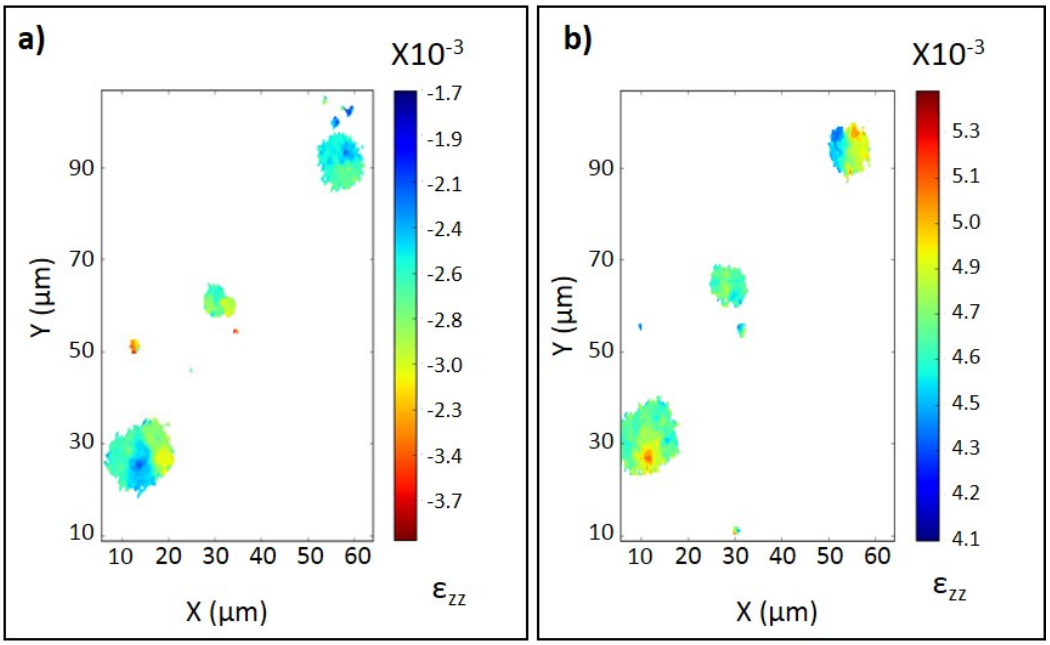

Figure 6.5: Strain maps of (444)-oriented copper grains inside a 500 nm thick copper layer deposited on top of a silicon wafer, a) at room temperature; b) at 400°C. Color maps are adapted in order for the stronger strain (either in tension or compression) to appear in red.

6.3 Conclusion

In this chapter, strain has been measured for two silicon and copper stacks, aimed for the field of 3D integration. ID01 was shown to be well-fitted for the simultaneous measurement of local strain in two silicon layers, bonded with hybrid bonding. It was also possible to combine the said maps with morphology observations, and confirm that the shapes observed in the strain maps were the copper pads present in the sample.

To study the strain in bonding copper before and during heating, a non-functionnal and much simpler sample was also analyzed. The experiment setup allowed to measure the strain in (444)-oriented grains of copper, and to follow the grains during a 400°C annealing, in order to measure the strain in those same grains, at 400°C.

ID01 is a long beamline, which has already been used for microelectronics, in particular for the analysis of Though Silicon Vias (TSV) [120, 121, 122]. This study enlarges the possibilities of ID01 to multi-layered stacks. It allows for acquisitions or large areas of the sample (100 x 100 μm^2), together with a spatial resolution of several hundred of nanometers, providing a local information. Therefore, it allows for statistical and possibly in-situ analyses. Moreover, correlation between two techniques (ID01 diffraction imaging and ID16A tomography) is here shown to be possible, and could lead to a better understanding of the links between strain and morphology inside 3D integration stacks. In the case of strain measurements in copper, since it is here polycrystalline, one could benefit from a Laue analysis of the sample, which would provide a more general information, regarding the strain in all the grains. The technique used here is however simpler to post-process, and still provides an approximation of the strain in a copper layer, together with an information about the grain size.

Mesure locale de déformations au sein d'empilements Résumé du chapitre

Dans ce chapitre, nous décrivons deux mesures locales de déformations, réalisées par nano-diffraction sur la ligne de lumière ID01 de l'ESRF.

Dans une première mesure, un empilement réalisé par collage hybride est analysé. Il est composé de deux wafers de silicium, entre lesquels se situent des structures de cuivre. Le but de cette étude est la mesure simultanée des déformations des deux couches de silicium. Pour cela, les faibles décalages des plans cristallins des deux couches sont exploités : sur le détecteur 2D, deux tâches de diffraction distinctes apparaissent, permettant d'obtenir deux cartes de déformations indépendantes en un seul scan de l'échantillon. La corrélation entre les déformations et la morphologie de l'échantillon a pu être établie grâce à des mesures de tomographie, obtenues sur ID16A.

Une seconde expérience a été menée sur un échantillon plus simple, destiné lui aussi au collage. Il s'agit d'un wafer de silicium, sur lequel une couche de cuivre a été déposée. On cherche ici à observer les déformations dans le cuivre, à température ambiante et à 400°C. Le faisceau étant monochromatique, une seule famille de grains (orientée (444)) a pu être observée. Entre les deux températures, les grains de cuivre ont pu être suivis, et les mêmes grains ont donc été imagés à température ambiante et à 400°. Cette technique nous donne une information sur la taille des grains, ainsi que sur la déformation globale dans une telle couche de cuivre, avant et après recuit.

Dans ces deux expériences, de grandes zones de l'échantillon ont pu être analysées, typiquement 100 x 100 μm^2, avec un pas d'échantillonnage de moins de 500 nm, ce qui permet d'obtenir une information locale. Si le traitement des données reste assez long (quelques heures), il est probable qu'il soit réduit par la nouvelle interface utilisateur développée sur ID01, ce qui permettra une utilisation routinière de cette ligne.

Concluding remarks and perspectives

In this work, we explored the requirements of 3D integration devices in terms of characterization, and more specifically in terms of imaging. In fact, it provides upstream information about the samples, and allows for the understanding of the mechanisms happening during the fabrication process, and therefore a monitoring of the said process over time. To do so, several experimental setups have been investigated and developed, in order to obtain a large enough field of view, with optimal resolution available. The focus was set on the automation of all those procedures, for the techniques to be used as routine characterization means for the industry.

The first three chapters of this manuscript are dedicated to the presentation of the context of the study. The first one describes 3D integration principles, together with the specific objects of interest and their characterization needs. The second chapter presents the physical principles of electron and ion based scanning microscopes. Finally, chapter 3 focuses on x-ray based characterization methods, presenting both laboratory and synchrotron experimental setups. The next chapters rely on those basis to present the work done during this PhD thesis.

The main development performed during this PhD thesis concerns x-ray tomography and is widely discussed in chapter 5. The ID19 beamline of the ESRF (European Synchrotron Radiation Facility) provides tomography reconstructions in little time (less than one hour), making it well-suited for statistical measurements, and therefore of great interest for industry. The experiments conducted on this beamline showed the possibility to image samples as large as 2 mm by tomography and several centimeters by laminography, for a final voxel size reaching 0.65 μm. Although smaller voxel sizes (150 nm) can be reached, small features such as voids in copper pillars and copper pads, which are several tens of nanometer large, cannot be imaged on this beamline.

Much higher resolution can be achieved on ID16A. This newly-built long beamline aims at nano-tomography with a sub-50 nm resolution, by exploiting the high coherence of the source. Its allows for a field of view of several tens of micrometers. Such an experiment however, from the sample preparation to the final reconstructed volume, required too much time and human intervention for an industrial application. A major result of this work is the reduction of this overall experimental time by a factor 2, and more specifically of the required human intervention by a factor 3. Our contribution to the ID16A workflow makes it possible to routinely perform statistical measures on samples such as copper pillars and hybrid bonding stacks, with little human intervention during the whole process. Automatic post-processing has been shown possible, and it should be applicable during the experiment itself in

the future, in order to obtain ready to process reconstructed volumes at the end of the beamtime.

An insight on other possible characterization methods offered by a synchrotron setup was provided in chapter 6. On the ID01 beamline, local strain measurements could be conducted, thanks to a fast scanning technique allowing for acquisitions on large areas (100 x 100 μm^2) with relatively high spatial sampling, as the beam can be focused down to 200 nm. A first study exploited the x-ray penetration depth and simultaneously measured the strain in two silicon layers of the same stack, with no sample preparation. A second study was conducted *in situ*, on the copper used for wafer bonding. The obtained strain only concerns a family of grains, but still provides information about average strain before and after annealing.

The use of a monochromatic beam such as the one available at ID01 is particularly well-suited for studies performed on monocrystals, and one can imagine such studies performed on multi-layer stacks, with no need of sample preparation. For polycrystalline materials such as copper here, other methods such as Laue diffraction would seem more relevant, although the acquired data seem more tedious to post-process and interpret. For both experiments, the post-processing of the data requires several hours of human intervention, but the user interface lately developed on the beamline should pave the way for a more user friendly procedure.

Synchrotron characterization methods, be they by morphology or diffraction imaging, therefore offer great possibilities for 3D integration samples, and can be adapted for routine characterization procedures. At the ESRF, their global performances are likely to increase in the next few years, thanks to the second phase of the ESRF upgrade. This phase, which follows the one during which ID16A and ID01 were built, represents an investment of 150 millions of euros between 2015 and 2022. The main goal is to limit the emittance (especially the horizontal one) of the electron source. This will allow for higher flux and more coherent beams, which will improve both imaging and diffraction results, and decrease experimental times. Newly developed techniques, such as ptychography, will benefit from this improvement, and their development could lead to industry-compatible ptycho-tomography, a concept already shown relevant for microelectronics by Holler et al. [123]. As mentioned in this article, the high resolution achievable by ptychography (below 20 nm) could even be combined with laminography, in order to obtain large field of view imaging, with no or little sample preparation. Such adjustments would make synchrotron sources (and maybe future lab ones) even more relevant for routine statistical characterization of 3D integration devices, and more generally of microelectronics ones. Together with those technical improvements, a shift in perception has been occurring in the last few years. The ESRF aims at offering more routine services to industry actors in the future, through direct access beamtime or for example through programs such as the IRT Nanoelec, for more upstream studies and proofs of concept. The work presented here also contributes to a new vision of synchrotron-based characteriza-

tion techniques, that can be compatible with the industry efficiency and reactivity requirements.

In parallel to the synchrotron development, laboratory based equipment is also improving. As table-top synchrotrons appear on the market, one can hope that results obtained today in a synchrotron may be approached in the future in the lab. Although today, laboratory equipment still either lack field of view (in the case of TEM or slice and view) or resolution (in the case of lab tomographs or diffractometers), they still offer the great advantage of being available at all time, with no or little time notice.

For this reason, during this work, a laboratory-based 3D imaging procedure has been implemented inside a single-beam PFIB (Plasma Focused Ion Beam). The details of this implementation, together with the obtained results, are presented in chapter 4. It was shown to offer both resolutions and fields of view compatible with 3D integration. Its automation was made possible and it has been shown to be stable for several tens of hours long data acquisitions, with a slicing step down to 50 nm. Some limits, mainly regarding the required acquisition time, are imposed by the machine itself. In addition to the reduction of the data acquisition time, made by the use of a dual beam microscope or by tuning the stage and beam parameters of the single beam one, this technique could be improved by the addition of new features. In fact, the technique could easily benefit from an additional EDX detector for example, which would provide 3D chemical information on large volumes, which today is hard to obtain.

In this work, we had the opportunity to work on many recent setups, for the characterization of 3D integration devices, as they rise new challenges. When possible, comparison have been made between the different techniques, in order to point out their assets and drawbacks, from a user and industrial point of view. Some development have been made to make those techniques possible to use routinely for microelectronics failure analysis. Many foreseeable developments are likely to strengthen this trend.

Conclusion générale et perspectives

Durant le travail présenté ici, certains besoins de caractérisation d'une nouvelle tendance en micro-électronique, appelée intégration 3D, ont été étudiés. Plus particulièrement, nous nous sommes intéressés à son imagerie, qui fournit une information amont sur l'échantillon, pemettant à la fois une meilleure compréhension des mécanismes guidant son procédé de fabrication et un suivi dudit procédé dans le temps. Pour répondre à ces besoins de caractérisation, plusieurs dispositifs expérimentaux ont été testés et développés, afin d'obtenir un large champ de vue, tout en maximimisant la résolution atteignable. Une attention particulière a été portée sur l'automatisation des toutes ces procédures, pour que les techniques considérées puissent être utilisées de manière routinière dans l'industrie.

Les trois premiers chapitres présentent le contexte de l'étude. Le premier présente les grands principes de l'intégration 3D, ainsi que ses besoins de caractérisation spécifiques. Un second chapitre présente les microscopes à balayage (électroniques et ioniques) ainsi que leur utilisation au cours de ce travail. Le chapitre 3 introduit les méthodes de caractérisation utilisant les rayons X, qu'ils soient issus d'une source synchrotron ou de laboratoire. Ces chapitres posent les bases physiques sur lesquelles s'appuient les chapitres suivants.

Les principaux développements réalisés durant ce travail de thèse concernent la tomographie par rayons X, et sont discutés en détails au chapitre 5. La ligne de lumière ID19 de l'ESRF (European Synchrotron Radiation Facility) est capable de fournir en peu de temps (moins d'une heure) des reconstructions tomographiques, ce qui en fait une technique adaptées aux mesures à grande échelle, et donc à l'industrie. Les mesures réalisées sur cette ligne ont montré sa capacité à imager des échantillons relativement grands par tomographhie (2 mm) et laminographie (quelques centimètres), avec une taille de voxel de 0.65 μm. Bien que des tailles de voxels plus petites puissent être obtenues (150 nm) au détriment du champ de vue, de petits défauts au sein des structures étudiées, comme des trous aux interfaces entre pads, ne peuvent être observés sur cette ligne.

Une résolution bien plus importante peut être obtenue sur la ligne de lumière ID16A. Il s'agit d'une ligne récente, visant une résolution de 50 nm en tomographie. Pour cela, elle exploite la forte cohérence du faisceau de rayons X. Le champ de vue qu'elle permet alors est de quelques dizaines de micromètres. Cependant, le procédé d'analyse original de cette ligne nécessitait de nombreuses heures, et surtout beaucoup d'intervention humaine. Afin de rendre cette ligne compatible avec les exigences de l'industrie, un nouveau procédé d'analyse à été mis en place. Un résultat majeur de ce travail est la réduction par un facteur 2 du temps global

d'analyse, avec une réduction par un facteur 3 du temps d'intervention humaine. Ce développement sur ID16A permet de réaliser des mesures statistiques sur cette ligne sur des échantillons tels que les piliers de cuivre et des empilements de plusieurs niveaux de cuivre et de silicium, de manière automatisée. Le post-traitement a été automatisé, et il devrait être possible dans un futur proche d'obtenir les volumes reconstruits pendant le temps de faisceau alloué.

Une illustration d'autres caractérisations réalisables à l'ESRF est donnée au chapitre 6. En effet, sur la ligne ID01, des mesures de déformations ont pu être réalisées, en utilisant une technique de scan rapide permettant d'analyser des zones larges de l'échantillon (typiquement 100 x 100 μm^2). La taille du faisceau étant de 200 x 500 nm^2, il a été possible sur cette ligne d'obtenir des mesures locales. Une première étude présentée ici a permis, en exploitant la grande profondeur de pénétration des rayons X dans le silicium et le cuivre, d'analyser simultanément deux couches de silicium d'un même empilement. Une seconde étude a été réalisée *in situ*, sur un échantillon destiné à un collage direct pleine plaque. Les déformations dans le cuivre ont pu être mesurées à température ambiante ainsi qu'à 400°C. Les résultats obtenus ne concernent qu'une famille de grains, mais fournissent tout de même une information sur la déformation moyenne avant et après recuit.

La ligne ID01 présentant un faisceau monochromatique, elle est particulièrement bien adaptée à l'étude d'un matériau monocristallin tel que le silicium. Il est même possible d'imaginer la mesure de déformations dans le silicium telle que celle présentée ici, mais réalisée sur un empilement contenant plus de deux niveaux de silicium, sans aucune préparation d'échantillon. Dans le cas de matériaux polycristallins tels que le cuivre, d'autre méthodes telles que la diffraction Laue semblent plus pertinentes que la diffraction de Bragg décrite ici. Cependant, elle nécessite un traitement de données et une interprétation des résultats plus fastidieux. Sur ID01, le post-traitement des données nécessite aujourd'hui plusieurs heures d'intervention humaine. Cependant, l'interface graphique récemment développée devrait permettre de rendre cette étape plus simple pour l'utilisateur.

Les méthodes de caractérisation accessibles dans un synchrotron, qu'il s'agisse d'imagerie ou de mesure des contraintes, ont manifestement beaucoup à offrir pour la caractérisation d'échantillons d'intégration 3D, d'autant plus qu'elles peuvent être adaptées pour une utilisation routinière. A l'ESRF, les performances de ces techniques vont être amenées à s'améliorer dans les années à venir, au vu de la deuxième phase du programme "Upgrade". Cette phase représente un investissement d'une hauteur de 150 millions d'euros entre 2105 et 2022, et a pour but majeur de limiter l'emittance (surtout horizontale) de la source primaire d'électrons. Ce changement va se répercuter sur l'ensemble des chemins optiques : un flux plus important sera accessible, de même que des sources secondaires plus cohérentes, menant à une réduction du temps d'analyse pour une augmentation de la qualité des résultats.

Des techniques en cours de développement, telles que la ptychographie, con-

naitront probablement un essor grâce à ces améliorations. En effet, en limitant le temps d'acquisition, des expériences de ptycho-tomographie pourront être réalisées dans des temps compatibles avec l'industrie. Cette technique a d'ailleurs déjà été testée sur des échantillons issus de la micro-électronique par Holler et al. [123]. Comme mentionné dans cet article, il pourrait même être possible de combiner la haute résolution de la ptcyhographie (20 nm) avec la laminographie, afin d'obtenir un large champ de vue tout en limitant la préparation d'échantillons. Toutes ces évolutions permettront aux sources synchrotron de s'imposer comme des outils possibles pour la caractérisation d'échantillons issus de l'intégration 3D, et plus généralement de la micro-électronique.

En parallèle de ces développements techniques, un récent changement de perception des synchrotrons est à noter. En effet, l'ESRF par exemple cherche aujourd'hui à développer son offre pour les industriels, que ce soit par l'achat de temps de faisceau ou par des projets tels que l'IRT Nanoelec, orienté vers ds études amont et des tests de faisabilité. De son côté, le travail présenté ici participe à changer la perception du milieu de la microélectronique concernant les sources synchrotron, en les présentant comme un outil de caractérisation qui peut être routinier, réactif, et efficace.

Par ailleurs, de nombreux développements ont aussi été réalisés sur les équipements de laboratoire. Des sources de rayons X dites "synchrotron de laboratoire" sont aujourd'hui commercialisés, et des résultats aujourd'hui seulement accessibles en synchrotron le seront peut-être demain en laboratoire. Aujourd'hui cependant, les équipements de laboratoire sont toujours limités soit par la résolution (dans le cas de tomographes de laboratoire), soit par le champ de vue (dans le cas du MET ou du FIB/SEM). Il ne faut pas oublier cependant qu'ils offrent l'avantage indéniable d'être disponibles à tout moment, contrairement aux expériences en synchrotron.

Pour cette raison, une technique d'imagerie 3D en laboratoire a également été développée during cette thèse. Il s'agit d'une procedure Slice and View implementée dans un PFIB (Plasma Focused Ion Beam). Les détails de ce développement, ainsi que les résultats obtenus, sont présentés au chapitre 4. Les champs de vue et la résolution ateignables sur un tel dispositif sont compatibles avec la caractérisation pour l'intégration 3D. L'acquisition des données a été rendue automatique et stable pendant plusieurs dizaines d'heures, avec un pas d'échantillonage dans la direction de découpe pouvant aller jusqu'à 50 nm. Les limites de cette technique ont été identifiées et discutées. Elles concernent surtout le temps d'acquisition, qui pourrait bien sûr être réduit par l'utilisation d'un microscope équipé de deux colonnes, une pour la coupe et l'autre pour l'imagerie. Au delà de ces considérations, il peut être intéressant de noter que l'ajout de nouvelles fonctionnalités à cette méthode pourrait être d'un grand intérêt. En effet, l'ajout d'un détecteur EDX par exemple pourrait permettre d'obtenir une information chimique tridimensionnelle sur une large région d'intérêt, ce qui est aujourd'hui difficile.

Ce travail de thèse a été l'occasion de réaliser des expériences sur bon nombre de dispositifs expérimentaux récents, et de les appliquer à des échantillons en plein développement. Lorsque cela a été possible, des comparaisons et corrélations ont été réalisées entre ces différentes techniques, afin de mettre en lumière leurs avantages et inconvénients, d'un point de vue industriel. Ces techniques ont été adaptées pour le milieu de la microélectronique, afin de fournir rapidement et facilement des informations statistiques, rapides à traiter. De nombreuses évolutions à venir, certaines évoquées ici, sont à même de continuer dans cette direction et d'installer le synchrotron en tant que technique de caractérisation parfaitement adaptée à l'industrie.

Bibliography

[1] Philip Garrou, Peter Ramm, and Mitsumasa Koyanagi. *3D IC Integration since 2008*, pages 1–12. Wiley-VCH Verlag GmbH & Co. KGaA, 2014. (Cited on pages 1, 5 and 15.)

[2] S. Lhostis, A. Farcy, E. Deloffre, F. Lorut, S. Mermoz, Y. Henrion, L. Berthier, F. Bailly, D. Scevola, F. Guyader, F. Gigon, C. Besset, S. Pellissier, L. Gay, N. Hotellier, A. . Le Berrigo, S. Moreau, V. Balan, F. Fournel, A. Jouve, S. Cheramy, M. Arnoux, B. Rebhan, G. A. Maier, and L. Chitu. Reliable 300 mm wafer level hybrid bonding for 3D stacked cmos image sensors. In *Proceedings - Electronic Components and Technology Conference*, volume 2016-August, pages 869–876, 2016. (Cited on pages 2, 6, 15, 16, 17 and 130.)

[3] Aaron D. Franklin, Mathieu Luisier, Shu-Jen Han, George Tulevski, Chris M. Breslin, Lynne Gignac, Mark S. Lundstrom, and Wilfried Haensch. Sub-10 nm carbon nanotube transistor. *Nano Letters*, 12(2):758–762, 2012. PMID: 22260387. (Cited on page 12.)

[4] J.R. Powell. The quantum limit to Moore's law. *Proceedings of the IEEE*, 96(8):1247–1248, 2008. cited By 26. (Cited on page 12.)

[5] R. Zhang, K. Roy, C.-K. Koh, and D.B. Janes. Power trends and performance characterization of 3-dimensional integration. In *ISCAS 2001 - 2001 IEEE International Symposium on Circuits and Systems, Conference Proceedings*, volume 4, pages 414–417, 2001. cited By 8. (Cited on page 13.)

[6] J.H. Lau. Overview and outlook of three-dimensional integrated circuit packaging, three-dimensional Si integration, and three-dimensional integrated circuit integration. *Journal of Electronic Packaging, Transactions of the ASME*, 136(4), 2014. cited By 12. (Cited on pages 13 and 14.)

[7] Y. Guillou and A.-M. Dutron. 3D IC products using tsv for mobile phone applications: An industrial perpective. In *2009 European Microelectronics and Packaging Conference, EMPC 2009*, 2009. cited By 10. (Cited on pages 13 and 15.)

[8] S. Sukegawa, T. Umebayashi, T. Nakajima, H. Kawanobe, K. Koseki, I. Hirota, T. Haruta, M. Kasai, K. Fukumoto, T. Wakano, K. Inoue, H. Takahashi, T. Nagano, Y. Nitta, T. Hirayama, and N. Fukushima. A 1/4-inch 8mpixel back-illuminated stacked cmos image sensor. In *Digest of Technical Papers - IEEE International Solid-State Circuits Conference*, volume 56, pages 484–485, 2013. cited By 67. (Cited on pages 14 and 15.)

[9] System Plus consulting. Samsung 3D TSV stacked DRAM, 2015. (Cited on pages 14 and 15.)

[10] Yole developpement. 3D TSV & 2.5D interconnect for advanced packaging, 2016. (Cited on page 15.)

[11] G. Druais, P. Ancey, C. Aumont, V. Caubet, L.-L. Chapelon, C. Chaton, S. Cheramy, S. Cordova, E. Cirot, J.-P. Colonna, P. Coudrain, T. Divel, Y. Dodo, A. Farcy, N. Guitard, K. Haxaire, N. Hotellier, F. Leverd, R. Liou, J. Michailos, A. Ostrovsky, S. Petitdidier, J. Pruvost, D. Riquet, O. Robin, E. Saugier, and N. Sillon. 3D integration demonstration of a wireless product with design partitioning. In *2011 IEEE International 3D Systems Integration Conference, 3DIC 2011*, 2011. cited By 11. (Cited on page 15.)

[12] P. Coudrain, J.-P. Colonna, C. Aumont, G. Garnier, P. Chausse, R. Segaud, K. Vial, A. Jouve, T. Mourier, T. Magis, P. Besson, L. Gabette, C. Brunet-Manquat, N. Allouti, C. Laviron, S. Cheramy, E. Saugier, J. Pruvost, A. Farcy, and N. Hotellier. Towards efficient and reliable 300mm 3D technology for wide I/O interconnects. In *Proceedings of the 2012 IEEE 14th Electronics Packaging Technology Conference, EPTC 2012*, pages 330–335, 2012. cited By 13. (Cited on page 15.)

[13] J. Michailos, P. Coudrain, A. Farcy, N. Hotellier, S. Cheramy, S. Lhostis, E. Deloffre, Y. Sanchez, A. Jouve, F. Guyader, E. Saugier, V. Fiori, P. Vivet, M. Vinet, C. Fenouillet-Beranger, F. Casset, P. Batude, F. Breuf, Y. Henrion, B. Vianne, L. . Collin, J. . Colonna, L. Benaissa, L. Brunet, R. Prieto, R. Velard, and F. Ponthenier. New challenges and opportunities for 3D integrations. In *Technical Digest - International Electron Devices Meeting, IEDM*, volume 2016-February, pages 8.5.1–8.5.4, 2016. (Cited on page 15.)

[14] Y. Kim, J. Baek, and D. Hwang. Ring artifact correction using detector lineratios in computed tomography. *Optics Express*, 22(11):13380–13392, 2014. (Cited on page 15.)

[15] Sarah Eunkyung Kim and Sungdong Kim. Wafer level Cu-Cu direct bonding for 3D integration. *Microelectronic Engineering*, 137:158 – 163, 2015. Materials for Advanced Metallization 2014. (Cited on page 17.)

[16] Y. Beilliard, S. Moreau, L. Di Cioccio, P. Coudrain, G. Romano, A. Nowodzinski, F. Aussenac, P.-H. Jouneau, E. Rolland, and T. Signamarcheix. Advances toward reliable high density Cu-Cu interconnects by Cu-SiO_2 direct hybrid bonding. In *2014 International 3D Systems Integration Conference, 3DIC 2014 - Proceedings*, 2014. cited By 4. (Cited on page 16.)

[17] J. De Vos, L. Bogaerts, T. Buisson, C. Gerets, G. Jamieson, K. Vandersmissen, A.L. Manna, and E. Beyne. Key elements for sub-50Î$\frac{1}{4}$m pitch micro bump processes. pages 1122–1126, 2013. cited By 14. (Cited on page 16.)

[18] P. Gondcharton, B. Imbert, L. Benaissa, V. Carron, and M. Verdier. Kinetics of low temperature direct copper – copper bonding. *Microsystem Technologies*, 2015. Article in Press. (Cited on page 16.)

[19] B. Imbert, P. Gondcharton, L. Benaissa, F. Fournel, and M. Verdier. Wafer level metallic bonding: Voiding mechanisms in copper layers. In *2015 IEEE International Interconnect Technology Conference and 2015 IEEE Materials for Advanced Metallization Conference, IITC/MAM 2015*, pages 201–204, 2015. (Cited on page 16.)

[20] P. Gondcharton. *Intégration du collage direct: couches minces métalliques et évolutions morphologiques*. PhD thesis, Université de Grenoble, 2015. (Cited on pages 18 and 21.)

[21] F. Lorut, Hotellier N., S. Lhostis, and Ponthenier F. Imaging techniques comparison for advanced 3Di devices characterization. In *Fourty First International Symposium for Testing and Failure Analysis*, 2015. (Cited on page 18.)

[22] J. Bertheau. *Étude et caractérisation d'interconnexions intermétalliques á partir de plots de cuivre et d'alliages SnAgSn pour l'empilement tridimentionnel de composants actifs*. PhD thesis, Université de Grenoble, 2014. (Cited on page 18.)

[23] J. Bertheau, F. Hodaj, N. Hotellier, and J. Charbonnier. Effect of intermetallic compound thickness on shear strength of 25 μm diameter Sn-pillars. *Intermetallics*, 51:37–47, 2014. (Cited on pages 19 and 20.)

[24] Y. . Chang and K. . Chen. Fabrication and reliability investigation of copper pillar and tapered through silicon via (TSV) for direct bonding in 3D integration. In *Proceedings of the International Symposium on the Physical and Failure Analysis of Integrated Circuits, IPFA*, volume 2015-August, pages 439–442, 2015. (Cited on page 19.)

[25] M. Huang, O. G. Yeow, C. Y. Poo, and T. Jiang. Intermetallic formation of copper pillar with Sn-Ag-Sn for flip-chip-on-module packaging. *IEEE Transactions on Components and Packaging Technologies*, 31(4):767–775, 2008. (Cited on page 19.)

[26] S. Lee, Y. X. Guo, and C. K. Ong. Electromigration effect on Sn-pillar(Sn) bumps. In *Proceedings of 7th Electronics Packaging Technology Conference, EPTC 2005*, volume 1, pages 135–139, 2005. (Cited on page 19.)

[27] Z. Min-Bo, M. Xiao, and Z. Xin-Ping. Size effect on the intermetallic compound coalescence in Sn-Ag-Sn solder and Sn-Ag-Sn/Sn solder joints. In *ICEPT-HDP 2011 Proceedings - 2011 International Conference on Electronic Packaging Technology and High Density Packaging*, pages 248–253, 2011. (Cited on page 19.)

[28] O. Vallin, K. Jonsson, and U. Lindberg. Adhesion quantification methods for wafer bonding. *Materials Science and Engineering R: Reports*, 50(4-5):109–165, 2005. cited By 74. (Cited on page 20.)

[29] R. Schurch, S. Rowland, R. Bradley, and P. Withers. Comparison and combination of imaging techniques for three dimensional analysis of electrical trees. *IEEE Transactions on Dielectrics and Electrical Insulation*, 22(2):709–719, 2015. (Cited on page 21.)

[30] T. L. Burnett, R. Kelley, B. Winiarski, L. Contreras, M. Daly, A. Gholinia, M. G. Burke, and P. J. Withers. Large volume serial section tomography by xe plasmaFIB dual beam microscopy. *Ultramicroscopy*, 161:119–129, 2016. (Cited on pages 21, 34, 40 and 85.)

[31] J. Goldstein, D. Newbury, D. Joy, C. Lyman, P. Echlin, E. Lifshin, L. Sawyer, and J. Michael. *Scanning Electron Microscopy and X-ray Microanalysis, Third edition*. Luwer Academic /Plenum Publishers, New York, 2003. (Cited on pages 24 and 31.)

[32] L.A. Giannuzzi, B.W. Kemshall, S.M. Schwarz, J.K. Lomness, B.I. Prenitzer, and F.A. Stevie. *Introduction to Focused Ion Beams - Instrumentation, Theory, Techniques and Practice*. Springer, 2005. (Cited on pages 24, 33 and 36.)

[33] P. Tesch, N. Smith, N. Martin, and D. Kinion. High current focused ion beam instrument for destructive physical analysis applications. In *Conference Proceedings from the International Symposium for Testing and Failure Analysis*, pages 7–13, 2008. (Cited on pages 24 and 29.)

[34] A. H. V. Van Veen, C. W. Hagen, J. E. Barth, and P. Kruit. Reduced brightness of the ZrO/W schottky electron emitter. *Journal of Vacuum Science and Technology B: Microelectronics and Nanometer Structures*, 19(6):2038–2044, 2001. (Cited on pages 26 and 28.)

[35] M. Bronsgeest. *Physics of Schottky electron sources: Theory and optimum operation*, pages 1–256. Physics of Schottky Electron Sources: Theory and Optimum Operation. Pan Stanford, 2014. (Cited on page 28.)

[36] H. Kawano. Effective work functions for ionic and electronic emissions from mono- and polycrystalline surfaces. *Progress in Surface Science*, 83(1-2):1–165, 2008. (Cited on page 28.)

[37] D. W. Tuggle, J. Z. Li, and L. W. Swanson. Point cathodes for use in virtual source electron optics. *Journal of microscopy*, 140(3):293–301, 1985. (Cited on page 28.)

[38] M. J. Fransen, M. H. F. Overwijk, and P. Kruit. Brightness measurements of a ZrO/W Schottky electron emitter in a transmission electron microscope. *Applied Surface Science*, 146(1):357–362, 1999. (Cited on page 28.)

[39] L. W. Swanson, G. A. Schwind, S. M. Kellogg, and K. Liu. Computer modeling of the schottky electron source. *Journal of Vacuum Science and Technology B: Nanotechnology and Microelectronics*, 30(6), 2012. (Cited on page 28.)

[40] N. S. Smith, W. P. Skoczylas, S. M. Kellogg, D. E. Kinion, P. P. Tesch, O. Sutherland, A. Aanesland, and R. W. Boswell. High brightness inductively coupled plasma source for high current focused ion beam applications. *Journal of Vacuum Science and Technology B: Microelectronics and Nanometer Structures*, 24(6):2902–2906, 2006. (Cited on page 29.)

[41] R. Smith and J.-M. Walls. *Ion erosion in surface analysis*, chapter 2, pages 20–56. Elsevier Science Ltd, 1990. (Cited on page 29.)

[42] J. Keller, N. Smith, R. Boswell, L. Scipioni, C. Charles, and O. Sutherland. Magnetically enhanced, inductively coupled plasma source for a focused ion beam system. (Cited on page 29.)

[43] P. Sigmund. sputtering processes: collision cascades and spikes. In N.H. TOLK, J.C. TULLY, W. HEILAND, and C.W. WHITE, editors, *Inelastic Ion – Surface Collisions*, pages 121 – 152. Academic Press, 1977. (Cited on page 33.)

[44] S Rubanov and PR Munroe. FIB-induced damage in silicon. *JOURNAL OF MICROSCOPY-OXFORD*, 214(3):213–221, JUN 2004. Meeting on Advances in Focused Ion Beam Microscopy (NanoFIB 2003), Corpus Christi College, Cambridge, ENGLAND, APR 04, 2003. (Cited on pages 33 and 34.)

[45] T. Hrnčíř, M. Šikula, Obonă J.-V., and P. Gounet. How to achieve artifact-free FIB milling on polyimide packages. In *Proceeding of ISTFA 2016*, 2016. (Cited on page 33.)

[46] S. Moreau, D. Bouchu, and G. Audoit. Fast and easy sample preparation with reduced curtaining artifacts using a P-FIB. In *2014 IEEE 21ST INTERNATIONAL SYMPOSIUM ON THE PHYSICAL AND FAILURE ANALYSIS OF INTEGRATED CIRCUITS (IPFA)*, IEEE International Symposium on the Physical and Failure Analysis of Integrated Circuits, pages 231–235. IEEE; FEI Co USA; IEEE Singapore Reliabl CPMT ED Chapter; Elect Devices Soc; Reliabl Soc, 2014. 21st IEEE International Symposium on the Physical and Failure Analysis of Integrated Circuits (IPFA), SINGAPORE, JUN 30-JUL 04, 2014. (Cited on page 33.)

[47] L. Kwakman, G. Franz, M. M. V. Taklo, A. Klumpp, and P. Ramm. Characterization and failure analysis of 3D integrated systems using a novel plasma-FIB system. In *AIP Conference Proceedings*, volume 1395, pages 269–273, 2011. (Cited on page 34.)

[48] T. Hrnčíř and L. Hladík. Fast and precise 3D tomography of TSV by using Xe plasma FIB. In *Conference Proceedings from the International Symposium for Testing and Failure Analysis*, pages 27–32, 2013. (Cited on pages 34 and 40.)

[49] NI Kato. Reducing focused ion beam damage to transmission electron microscopy samples. *JOURNAL OF ELECTRON MICROSCOPY*, 53(5):451–458, 2004. (Cited on page 34.)

[50] G. Spoldi, S. Beuer, M. Rommel, V. Yanev, A. J. Bauer, and H. Ryssel. Experimental observation of FIB induced lateral damage on silicon samples. *Microelectronic Engineering*, 86(4-6):548–551, 2009. (Cited on page 34.)

[51] M. Rommel, G. Spoldi, V. Yanev, S. Beuer, B. Amon, J. Jambreck, S. Petersen, A. J. Bauer, and L. Frey. Comprehensive study of focused ion beam induced lateral damage in silicon by scanning probe microscopy techniques. *Journal of Vacuum Science and Technology B: Nanotechnology and Microelectronics*, 28(3):595–607, 2010. (Cited on page 34.)

[52] H. Seiler. Secondary electron emission in the scanning electron microscope. *Journal of Applied Physics*, 54(11):R1–R18, 1983. (Cited on page 36.)

[53] J. Orloff, L. Swanson, and M. Utlaut. *High Resolution Focused Ion Beams: FIB and its Applications*. Springer US, first edition, 2003. (Cited on page 36.)

[54] Stefan Zaefferer and Nahid-Nora Elhami. Theory and application of electron channelling contrast imaging under controlled diffraction conditions. *Acta Materialia*, 75:20 – 50, 2014. (Cited on page 36.)

[55] L.A. Giannuzzi and J.R. Michael. Ion channeling vs. electron channeling image contrast. *Microscopy and Microanalysis*, 18:694–695, 7 2012. (Cited on page 36.)

[56] C. Langlois, T. Douillard, H. Yuan, N. P. Blanchard, A. Descamps-Mandine, B. Van de Moortèle, C. Rigotti, and T. Epicier. Crystal orientation mapping via ion channeling: An alternative to EBSD. *Ultramicroscopy*, 157:65–72, 2015. (Cited on page 36.)

[57] N. Bassim, K. Scott, and L. A. Giannuzzi. Recent advances in focused ion beam technology and applications. *MRS Bulletin*, 39(4):317–325, 2014. (Cited on page 37.)

[58] W. Denk and H. Horstmann. Serial block-face scanning electron microscopy to reconstruct three-dimensional tissue nanostructure. *PLoS Biology*, 2(11), 2004. (Cited on page 37.)

[59] L. Holzer, F. Indutnyi, Ph. Gasser, B. Münch, and M. Wegmann. Three-dimensional analysis of porous $BaTiO_3$ ceramics using FIB nanotomography. *Journal of microscopy*, 216(1):84–95, 2004. (Cited on pages 37 and 39.)

[60] M. A. Mangan, P. D. Lauren, and G. J. Shiflet. Three-dimensional reconstruction of widmanstatten plates in Fe-12.3Mn- 0.8C. *Journal of microscopy*, 188(1):36–41, 1997. (Cited on page 37.)

[61] A. Zankel, J. Wagner, and P. Poelt. Serial sectioning methods for 3D investigations in materials science. *Micron*, 62:66–78, 2014. (Cited on page 37.)

[62] A. Kirubanandham, I. Lujan-Regalado, R. Vallabhaneni, and N. Chawla. Three dimensional characterization of tin crystallography and Sn_6Sn_5 intermetallics in solder joints by multiscale tomography. *JOM*, 68(11):2879–2887, 2016. (Cited on page 37.)

[63] M. Ito and J. Kato. 3D analysis of a copper flip-chip interconnection using FIB-SEM slice and view. *Electronic Device Failure Analysis*, 18(1):14–20, 2016. (Cited on page 37.)

[64] M. D. Uchic, L. Holzer, B. J. Inkson, E. L. Principe, and P. Munroe. Three-dimensional microstructural characterization using focused ion beam tomography. *MRS Bulletin*, 32(5):408–416, 2007. (Cited on page 39.)

[65] M. Cantoni and L. Holzer. Advances in 3D focused ion beam tomography. *MRS Bulletin*, 39(4):354–360, 2014. (Cited on page 39.)

[66] K. Kim, N. Green, and W. Griffiths. Focused ion beam milling and imaging: An advanced method to detect fine inclusions in cast aluminium alloys. *Materials Science Forum*, 765:150–154, 2013. (Cited on page 39.)

[67] Y. Miyamura, T. Sekiguchi, J. Chen, J. Y. Li, K. Watanabe, K. Kumagai, and A. Ogura. Focused ion beam imaging of defects in multicrystalline Si for photovoltaic application. *Acta Physica Polonica A*, 125(4):991–993, 2014. (Cited on page 39.)

[68] T. Hrnčíř, L. Hladík, and M. Zadrazil. Fast 3D tomography at package level by using Xe plasma focused ion beam. In *Proceedings of the International Symposium on the Physical and Failure Analysis of Integrated Circuits, IPFA*, pages 112–115, 2013. (Cited on pages 40 and 85.)

[69] L. A. Giannuzzi, J. L. Drown, S. R. Brown, R. B. Irwin, and F. A. Stevie. Focused ion beam milling and micromanipulation lift-out for site specific cross-section TEM specimen preparation. In *Materials Research Society Symposium - Proceedings*, volume 480, pages 19–27, 1997. (Cited on page 40.)

[70] L.A. Giannuzzi, B.W. Kemshall, S.M. Schwarz, J.K. Lomness, B.I. Prenitzer, and F.A. Stevie. *FIB lift-out sample preparation techniques - in situ and ex situ methods*, chapter 10. Springer, 2005. (Cited on page 40.)

[71] D. Tomus and H. P. Ng. In situ lift-out dedicated techniques using fib-sem system for tem specimen preparation. *Micron*, 44(1):115–119, 2013. (Cited on page 40.)

[72] G. Divitini, O. Stenzel, A. Ghadirzadeh, S. Guarnera, V. Russo, C. S. Casari, A. L. Bassi, A. Petrozza, F. Di Fonzo, V. Schmidt, and C. Ducati. Nanoscale

analysis of a hierarchical hybrid solar cell in 3D. *Advanced Functional Materials*, 24(20):3043–3050, 2014. (Cited on page 40.)

[73] J. Mahamid, R. Schampers, H. Persoon, A. A. Hyman, W. Baumeister, and J. M. Plitzko. A focused ion beam milling and lift-out approach for site-specific preparation of frozen-hydrated lamellas from multicellular organisms. *Journal of structural biology*, 192(2):262–269, 2015. (Cited on page 40.)

[74] T. J. Prosa and D. J. Larson. Modern focused-ion-beam-based site-specific specimen preparation for atom probe tomography. *Microscopy and Microanalysis*, pages 1–16, 2017. Article in Press. (Cited on page 40.)

[75] S. Padalkar, J. R. Riley, Q. Li, G. T. Wang, and L. J. Lauhon. Lift-out procedures for atom probe tomography targeting nanoscale features in core-shell nanowire heterostructures. *Physica Status Solidi (C) Snrrent Topics in Solid State Physics*, 11(3-4):656–661, 2014. (Cited on page 40.)

[76] P. Bleuet, G. Audoit, J. . Barnes, J. Bertheau, Y. Dabin, H. Dansas, J. . Fabbri, B. Florin, P. Gergaud, A. Grenier, G. Haberfehlner, E. Lay, J. Laurencin, R. Serra, and J. Villanova. Specifications for hard condensed matter specimens for three-dimensional high-resolution tomographies. *Microscopy and Microanalysis*, 19(3):726–739, 2013. (Cited on page 40.)

[77] M. Hubert, J. Laurencin, P. Cloetens, J. C. da Silva, F. Lefebvre-Joud, P. Bleuet, A. Nakajo, and E. Siebert. Role of microstructure on electrode operating mechanisms for mixed ionic electronic conductors: From synchrotron-based 3D reconstruction to electrochemical modeling. *Solid State Ionics*, 294:90–107, 2016. (Cited on page 40.)

[78] G. Audoit, P. Bleuet, G. Delpy, and L. Kwakman. Plasma-fib sample preparation for x-ray tomography of 3D-IC interconnects. In *Conference Proceedings from the 42nd International Symposium for Testing and Failure Analysis*, pages 583–585, 2016. (Cited on pages 40 and 42.)

[79] J. Als-Nielsen and D. McMorrow. *Elements of Modern X-ray Physics: Second Edition*. Wiley, 2011. (Cited on pages 46, 47, 48 and 53.)

[80] L. A. Gomes Perini, P. Bleuet, J. Filevich, W. Parker, B. Buijsse, and L. F. Tz. Kwakman. Developments on a SEM-based X-ray tomography system: Stabilization scheme and performance evaluation. *Review of Scientific Instruments*, 88(6):063706, 2017. (Cited on page 49.)

[81] Jean DOUCET and José BARUCHEL. Rayonnement synchrotron et applications. *Techniques de l'ingénieur CND: méthodes globales et volumiques*, base documentaire: TIB585DUO.(ref. article: p2700), 2011. fre. (Cited on pages 52 and 53.)

[82] E.B. Podgorsak. *Radiation Oncology Physics*. INTERNATIONAL ATOMIC ENERGY AGENCY, Vienna, 2005. (Cited on page 55.)

[83] ESRF. *UPBL4 Nano-Imaging and Nano-Analysis - Technical Design Report*, 2010. (Cited on page 59.)

[84] P. Kirkpatrick and A.V. Baez. Formation of optical images by x-rays. *Journal of the Optical Society of America*, 38(9):766–774, 1948. cited By 789. (Cited on page 59.)

[85] C. Morawe, R. Barrett, P. Cloetens, B. Lantelme, J-Ch. Peffen, and A. Vivo. Graded multilayers for figured kirkpatrick-baez mirrors on the new ESRF end station ID16A. In *Proceedings of SPIE - The International Society for Optical Engineering*, volume 9588, 2015. cited By 3. (Cited on page 59.)

[86] Julio Cesar Da Silva, Alexandra Pacureanu, Yang Yang, Sylvain Bohic, Christian Morawe, Raymond Barrett, and Peter Cloetens. Efficient concentration of high-energy x-rays for diffraction-limited imaging resolution. *Optica*, 4(5):492–495, May 2017. (Cited on page 59.)

[87] G. A. Chahine, M. Richard, R. A. Homs-Regojo, T. N. Tran-Caliste, D. Carbone, V. L. R. Jaques, R. Grifone, P. Boesecke, J. Katzer, I. Costina, H. Djazouli, T. Schroeder, and T. U. Schülli. Imaging of strain and lattice orientation by quick scanning x-ray microscopy combined with three-dimensional reciprocal space mapping. *Journal of Applied Crystallography*, 47(2):762–769, 2014. (Cited on pages 61, 80, 81 and 82.)

[88] C. Ponchut, J.M. Rigal, J. Clément, E. Papillon, A. Homs, and S. Petitdemange. Maxipix, a fast readout photon-counting x-ray area detector for synchrotron applications. *Journal of Instrumentation*, 6(1), 2011. cited By 78. (Cited on pages 61 and 78.)

[89] Roger J. Dejus and Manuel Sanchez del Rio. XOP: A graphical user interface for spectral calculations and x-ray optics utilities. *Review of Scientific Instruments*, 67(9):3356–3356, 1996. (Cited on pages 66 and 75.)

[90] U. Bonse and M. Hart. An x-ray interferometer. *Applied Physics Letters*, 6(8):155–156, 1965. cited By 738. (Cited on page 64.)

[91] D. Chapman, W. Thomlinson, R.E. Johnston, D. Washburn, E. Pisano, N. Gmür, Z. Zhong, R. Menk, F. Arfelli, and D. Sayers. Diffraction enhanced x-ray imaging. *Physics in Medicine and Biology*, 42(11):2015–2025, 1997. cited By 846. (Cited on page 64.)

[92] A. Momose. Phase-sensitive imaging and phase tomography using x-ray interferometers. *Optics Express*, 11(19):2303–2314, 2003. cited By 185. (Cited on page 64.)

[93] A. Olivo and R.D. Speller. A novel x-ray imaging technique based on coded apertures making phase contrast imaging feasible with conventional sources. In *IEEE Nuclear Science Symposium Conference Record*, pages 1447–1450, 2008. cited By 0. (Cited on page 64.)

[94] J.W. Goodman. *Introduction to Fourier optics*. New York: Roberts and Company Publishers, 2005. (Cited on page 66.)

[95] J.P. Guigay. Fourier transform analysis of fresnel diffraction patterns and in-line holograms. *Optik (Jena)*, 49(1):121–125, 1977. cited By 124. (Cited on page 66.)

[96] Anna Burvall, Ulf Lundström, Per A. C. Takman, Daniel H. Larsson, and Hans M. Hertz. Phase retrieval in x-ray phase-contrast imaging suitable for tomography. *Opt. Express*, 19(11):10359–10376, May 2011. (Cited on page 67.)

[97] L. Weber, M. Langer, S. Tavella, A. Ruggiu, and F. Peyrin. Quantitative evaluation of regularized phase retrieval algorithms on bone scaffolds seeded with bone cells. *Physics in Medicine and Biology*, 61(9):N215–N231, 2016. (Cited on page 67.)

[98] Michael Reed Teague. Irradiance moments: Their propagation and use for unique retrieval of phase. *J OPT SOC AM*, V 72(N 9):1199–1209, 1982. cited By 140. (Cited on page 67.)

[99] Peter Cloetens. *Contribution to Phase Contrast Imaging, Reconstruction ans Tomography with Hard Synchrotron Radiation*. PhD thesis, Vrije Universiteit Brussel, 1999. (Cited on page 67.)

[100] P. Cloetens, W. Ludwig, J. Baruchel, D. Van Dyck, J. Van Landuyt, J. P. Guigay, and M. Schlenker. Holotomography: Quantitative phase tomography with micrometer resolution using hard synchrotron radiation x rays. *Applied Physics Letters*, 75(19):2912–2914, 1999. (Cited on page 67.)

[101] F. Peyrin, P. Cloetens, M Salome-Pateyron, J Baruchel, and P. Spanne. Reconstruction 3D en tomographie par rayonnement synchrotron coherent. *Seizième colloque GRETSI*, 1997. (Cited on page 70.)

[102] H. Yu, Q. Xu, X. Mou, and G. Wang. Recent progress in local reconstruction. In *Proceedings of SPIE - The International Society for Optical Engineering*, volume 7804, 2010. cited By 1. (Cited on page 71.)

[103] A. C. Kak and B. A. Roberts. Reconstruction from projections: applications in computerized tomography. *Handbook of pattern recognition and image processing*, pages 649–693, 1986. (Cited on page 71.)

[104] Steven W. Smith. *the scientist and engineer's guide the digital signal processing*. California Technical Pub., 1997, 1997. (Cited on page 72.)

[105] M. Beister, D. Kolditz, and W.A. Kalender. Iterative reconstruction methods in x-ray CT. *Physica Medica*, 28(2):94–108, 2012. cited By 222. (Cited on pages 73 and 74.)

[106] Avinash Kak and Malcolm Slaney. *Principles of Computerized Tomographic Imaging*. Society for Industrial and Applied Mathematics, 1988. (Cited on page 74.)

[107] W. Van Aarle, W. J. Palenstijn, J. De Beenhouwer, T. Altantzis, S. Bals, K. J. Batenburg, and J. Sijbers. The ASTRA toolbox: A platform for advanced algorithm development in electron tomography. *Ultramicroscopy*, 157:35–47, 2015. (Cited on pages 74 and 123.)

[108] Delei Chen, Bart Goris, Folkert Bleichrodt, Hamed Heidari Mezerji, Sara Bals, Kees Joost Batenburg, Gijsbertus de With, and Heiner Friedrich. The properties of SIRT, TVM, and DART for 3D imaging of tubular domains in nanocomposite thin-films and sections. *Ultramicroscopy*, 147:137 – 148, 2014. (Cited on page 74.)

[109] FEI. ifast. (Cited on page 86.)

[110] M. Salzer, S. Thiele, R. Zengerle, and V. Schmidt. On the importance of fib-sem specific segmentation algorithms for porous media. *Materials Characterization*, 95:36–43, 2014. (Cited on page 106.)

[111] T. Prill, K. Schladitz, D. Jeulin, M. Faessel, and C. Wieser. Morphological segmentation of fib-sem data of highly porous media. *Journal of Microscopy*, 250(2):77–87, 2013. (Cited on page 106.)

[112] Hiroshi Iwai, Naoki Shikazono, Toshiaki Matsui, Hisanori Teshima, Masashi Kishimoto, Ryo Kishida, Daisuke Hayashi, Katsuhisa Matsuzaki, Daisuke Kanno, Motohiro Saito, Hiroki Muroyama, Koichi Eguchi, Nobuhide Kasagi, and Hideo Yoshida. Quantification of sofc anode microstructure based on dual beam fib-sem technique. *Journal of Power Sources*, 195(4):955 – 961, 2010. (Cited on page 106.)

[113] A. Fraczkiewicz, E. Capria, P. Cloetens, J. Da Silva, A. Jouve, S. Lhostis, F. Lorut, T. Mourier, and P. Bleuet. High resolution x-ray computed tomography: what synchrotron sources can bring to 3Di devices failure analysis. *Conference Proceedings from the International Symposium for Testing and Failure Analysis 2016*, 2016. (Cited on page 112.)

[114] N Capit, G Da Costa, Y Georgiou, G Huard, C Martin, G Mounie, P Neyron, and O Richard. A batch scheduler with high level components. In *2005 IEEE INTERNATIONAL SYMPOSIUM ON CLUSTER COMPUTING AND THE GRID, VOLS 1 AND 2*, pages 776–783, 2005. (Cited on page 113.)

[115] R. Daudin, S. Terzi, P. Lhuissier, J. Tamayo, M. Scheel, N. Hari Babu, D.G. Eskin, and L. Salvo. Particle-induced morphological modification of Al alloy equiaxed dendrites revealed by sub-second in situ microtomography. *Acta Materialia*, 125(Supplement C):303 – 310, 2017. (Cited on page 114.)

[116] P.-O. Autran. Amélioration des algorithmes de reconstruction d'images d'objects 3d, fournis par le synchrotron. (Cited on page 123.)

[117] Wang Zhou, Alan Conrad Bovik, Hamid Rahim Sheikh, and Eero P Simoncelli. Image quality assessment: from error visibility to structural similarity. *IEEE transactions on image processing: a publication of the IEEE Signal Processing Society*, 13:600–612, April 2004. (Cited on page 123.)

[118] S. Moreau, D. Bouchu, V. Balan, A.-L.L. Berrigo, A. Jouve, Y. Henrion, C. Besset, D. Scevola, S. Lhostis, F. Guyader, E. Deloffre, S. Mermoz, and J. Pruvost. Mass transport-induced failure of hybrid bonding-based integration for advanced image sensor applications. In *Proceedings - Electronic Components and Technology Conference*, volume 2016-August, pages 1940–1945, 2016. cited By 1. (Cited on page 130.)

[119] P. G. Evans, G. Chahine, R. Grifone, V. L. R. Jacques, J. W. Spalenka, and T. U. Schülli. Compact ultrahigh vacuum sample environments for x-ray nanobeam diffraction and imaging. *Review of Scientific Instruments*, 84(11), 2013. (Cited on page 148.)

[120] B. Vianne, S. Escoubas, C. Krauss, M. . Richard, S. Labat, G. Chahine, J. . Micha, T. Schülli, V. Fiori, A. Farcy, and O. Thomas. Temperature dependency of the strain distribution induced by tsvs in silicon: A comparative study between micro-laue and monochromatic nano-diffraction. *Microelectronic Engineering*, 156:59–64, 2016. (Cited on page 151.)

[121] D. F. Sanchez, S. Reboh, M. L. D. Weleguela, J. . Micha, O. Robach, T. Mourier, P. Gergaud, and P. Bleuet. In-situ x-ray μlaue diffraction study of copper through-silicon vias. *Microelectronics Reliability*, 56:78–84, 2016. (Cited on page 151.)

[122] A.S. Budiman, H.-A.-S. Shin, B.-J. Kim, S.-H. Hwang, H.-Y. Son, M.-S. Suh, Q.-H. Chung, K.-Y. Byun, N. Tamura, M. Kunz, and Y.-C. Joo. Measurement of stresses in Sn and Si around through-silicon via by synchrotron x-ray microdiffraction for 3-dimensional integrated circuits. *Microelectronics Reliability*, 52(3):530 – 533, 2012. Special section on International Seminar on Power Semiconductors 2010. (Cited on page 151.)

[123] Mirko Holler, Manuel Guizar-Sicairos, Esther H. R. Tsai, Roberto Dinapoli, Elisabeth Muller, Oliver Bunk, Jorg Raabe, and Gabriel Aeppli. High-resolution non-destructive three-dimensional imaging of integrated circuits. *NATURE*, 543(7645):402+, MAR 16 2017. (Cited on pages 154 and 159.)

Scientific contributions

Communications in conferences

A. Fraczkiewicz, E. Capria, P. Cloetens, J. Da Silva, P. Gondcharton, A. Jouve, F. Lorut, T. Mourier, P. Bleuet, Tomographie par rayons X appliquée à l'intégration 3D: vers une information statistique sub-50 nm **poster**, *RX et matière 2015*, Grenoble, France

A.Fraczkiewicz, E.Capria, G.Chahine, P.Cloetens, J.Da-Silva, A.Jouve, F.Lorut, S.Lhostis, M-I. Richard, P.Bleuet, 3D morphological and structural nanocharacterization for microelectronics: the potential of recent, long synchrotron beamlines, **poster**, *XRM 2016*, Oxford, UK

A.Fraczkiewicz, E.Capria, P.Cloetens, J.Da Silva, A.Jouve, S.Lhostis, F.Lorut, T.Mourier, P.Bleuet, High resolution x-ray computed tomography: what synchrotron sources can bring to 3Di devices failure analysis, **oral presentation and published proceeding**, *42nd International Symposium on Testing and Failure Analysis 2016*, Fort Worth, Texas, US

A.Fraczkiewicz, P.-O. Autran, E.Capria, P.Cloetens, J.Da Silva, S.Lhostis, F.Lorut, S. Moreau, T.Mourier, P.Bleuet, Making synchrotron tomography a routine tool for 3D integration failure analysis through a limited number of projections, an adapted sample preparation scheme, and a fully-automated post-processing, **oral presentation and published proceeding**, *43rd International Symposium on Testing and Failure Analysis 2016*, Pasadena, California, US

Articles submitted to peer-reviewed journals

A.Fraczkiewicz, F.Lorut, G.Audoit, E.Boller, E.Capria, P.Cloetens, J.Da Silva, A.Farcy, T.Mourier, F.Ponthenier, P.Bleuet, 3D high resolution imaging for microelectronics: a multi-technique survey on copper pillars, *Ultramicrosopy*, **submitted**

A.Fraczkiewicz, M.-I. Richard, E. Capria, G. Chahine, P. Cloetens, J. Da Silva, A. Jouve, S. Lhostis, F. Lorut, P. Bleuet, In-situ local strain measurement and morphology correlation in hybrid bonding stacks using nano-focused x-ray and electron microscopy, **to be submitted**

Résumé

Ce travail de thèse vise à développer de nouvelles techniques de caractérisation pour l'intégration 3D en micro-électronique. Plus précisément, ce travail porte sur l'imagerie 3D de tels objets et la mesure des contraintes par diffraction de Bragg, réalisées sur de récentes lignes de lumière de l'ESRF (European Synchrotron Radiation Facility).

L'intégration 3D a pour but de répondre aux besoins de performance de la micro-électronique, en empilant les différents éléments constituant les puces au lieu de les placer les uns à côté des autres; ceci permet de limiter la place qu'ils occupent et la longueur des connections. Pour ce faire, de nouvelles connections entre puces ont du être développées, telles que les piliers de cuivre et les pads de cuivre, utilisés dans le cas du collage hybride. Afin de maîtriser leurs procédés de fabrication, il est important de pouvoir caractériser ces objets, à la fois par des moyens d'imagerie et de mesure de la déformation dans les puces. Ces mesures doivent permettre un large champ de vue (100 μm^2), ainsi qu'une haute résolution (50 nm). De plus, afin de satisfaire les besoins en temps de l'industrie micro-électronique, les techniques choisies doivent être aussi rapides et automatiques que possible.

Pour satisfaire ces besoins, plusieurs techniques ont été étudiées durant ces travaux de thèse.

Une technique d'imagerie 3D par Slice and View, inspirée de la technique classique du FIB/SEM et implémentée dans un PFIB (Plasma Focused Ion Beam), a été développée durant ces travaux de thèse. Elle permet aujourd'hui l'acquisition de larges volumes de manière automatique. De même, le procédé d'analyse des mesures de tomographie réalisées sur la ligne de lumière ID16A de l'ESRF a été adapté, afin de limiter au maximum l'intervention humaine et le temps global d'analyse.

Des mesures de déformations ont également été menées à l'ESRF, sur une ligne de nano-diffraction, ID01. Ces expériences ont été réalisées sur des empilements dédiés au collage, hybride ou direct. Il a été possible de mesurer en une seule expérience les déformations présentes dans deux couches de silicium, et de réaliser des mesures *in situ* dans le cuivre.

Dans les travaux de thèse présentés ici, nous montrons les possibilités de techniques synchrotron (imagerie et mesure de déformations) pour la caractérisation d'objets issus de l'intégration 3D. Nous montrons que certaines adaptations des techniques existantes peuvent permettre des analyses routinières à haute résolution pour le milieu de la micro-électronique.

Mots clés : Synchrotron, Tomographie, Intégration 3D, Imagerie 3D, Slice and View, Plasma FIB, Diffraction, Piliers de cuivre, Collage hybride, Analyse de défaillance

---

Abstract

This PhD thesis aims at developing new characterization techniques for 3D integration in microelectronics. More specifically, the focus is set on recent ESRF (European Synchrotron Radiation Facility) beamlines, both for 3D imaging by tomography and for strain measurements by Bragg diffraction.

3D integration aims at reducing the global microelectronics devices footprint and connections length, by stacking the dies on top of one another instead of setting them one to another. This new geometry however requires new connections, such as copper pillars (CuP) and copper pads, used in hybrid bonding. The monitoring of their fabrication process requires their imaging in three dimensions, and the measurement of the strain inside them. Those measurements must be conducted on large areas (100 μm^2), with high resolution (500 nm for strain and 100 nm for imaging). Moreover, given the industrial context of this study, the characterization methods must be as routine and automatic as possible.

To answer those needs, several techniques have been developed in this work.

Two 3D imaging techniques have been made compatible with the requirements of 3D integration characterization. A Slice and View procedure has been implemented inside a single beam PFIB, leading to large volumes 3D automated imaging. The tomography workflow accessible on the ID6A beamline of the ESRF has been adapted, in order to limit the human intervention and beam times. This leads to possible statistical measurements on this beamline.

Strain measurements have been conducted on the ID01 beamline of the ESRF, on silicon and copper stacks meant for direct and hybrid bonding. They allowed for simultenous local strain measurements in two independent layers of silicon, and *in situ* measurements in copper.

In this work, we show the possibilities of synchrotron based techniques (here, tomography and Bragg diffraction) for the chacracterization of 3D integration devices. We show that, provided some adjustments, these techniques can be used routinely for the microelectronics field.

Keywords: Synchrotron, Tomography, 3D integration, 3D imaging, Slice and View, Plasma FIB, Diffraction, Copper pillars, Hybrid bonding, Failure analysis